Matter-Wave Optics with Bose-Einstein Condensates in Microgravity

Von der QUEST-Leibniz-Forschungsschule der
Gottfried Wilhelm Leibniz Universität Hannover

zur Erlangung des akademischen Grades
Doktor der Naturwissenschaften
– Dr. rer. nat. –

genehmigte Dissertation von

Dipl.-Phys. Jan Rudolph
geboren am 26.02.1984
in Hannover

2016

Referent: Prof. Dr. Ernst M. Rasel
Korreferent: Priv. Doz. Dr. Carsten Klempt
Korreferent: Prof. Dr. David Guéry-Odelin

Tag der Promotion: 29.09.2016

Abstract

Quantum sensors based on the interference of cold atoms have advanced to the forefront of precision measurements in geodesy, metrology and tests of fundamental physics. The ultimate potential of these devices is realized using quantum degenerate atoms in extended free fall. This can be achieved on microgravity platforms such as drop towers, parabolic flights, ballistic rockets, satellites and space stations. The transition to mobile and robust devices that can withstand the demands of these environments comes with many challenges. Quantum sensors need to be scaled down and integrated without compromising their performance. In fact, they need to significantly outpace conventional instruments, since microgravity time is an expensive resource and limited to a few seconds at a time on the most accessible platforms.

This thesis describes the construction, qualification and operation of a miniaturized ultra-cold atom experiment that meets these challenges. The QUANTUS-2 apparatus features a payload weight of 147 kg and a payload volume of 0.3 m^3. It generates Bose-Einstein condensates of 4×10^5 ^{87}Rb atoms every 1.6 seconds, a flux of ultra-cold atoms that is on par with the best lab-sized devices. Ensembles of 1×10^5 atoms can be created at a 1 Hz rate. It is currently the fastest machine of its kind and achieves the highest atom number of any atom chip setup. The apparatus continuously withstands peak accelerations of up to 45 g during microgravity campaigns at the drop tower facility in Bremen, Germany. Here, the payload has accrued 208 drops and 9 catapult launches over 24 month. The setup is the first atom optics experiment to stand up to the technical demands of catapult operation. Four condensates can be created and observed consecutively during nine seconds of free fall in a single catapult launch. In total, the experiment has been suspended in microgravity for over 17 minutes. With the record source performance, the repetition rate for microgravity experiments with ultra-cold atoms was increased by a factor of four compared to previous devices. The total atom number was increased by a factor of 40, vastly improving the signal to noise ratio for absorption images of spatially extended clouds. The ensembles can be prepared consistently over many weeks of drop tower operation. The variance of the mean center of mass velocity in two observable directions is 7.3 µm/s and 6.9 µm/s. Magnetic lensing techniques were employed to manipulate the expansion of the ensembles. First results yield a residual expansion rate in three dimensions of $\sigma_v = 116.9 \pm 13.9$ µm/s, which implies a three-dimensional effective temperature of $T = 47.6 \pm 11.3$ pK at an average condensate atom number of $N = 93000$. These values constitute the best collimation of any atomic ensemble and the most promising source for atom interferometry reported to date. Optimizing the current lensing sequence will reduce the expansion rate further to effective temperatures in the femtokelvin regime.

The level of control demonstrated over the condensates is highly relevant for the advancement of matter-wave optics and quantum sensors. Controlling the motion and size of atomic clouds is intrinsically tied to many systematic effects in high precision measurements. QUANTUS-2 will provide a platform to explore and mitigate these limitations on unprecedented time scales of up to seven seconds of free evolution.

Keywords: Bose-Einstein condensates, matter-waves, microgravity

Zusammenfassung

Quantensensoren basierend auf der Interferenz von kalten Atomen sind an die Spitze von Präzisionsmessungen in der Geodäsie, Metrologie und fundamentaler Tests in der Physik gerückt. Das ultimative Potenzial dieser Geräte wird mit quantenentarteten Atomen im freien Fall realisiert. Dies kann in Schwerelosigkeit auf Plattformen wie Falltürmen, Parabelflügen, ballistische Raketen, Satelliten und Raumstationen erreicht werden. Der Übergang zu mobilen und robusten Instrumenten, die den Anforderungen dieser Umgebungen gewachsen sind ist mit vielen Herausforderungen verbunden. Quantensensoren müssen verkleinert und integriert werden ohne dabei ihre Leistung zu vermindern. Tatsächlich müssen sie deutlich schneller operieren als konventionelle Instrumente, da Zeit in Schwerelosigkeit eine teure Ressource ist, die auf den zugänglichsten Plattformen auf wenige Sekunden beschränkt ist.

Diese Arbeit beschreibt die Konstruktion, Qualifizierung und den Betrieb eines Experiments, das diesen Herausforderungen gerecht wird. Die QUANTUS-2 Apperatur verfügt über eine Nutzlast von 147 kg und ein Nutzlastvolumen von 0.3 m^3. Sie erzeugt Bose-Einstein-Kondensate von $4{\times}10^5$ ^{87}Rb Atomen alle 1.6 Sekunden. Dieser Fluss von ultrakalten Atomen ist gleichwertig mit den besten laborgroßen Geräten. Ensembles von $1{\times}10^5$ Atomen können mit einer 1 Hz Rate erzeugt werden. Die Machine ist derzeit die schnellste ihrer Art und erreicht die höchste Atomzahl aller Atom-Chip-Experimente. Während des Betriebs in Schwerelosigkeit am Fallturm in Bremen hält das Experiment kontinuierlich Spitzenbeschleunigungen von bis zu 45 g stand. Über einen Zeitraum von 24 Monaten wurden hier 208 Abwürfe und 9 Katapultstarts durchgeführt. Die Kapsel ist das erste atomoptische Experiment, dass den technischen Anforderungen des Katapultbetriebs gerecht wird. Vier Kondensate können nacheinander während der 9 Sekunden eines Katapultstarts erzeugt und beobachtet werden. Insgesamt hat das Experiment mehr als 17 Minuten in Schwerelosigkeit verbracht. Mit der Leistung der atomaren Quelle wurde die Datenrate für Experimente in Schwerelosigkeit mit ultrakalten Atomen im Vergleich zu vorherigen Geräten um einen Faktor vier erhöht. Die Gesamtatomzahl wurde um einen Faktor 40 verbessert, was in beträchtlichem Ausmaß das Signal-zu-Rausch-Verhältnis für Absorptionsbilder von räumlich ausgedehnten Wolken verbessert. Die Ensembles können konsistent über viele Wochen im Fallturmbetrieb präpariert werden. Die Varianz der mittleren Schwerpunktsgeschwindigkeit in zwei beobachtbaren Richtungen ist 7.3 µm/s und 6.9 µm/s. Eine magnetische Linse wurde verwendet um die Expansion der Ensembles zu manipulieren. Erste Ergebnisse ergeben eine Restexpansionsrate in drei Dimensionen von $\sigma_v = 116.9 \pm 13.9$ µm/s, was einer dreidimensionalen, effektiven Temperatur von $T = 47.6 \pm 11.3$ pK entspricht, bei einer durchschnittlichen Atomzahl im Kondensat von $N = 93000$. Diese Werte stellen die beste Kollimation eines atomaren Ensembles und die aktuell vielversprechendste Quelle für Atominterferometrie dar. Die Optimierung der Linsensequenz wird die Expansionsrate weiter reduzieren zu effektiven Temperaturen im femtokelvin Regime.

Die demonstrierte Kontrolle über die Atome ist höchst relevant für die Weiterentwicklung von Materiewellenoptik und Quantensensoren. Das Beherrschen von Restbewegung und Expanion der Atomwolken ist eng mit vielen systematischen Fehlern in Hochpräzisionsmessungen verbunden. QUANTUS-2 bietet eine Plattform um diese Effekte auf noch nie dagewesenen Zeitskalen von bis zu sieben Sekunden freier Entwicklungzeit zu untersuchen.

Schlagwörter: Bose-Einstein Kondensate, Matteriewellen, Mikrogravitation

Contents

List of Figures 11

List of Tables 15

List of Acronyms 17

1 Introduction 19
  1.1 Matter-Wave Interferometry 20
  1.2 Quantum Degenerate Atoms 22
  1.3 Testing the Universality of Free Fall 24
  1.4 Quantum Sensors in Microgravity 25

I Experimental Setup and Ground-Based Pre-Studies 29

2 Experimental Apparatus 31
  2.1 Catapult Capsule Footprint 32
  2.2 The QUANTUS-2 Capsule 33
  2.3 Laser Systems 34
    2.3.1 First Generation Laser System 34
    2.3.2 Second Generation Laser System 35
    2.3.3 Distribution 38
  2.4 Vacuum Chambers 39
    2.4.1 2D Chamber 40
    2.4.2 3D Chamber 41
  2.5 Atom Chip 42
    2.5.1 Biot-Savart Simulations 43
    2.5.2 Chip Coordinate System 43
  2.6 Detection 43
    2.6.1 Absorption Imaging 44
    2.6.2 Fluorescence Detection 46
  2.7 Magnetic Shielding 47

2.8 Electronics . . . 49
2.8.1 Laser System Stack . . . 49
2.8.2 Computer Control System . . . 50
2.8.3 Current Drivers, Current Response and Switching Times . . . 50
2.8.4 Programmable Chip Fuse . . . 52
2.8.5 Batteries and Power Consumption . . . 52
2.9 Remote Control and Automation . . . 53
2.10 Summary . . . 54

3 Rapid Production of Large BECs with Atom Chips 57
3.1 Loading of the Chip-MOT . . . 57
3.1.1 $2D^+$MOT . . . 58
3.1.2 Chip-MOT . . . 61
3.2 Compression MOT and Optical Molasses . . . 63
3.3 Magnetic Trapping . . . 63
3.3.1 Transfer to Initial Magnetic Trap . . . 63
3.3.2 Transfer to Final Magnetic Trap . . . 64
3.4 Evaporative Cooling to BEC . . . 64
3.5 Comparison . . . 69
3.6 Adiabatic Rapid Passage . . . 71
3.7 Summary . . . 71

II Mobile Operation and Microgravity Campaigns 75

4 Ultra-Cold Atoms in Microgravity 77
4.1 Modifications . . . 77
4.2 Pre-Tests . . . 78
4.2.1 Payload Rotation . . . 79
4.3 Drop Tower Qualification . . . 80
4.3.1 Drop Qualification . . . 81
4.3.2 First Drop . . . 82
4.3.3 Catapult Qualification . . . 83
4.3.4 First Catapult Launch . . . 85
4.4 Post-Correction of Data and Flight Systematics . . . 87
4.4.1 Displacement of Imaging Optics . . . 87
4.4.2 Microgravity Quality and Residual Accelerations . . . 87
4.4.3 Rotations . . . 89
4.5 Summary . . . 93

5 Decompression, Transport and Release 95
5.1 Detection Volume Constraints and Trap Configurations . . . 97
5.2 Adiabaticity . . . 98

5.3 Shortcuts to Adiabaticity (STA) 99
  5.3.1 Non-Interacting Gas in One Dimension 101
  5.3.2 Bose-Einstein Condensates 101
  5.3.3 STA for Atom Chips 102
5.4 Implementation 107
5.5 Decompression and Transport 108
  5.5.1 Transfer to Location **b** 108
  5.5.2 Transfer to Location **c** 114
5.6 Switch-Off 122
5.7 COM Motion and Position Uncertainty 123
5.8 Gradients 128
5.9 Summary 130

6 Matter-Wave Lensing with Atom Chips 131
6.1 BEC Dynamics in Time Dependent Potentials 132
6.2 Magnetic Lensing 135
6.3 Velocity Spread and Effective Temperatures 138
  6.3.1 Anharmonicities 140
  6.3.2 Mitigation Strategies 144
  6.3.3 Experimental Implementation 146
6.4 Magnetic Lensing in Microgravity 147
  6.4.1 First Results 148
  6.4.2 BC-SC-Lens 148
  6.4.3 BC-Lens 160
6.5 Summary 168

7 Conclusion and Outlook 171
7.1 Sensitivity Limits for High-Precision Measurements 174
7.2 Potassium Upgrade for Dual Species Interferometry 175
7.3 Future Microgravity Missions 176
7.4 Other Applications 177
7.5 Summary 177

Bibliography 179

List of Publications 195

Acknowledgements 197

List of Figures

1 Atom interferometry schemes 21
2 A cloud of ^{87}Rb atoms on the onset of Bose Einstein condensation 23
3 The Bremen Drop Tower and drop system schematics 27
4 Schematics of the QUANTUS-2 capsule payload 33
5 CAD drawing of the first generation laser system 34
6 CAD drawings of the individual modules of the first generation laser system . . 36
7 CAD drawing of the second generation laser system 37
8 Layout of the Rb MOPA module 38
9 Hyperfine structure of the ^{87}Rb D_2 line 39
10 Comparison of detection line scans 40
11 CAD drawings of chambers and atom chip setup 41
12 Wire topologies of the atom chip layers 42
13 Schematics of the primary absorption imaging telescope 45
14 Absorption images of an atomic cloud with varying detuning 46
15 Comparison of the two detection angles 47
16 Illustration of the finite element mesh for the magnetic shield simulations . . . 48
17 Picture of the assembled T-Bus stack 50
18 Switching dynamics of the y-coil 51
19 Circuit concept for the coil sets and current drivers 52
20 Switching dynamics of the z-coil 52
21 Measured step response of the coils after circuit extension 53
22 Source scheme to prepare 4×10^5 quantum degenerate atoms in 1.6 s 58
23 Exemplary scan of the longitudinal velocity profile of the 2D$^+$MOT 59
24 Capture volume of the chip-MOT 60
25 Loading rate and decay of the chip-MOT 62
26 Number of atoms captured in the magnetic trap 64
27 Cumulative atom number distribution over the truncation parameter 66
28 Evaporation performance 68
29 Comparison of the fastest BEC machines 70
31 Energy of the adiabatic states over the relative detuning of the RF field 71
30 Absorption images of the m_F state population 71
32 Capsule hull is lowered onto the capsule for the first pre-test 78

33 Rotation of the QUANTUS-2 capsule . . . 80
34 The capsule being hoisted to the top of the drop tube . . . 81
35 Comparison of the standard BEC sequence during the first drop . . . 83
36 Vacuum chamber pressure levels after the first drops . . . 84
37 The capsule sits in the catapult receptacle . . . 85
38 Absorption images from the first successful catapult launch . . . 86
39 Drag deceleration over free fall time . . . 88
40 Tower pressure during the last pumping stage . . . 89
41 Acceleration measurement during a catapult launch . . . 90
42 Rotation rates of the capsule during drop and catapult operation . . . 91
43 Angular speeds of the capsule during drops and catapult launches . . . 92
44 Absorption image of a BEC after transport and decompression . . . 96
45 Comparison of frequency ramps for decompression . . . 99
46 Relationship between trap frequency and trap position . . . 103
47 Comparison of trap trajectories for various transfer times . . . 104
48 Comparison of a polynomial and sinusoidal trajectory . . . 106
49 Comparison of a sinusoidal and two polynomial trajectories . . . 107
50 Scaling of the chip distance and trap frequency with bias coil current . . . 108
51 COM position over hold time at location **b** in lab operation . . . 109
52 Analysis of the sigmoid current ramp . . . 110
53 COM position over hold time at location **b** . . . 112
54 Fitted COM dynamics at location **b** . . . 112
55 COM position uncertainty after transfer to location **b** . . . 112
56 System performance over the µg campaign . . . 114
57 Rescaled TF radii and aspect ratios over hold time in the trap . . . 115
58 Analysis of the sinusoid transfer ramp . . . 116
59 COM position over hold time at location **c** . . . 117
60 Rescaled TF radii and aspect ratio over hold time in the trap . . . 118
61 Frequencies of low-lying modes of the BEC during transfer . . . 119
62 Quadrupole mode fit to TF radii over hold time in the trap . . . 120
63 System performance over the µg campaign . . . 121
64 Measured current response to the switch-off protocol . . . 122
65 COM position uncertainty after transfer to location **b** . . . 123
66 COM position uncertainty over the trap frequency . . . 125
67 COM velocity and velocity scatter in microgravity . . . 126
68 COM velocity and velocity scatter in microgravity after magnetic lens . . . 127
69 A lensed BEC in m_F state mixture . . . 128
70 COM position after magnetic lensing . . . 129
71 Free expansion of the condensate observed at different times of flight . . . 133
72 Four BECs observed 25, 50, 75 and 100 ms after instantaneous switch-off . . . 134
73 Time evolution of the size of the cloud during a magnetic lensing sequence . . 136
74 Phase space evolution during magnetic lensing with harmonic potential . . . 137
75 Evolution of the phase space distribution during an anharmonic lensing pulse . 141

76 Comparison of the lensing potential with and without anharmonicities 142
77 Time evolution of the radii 142
78 Phasespace evolution during anharmonic lensing with position offset 143
79 Time evolution in phase space after magnetic lensing 145
80 Size and shape comparison between lensed clouds and a freely expanding BEC 149
81 Scaling functions for the trap frequencies 150
82 Calculated field response of the BC-SC-lens 151
83 Lens pulses optimized to collimate the two steep trap axes with a BC-SC-lens . 152
84 Comparison of optimal z-collimation conditions for different values of T_0 . . . 153
85 Absorption images of lensed clouds after 300 ms TOF (Drop #111) 154
86 Time series of BECs after a BC-SC-lens in the $m_F = 2$ hyperfine state 155
87 Time series of BECs after a BC-SC-lens in the $m_F = 0$ hyperfine state 157
88 Comparison of the BC-SC-lens data to the scaling approach simulations 158
89 Linear fits to the accumulated BC-SC-lens data 158
90 Scaling functions of the BC-lens over the current scaling 160
91 Time series of BECs after a BC-lens in the $m_F = 2$ hyperfine state 162
92 Time series of BECs after a BC-lens in the $m_F = 0$ hyperfine state 165
93 Comparison of the BC-lens data to the scaling approach simulations 166
94 Linear fits to the accumulated BC-lens data 166
95 Composite BC-lens data for the three geometric axes 167
96 Three-dimensional illustration of the TOF series for both lens sequences 169
97 CAD drawing of the MAIUS-1 mission payload 176

List of Tables

1 Comparison of microgravity platforms 26
2 Weights of the capsule components 32
3 Technical data of the magnetic shield assembly 48
4 Simulations and measurements of the magnetic field attenuation 48
5 Properties of the various current carrying structures 54
6 Summary of the test conditions 79
7 Parameters of the trap configurations used in the microgravity campaigns . . . 97
8 Calculated time constraint for pseudo-adiabatic decompression 98
9 Comparison of lens attributes 147
10 Systematic phase contributions of a Mach-Zehnder type atom interferometer . 174

List of Acronyms

μg	Microgravity
AI	Atom Interferometry
AOM	Acousto-Optic Modulator
ARP	Adiabatic Rapid Passage
BC	Base Chip
BEC	Bose-Einstein Condensate
CCD	Charge-Coupled Device
CCS	Computer Control System
COM	Center of Mass
DDS	Direct Digital Synthesis
DFB	Distributed Feedback
DKC	Delta-Kick Cooling
ECDL	External Cavity Diode Laser
EOM	Electro-Optic Modulator
FPGA	Field-Programmable Gate Array
GPE	Gross-Pitaevskii Equation
GR	General Relativity
HV	High Vacuum
IMU	Inertial Measurement Unit
IP	Ioffe-Pritchard
MOPA	Master Oscillator Power Amplifier
MOT	Magneto-Optical Trap
OD	Optical Density
PD	Photo Diode
PSD	Phase Space Density
QPN	Quantum Projection Noise
RF	Radio Frequency
SC	Science Chip
TA	Tapered Amplifier
TF	Thomas-Fermi
TOF	Time of Flight
UFF	Universality of Free Fall
UHV	Ultra-High Vacuum

CHAPTER 1

Introduction

Precision measurements with cold atoms have become a cornerstone in many research fields such as inertial sensing [1], metrology [2] and precision timekeeping [3]. The sensitivity of these measurements is quickly overtaking their classical counterparts while their full potential has yet to unfold. One of the limitations of atom interferometers is the tight restriction gravity imposes on the interrogation time. Increasing the free fall time of matter-waves on earth much further than the current limit of less than three seconds appears unfeasible for many reasons. Considerable efforts are being made to push quantum sensors beyond these limits by operating in extended free fall on microgravity (µg) platforms [4–6] and in space [7, 8]. Here, ultra-cold atoms can evolve and be probed on unprecedented time scales, improving their sensitivity to inertial effects by orders of magnitude. The advent of space worthy quantum sensors will enable many applications in navigation, Earth observation [9], geophysics, seismology, geodesy and tests of fundamental physics beyond the lab environment.

A prominent proposal for fundamental physics research with atom interferometry is testing general relativity (GR) [10–16] and seeking constrains for theories beyond the standard model. One of the pillars of GR is Einstein's equivalence principle with its three elements: Lorentz invariance, local position invariance and the universality of free fall (UFF) [17]. The UFF asserts that in the absence of any additional forces, all bodies fall under the same acceleration i.e. the gravitational acceleration of a body is independent of its composition. Matter-wave interferometry allows for the precise comparison of the gravitational acceleration of individual atoms. Thus, atom interferometry (AI) allows to probe properties inaccessible to classical tests such as neutron excess, nuclear binding energy, electrostatic energy density and spin [18, 19]. Many proposals suggest performing GR tests in µg and in space to reap the benefits of long interrogation times and a quiet, seismic noise-free environment with large variations in altitude, velocity and gravitational potential.

However, most cold atom experiments are lab-sized, cumbersome devices which need to be miniaturized significantly for µg operation. Moreover, the challenging conditions of the particular µg environment are often in stark contrast to the well controlled conditions of a typical lab setting. More importantly, all the necessary alterations need to be made without compromising the source performance of the systems. Since the projected source flux requirements are on par with the best lab-based devices [7], cold atom technology is pushed to its limits.

Apart from the technological constrains, many scientific challenges need to be addressed when advancing to new parameter ranges. Taking atom interferometry to mascroscopic time scales of several seconds significantly raises the requirements for the control over the atomic clouds. For high precision measurements, the position and velocity of the ensemble need to be controlled on the micrometer and micrometer per second level, respectively. First, the atoms move independently of the apparatus while in free evolution and any residual dynamics may cause them to drift away from the detection volume. Second, the sensitivity of the interferometric measurement is bounded by the residual motion of the atoms. Additionally, new collimation techniques must be developed to manage the expansion of the cloud. The effective temperature of the ensemble needs to be reduced to the picokelvin range to sufficiently reduce systematic effects in the interferometer linked to the cloud size.

To accomplish these goals and realize competitive tests of fundamental physics in extended free fall, one requires a suitable source setup, continuous access to a µg environment for extended measurement campaigns, and precise modeling of the experimental steps to guide the investigations. These requirements are uniquely realized within the QUANTUS collaboration, a consortium of German universities led by the Leibniz Universiät Hannover and funded by the German space agency DLR (Deutsches Zentrum für Luft- und Raumfahrt). The ultimate goal of the collaboration is a competitive test of the UFF comparing rubidium and potassium atoms in a dual species matter-wave interferometer in space. The experiment described in this thesis is the second generation of ultra-cold atom experiments built within the QUANTUS project.

1.1 Matter-Wave Interferometry

Atoms display wave-like properties at low energy scales, undergoing classical wave phenomena like deflection and interference [20]. Interferometers based on matter-waves have become a widespread and versatile tool in precision measurements [21]. Atoms are put into a quantum superposition of at least two distinct states that follow spatially different paths. Afterwards, the separate parts are brought back together and interfered. The interference pattern is indicative of the difference in phase accumulated along the different paths. The evolution of the phase for each part of the wave packet is influenced by the forces acting on the atom, making it a sensitive probe for a variety of inertial effects. Matter-waves have been used to measure the

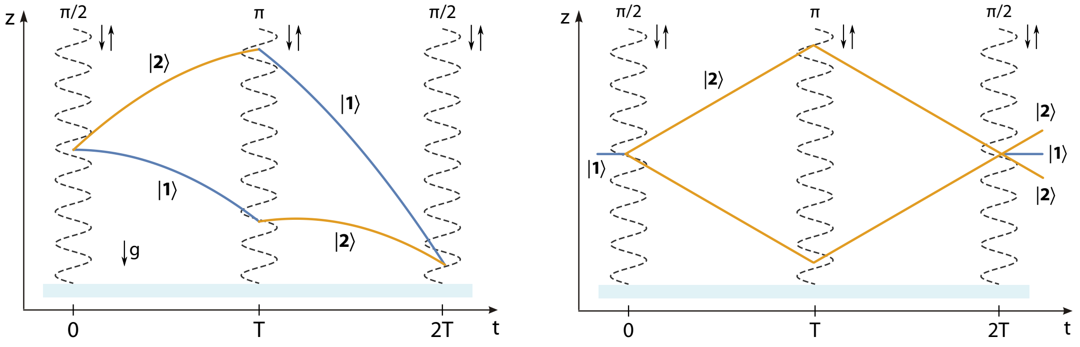

(a) A Mach-Zehnder interferometer under gravity.

(b) A double diffraction scheme in microgravity.

Figure 1: Atom interferometry schemes plotting the center of mass for the separated parts of the wave packet. Pairs of appropriately designed laser beams originate at the top and are retro-reflected at the bottom mirror. The four individual light fields form two pairs of beams. In figure (a), only one of the pairs is resonant due to the Doppler shift causes by the gravitational acceleration. In figure (b) both pairs are degenerate and can drive transitions simultaneously, resulting in a symmetric diffraction in opposite directions. The two distinct states of the atom are labeled as $|1\rangle$ and $|2\rangle$.

gravitational constant [22, 23] and the fine-structure constant [2], as well as accelerations [24–26] and rotations [27–31].

There are various ways to coherently split, redirect and interfere matter-waves [21, 32]. The atoms can be separated in momentum space via transfer of photon momenta either through stimulated Raman transitions, which also put them into a superposition of internal states [33], or via Bragg diffraction [34], leaving the internal state unchanged. Raman transitions have the advantage of internal state labeling, allowing for state selective imaging even if the output ports of the interferometer can not be resolved spatially. This is well suited for thermal sources of laser-cooled atoms where the kinetic energy of the ensemble exceeds the photon recoil energy. Bragg diffraction is a promising tool for AI with ensembles at sub-recoil temperatures as they can more easily be resolved due to their reduced expansion rate. Since the internal state remains unchanged in this case, to lowest order the interferometer is intrinsically insensitive to many systematic effects such as the ac Stark shift and temporal variations of the Zeeman effect. Additionally, the method can easily be extended to higher order Bragg diffraction and combined with Bloch oscillations to increase the momentum transfer and wave packet separation [35–38].

The most common interferometry scheme to measure the gravitational acceleration acting on an ensemble of atoms is a Mach-Zehnder type configuration (see Figure 1a). A $\pi/2$-pulse splits the atomic sample by putting every atom in an equal superposition of two distinct states, $|1\rangle$ and $|2\rangle$, and transfers momentum to one part of the superposition. After some time T of free evolution, a π-pulse reverses the superposition and thus redirects the paths to coincide after another time T. At this point, both paths can be superimposed by another $\pi/2$-pulse. Assuming a uniform gravitational field over the size of the interferometer, the total detected phase difference between the two interferometer paths to lowest order is

$$\Delta\phi = -k_{\text{eff}}\, g\, T^2. \tag{1.1}$$

It only depends on the acceleration g experienced by the atoms, the frequency of the lasers with effective wavenumber $k_{\text{eff}} \approx 2\hbar k$ and the total time $2T$ spent in the interferometer. Hence, the two strategies to enhance the sensitivity are increasing the momentum transfer from the lasers through large momentum beam splitters [39, 40] and increasing the measurement time. The main disadvantages of large momentum transfer are the decreasing beam splitting efficiency and the need for high laser power to suppress spontaneous emission. On the other hand, extending the interferometry time to more than two seconds in a lab experiment requires the construction of an interferometer setup approaching ten meters in length [41–43]. The extraordinary limitation in extending the free fall time in lab-based experiments further is the biggest motivation behind taking matter-wave sensors to microgravity.

On timescales of several seconds, it is desirable that the atoms reconvene at their point of origin as the recoil velocity exceeds one centimeter per second. This is especially useful in μg operation, where the apparatus is at rest with respect to the atoms and the ensemble would migrate out of the interferometry beams. Instead, a double diffraction configuration can be used to symmetrically diffract the atoms in opposite directions with two light gratings of perpendicular polarization [44, 45]. This increases the momentum transfer, the wave packet separation and thereby the phase sensitivity by a factor of two (see Figure 1b). The center of mass (COM) of the atoms remains at the same location throughout the sequence, an ideal condition for UFF tests. First results using double Bragg diffraction techniques reached transfer efficiencies of over 95% [46], making it a promising technique for high precision matter-wave interferometry on macroscopic time scales.

1.2 Quantum Degenerate Atoms

The quantum superposition prepared in these experiments is a single particle phenomenon. Using more than one atom at a time allows for many simultaneous measurements, the results of which can be averaged to reduce the influence of random noise sources on the signal. If the measurement is extended to an ensemble of atoms, collective properties such as the temperature play a huge role in the usefulness of the sample since it determines the momentum width and expansion rate of the cloud. Thermal atoms at temperatures of several microkelvin have been used successfully in many experiments. However, a lower momentum width is required to

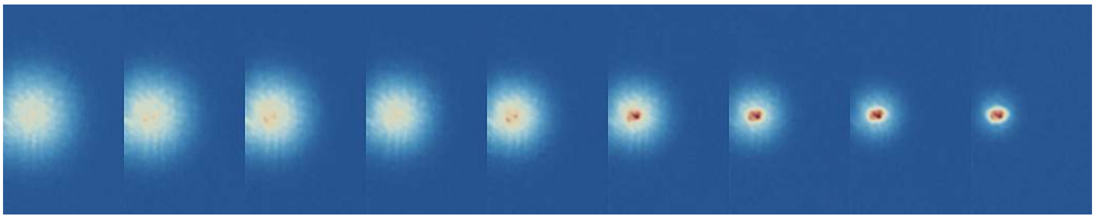

Figure 2: A cloud of ^{87}Rb atoms on the onset of Bose Einstein condensation. From left to right, the absorption images show an ensemble of atoms being cooled passed the critical temperature. All images were taken after 18 ms time of flight (TOF), showcasing the disparity in size and expansion rate between thermal and degenerate clouds after release from a typical trapping potential with geometric mean trap frequency $f_{\text{geo}} = 225\,\text{Hz}$.

realize high fidelity beam splitters and may be imperative to reduce systematic errors such as inhomogeneous dephasing and wave front distortions [47]. Therefore, most experiments employ velocity selection methods along at least on geometric axis which greatly reduces the atom number[33].

Cooling an ensemble of bosonic atoms such as ^{87}Rb past a critical temperature leads to macroscopic occupation of the lowest energy level of the confining potential, thus realizing a state of matter called Bose-Einstein condensate (BEC) [48]. The atoms in the condensate become indistinguishable and can now be described by a single macroscopic wave function, similar to photons in a laser occupying the same mode of the electromagnetic field. Cooling atoms to quantum degeneracy comes with many advantages for high precision AI. BECs feature a smaller initial size, slower expansion rates and a coherence length that extends over the entire cloud (see Figure 2).

BECs have not always been considered a useful source for AI for two reasons. First, the extensive cooling process generally leads to a low source flux. For example, laser cooled atoms are typically produced at a rate of 10^9 atoms per second whereas producing a BEC of 10^6 atoms can take several tens of seconds. Second, quantum degenerate atoms exhibit high densities and strong mean field interaction that lead to unwanted systematic effects. The first concern can be alleviated by showcasing outstanding technological improvements that put the atomic flux of BEC machines in competition with thermal sources (see Chapter 3). The second reservation becomes irrelevant in a µg environment, where the ensemble can freely expand to several times their initial size before the first interferometry pulse.

Additionally, magnetic and optical lensing techniques enable the manipulation of the size and density of the ensemble and allow for the operation in a regime where mean field effects are negligible. One experiment demonstrated that the expansion rate of an atomic cloud can be reduced to 69 µm/s in two dimensions, equivalent to one-dimensional effective temperatures of 50 pK [49]. However, the three-dimensional effective temperature remained at 567 pK due to the unaltered expansion along the third axis. The requirements for a ten second interferometer on a dedicated space mission have been stated as 70 pK in three dimensions [7]. The quality of the lens has since become the most relevant criterion for AI on macroscopic timescales. The performance of the lens scales with the ratio of initial to final size, thus achieving the same expansion rates with thermal clouds as with BECs entails an increase in cloud size to several tens of millimeters – challenging sizes for aberration-free lensing (see Chapter 6). Therefore, using quantum degenerate atoms may be a mandatory requirement to perform high-precision interferometric measurements such as UFF tests on macroscopic timescales.

1.3 Testing the Universality of Free Fall

The sensitivity of UFF tests is typically defined by a quantity called the Eötvös-ratio:

$$\eta \equiv \frac{\Delta a}{a} = 2\frac{|a_1 - a_2|}{|a_1 + a_2|}. \tag{1.2}$$

Here, a_1 and a_2 are the accelerations experienced by two test bodies. The best constrains for violations of the UFF using classical test masses have been set by lunar laser ranging at $\eta = (-1.0 \pm 1.4) \times 10^{-13}$ [50] and torsion balance experiments at $\eta = (0.3 \pm 1.8) \times 10^{-13}$ [51]. The former compares the free fall of the earth and the moon in the gravitational field of the sun while the latter compares beryllium and titanium test bodies in the gravitational field of the earth. A hybrid test, comparing the free fall of ^{87}Rb atoms to a falling corner cube resulted in an Eötvös-ratio of $(4.3 \pm 6.4) \times 10^{-9}$ [52].

Quantum tests of the UFF comparing free falling matter-waves have currently reached $\eta = (2.8 \pm 3.0) \times 10^{-8}$ comparing the two rubidium isotopes ^{85}Rb and ^{87}Rb [53], $\eta = (0.2 \pm 1.6) \times 10^{-7}$ comparing the two strontium isotopes ^{87}Sr and ^{88}Sr [54], and $\eta = (0.3 \pm 5.4) \times 10^{-7}$ comparing ^{87}Rb to ^{39}K atoms [55]. Despite not yet having caught up with the classical tests, they are quickly improving as highlighted by the fact that all these tests were reported within the last 24 month. Large atomic fountains setups with target sensitivities starting in the 10^{-13} range are under construction or already in operation [41–43].

Taking differential matter-wave interferometry to a sensitivity beyond classical UFF tests comes with a set of challenges that can be divided into three groups [7, 15, 43]:

- Systematic errors specific to the device design and measurement environment. These include gravity gradients, magnetic fields and gradients, the linewidth and wavefront curvature of the interferometer beams, and spurious accelerations and vibrations in the setup.

- Systematic errors due to the operation of the differential measurement. The most crucial quantities are the co-location of the two atomic clouds, their differential velocity, their interactions, the mixing between the two, and the overlap of the interferometers.

- Demands on the maturity of ultra-cold atom technology. These include a high degree of robustness and miniaturization, a sufficiently short cycle time, a high source atom number, excellent control of the COM dynamics, and the ability to engineer the velocity spread of an atomic cloud to tailor its density over the entire measurement cycle.

The first group of systematic errors must be addressed on a case by case bases as many of the requirements scale with the size of the apparatus. The individual items can generally be investigated in lab-based devices. The limitations listed in the second group require extensive modeling and careful selection of proper atomic species. The requirements in the third group shape up to be the most crucial milestones in the development high precision quantum sensors. Miniaturizing the sensors can alleviate some of the most stringent limitations such as magnetic field and gravity gradients. However, many of the items can only be tested and investigated in a µg environment. The experiment described in this thesis aims to resolve the obstacles listed in that third group.

1.4 Quantum Sensors in Microgravity

The efforts of bringing ultra-cold atoms to space are rewarded with pristine conditions for high precision measurements. The low noise environment permits long interrogation times and excellent control of starting conditions to coherently address multiple atomic species simultaneously. The absence of gravitational sag allows for shallower traps and smaller expansion rates. Several atomic species can be prepared with the same COM position and dynamics. The atoms are initially at rest and no launch or levitation technique is necessary. This is advantageous since such methods generally act differently on different atomic species.

Bringing matter-wave sensors to space can ideally be accomplished in a step by step approach. There are several µg platforms that can be used to expand and test the technology before a dedicated satellite mission (see Table 1). While the µg duration is highly limited in the most accessible platforms, these environments allow for continuous maintenance and adjustments on the setup. Such missions aim to extend the ability of the sensors to new limits and pave the way for autonomous devices that benefit from longer continuous measurements. Pioneering µg experiments have been demonstrated on parabola flights by the ICE collaboration [6] and at a drop tower facility by the QUANTUS project [4, 56].

The QUANTUS collaboration spans several generations of experiments that have established and advanced the field of ultra-cold atoms in µg. In 2007, the first generation (QUANTUS-1)

Table 1: Comparison of microgravity platforms sorted by continuous µg duration. While the lowest residual acceleration budgets are achieved on space platforms, adequate conditions can be found on more accessible facilities.

Platform	µg quality [g]	µg duration
Satellite	$< 10^{-6}$	months to years
International Space Station	10^{-5}	days to months
Space carrier	10^{-6}	days to months
Ballistic rocket	10^{-5}	several minutes
Parabola flights	10^{-2}	20 seconds
Drop Tower Bremen	10^{-5}	4.7 to 9.4 seconds
Einstein Elevator^{+}	$< 10^{-5}$	4 seconds

$^{+}$ currently under construction at the Leibniz Universität Hannover

created the first BEC in weightlessness, dropping a miniaturized ^{87}Rb BEC machine at the Bremen Drop Tower (see Figure 3). The Bremen Drop Tower offers a 110 m drop tube that can be evacuated for free fall experiments up to three times per day. Devices need to be integrated into one of two capsule variants, a 2.1 m long drop version or a 1.3 m long catapult capsule. The former is hoisted up and dropped from the top of the tower for 4.7 s of free fall. The smaller and lighter catapult capsules are launched from the bottom via a hydraulically driven system under the drop tube with a peak acceleration of 35 g (see Figure 3). While the catapult doubles the time in microgravity to 9.4 s, it puts additional demands on the robustness of the setup. In both cases, the capsule is decelerated by quasi-viscous friction in a container filled with Styrofoam grain. The peak deceleration reaches values of up to45 g. The QUANTUS-1 setup is housed in a drop capsule and has been dropped 441 times, which amounts to approximately 35 min in µg. It pioneered matter-wave interferometry with magnetically collimated BECs and extended the interferometry time to $2T = 670$ ms. A collimated BEC was observed after two seconds of free expansion in µg [56].

QUANTUS-1 was conceived as a pathfinder mission to demonstrate the preparation of BECs in µg and while interferometry equipment was later added to the system, it was never designed for high precision measurements. The main obstacles are the vacuum quality, the source performance, the magnetic shielding, the magnetic permeability of vacuum chamber components, and limited optical access for the interferometry beams.

This Thesis

The subject of this thesis is the second generation drop tower experiment QUANTUS-2, an even further miniaturized ^{87}Rb BEC machine that is integrated into the catapult capsule. It

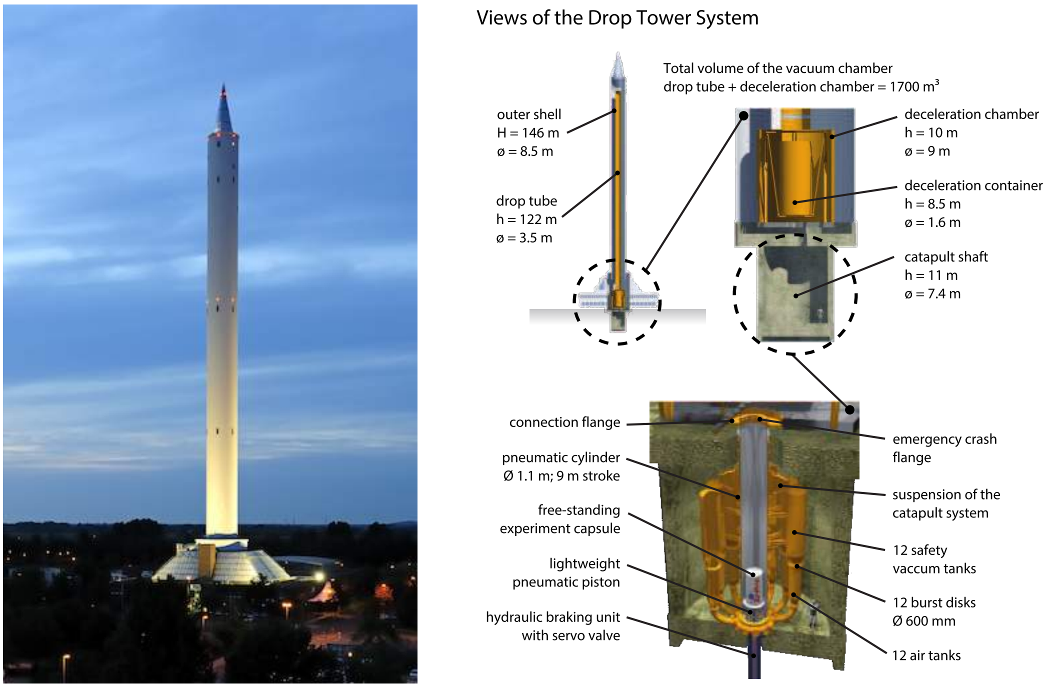
Views of the Drop Tower System
Total volume of the vacuum chamber
drop tube + deceleration chamber = 1700 m³
outer shell
H = 146 m
ø = 8.5 m
drop tube
h = 122 m
ø = 3.5 m
deceleration chamber
h = 10 m
ø = 9 m
deceleration container
h = 8.5 m
ø = 1.6 m
catapult shaft
h = 11 m
ø = 7.4 m
connection flange
pneumatic cylinder
Ø 1.1 m; 9 m stroke
free-standing
experiment capsule
lightweight
pneumatic piston
hydraulic braking unit
with servo valve
emergency crash
flange
suspension of the
catapult system
12 safety
vaccum tanks
12 burst disks
Ø 600 mm
12 air tanks

Figure 3: The Bremen Drop Tower and drop system schematics. The facility is the most accessible μg environment that a comparable μg quality as dedicated space missions. It features two operating modes, dropping capsules from the top for 4.7 s and catapulting capsules from the bottom for 9.4 s of free fall time [57].

features a novel source setup consisting of a pre-cooled atomic beam from a two-dimensional magneto-optical trap that is fed directly into a multi-layer atom chip. The two-chamber design is machined from non-magnetic materials such as titanium and aluminum alloys and is encased by a two-layer cylindrical magnetic shield. Additionally, the device is equipped with a laser system that provides light beams for Bragg and Raman interferometry. Despite these upgrades, the payload volume of the apparatus was reduced by a factor of two to use the catapult mode of the drop tower and enable the adaptation of the device for a sounding rocket mission.

Construction of the apparatus began in July 2009 while the μg qualification process of the device was completed in 2014 with the first successful catapult launch. The capsule has since been dropped and catapulted 217 times and continues its μg campaigns. This thesis covers the characterization of the atomic source, the tools and methods to produce large BECs with atom chip technology and a comparison to other approaches (Part I). Afterwards, the necessary engineering efforts for successful drop tower operation and the μg campaigns of the apparatus are presented (Part II). Here, the systematic effects specific to the drop tower operation are analyzed and various strategies for post-correction of the data are discussed. An estimate of the residual acceleration budget and thus the µg quality is derived from experimental data. Additionally, this part includes the methods and results of controlling the center-of-mass dynamics of the condensates via adiabatic and non-adiabatic transfer and decompression protocols. These strategies are efforts to coherently transfer atomic ensembles away from the vicinity of the atom chip surface to allow for unimpeded interferometric measurements. Furthermore, the progress in developing matter-wave lensing techniques with anharmonic chip potentials, that enable observation of the BECs after several seconds of free evolution, are presented. Extensive modeling efforts are contrasted with experimental data acquired in µg campaigns. In the conclusion, the results of this work and its impact on high-precision measurements with transportable quantum sensors are discussed. Future extensions of the experimental payload are presented and prospective capabilities of QUANTUS-2 as a high-precision matter-wave interferometer are considered.

Part I:

Experimental Setup and Ground-Based Pre-Studies

A High-Flux BEC Source for Mobile Atom Interferometers

> ”It’s supposed to be automatic, but actually
> you have to push this button.”
>
> — JOHN BRUNNER

CHAPTER 2

Experimental Apparatus

This chapter covers the most relevant parts of the construction and qualification of the apparatus. As the second generation of the drop tower experiments within the QUANTUS collaboration, the project builds on the experiences and successes of its predecessor, the first mobile BEC machine of its kind [58]. The greatest limitations of the first generation are the source performance, in both cycle time and atom number, and the infeasibility of performing high-precision measurements. The latter is a result of design and hardware limitations owing to the proof-of-principle nature of the setup and in parts simply due to lack of space in the crowded drop capsule. In many cases components are still comprised of standard lab equipment as most elements did not yet exist in miniaturized form.

The biggest challenges in designing and constructing the QUANTUS-2 apparatus were to reduce the payload weight and volume even further, by a factor of two, while simultaneously improving the performance of the setup by several orders of magnitude. This was achieved by continuing the miniaturization and integration efforts and by developing and implementing new technologies such as a dual vacuum chamber design, a multi-layer atom chip and a multi-species laser system that can withstand the mechanical strain of the drop tower's catapult mode. The objective of this generation is thus twofold: push the limits of ultra-cold atom technology to realize the most compact and robust BEC machine while improving the source performance and versatility of the setup to compete with the best lab-based devices. The use of non-magnetic materials and extensive magnetic shielding together with the expandability to multi-species operation lifts the scope of the project above a pure technology demonstrator, to a unique and promising tool for high-precision measurements in an environment that is inaccessible to other devices.

Next to the various upgrades and improvements, the first and second QUANTUS generations are differentiated by the high degree of customized integrated components as well as the overall ruggedness and autonomy of the latest device. Most electronics were specifically designed and developed for the use in QUANTUS-2. The compactness and modularization of the laser systems allows for a low maintenance machine that can be operated remotely for long periods of time without the need for manual optimization. The extensive design, construction and qualification of the apparatus is already documented in several theses and detailed accounts on specific components can be found in Refs. [59–65]. This chapter aims to summarize the essential elements and most interesting aspects of the device.

2.1 Catapult Capsule Footprint

Table 2: Weights of the capsule components

Capsule component	Weight (kg)
Stringers (4)	36.8
Platforms (4)	62
Base structure (batteries & CCS)	121
Top lid	30.2
Hull	38.5
Nose cone, connection rod	10.2
Taring weight	7.5
Capsule net weight	306.2
Payload component	Weight (kg)
MuMetal shield	42.6
Vacuum system	29.95
Laser system	29.35
Electronics & cables	42.9
Watercooling	2
Payload weight	146.8
Capsule gross weight	453

The design and layout of the apparatus is largely predetermined by the structure and dimensions of the catapult capsule (see Figure 4) as well as the other technical restrictions connected to catapult operation in the drop tower. These restrictions are the overall weight of capsule and payload, the weight distribution and the rigidity of the assembly. The base structure of a catapult capsule comprises four stringers with 1341 mm length, encasing a variable number of platforms with a diameter of 650 mm. These platforms can be distributed at arbitrary heights above the base structure at 259 mm and below the lid at 1212 mm, yielding a total payload volume of approximately 0.32 m^3.

To reach the full 9.5 s of free fall time available in the catapult mode, the gross weight of the complete capsule is limited to 400 kg. Any additional weight reduces the launch height and thereby the microgravity time. Due to technical limitations of the launch mechanism, the total mass may not exceed 500 kg [66]. Each individual capsule platform has a maximum weight of 100 kg and the point load may not exceed 50 kg. For catapult operation, the COM of the capsule needs to be within a cylinder of 1 mm diameter around the vertical axis. However, the overall weight distribution has to be very uniform as well, to minimize tilt and rotation during flight (see Chapter 4).

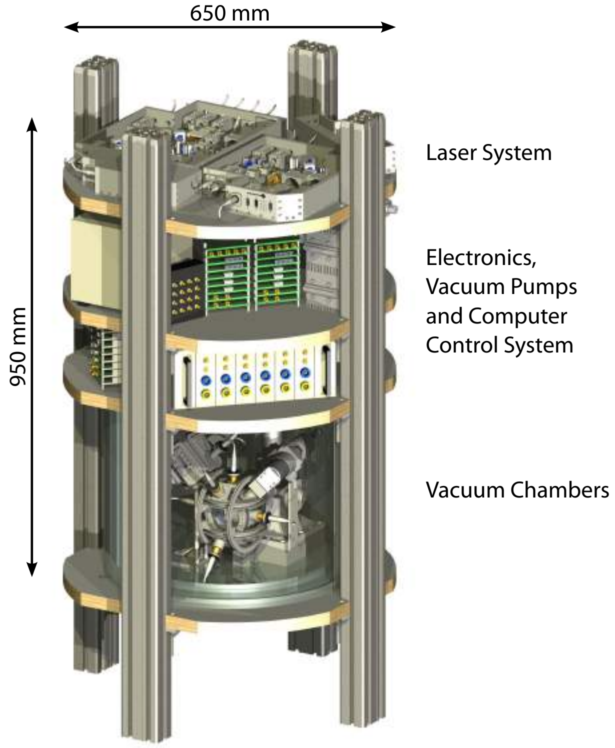

Figure 4: Schematics of the QUANTUS-2 capsule payload. The assembly consists of four platforms, each with a diameter of approximately 650 mm. The complete laser system for multi-species operation is restricted to the top platform. Depicted here is the first generation laser system. The two middle platforms house the electronics, the vacuum pumps and the computer control system. The volume between the middle and the bottom platform is magnetically shielded with a cylindrical two-layer MuMetal assembly. The vacuum chamber and atom chip setup is located within the shielded region. The batteries of the system are located on the outside of the magnetic shield and below the bottom platform. The total payload volume is approximately 0.32 m^3. The payload weight including the MuMetal shield is 146.8 kg.

The forces arising at launch and impact of the capsule call for stiff and rigid mounting of the components to withstand the accelerations without displacement. However, shock absorbers are not employed in the setup since most industrial absorbers are designed against shocks with a characteristic time scale of ~10 ms, while the acceleration in the tower is of a quasi-steady type (see Chapter 4). Thus, absorbers may lead to amplification of the accelerations [66]. Instead, all components are rigidly mounted to the capsule and the setup is smoothly decelerated by polystyrene grain in the deceleration container.

2.2 The QUANTUS-2 Capsule

The QUANTUS-2 setup is integrated in a capsule variant with a total of six platforms. The payload segment holds four platforms and the capsule bottom structure the remaining two. From top to bottom, the payload platforms are used for the laser system, vacuum pumps, computer control system (CCS) and electronics, MuMetal shield and vacuum chambers (see Figure 4). The capsule bottom holds an additional CCS necessary for the drop tower operation as well as the majority of the batteries.

The total weight of the setup is 453 kg, 306.2 kg of which is owed to the application specific capsule structure (see Table 2). The payload and its support structure (stringers and platforms)

Figure 5: CAD drawing of the first generation laser system. The system is split in two four modules: two functionally identical reference laser modules for Rb and K, a Rb module with the respective laser sources and a Rb+K mix module, in which the K lasers are located. Here, all light sources converge, are mixed, amplified and coupled to polarization maintaining single-mode optical fibers for distribution to the vacuum chambers. Adapted from Ref. [61].

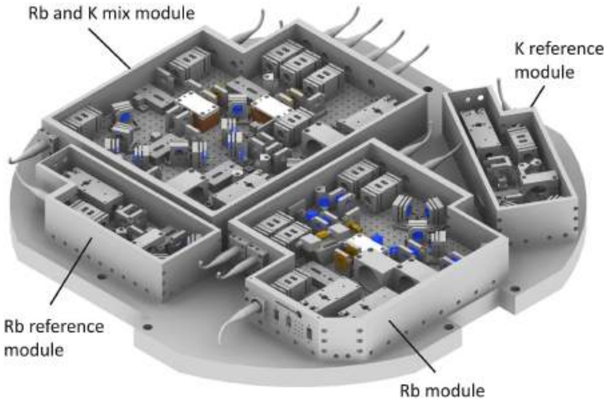

in the ground-based tests amounts to 245.8 kg, where the payload contributes only 146.8 kg of the mass, including a two-layer MuMetal shield (42.6 kg). Thus, depending on application the footprint of the assembly could be reduced further using a different support structure. The power consumption of the entire setup in operation is 363.9 W. Hence, it can easily be run on commercially available accumulators for several hours at a time.

2.3 Laser Systems

Two separate laser systems were constructed for the experiment. The first variant was used to operate the system early on in ground-based pre-studies (Part I) and characterize the apparatus while a second generation was under construction. The latter is designed for and tested in catapult operation (Part II). Each of the systems fits on a single catapult capsule platform.

2.3.1 First Generation Laser System

The first generation design is conceptualized to provide all the light fields for trapping, cooling and detecting both rubidium (Rb) and potassium (K) atoms. Due to the vicinity of their respective cooling transition, located at 780 nm and 767 nm, those light fields may share common optical components, both active and passive. This allows for a compact system using mostly conventional opto-mechanics and only moderate miniaturization efforts. Since the main focus of this laser system generation was the creation and optimization of ultra-cold gases, it lacks atom interferometry capabilities for K and the Rb Raman option was never implemented.

The system consists of four modules, each on its own 15 mm tall aluminum (Certal) breadboard with 10 mm thread spacing (see Figure 5). All modules are self-contained with solid aluminum walls and lid. The modules are interconnected via polarization maintaining optical fibers `[Schäfter-Kirchhoff PMC-780]` mounted in the walls.

All laser sources consist of ridge waveguide laser diodes `[Eagleyard EYP-RWE-0780-02000]` in a miniaturized external cavity diode laser (ECDL) configuration [67, 68]. Wavelength discrimination is achieved via an interference filter inside the cavity and adjustment of the cavity length through a piezo-electric actuator. Their design and construction are described in Refs. [60, 61].

Two reference laser modules for rubidium and potassium atoms provide light beams that are stabilized to the $|F = 2\rangle \rightarrow |F' = 2 \,/\, F' = 3\rangle$ crossover transition of the D2-line of ^{87}Rb and the $|F = 1\rangle \rightarrow |F' = 2\rangle$ transition of the D2-line of ^{39}K, respectively. The stabilization is accomplished via Doppler-free saturated absorption spectroscopy [69].

A Rb module houses the cooling and repumping lasers for that atomic species. Input light from the Rb reference module is mixed with the repumper for frequency stabilization. The cooling laser is in turn stabilized to the repumping laser using the same technique. The majority of the output power of both lasers is delivered to the Rb-K Mix module via optical fibers.

The Rb-K mix module has two functions: housing the K cooling and repumping lasers including their frequency stabilization and mixing all four laser beams for 2D- and 3D-MOT operation. The locking scheme between the lasers is identical to the Rb lasers. The most important feature that allows for such a compact system is the simultaneous amplification of all four laser beams in each of the two tapered amplifiers (TAs) `[m2k TA-0780-1000]`. This is possible due to the broad wavelength acceptance of the gain medium. The amplification spectrum is centered around 775 nm and can be shifted slightly by varying the temperature of the TA. We find that in dual wavelength operation the Rb lasers are dominant but leave enough gain for the K lasers. However, only the atomic source for Rb has been added to the system and all further descriptions refer to single species, Rb operation.

Each of the TAs generates up to 1 W of output power in a rubidium cooling to repumping ratio of more than ten to one. The total light power available for 2D-MOT operation is 120 mW, while the 3D-MOT is operated with a total power of 92 mW. A small part of about 2 mW of the cooling light is split off and used for optical state preparation via the $|F = 2\rangle \rightarrow |F^{'} = 2\rangle$ transition as well as for fluorescence detection and absorption imaging via the cooling transition.

The layout of the laser system is illustrated in Figure 6. Details on the design, construction and characterization of the individual modules can be found in Refs. [59–61].

2.3.2 Second Generation Laser System

The second generation laser system was designed and built by colleagues at the Humboldt-Universität zu Berlin to operate the QUANTUS-2 capsules during drop and catapult operation and makes use of state-of-the-art integrated laser sources developed by the Ferdinand-Braun Institut für Höchstfrequenztechnik (FBH). The higher level of miniaturization allows to fit a two-species laser system design with Bragg and Raman atom interferometry capabilities on a single capsule platform. The system is divided into six modules, mounted on a 5 cm tall

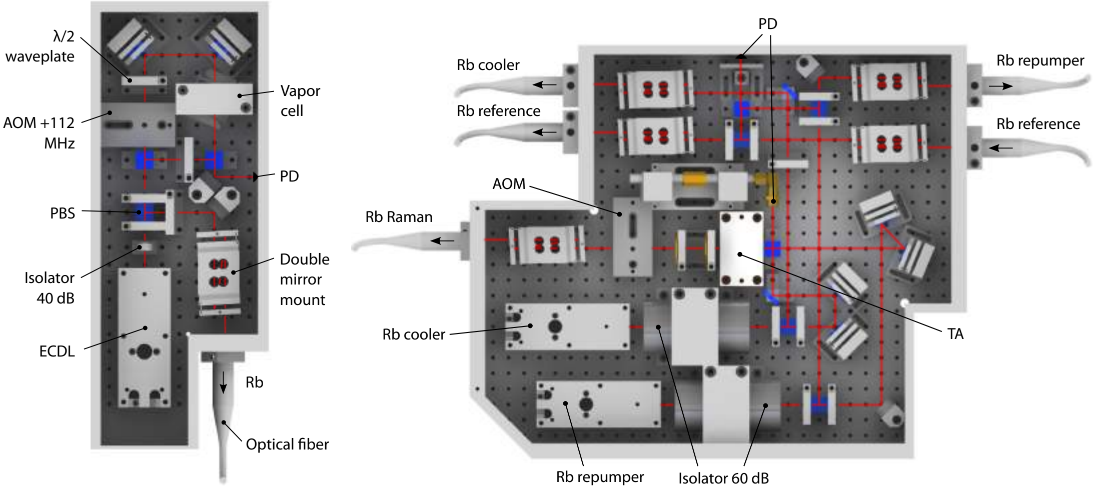
λ/2
waveplate
AOM +112
MHz
PBS
Isolator
40 dB
ECDL
Vapor
cell
PD
Double
mirror
mount
Rb
Optical fiber
PD
Rb cooler
Rb reference
Rb repumper
Rb reference
AOM
Rb Raman
Rb cooler
TA
Rb repumper
Isolator 60 dB

(a) Rb reference module (b) Rb module

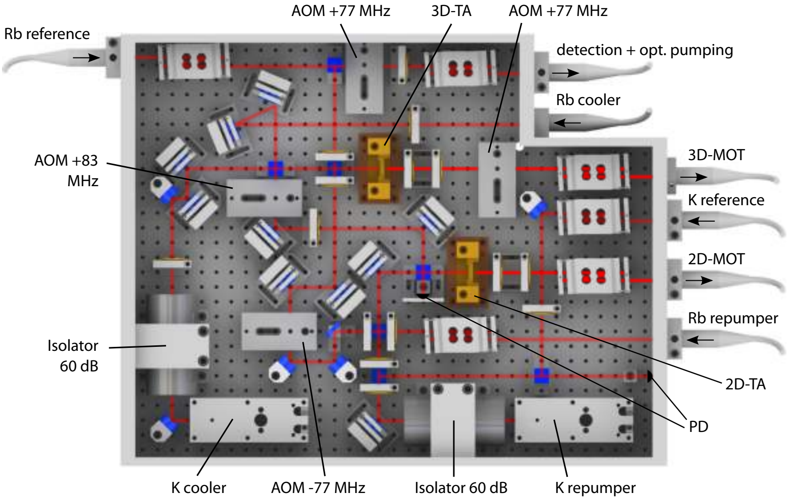
AOM +77 MHz
3D-TA
AOM +77 MHz
Rb reference
detection + opt. pumping
Rb cooler
AOM +83
MHz
3D-MOT
K reference
2D-MOT
Rb repumper
Isolator
60 dB
2D-TA
PD
K cooler
AOM -77 MHz
Isolator 60 dB
K repumper

(c) Rb and K mix module

Figure 6: CAD drawings of the individual modules of the first generation laser system. The potassium reference module is a mirror image of the Rb reference module and is omitted from this figure. Adapted from Ref. [61].

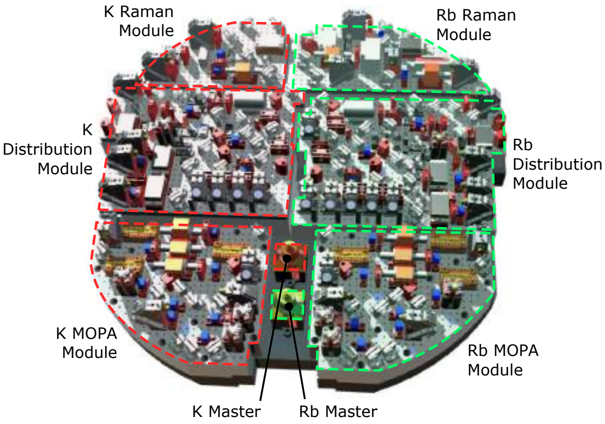

Figure 7: CAD drawing of the second generation laser system. The system is split in two parts: the Rb part on the right (green) and the K part on the left (red). Both are split into a MOPA module, containing three lasers and amplifiers each, a distribution module and a dedicated Raman module. Additionally, each species has a separate integrated master laser module with fiber coupled output. The modules are connected via polarization maintaining single-mode optical fibers.

honeycomb aluminum breadboard, and two master lasers. All of the adjustable opto-mechanics have been replaced by custom-made titanium components.

Especially the reference (master) laser modules are significantly smaller in comparison to the first generation laser system (see Figure 5 and Figure 7). However, the use of distributed feedback (DFB) diodes with relatively large intrinsic linewidth of a few MHz in comparison to the few hundred kHz of the ECDL laser sources in the 1st generation comes at a cost (see Figure 10). At the time of writing, only the Rb part of the new system is in operation, while the K part is still under construction. All design, testing and characterization steps of the Rb system are covered in great detail in Ref. [70].

The Rb MOPA module hold three master oscillator power amplifiers (MOPAs) which consist of a DFB diode, a ridge waveguide (RW) and TA. All three are offset locked to the Rb master laser. The master laser itself is stabilized to the $|F = 2\rangle \rightarrow |F' = 2\,/\,F' = 3\rangle$ crossover transition of the D2-line of ^{85}Rb. MOPA1 provides cooling light for the 2D-MOT and detection light on the $|F = 2\rangle \rightarrow |F' = 3\rangle$ transition of ^{87}Rb. It is also used for optical pumping via the $|F = 2\rangle \rightarrow |F' = 2\rangle$ transition. MOPA2 delivers repumping light for both the 2D- and 3D-MOT on the $|F = 1\rangle \rightarrow |F' = 2\rangle$ transition. It can also be used for Bragg interferometry. MOPA3 provides 3D-MOT cooling light and is also employed for Raman interferometry (see Figure 8). All MOPAs are operated close to an output power of 1 W and are fibercoupled for delivery to the Rb distribution module. Approximately 400 mW of each laser arrive in the distribution module.

The switching between the various functions of the three MOPAs is achieved via three acousto-optic modulators (AOMs) in the distribution module. Is is also used for mixing the light field in reasonable proportions and distribute them to five output ports for fiber coupling. The 2D- and 3D-MOT each have one designated fiber port, while two outputs are used for the two detection beams. The remaining fiber port in used for Bragg interferometry. If the Raman interferometry is to be used instead of the Bragg option, the laser light of MOPA3 is delivered to the Raman

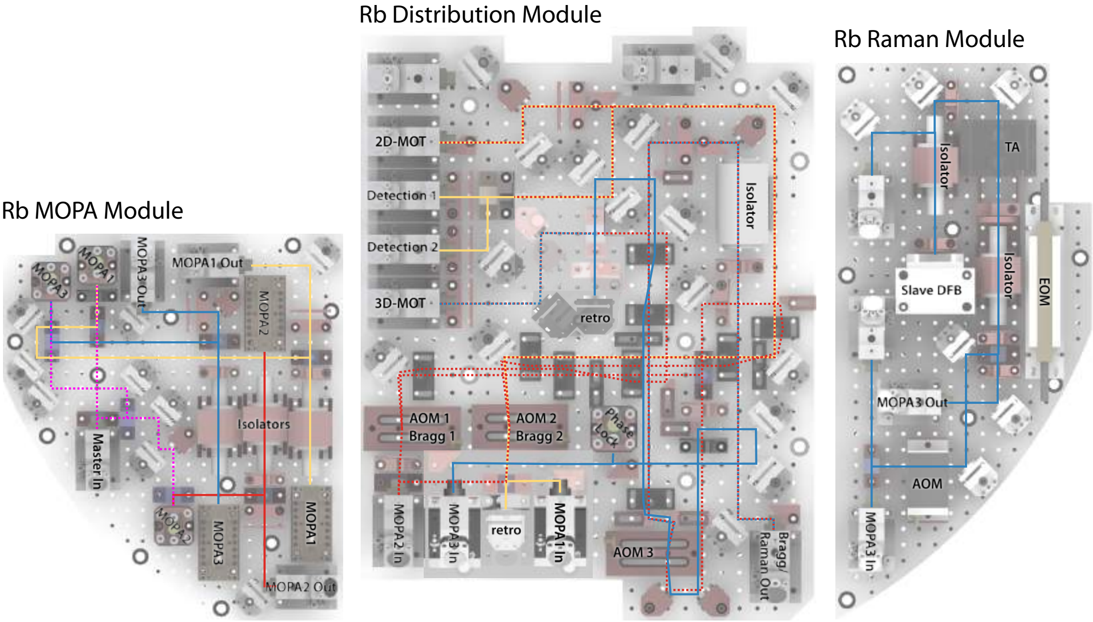
Rb Distribution Module
Rb Raman Module
Rb MOPA Module
MOPA3
MOPA1
MOPA3 Out
MOPA1 Out
MOPA2
Isolators
Master In
MOPA2
MOPA3
MOPA1
MOPA2 Out
2D-MOT
Detection 1
Detection 2
3D-MOT
retro
Isolator
AOM 1
Bragg 1
AOM 2
Bragg 2
Phase Lock
MOPA2 In
MOPA3 In
retro
MOPA1 In
AOM 3
Bragg/
Raman Out
Isolator
TA
Isolator
Slave DFB
EOM
MOPA3 Out
AOM
MOPA3 In

Figure 8: CAD drawings and schematics of the 2^{nd} generation laser system (rubidium part). The beam paths through the modules are color coded as yellow (MOPA1), red (MOPA2) and blue (MOPA3). The light for the offset locks from the master laser is shown in magenta. Only the MOPA and Distribution Module are necessary for standard operation and Bragg interferometry. For optional Raman operation, the MOPA3 beam is fed through to the Raman module first, where a portion of the light is split off, shifted in frequency via an electro-optic modulator (EOM) and amplified by an additional TA to create the Raman beam pair.

module first, where it is amplified again by an additional TA. After amplification, parts of the beam is introduced to the distribution module.

2.3.3 Distribution

For both systems, the distribution of laser light to the vacuum chambers is achieved with optical fiber splitters for the 2D- and 3D-MOT. The 2D-MOT fiber splitter `[OZ-Optics 770-45/45/9/1]` has one input ports for the Rb and K source light. The input light is partitioned to four output ports with absolute proportions of45%, 45%, 9% and 1%. The majority of the light is distributed to the two optical fibers who provide the transverse cooling and repumping light for the 2D-MOT. The other two output ports with 9% and 1% of the overall power deliverer the light for the pusher and retarder beams, respectively (see Chapter 3). The 3D-MOT fiber splitter `[Canadian Instruments 954P]` has two input and four output ports, while every output port delivers approximately 25% of the total input power to the experiment. The detection light

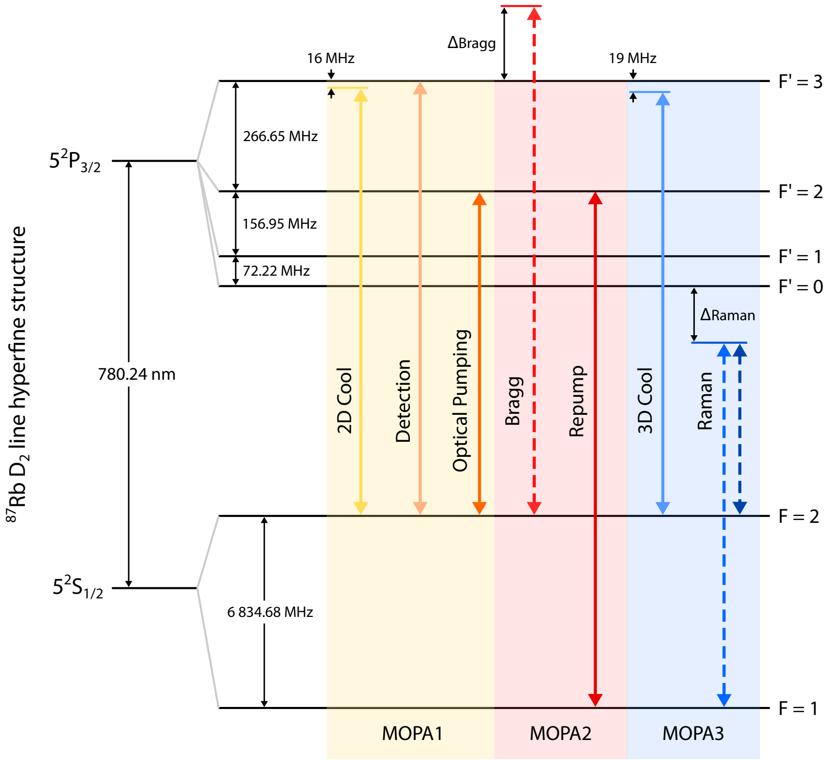
^{87}Rb D$_2$ line hyperfine structure
ΔBragg
16 MHz
19 MHz
F' = 3
266.65 MHz
$5^2P_{3/2}$
F' = 2
156.95 MHz
F' = 1
72.22 MHz
F' = 0
ΔRaman
780.24 nm
2D Cool
Detection
Optical Pumping
Bragg
Repump
3D Cool
Raman
F = 2
$5^2S_{1/2}$
6 834.68 MHz
F = 1
MOPA1
MOPA2
MOPA3

Figure 9: Hyperfine structure of the ^{87}Rb D$_2$ line. The relevant transitions addressed by the three MOPAs in the 2$^{\text{nd}}$ generation laser system are marked in the figure. Switching from MOT to interfrometry operation is achieved via three acousto-optical modulators in the distribution module. The second Raman frequency is produced from the master beam via an electro-optical modulator in the Raman module. The hyperfine scheme and frequency offsets are adopted from Ref. [71].

as well as the interferometry beams are delivered directly to the vacuum chambers. All fiber connections use single-mode polarization maintaining fibers.

2.4 Vacuum Chambers

The vacuum setup consists of two chambers separated by a differential pumping stage (see Figure 11), allowing for a pressure difference of up to three orders of magnitude. A high vacuum (HV) area (2D chamber) is used for the atomic source and is operated slightly below the room temperature vapor pressure of rubidium at 10^{-7} mbar. It generates a pre-cooled beam of atoms towards an ultra-high vacuum (UHV) chamber. The UHV region (3D chamber) is used to capture the atoms, cool them to degeneracy and perform atom interferometry. Its pressure

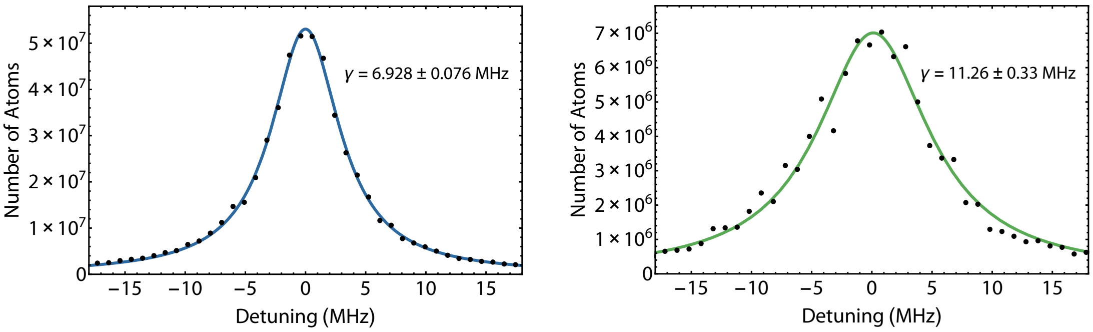

(a) 1st generation laser system

(b) 2nd generation laser system

Figure 10: Comparison of detection line scans with the 1st and 2nd generation laser systems. Figure (a) shows a single scan of the detection laser frequency detuning while imaging equally prepared atomic clouds. The fitted Lorentzian linewidth of $\gamma = 6.928 \pm 0.076$ MHz is close to the natural linewidth of the transition: $\Gamma = 6.0666(18)$ MHz [71]. Figure (b) shows the linewidth acquired with the 2nd generation system as an average over three identical scans. The fitted linewidth of $\gamma = 11.26 \pm 0.33$ MHz is substantially wider due to the use of DFB diodes with larger intrinsic linewidth. The increased noise in the second measurement is a result of the digital and highly integrated lock electronics.

level is maintained at a few 10^{-11} mbar by a 25 l/s ion pump `[IGP Meca 2000]` and two passive vacuum pumps `[VG Scienta SBST110, SAES Getters CapaciTorr D200]`.

The chambers are machined from a non-magnetic Titanium alloy `[Ti-6AL-4V]`. The differential pumping stage between the two is a threaded copper rod with an 1.5 mm aperture in the center, which after 10 mm expands conically with an aperture angle of 8° for another 30 mm. The conical part is partially replaced by a graphite tube to improve differential pumping. On the 2D side, the pumping stage has a 45° cutaway with a polished surface that grants upwards of 95% reflectivity at a wavelength of 780 nm.

2.4.1 2D Chamber

The 2D chamber has a cuboid shape with a head section that holds three CF- 10 vacuum ports for dispensers, a CF-16 vacuum port to access a Rb reservoir and a window for optical access along the main axis of the chamber. The inner (outer) dimensions of the 2D chamber are 60 mm × 20 mm × 20 mm (140 mm × 74 mm × 74 mm).

The lateral chamber windows `[N-BK7]` are anti-reflection (AR) coated on the outside and attached to the chamber via indium sealing. Each lateral axis has one linearly polarized input beam that is expanded to a diameter of 18 mm, split into two parallel beams and transformed to circular polarization. After passing the chamber, rectangular $\lambda/4$ waveplates, which are AR coated on one and high-reflection (HR) coated on the other side, retro reflect the beams to create

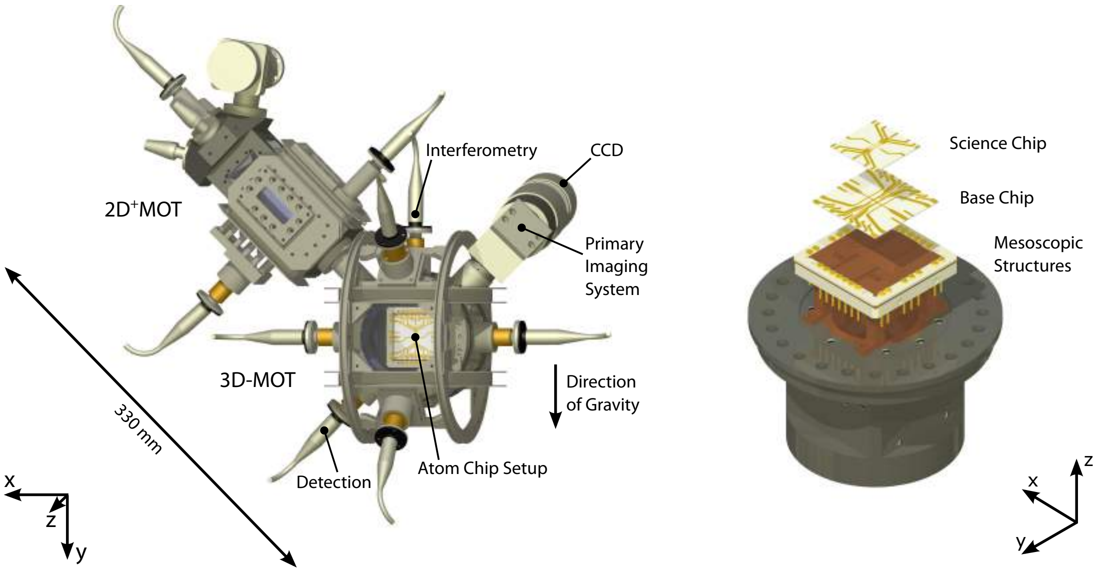

Figure 11: CAD drawings of chambers (left) and atom chip setup (right). The compact two-chamber design is interconnected via a differential pumping stage. The three layers of the chip setup are depicted in an exploded view.

two cooling regions along the longitudinal axis. Additionally, a pushing and a retarding beam are counter-propagating along the longitudinal axis to create a 2D$^+$MOT configuration. The retarding beam is reflected off the differential pumping stage and hence has a 1.5 mm cutaway in its center. The magnetic fields for the 2D$^+$MOT are provided by four coils in racetrack configuration, generating a two-dimensional quadrupole field perpendicular to the atomic beam.

2.4.2 3D Chamber

The 3D chamber has a cylindrical shape with outer dimensions of ø 102 mm × 62 mm. It has eight viewports on its lateral surface, seven of which have indium-sealed windows `[N-BK7]` with AR coatings on both sides. The window sizes grant a free aperture of 20 mm. The remaining port holds the differential pumping stage towards the 2D chamber. The axis perpendicular to the differential pumping stage is used for absorption imaging. The atoms are illuminated from the lower left viewport and detected via a charge-coupled device (CCD) camera that sits behind a two-lens detection telescope on the upper right. The horizontal axis is used for a pair of MOT beams while the vertical axis is used for atom interferometry.

The chamber features a large front window that grants optical access for two more MOT beams. Each of these beams enters the chamber in an angle of 45° to the plane of the window and is reflected by the atom chip [72]. A large aperture lens system `[Thorlabs MAP105050-B]` sits

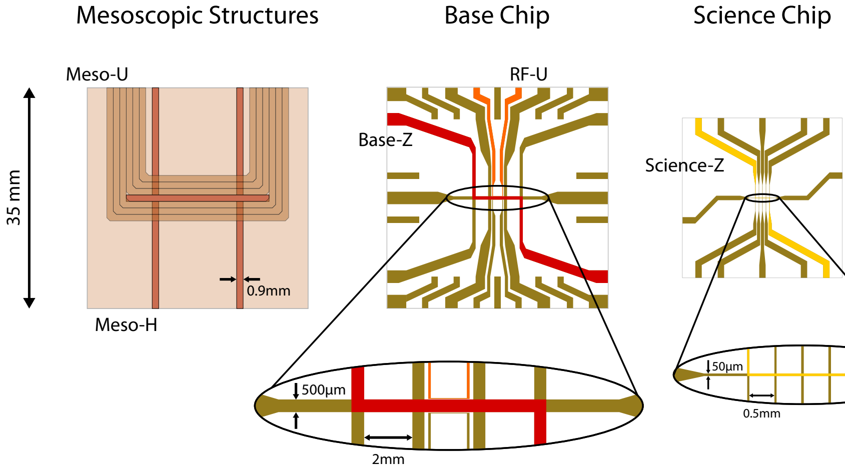

Figure 12: Wire topologies of the atom chip layers. Each layer features a different characteristic wire width from 900 µm for the mesoscopic structures, to 500 µm for the base chip and 50 µm for the science chip.

in front of the window, collecting light emitted by the atoms onto a photodetector `[Hamamatsu S5107]`. An additional detection beam enters the front window at an angle of 52.5° to the plane of the window and is reflected off the atom chip surface before it enters a second two-lens detection telescope.

Three pairs of Helmholtz coils are attached to the outside of the 3D chamber, one of which is wound around the chamber itself. The chip setup constitutes the back side of the assembly and provides access to the vacuum pumps.

2.5 Atom Chip

The magnetic fields for trapping the atoms are created by current carrying wire structures in combination with magnetic bias fields [72]. Three layers of wire structures, each featuring a different characteristic wire size, are used in the atom chip setup (see Figure 12).

The first layer holds the largest, mesoscopic structures which are constructed from Kapton isolated 0.9 mm diameter copper wires. These are used in the generation of the quadrupole field for the 3D-MOT with a U-shaped layout [73] that comprises six windings of a single wire. Additionally, three individual copper wires form an H-shaped structure to generate a Ioffe-Pritchard (IP) type potential, that is used in the first magnetic trap.

The second layer base chip (BC) features intermediate sized gold wires of 0.5 mm width, electroplated onto a 35 mm × 35 mm Aluminum nitride substrate. A 25 mm × 25 mm science chip (SC) forms the third and final layer with structures of 50 µm width. It is covered with a dielectric transfer coating `[OIB Jena]` to reflect two of the four MOT beams, creating a mirror MOT configuration [72]. Its reflectivity at 780 nm was measured to be 97.7% at a 45° angle of incidence. The base and science chip feature a set of four and five parallel wires, respectively, in each case intersecting with one central orthogonal wire. They both offer an abundance of possible U-, Z- and H-shaped trap configurations including dimple traps [74].

Previous experiments with mesoscopic structures observed an increase in the number of captured atoms [73]. However, the ability to create high trap frequencies with the same structures is limited, leading to slow evaporative cooling. Other experiments, that exclusively employ small chip structures typically show fast evaporation performances but are highly limited by the initial number of atoms [4]. The three-layer chip presented here is designed to bridge the gap between these two scenarios by using traps composed of different chip layers to span a wide range of trap configurations (see Chapter 3).

2.5.1 Biot-Savart Simulations

The magnetic field generated by the atom chip setup and the external bias coils is modeled using Biot-Savart simulations. The exact modeling of the chip potential is necessary to guide the transition between gravity and microgravity operation. Many of the targeted magnetic field topologies in microgravity are unattainable in lab operation and the limited μg time is insufficient to find the proper trap configurations experimentally. A detailed account on the Biot-Savart simulations for the QUANTUS-2 apparatus can be found in Ref. [65].

2.5.2 Chip Coordinate System

The origin of the absolute coordinate system used in the following experiments is the center point of the science chip, on top of its mirror coating. It is thus located just above the center of the horizontal science ship wire structure. From here, the z-axis is oriented perpendicular to the atom chip surface, the y-axis points downwards parallel to the main capsule axis and the x-axes runs along the horizontal wire structure. In the following, this absolute reference is referred to as the chip coordinate system. Note that this location does not coincide with the central capsule axis nor with the center of the magnetically shielded region in the capsule. The respected offsets between the latter and the chip coordinate systems are $(x_{\text{offset}}, y_{\text{offset}}, z_{\text{offset}}) = (+47.0, -55.5, -54.2)$ mm.

2.6 Detection

When atoms are exposed to near resonant radiation, they absorb and spontaneously re-emit photons from the probe beam. These two processes are widely used in absorption and fluorescence imaging techniques [48]. In the QUANTUS-2 setup, absorption imaging is employed to visualize the atomic ensembles. The fluorescence signal of the atoms is used for some applications such as monitoring the performance of the magneto-optical trap.

2.6.1 Absorption Imaging

Absorption imaging uses the variation in probe beam intensity through absorption by an ensemble of atoms. The Beer-Lambert law gives the attenuation of light intensity I along the beam direction z' as

$$\frac{\mathrm{d}I}{\mathrm{d}z'} = -n\,\sigma\,I, \tag{2.1}$$

where n is the local density of the atomic cloud and σ the scattering cross section. The latter is given by

$$\sigma = \frac{\sigma_0}{1 + 4\left(\frac{\delta}{\Gamma}\right)^2 + \frac{I}{I_\mathrm{sat}}}, \tag{2.2}$$

with the on-resonance cross section

$$\sigma_0 = \frac{\hbar\omega\,\Gamma}{2\,I_\mathrm{sat}}. \tag{2.3}$$

Here, I_sat is the saturation intensity, which depends on the polarization of the probe beam and the atomic alignment relative to a quantization field [71], Γ is the natural linewidth of the transition and δ the detuning from the resonance frequency.

With the optical density (OD) defined by the ratio of initial to final intensity

$$\frac{I_\mathrm{f}}{I_0} = e^{-\mathrm{OD}}, \tag{2.4}$$

the column density is given by

$$n(x', y') = \frac{1 + 4\left(\frac{\delta}{\Gamma}\right)^2}{\sigma_0} \ln\left(\frac{I_0}{I_\mathrm{f}}\right) + \frac{I_0 - I_\mathrm{f}}{\sigma_0\,I_\mathrm{sat}}. \tag{2.5}$$

The two-dimensional density distribution of the ensemble perpendicular to the beam direction z' can thus be obtained by comparing the initial to the final beam intensity. The density, position, size, shape and atom number can all be obtained from that distribution.

Experimentally, this is achieved by imaging a probe beam with $1/e^2$ radius of 9 mm on a CCD-camera, once with and once without atoms in the beam (see Figure 13). The laser beam has σ^+ polarization and the appropriate quantization field is applied using the x- and y-coils with equal field strength, generating a field vector that is collinear to the beam propagation. To reduce noise, a dark image is obtained and subtracted from both raw images of the probe beam. The final image gives the column density of the cloud over on array of 1344×1024 pixels

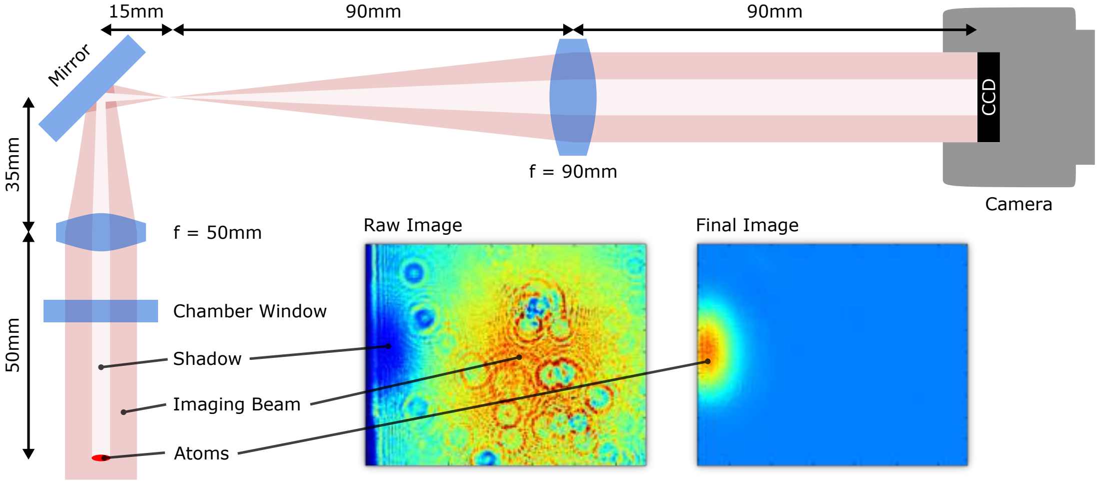

Figure 13: Schematics of the primary absorption imaging telescope. After the probe beam passes the atomic cloud, it leaves the 3D chamber through a chamber window and is then imaged onto a CDD-camera with a magnification factor of 1.8 using a two-lens telescope. Due to the length of the optical system, the beam has to be folded over by a high-reflective mirror in between the two lenses to fit inside the magnetic shield. A raw image of the probe beam with distinct shadow from the atomic cloud is presented next to the final image, which was acquired via (2.5). The figure was adapted from Ref. [65].

defined by the CCD chip `[Hamamatsu C8484-15C]`. The two identical detection telescopes for absorption imaging by design have a magnification factor of 1.8, resulting in an effective pixel size of 3.58 µm × 3.58 µm, while the total image area is 4.82 mm × 3.67 mm. The characterization of the the primary imaging setup prior to integration yielded an imaging resolution of 5.52 µm [63]. A secondary imaging setup was added to the system in the course of the microgravity campaigns and was characterized in Ref. [75]. The imaging resolution was determined to be 7.81 µm.

In both telescopes, the atoms are located in the focus of the first lens `[Edmund Optics NT49-957]` while the CCD-chip is located in the focal plane of the second `[Linos G322389525]`. The detection systems were optimized externally to ensure that the relative distances between the lenses are properly set. After integration, the magnification of the system can be measured by releasing an ensemble of atoms and tracing its free fall under gravity. Comparing the trajectory to the expected acceleration yields the magnification factor of the setup. The telescope are then optimized by imaging a small, low-density cloud and adjusting the distance between first lens and atoms as well as between second lens and CDD-camera. Initially, the goal is to reduce the size of the atomic cloud as much as possible by adjusting the distance to the first lens. Afterwards, the atoms are imaged at varying detuning from resonance. Non-resonant imaging leads to a change of the index of refraction over the atomic cloud causing distinct refraction patterns, particularly if the atoms are not in the focal plane. The distance between the CCD-camera and the second

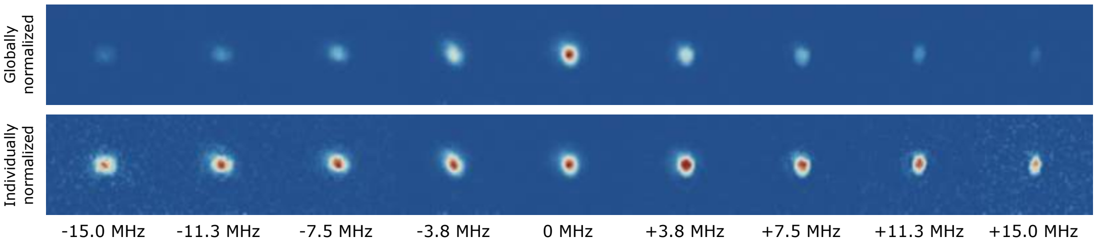

Figure 14: Absorption images of an atomic cloud with varying detuning. The figures show the size and shape of identically prepared clouds after 10 ms TOF imaged at different detection laser frequencies (1^{st} generation laser system). In the top picture, all images are presented with the same scaling while the bottom picture shows each image scaled individually for comparison.

lens is then adjusted successively until the shape and size of the cloud appears uniform over a broad range of detunings, thus ensuring proper focusing of the atoms (see Figure 14).

The secondary detection telescope is identical to the one presented in Figure 13, the only difference is that the probe beam is reflected of the chip surface mirror prior to entering the telescope. For clarity, the two detection angles are contrasted in Figure 15. The position of the atoms on images from two detection angles can be transformed back into the chip coordinate system by using characteristic patterns that relate to the geometry of the system. In case of the primary imaging setup those characteristic patterns are the diffraction fringes of the probe beam on the chip edge as well as diffraction rings from static impurities in the detection path. For the second imaging setup, the science chip wire structures dimly visible on all images are used as reference (see Chapter 4).

The secondary absorption imaging setup is peculiar in showing the atomic cloud from two different angles. Three-dimensional spatial information can thus be gained from the absolute and relative distance of the two clouds on the image. Unfortunately, the polarization of the probe beam and the atomic alignment via a quantization field can not be optimized for both clouds at the same time. The same is the true for simultaneously imaging the atoms with both imaging setups.

2.6.2 Fluorescence Detection

Another tool employed in the QUANTUS-2 apparatus is the detection of the fluorescence signal of the atoms that is a result of re-emittance of absorbed radiation. To this end, a large-aperture lens system `[Thorlabs MAP105050-B]` sits in front of the 3D-chamber front window to collect photons onto a sensitive photo detector `[Hamamatsu S5107]`. The acquired photo current is translated to a voltage and amplified using a low-noise transimpedance amplifier `[Femto DLPCA-200]`. The solid angle of the lens system is $d\Omega = 0.286\,\mathrm{sr}$. The sensitivity of the photo detector is $S = 0.595\,\mathrm{A/W}$. Together with the gain setting G of the amplifier (adjustable

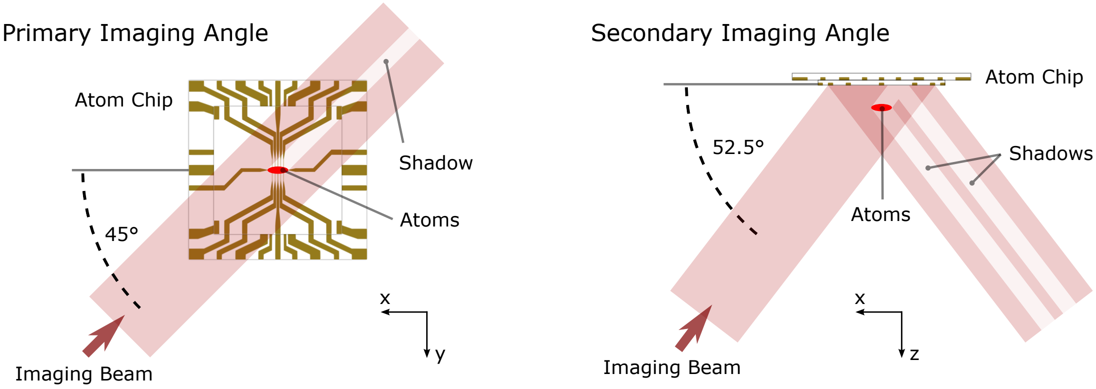

Figure 15: Comparison of the two detection angles used for absorption imaging. The probe beam for the primary imaging setup originates in the lower left viewport and passes the 3D chamber in front of the atom chip setup at an angle of 45° in respect to the horizontal. For the secondary detection angle, the probe beam originates outside of the large front window of the 3D chamber and enters at an angle of 52.5° with respect to the atom chip surface. The beam passes the atoms twice, once before and once after reflection on the chip's mirror coating. This results in an a double image of the atomic cloud.

from 10^3 to 10^{11} V/A) the number of atoms N in the cloud can thus be derived from voltage ΔS via

$$N = \frac{4\pi\,\Delta S}{d\Omega\, S\, G\, \hbar\omega\, \gamma}. \tag{2.6}$$

Here, $\hbar\omega$ is the photon energy and the scattering rate γ is given by

$$\gamma = \frac{\Gamma}{2}\frac{I/I_{\mathrm{sat}}}{1 + 4\left(\delta/\Gamma\right)^2 + I/I_{\mathrm{sat}}}. \tag{2.7}$$

Details and characterization of the fluorescence imaging setup can be found in Ref. [63].

2.7 Magnetic Shielding

The susceptibility to magnetic fields is one explicit advantages of the alkali atoms prevalently chosen in atom optics and atom interferometry. The ease of trapping and cooling the atoms in magnetic potentials is one cornerstone in the preparation of pristine source for precise interferometric measurements. However, during such measurements the susceptibility to magnetic fields can introduce additional phase shifts in the interferometer and thus limit the accuracy. Bosonic atoms such as ^{87}Rb have the advantage of an $m_F = 0$ hyperfine state which is insensitive to the first-order Zeeman effect. However, in dual species measurements, the differential second-order Zeeman shift between two species is cause for concern. Additionally, the atoms remain in

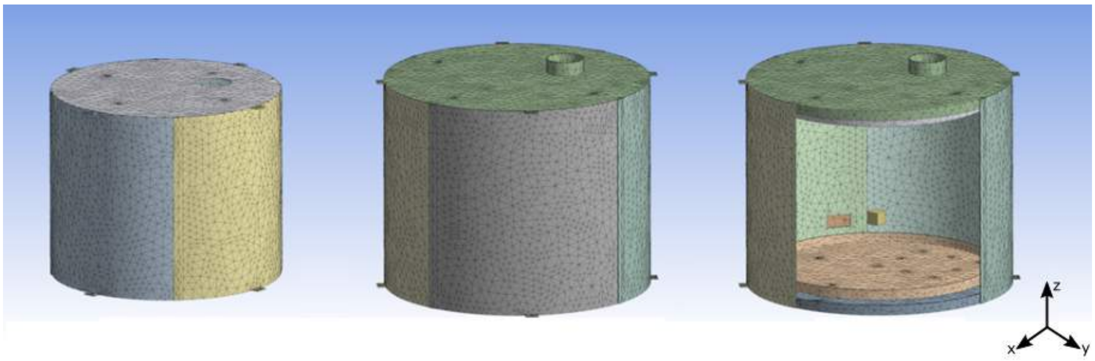

Figure 16: Illustration of the finite element mesh for the magnetic shield simulations. The figure shows from left to right, the inner shield, the outer shield and the partially opened shield assembly where the origin location is marked with a box. It represents the location of the atoms in the 3D chamber in the finished setup. Adapted from Ref. [76].

Table 3: Technical data of the magnetic shield assembly

Parameter	size (mm)
Layer thickness	2
Outer radius	265
Inner radius	229
Axial separation	34
Vertical separation	20
Top access port radius	36
Auxiliary port	25 × 50

Table 4: Results of finite element simulations and measurements of the magnetic field attenuation.

Direction	Q-1 attenuation	Q-2 attenuation	
	Simulation	Simulation	Measurement
x-axis	88	11944	658[+]
y-axis	37	12987	221[+]
z-axis	72	5875	117[+]

[+] measured with an external magnetic field flux of 100 µT at a frequency of 10 Hz along the respective axis [65]

magnetically sensitive hyperfine states for the majority of the preparation process which can be adversely affected at many stages. Excellent magnetic field control is especially important during polarization gradient cooling, on the onset of cooling the atoms to Bose-Einstein condensation (see Chapter 3) as well as during all subsequent transport, release and magnetic lensing procedures (see Chapter 5 and Chapter 6). An additional peculiarity of performing quantum optics experiments in the drop tower is the fact that the capsule traverses a 110 m steel tube which may cause a variety of magnetic field disturbances without proper shielding. This is why improving on the shielding capabilities of the first generation was an expressed design condition.

The magnetic shielding for QUANTUS-2 consist of two cylindrical MuMetal layers with 2 mm thickness. The inner and outer radii of the total shield assembly are 229 mm and 265 mm, respectively. The inner and outer heights of the assembly are 375 mm and 420 mm, respectively. Thus, the total volume of the shielded region is 0.062 m^3. Additional design parameters are listed in Table 3. Each shield is segmented into six parts, the top and bottom base plates and four side quadrants. An access port through the top of both shields is used for connecting the vacuum chamber setup to the vacuum pumps and sensor via CF vacuum tubing. Each shield has a rectangular auxiliary access port on one of the quadrant segments for cable and fiber optic connections.

The shielding factor of the MuMetal setup was determined via finite element simulation (see Figure 16) prior to commissioning as well as measurements performed on the finished assembly by the manufacturer. The results are summarized in Table 4. All simulations and measurements are performed in close proximity to the origin of the chip coordinate system and thus to the position of atomic ensembles in the experiments and not at the center of the magnetic shield.

The single-layer magnetic shield design for QUANTUS-1 was a late addition to the machine and does not share the same favorable symmetric design of QUANTUS-2. The finite element simulations of both designs suggest a two hundredfold average improvement in attenuation. The measurements performed by the manufacturer show a striking divergence between simulated and actual attenuation. This is especially true for the y-axis where the measured value is smaller by a factor of 60. The auxiliary access port, visible in the rightmost image in Figure 16, is one potential explanation for the discrepancy between the attenuation factors along x and y. A detailed account of the magnetic shield design and finite element simulations can be found in Ref. [76].

2.8 Electronics

2.8.1 Laser System Stack

The majority of the electronics used in the QUANTUS-2 capsule have been designed within the LASUS project at the Universität Hannover [77]. The goal of the project is to develop miniaturized electronics and laser systems for the use in quantum optics experiments in microgravity.

The so called T-Bus electronics share the form factor of the PC/104 standard and provide all of the necessary components to operate a laser system. The 1st generation laser system is run with a hybrid set of T-Bus and analog lock electronics, while the second generation relies completely on the T-Bus standard. The electronics package consists of a single stack with 19 cards see Figure 17. They include laser and TA current drivers, temperature controllers for all laser sources, frequency generation via direct digital synthesis (DDS) cards for AOMs, frequency controllers for laser frequency stabilization and shutter drivers. The stack is connected to an FPGA controller in the PXI computer control system and is set up and operated exclusively via a software interface. Construction and configuration of the T-Bus stack happened alongside of the second generation laser system and is covered in detail in Ref. [70].

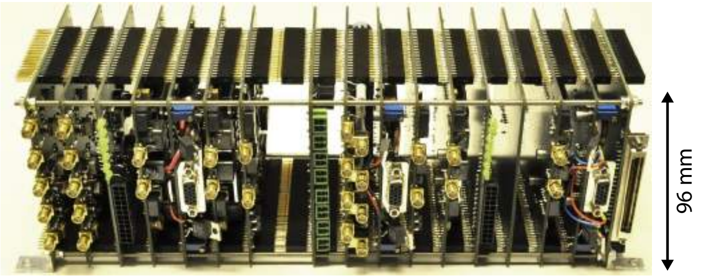

Figure 17: Picture of the assembled T-Bus stack prior to integration. The single stack holds 6 laser current drivers, 4 TA current drivers, 6 temperature controllers, 2 DDS-based AOM controllers with 4 channels each, a frequency controller to stabilize 4 lasers and a shutter driver with 8 channels. The total power consumption amounts to approximately 122 W.

2.8.2 Computer Control System

The CCS operating the experiment is a commercial PXI system `[NI PXI-1036DC, PXI-8183, PXI-6723]` equipped with a field-programmable gate array (FPGA) `[NI PXI-7854R]` responsible for timing control. Two camera link adapter cards `[NI PXI-1428]` are used to communicate with and control the CCD-cameras used for absorption imaging. Additionally, the CCS possesses an arbitrary waveform generator `[NI PXI-5421]` used to provide a RF signal for evaporative cooling (see Chapter 3) and adiabatic rapid passages (see Chapter 4). The CCS is operated using a custom LabVIEW GUI developed specifically for QUANTUS-2. A description of the interface, the FPGA module and workflow of the control system can be found in Ref. [65].

2.8.3 Current Drivers, Current Response and Switching Times

The currents for the coils and atom chip structures are provided via commercial current drivers `[High Finesse BCS 10A]`, which are rated at a noise level below −108 dB V_{RMS} between 0 and 2500 Hz. The drivers provide currents of up to 10 A and are supplied by dedicated batteries. The modules are designed as chip current drivers for low-inductance loads and feature a pair of 4.7 µF capacitors to smooth the current output. Unfortunately, the capacitance of the drivers$C$ and the inductance of the coils L form a resonant circuit with frequency

$$f_0 = \frac{1}{2\pi\sqrt{LC}}. \tag{2.8}$$

Therefore, using the chip current drivers with the y-coil results in an oscillating current, damped by the resistance of the coil. Figure 18 shows the measured step response of the y-coil. The fitted frequency of $f = 740.1$ Hz is close to the resonance frequency of $f_0 = 759.1$ Hz predicted by

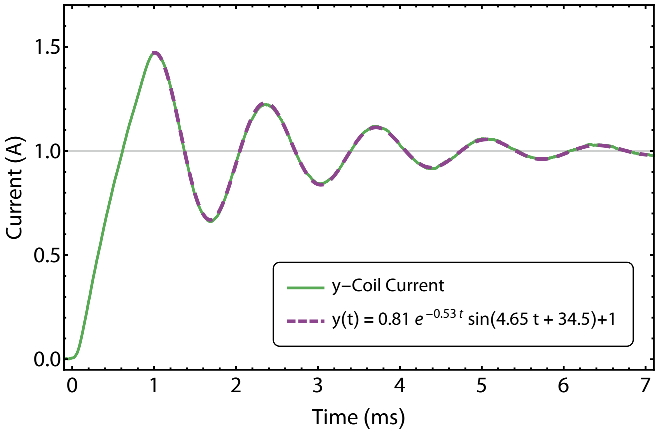

Figure 18: Switching dynamics of the y-coil with chip current driver without additional circuitry. The figure shows the step response for a 0 A → 1 A transition on a supply voltage of 13.9 V. The current first crosses the target value after less than 1 ms, but oscillates for another 8 ms. Fitting the damped oscillation yields a frequency of $f = 740.1$ Hz.

(2.8). This behavior significantly inflates the settle time of the system and can cause serious harm to current drivers.

The unwanted oscillations can be remedied by adding a secondary circuit loop with an additional resistor R_2 and capacitor C_2 (see Figure 19). The increased total capacitance $C = 2 \times 4.7\,\mu\text{F} + C_2$ lowers the resonance frequency of the overall system which can be helpful in achieving the desired current progression, which is the aperiodic case. Some of the coils only require the additional damping provided by the extended circuit, while others need to be shifted in frequency to attain the proper shape. For example, the unaltered z-coil step response runs through two full oscillations before reaching its target value for the first time. Adding capacitance to the system transforms the step response into a curve that can be turned into the aperiodic case with sufficient damping (see Figure 20). The slope of the response function noticeably declines with added capacitance. Thus, the switching time was intentionally increased to attain a clean current response and avoid oscillations in the circuit. Furthermore, the slope depends on the voltages provided to the current drivers which in turn depends on the charge of the designated batteries.

The final step response functions of the three coil pairs after circuit extension are displayed in Figure 21. With knowledge of the step response functions, calculated ramp shapes can be translated into proper request functions that produce the desired current progressions. Thus, even slow structures with high inductivity such as the y-coil can follow elaborate trajectories (see Chapter 5). The characteristic response functions not only define the switching times but also put restrictions on the steepness of the ramps. In contrast, the base and science chip structures can both be switched in 175 μs without modifications. The extension parameters, switching times and other characteristics are summarized in Table 5.

Figure 19: Circuit concept for the coil sets and current drivers. Each coil has a characteristic inductance L and resistance R_1. These parameters are measured at the interface to the current driver and include feedthroughs, cables and connectors. The secondary loop changes the behavior of the system by extending the capacitance and adding damping to the system. The inherent capacitance of the current drivers is $C_1 = 2 \times 4.7\,\mu\mathrm{F}$.

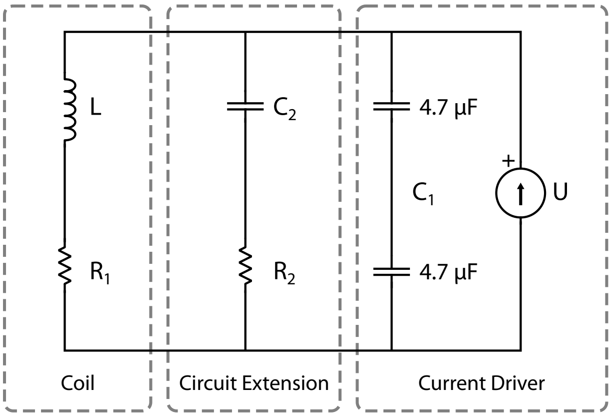

Figure 20: Switching dynamics of the z-coil for varying total capacitance C. The figure shows the step response for a 0 A to 1 A transition on a supply voltage of 6.9 V. All of the curves were measured without additional damping ($R_2 = 0$). The resonance frequency f_0 for the final configuration (red curve) was reduced by a factor of 2.5 compared to the original setup (blue curve).

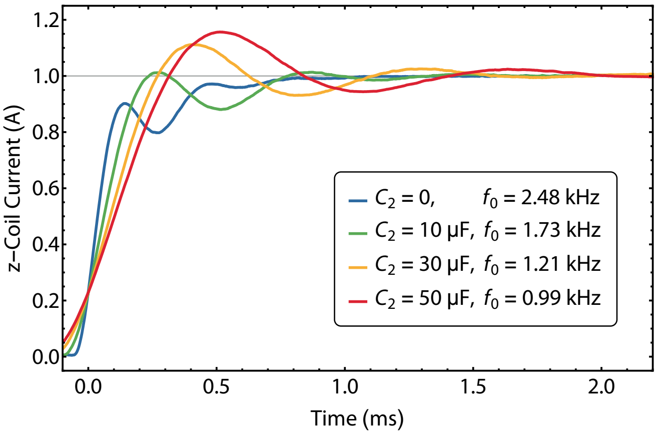

2.8.4 Programmable Chip Fuse

A programmable electronic chip fuse connects the current drivers to the chip structures and coils. Its main purpose is to protect the atom chip from excessive current and prolonged current load. This is achieved by requiring a trigger signal to run any currents, disconnecting the structures after a set maximal time and setting a dead time in between runs during which no new trigger signal is accepted. Additionally, the fuse device can disconnect all current carrying structures via trigger signals, which is a necessity manage residual currents and magnetic field gradients in the experiments (see Chapter 5). The design and characterization is documented in Ref. [78].

2.8.5 Batteries and Power Consumption

The capsule is powered by lithium iron phosphate (LiFePo4) accumulators [`LiNANO 10 Ah 3.2 V LiFePo SL-FHC (5C) 140 mm`]. Each cell (S) has a characteristic buffered (unbuffered) voltage of 3.45 (3.2) V. The following cell configurations and voltages are used in the apparatus: +1S,

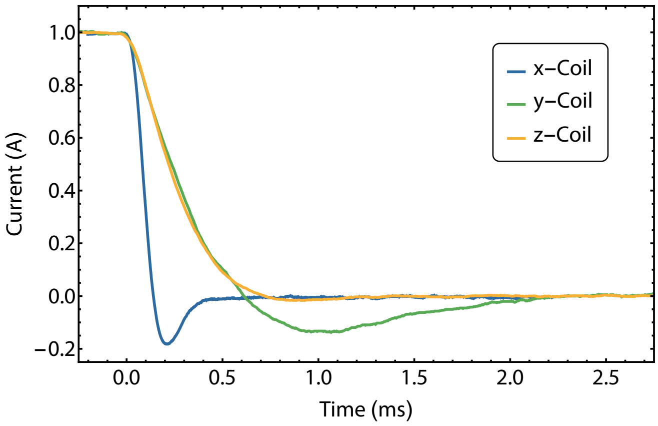

Figure 21: Measured step response of the coils after circuit extension. All three coils are critically damped and respond according to the aperiodic case with settle times of 0.6 ms, 2.5 ms and 1.2 ms for the x-, y- and z-coil, respectively. The z-coil shows the least amount of overshoot due to the significant increase in capacitance from the circuit extension.

±2S, ±4S and ±6S. The load is unequally distributed over the voltages and the battery run-time of the system is mostly limited by the +2S and +4S power lines. Thus, the run-time could easily be extended further by optimizing the battery concept. The current drivers have their own separate battery supply with the available voltages listed in Table 5. The second CCS, which is part of the capsule base structure, has its own dedicated batteries with a voltage of 28 V. A detailed account of the battery concept can be found in Ref. [79].

The power consumption of the entire setup in operation (idle) is 363.9 (314.7) W. Here, the idle state refers to a configuration where all components are switched on but no sequence is running. On the current battery setup the capsule can be run in continuous sequence mode for four hours at a time without recharging (see Chapter 4).

2.9 Remote Control and Automation

The apparatus is controlled remotely via LAN or WiFi connection, to a desktop PC for ground-based operation or to a laptop PC for drop tower operation. Via the remote PC, the system can be accessed from any place with an internet connection. Due to the complete digitization of the electronics interface, all day-to-day operations of the apparatus, such as switching it on and off, performing measurements and sequence optimizations can be done remotely. The complete autonomy of the setup is a necessary feature to ensure successful operation in the drop tower, where manual excess to the experiment is unavailable. The stability of both laser systems due to their compactness and modularization paired with integrated laser sources, reduces their maintenance demand substantially. Under normal conditions, the setup can run for weeks without the need to optimize the fiber couplings. This ruggedness of the apparatus is paramount to conduct continuous drop tower operation over a span of several weeks with up to three flights per day.

Table 5: Properties of the various current carrying structures used in the experiment.

Structure	R_1	L	C_1	C_2	R_2	Response	Max. voltage	Settle time
	Ω	mH	µF	µF	Ω	G/A	V	ms
Base-Z	0.5	–	–	–	–	–	6.9 (6.4)	0.175
Science-Z	1.0	–	–	–	–	–	6.9 (6.4)	0.175
Meso-H	0.332	–	–	–	–	–	13.9 (12.8)	0.15
x-coil	0.603	0.177	9.4	30.0	5.08	1.928	6.9 (6.4)	0.6
y-coil	2.55	4.676	10.0^+	20.0	31.97	14.303	13.9 (12.8)	2.5
z-coil	0.875	0.438	9.4	50.0	3.33	6.946	6.9 (6.4)	1.2

[+] the intrinsic capacitors of the y-coil current driver (HF-5) were removed and replaced by an second external loop with $C = 10\,\mu\text{F}$ and $R = 22\,\Omega$

Additionally, the apparatus can perform self-optimization routines using a genetic algorithm [80, 81]. The algorithm creates sets of parameters in preset intervals and evaluates the fitness of the set using a measurement quantity arbitrarily chosen by the experimenter. This quantity can simply be a fluorescence signal or, using a more sophisticated approach, the size or density of an atomic cloud as determined from fitting absorption images. After sorting the results of a given number of sets (one generation), the most successful ones reproduce to future generations. Random mutations of the parameter sets ensure that the algorithm does not converge on local maxima. This method has proven very useful in cold atom experiments due to the complexity of such setups [82]. Atom chip experiments specifically benefit from such a routine, as most experimental sequences require a large number of interdependent parameters that simply can not be optimized sequentially in a reasonable time frame. In the QUANTUS-2 apparatus, the algorithm is used to optimize the chip-MOT sequence, the transfer from chip-MOT to the magnetic trap and the RF-frequency evaporation to BEC (see Chapter 3). A detailed description with measurement examples can be found in the appendix of Ref. [65].

2.10 Summary

A second generation, compact BEC machine was created, building on the successes of the QUANTUS-1 payload [4]. The payload volume of0.32 m^3 was reduced by a factor of two compared to the previous generation, while significantly increasing the complexity of the apparatus. The total weight of 453 kg and power consumption of 363.9 W are well within the restrictions set by the drop tower facility and allow for autonomous, mobile operation for four hours at a time.

Two laser systems have been developed for the use in QUANTUS-2. The 1st generation system was used for the ground-based pre-studies and has since been passed on to the third and fourth apparatus within the QUANTUS collaboration, the sounding rocket payloads MAIUS-A and MAIUS-B. The 2$^{\text{nd}}$ generation laser system is even more highly integrated, with the rubidium part of the two-species system filling only half of a single capsule platform. At the same time, it delivers Raman and Bragg atom interferometry options and is designed to be operated in the catapult mode of the drop tower.

Key features and improvements of the presented apparatus are the new dual-chamber source design, with a multi-layer atom chip setup. Two detection angles for absorption imaging, one of which uses the chip surface mirror to detect a double image, in principle allow for 3D reconstruction of the atomic clouds. The magnetic shielding was significantly improved with respect to the previous apparatus, promising sufficient isolation from external magnetic fields to perform high-precision measurements in the drop tower. Newly developed compact electronics play a significant role in the ongoing miniaturization efforts and enable the completely autonomous operation of the system.

CHAPTER 3

Rapid Production of Large BECs with Atom Chips

This chapter will outline the experimental steps to produce BECs with high atom number in less than two seconds, using steep trapping potentials provided by an atom chip. Generally, chip traps feature high trap frequencies over small volumes and thus are excellent tools for rapid evaporative cooling of moderately small atomic clouds. Producing BECs with high atom numbers akin to macroscopic coil setups and dipole traps requires considerable efforts in bridging the spatial mismatch between large laser-cooled ensembles and small chip trap topologies. This is accomplished by loading a multi-layer chip setup directly from a vapor cell source with adjustable atomic beam parameters. The different characteristic structure sizes of the individual layers allow for sequential compression of large atomic samples into the final magnetic trap. Here, the atoms are cooled to quantum degeneracy at high collision rates on the verge of the inelastic regime.

The experimental sequence for the rapid production of BECs can be divided into five steps, as illustrated in Figure 22. The synergy of the tunable atomic beam source with the custom atom chip setup stands out as one of the most important technological improvements with respect to the predecessor experiment QUANTUS-1. The novel loading scheme plays to the advantages of both state-of-the-art vapor cell sources and atom chip technology, with the multi-layer chip design as the crucial link between them.

3.1 Loading of the Chip-MOT

The experimental sequence to prepare ultra-cold clouds of ^{87}Rb begins with collecting atoms from a background vapor using a two-stage magneto-optical trap (MOT) [83]. The apparatus is equipped with a rubidium reservoir as a vapor source. The temperature of the reservoir is maintained at approximately 70°C and the vapor pressure inside the 2D chamber equilibrates

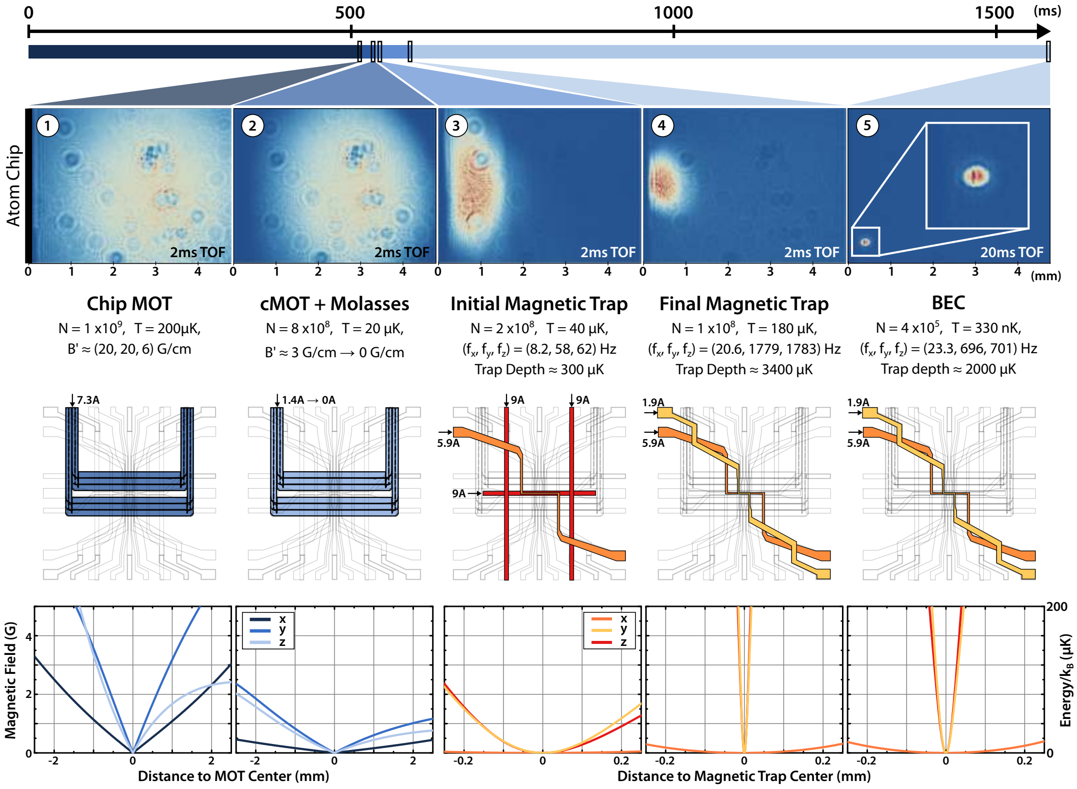

Figure 22: Source scheme to prepare 4×10^5 quantum degenerate atoms in 1.6 s. Five absorption images of the atoms illustrate the steps involved. The chip structures used as well as the simulated magnetic field are shown below the images. The trap bottom has been subtracted for the magnetic traps. All chip configurations are used in conjunction with external bias fields. ① After 500 ms 1×10^9 atoms are loaded into the chip-MOT. ② The atoms are compressed and molasses cooled to 20 μK. ③ 2×10^8 atoms can be captured in the initial magnetic trap, formed by the mesoscopic H and a base chip Z structure. ④ The trap is compressed by switching from the mesoscopic H structure to a science chip Z structure, while keeping the base chip Z switched on. ⑤ During evaporation to BEC the trap is decompressed once to avoid losses from inelastic collisions.

around 8×10^{-8} mbar. In this environment, an atomic beam is generated and guided to the 3D chamber that is maintained in UHV.

3.1.1 2D$^+$MOT

A conventional 2D-MOT collects and cools atoms along its longitudinal axis without manipulating the longitudinal velocity component of the atoms. The only modification to the thermal Maxwell-Boltzmann distribution stems from the aperture, i.e. the differential pumping stage the atoms need to pass to reach the UHV chamber. A small number of atoms have the correct

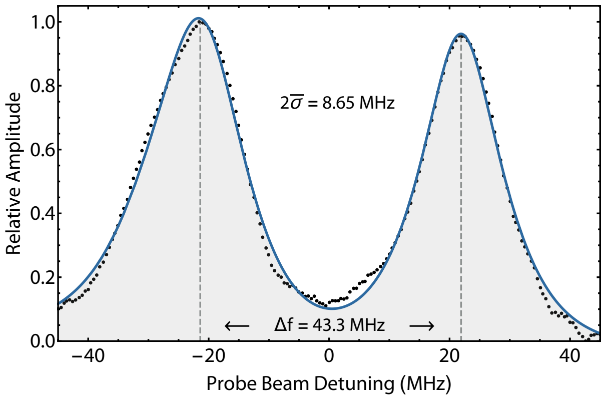

Figure 23: Exemplary scan of the longitudinal velocity profile of the $2D^+$MOT. The signal was fitted with the sum of two Voigt distributions, both of which include the natural linewidth of the transition. The mean standard deviation of both Gaussian components $\overline{\sigma}$ gives the velocity spread of the atomic beam, while the frequency difference of the peaks Δf gives the mean longitudinal velocity via (3.2). The inferred atomic beam velocity and 2σ uncertainty are $v = 23.89$ m/s and 11.24 m/s, respectively.

initial trajectory to pass the aperture without being affected by the cooling beams (funneling). Atoms with very low longitudinal velocity may experience too much transverse drift to pass the pumping stage, resulting in a cut-off velocity.

The flux of a 2D-MOT can be increased by adding a pushing beam along the longitudinal axis. Not only does the radiation pressure of the beam push more atoms over the velocity threshold, it also redirects atoms previously traveling in the opposite direction. However, the increase in flux which scales with the pushing beam power also elevates the mean velocity of the atomic beam. A $2D^+$MOT [84] provides control over the longitudinal velocity profile by employing an unbalanced pair of counter-propagating laser beams along the longitudinal axis, the pusher and the retarder beam. The retarder beam is reflected of the differential pumping stage and hence has a cutaway in its center corresponding to the aperture. The beam pair simultaneously cools the atoms along the axis and guides them through the differential pumping stage. Using this technique, the flux can be increased by an order of magnitude while gaining control over the longitudinal velocity profile. Thus, the performance of the source can be increased without putting harsh demands on the capture velocity of the 3D chip-MOT, which is characteristically low.

The performance of the $2D^+$MOT can be characterized by measuring the fluorescence of resonant probe light intersecting with the atomic beam in the 3D chamber. The probe beam is aligned at an angle of 45° with respect to the atomic beam axis. The atomic flux Φ in the detection volume can be obtained from the magnitude of the fluorescence signal on a photo diode (PD):

$$\Phi \propto \Delta S \, \langle v \rangle \,, \qquad [\Phi] = \text{atoms/s}, \tag{3.1}$$

where ΔS is the PD signal and $\langle v \rangle$ the mean longitudinal velocity.

The mean longitudinal velocity $\langle v \rangle$ is measured by retro-reflecting the probe beam, effectively creating a beam pair [85], and scanning its frequency over the resonance of the cooling transition

Figure 24: Capture volume of the chip-MOT. The red curve shows the estimated cooling light intensity along the atomic beam axis. The grey curve plots the magnitude of the magnetic field from Biot-Savart simulations of the chip potential. The atoms experience significant deceleration only over a 15 mm distance in the center of the MOT. The small capture volume limits the capture velocity of the chip-MOT to approximately 30 m/s.

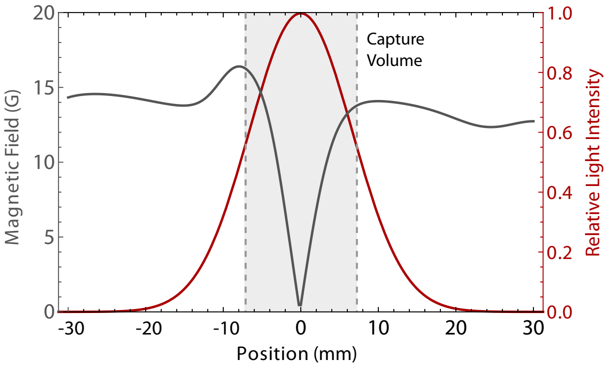

(see Figure 23). Due to the Dopplershift, different velocity classes are resonant with the probe light at different detunings, yielding a velocity distribution convoluted with the natural linewidth of the transition. It features two peaks, one for each of the two counter-propagating beams. The mean longitudinal velocity $\langle v \rangle$ can be calculated from the frequency difference of the central peaks:

$$\langle v \rangle = \frac{\Delta f \, \lambda}{2 \cos\left(\theta\right)}. \tag{3.2}$$

The width of the velocity distribution can be estimated from the width of the Doppler component of a Voigt distribution fitted to the profile. Alternatively, the full velocity distribution can be obtained from switching of the atomic beam and measuring the arrival time of the atoms with the probe beam [84].

The magnitude of the fluorescence signal was used to find the optimal cooling light detuning of −18 MHz and magnetic field gradient of 19.8 G/cm. The magnetic field coils were adjusted individually to maximize flux through the differential pumping stage and compensate for small inequalities in laser power balance stemming from the mirror MOT configuration. The performance of the 2D$^+$MOT does not saturate at the total cooling laser power of 120 mW that is currently available in the setup.

The longitudinal velocity profile of the atoms can be manipulated by changing the pusher-retarder power ratio (P/R) and the ratio between transverse and axial cooling power (T/A) [85]. The capture velocity of the chip-MOT was found to be limited to approximately 30 m/s by simulating the capture process through solving the equation of motion of the atoms numerically. This relatively low value is caused by the small beam diameters of 18 mm and the fact that the magnetic field only has a true quadrupole shape in the vicinity of the trap center (see Figure 24). Therefore, the velocity profile of the source was tailored to the capture performance of the chip-MOT with final power ratios of P/R = 4 and T/A = 18.

3.1.2 Chip-MOT

Capture Volume and Velocity

The chip-MOT configuration has been modeled to find its capture velocity in dependence of applied currents, bias field strengths, laser power and detuning. Due to the small size, the chip-MOT features a low capture velocity in comparison to typical macroscopic devices. Increasing the beam diameter at constant intensity is the easiest way to increase the capture velocity, but in our compact setup the maximal size is hard set by the size of the vacuum chamber and its windows. The magnetic field gradient and laser detuning can be adjusted to improve capture, but their parameters also significantly influence the total atom number in the MOT. Thus, it is more convenient to manipulate the velocity profile of the atomic beam from the 2D$^+$MOT to efficiently load into the chip-MOT.

The deceleration dynamics are given by the radiative interaction of the atoms with the MOT laser beams in presence of the magnetic field. The force from spontaneous absorption out of any one beam is

$$\mathbf{F} = \pm\hbar\mathbf{k}\,\frac{\Gamma}{2}\,\frac{\Omega s_0}{1 + \Omega s_0 + (2\delta_\pm/\Gamma)^2} \tag{3.3}$$

with

$$\delta_\pm = \delta \mp \mathbf{kv} \pm \mu B/\hbar. \tag{3.4}$$

Here Γ is the natural line width of the cooling transition for ^{87}Rb, δ the laser detuning from the resonance of that transition, $s_0 = I/I_{\text{sat}}$ the saturation parameter, Ω the Gaussian intensity distribution of the laser beams, $\mathbf{k}$ the wave vector of the laser, $\mathbf{v}$ the velocity of the atoms. B is the magnetic field magnitude along the atomic beam as seen by the atoms coming from the source (see Figure 24) and $\mu = 5/6\mu_{\text{B}}$ denotes the effective magnetic moment of the atoms, where μ_{B} is the Bohr magneton.

Since there is no laser beam in the 3D chamber counter propagating to the atoms and the beam diameters are small, the cooling force is highly position dependent and most cooling happens close to the trap center. The capture velocity for the chip-MOT configuration has been simulated for varying cooling light intensity. In our setup, up to 15 I_{sat} of laser power are available. However, due to the small beam diameter an increase in power does not significantly improve capture due to saturation.

Atom Numbers

The loading rate of the 3D-MOT was measured using its fluorescence signal (see Figure 25). The MOT starts to fill with the initial flux but saturates fast as the atomic clouds becomes denser and partially non-transparent to the cooling light. Additionally, the rescattered light from the

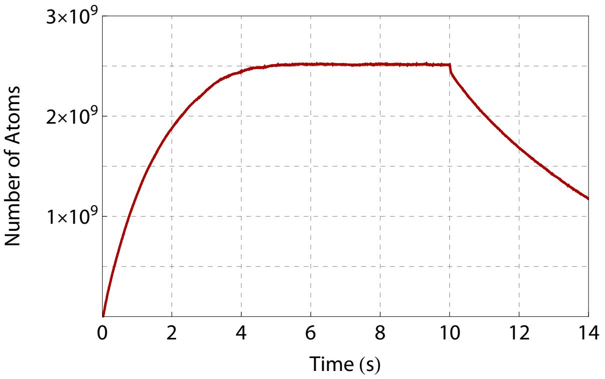

Figure 25: Loading rate and decay of the chip-MOT. The initial loading of the 3D-MOT features an effective flux of 1.4 × 10^9 atoms/s. The total atom number saturates at 2.5 × 10^9 atoms after four seconds. The lifetime of the MOT is approximately 5.5 s, limited by laser beam imbalance of the mirror MOT configuration. The achieved atom numbers are comparable to typical macroscopic lab experiments.

atoms creates radiation pressure from within the MOT, further limiting its density. Close to saturation, the total density remains constant and an increase in atoms causes the cloud to grow in size much faster. In its saturated state, the effective flux $\Phi(N)$ is equal to the atom loss from the trap, and the time derivative of the atom number

$$\frac{dN}{dt} = \Phi(N) - N\left(\frac{1}{\tau_{\mathrm{bg}}} + \frac{1}{\tau_{\mathrm{Rb}}}\right) - \beta \int d^3r\, n^2(\mathbf{r}, t) \tag{3.5}$$

becomes zero. Here τ_{bg} and τ_{Rb} are the lifetimes associated with collisions with the background gas and other rubidium atoms, respectively, and β is the loss coefficient for light assisted collisions. These light assisted losses scale with density and are therefore integrated over the density profile $n(\mathbf{r})$ of the trapped atoms. Since the MOT is being loaded from an atomic beam and the background pressure in the 3D chamber is less than 10^{-10} mbar, light assisted collisions are the dominant loss mechanism. Accordingly, the cooling light power cannot be increased arbitrarily to enhance the flux and the highest atom numbers in the 3D-MOT are found at a moderate cooling light power of 15 mW in each of the four MOT beams.

In its final configuration, the 3D-MOT features magnetic field gradients of$(B'_x, B'_y, B'_z) \approx (6, 20, 20)$ G/cm and a cooling laser detuning of −20 MHz. Optimized for highest atom number, the initial flux of atoms is 1.4 × 10^9 atoms/s and the MOT saturates at 2.5 × 10^9 atoms after 4 s (see Figure 25). However, the loading can also be optimized for shorter times, featuring a higher initial flux while saturating at a lower total atom number. A typical MOT loading phase prepares about 1 × 10^9 atoms in 500 ms. This phase can be reduced to as little as 150 ms without a significant decrease in BEC performance, as the transfer to the magnetic trap is the most critical step of the loading process.

3.2 Compression MOT and Optical Molasses

After MOT loading, the center of the cloud is located at a distance of approximately 3 mm from the chip surface. Several measures are employed to optimize loading into the first magnetic trap which is centered only 500 µm away from the atom chip.

First, the cloud is compressed by reducing the magnetic field gradient to 3 G/cm and increasing the detuning to −48 MHz. The atoms are then shifted towards the chip by adjusting the bias field. The entire process lasts approximately 40 ms. Since the cloud diameter is still 1 mm at this time, it is not possible to match the cloud position and the magnetic trap position perfectly without moving a portion of the atoms into the chip.

Second, the atoms are subjected to a brief cooling period in an optical molasses [86]. To this end, the magnetic field is switched off and light detuned by −116 MHz from the cooling transition is applied for 2 ms. The final temperature of the cloud is 20 µK. Smaller molasses temperatures cannot be obtained in our setup due to the inherently poor beam balance in the mirror MOT configuration.

Third, the atoms are optically pumped into the $|F = 2, m_F = 2\rangle$ state by applying cooling light with a linear frequency sweep from −265 to −244 MHz over 0.73 ms. This state preparation pulse increases the number of atoms transferred to the initial magnetic trap by a factor of three.

3.3 Magnetic Trapping

3.3.1 Transfer to Initial Magnetic Trap

Efficient transfer into the first magnetic trap depends on several parameters: co-location of atoms and trap, trap volume and mode matching. Mode matching is achieved by minimizing the change in entropy $\Delta S \geq 0$ and thereby heating caused by the transfer. Ideally, the phase space density (PSD) of the molasses cooled cloud,

$$n_0 \Lambda^3 = \exp\left[\frac{5}{2} + \gamma - \frac{S}{N}\right], \tag{3.6}$$

should be conserved to the thermalized magnetically trapped ensemble. Here, n_0 is the peak density, Λ the thermal de Broglie wavelength, $\gamma = 3/2$ the effective volume of a harmonic trap and S/N the entropy per particle [87]. Assuming instantaneous transfer and a normally distributed initial cloud [48] with width σ and temperature T, the optimal harmonic trap frequency is given by:

$$f = \frac{1}{2\pi\sigma}\sqrt{\frac{k_\mathrm{B} T}{m}}, \tag{3.7}$$

Figure 26: Number of atoms captured in the magnetic trap in dependence of MOT loading time. The atom number were derived from fitting the cloud profiles from absorption images after a holding time of 500 ms in the magnetic trap. The number of transferred atoms is saturated after 500 ms. Loading times as short as 150 ms are equally feasible, as the temperature of the transferred cloud also increases with loading time.

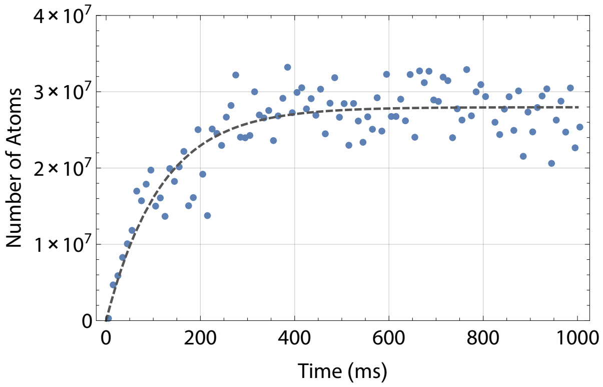

where k_B is the Boltzmann constant and m the particle mass [74]. In this case, an optimal transfer would require trap frequencies of approximately 6 Hz, which is not feasible in the presence of gravitational sag. Instead, the atoms are transferred into a IP type trap with trap frequencies (8.2, 58, 62) Hz, generated by the mesoscopic H structure, a base chip Z structure and the y-coil.

After transfer, the temperature increases by a factor of two. A transfer efficiency of 25% is recorded for saturated MOTs. The efficiency deteriorates with the number of atoms, i.e. smaller clouds can be transferred more efficiently. The highest number of atoms transferred is 2×10^8.

In summary, the transfer is limited by the spatial mismatch of cloud and trap center, the inability to use the correct trap frequencies and the depth of the magnetic trap. Both the spatial mismatch and the gravitational sag can be circumvented by operating the experiment in microgravity, where shallow enough traps can be used at larger distances from the atom chip.

3.3.2 Transfer to Final Magnetic Trap

Once the atoms are confined in a magnetic trap and have reached thermal equilibrium, they are transferred adiabatically to the final trap configuration in two steps. First, the atoms are loaded into a superposition trap of the base chip Z structure and a science chip Z structure, by simultaneously switching off the mesoscopic H while switching on the science chip over25 ms. Afterwards, the trap is compressed by increasing the bias current and the atoms are pulled closer to the chip over 100 ms. The final trap features trap frequencies of (20.6, 1779, 1783) Hz and the temperature increases to 180 μK. The initial PSD is 10^{-5} at an elastic collision rate of 500 Hz.

3.4 Evaporative Cooling to BEC

After transfer to the final magnetic trap, the atoms are cooled towards the critical temperature for Bose-Einstein condensation by selectively removing atoms with more than the average energy from the trap using radio frequency (RF) photons [88–90]. To this end, an RF source is connected to a dedicated U-structure on the base chip. Starting from 18.8 dBm, the output power is continually attenuated to less than 1 dBm at the end of the evaporation sequence.

Since the initial temperature T is much higher than the critical temperature

$$T_\mathrm{c} \approx 0.94 \frac{\hbar\overline{\omega}}{k_\mathrm{B}} N^{1/3}, \tag{3.8}$$

the energy ϵ of the ensemble follows a Boltzmann distribution

$$f(\epsilon) = n_0 \Lambda^3 e^{-\epsilon/k_\mathrm{B}T}, \tag{3.9}$$

while the distribution of atoms in the trap is governed by the density of states:

$$g(\epsilon) = \frac{\epsilon^2}{2(\hbar\overline{\omega})^3}. \tag{3.10}$$

Here $\overline{\omega}$ is the geometrical mean of the trapping frequencies. The total number of atoms can thus be obtained from

$$N = \int_0^\infty d\epsilon\ g(\epsilon) f(\epsilon) \tag{3.11}$$

and the number of atoms up to a given threshold energy ϵ_t can be expressed as [91]:

$$\begin{aligned} N_\mathrm{t} &= N - \int_{\epsilon_t}^\infty d\epsilon\ g(\epsilon) f(\epsilon) \\ &= N \left[1 - e^{-\frac{\epsilon_t}{k_\mathrm{B}T}} \left(1 + \frac{\epsilon_t}{k_\mathrm{B}T} + \frac{1}{2} \left(\frac{\epsilon_t}{k_\mathrm{B}T} \right)^2 \right) \right]. \end{aligned} \tag{3.12}$$

Applying an RF knife with frequency f limits the total energy for trapped atoms to

$$\epsilon_t = |m_F|\, h(f - f_0) = \eta\, k_\mathrm{B} T \tag{3.13}$$

by coupling atoms with higher energies to untrapped states and thus evaporating them from the trap. Here, f_0 is the resonance frequency at the bottom of the trap and η is called the truncation parameter. The distribution (3.12) can be measured by truncating at various energies and recording the remaining number of atoms. Fitting (3.12) to the experimental data yields the total number of atoms, the trap bottom frequency and the temperature (see Figure 27).

After truncation, the ensemble rethermalizes through elastic collisions and arrives at another energy distribution with lower temperature. To remove the same amount of energy over time, η is held approximately constant and f is ramped down exponentially. We break down the

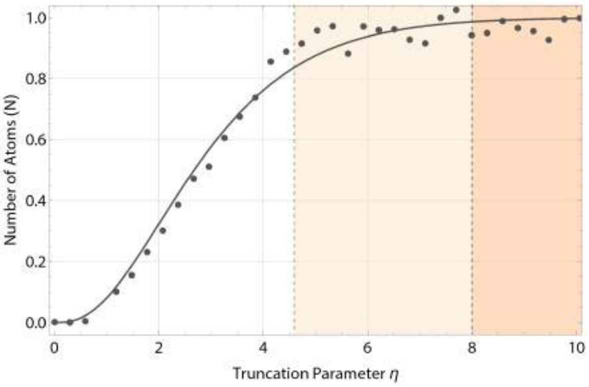

Figure 27: Cumulative atom number distribution over the truncation parameter $\eta = \epsilon/k_{\mathrm{B}}T$. The solid line is a fit of equation (3.12) to atom number data acquired by truncating the distribution at various energies. For efficient evaporative cooling, truncating at energies > 4.59 η is desirable. For minimal atom loss the truncation energies should exceed 8 η.

exponential frequency ramp into five linear ramps to be more flexible towards the conditions in each phase and optimize the efficiency of the cooling process step by step.

Generally, it is desirable to use a truncation parameter as high as possible to keep atom loss to a minimum. However, in the presence of other loss mechanisms the optimal truncation parameter and thereby maximal evaporation efficiency must be obtained from a comprehensive model of the process. The efficiency found experimentally for our optimized sequence is depicted in Figure 28a.

Efficiency Model

The figure of merit for efficient evaporative cooling is the ratio between the change in PSD to the change in atom number N of the ensemble:

$$\gamma = -\frac{\mathrm{d}\ \ln(\mathrm{PSD})}{\mathrm{d}\ \ln(N)}. \tag{3.14}$$

If we assume perfect forced evaporation, i.e. every atom with an energy higher than $\eta\, k_{\mathrm{B}}T$ is immediately evaporated, there is a simple relation between the truncation parameter η and γ

$$\gamma(\eta, R) = \frac{3\,\alpha(\eta)}{1 - \lambda(\eta)/R} - 1, \tag{3.15}$$

for a three-dimensional harmonic potential [92]. Here, α is the ratio between a change in temperature and a change in atom number, λ the ratio between the time constant of the evaporation and the elastic collision time and R the ratio of elastic to inelastic collisions. The functions $\alpha(\eta)$ and $\lambda(\eta)$ are independent of R and can be obtained from a suitable model [92]. For arbitrary values of η these functions need to be expressed in terms of incomplete gamma functions $P(n, \eta)$

to reflect the truncated Boltzmann distribution of the energy [93, 94]:

$$\begin{aligned}\alpha(\eta) &= \frac{1+\eta-\frac{P(5,\eta)}{\eta\,P(3,\eta)-P(4,\eta)}-3R(3,\eta)}{3R(3,\eta)+3\left(1-\frac{P(5,\eta)}{\eta\,P(3,\eta)-P(4,\eta)}\right)\left(1-R(3,\eta)\right)},\\ \lambda(\eta) &= \sqrt{2}\left[1-3\left(1-R(3,\eta)\right)\alpha(\eta)\right]\frac{P(3,\eta)}{\eta\,P(3,\eta)-4P(4,\eta)}\,e^{\eta}.\end{aligned} \tag{3.16}$$

These functions are related to the Euler gamma function Γ via

$$P(a,\eta)=\frac{1}{\Gamma(a)}\int_0^{\eta} dt\,t^{a-1}\,e^{-t} \tag{3.17}$$

and $R(n,\eta)$ is given by

$$R(a,\eta)=\frac{P(a+1,\eta)}{P(a,\eta)}=1-e^{-\eta}\frac{\eta^{a}}{\Gamma(a+1)}\frac{1}{P(a,\eta)}. \tag{3.18}$$

Using equations (3.15) and (3.16), the evaporation efficiency $\gamma(\eta,R)$ for perfect forced evaporation in a three-dimensional harmonic potential has been plotted in Figure 28b for the two trap configurations in use and their respective value of R.

Collision Rates

Having derived analytical expressions for $\alpha(\eta)$ and $\lambda(\eta)$, it is evident from (3.15), that in a system where η can be chosen arbitrarily, the maximum efficiency γ_{max} only depends on R, the ratio of good to bad collisions.

The good collisions are those between two trapped atoms in the same spin state which lead to rethermalization without atoms being lost from the trap. This process has the per atom rateΓ_{el}. The relevant inelastic processes are collisions with atoms from the background gas with rate Γ_{bg} and inelastic three-body collisions with per atom rate$\Gamma_{\text{3-body}}$. This leaves us with the final ratio

$$R=\frac{\Gamma_{\text{el}}}{\Gamma_{\text{loss}}}=\frac{\Gamma_{\text{el}}}{\Gamma_{\text{bg}}+\Gamma_{\text{3-body}}}. \tag{3.19}$$

Since Γ_{bg} is generally constant over the evaporation process, maximizing R means increasing the elastic collision rate as much as possible while staying dilute enough to not give rise to three-body collisions. For this reason, the trap is initially compressed to trap frequencies of (20.6, 1779, 1783) Hz to maximize the elastic collision rate. As the ensemble grows more and more dense, the trap is decompressed to trap frequencies of (23.3, 696, 701) Hz after four ramps

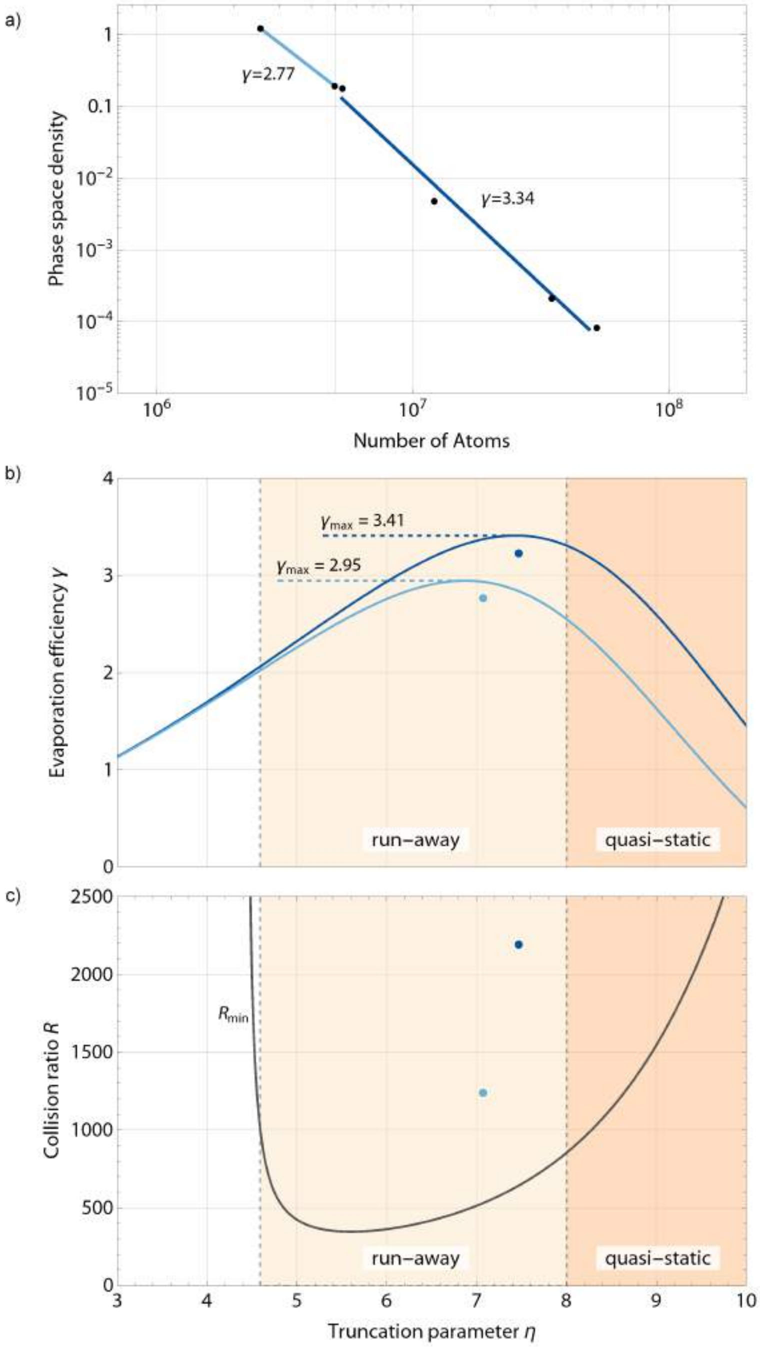

Figure 28: Evaporation performance. Figure (a) shows the phase space density of the ensemble over the atom number after each of the linear RF ramps. The γ factor has been averaged over the ramps in each trap configuration (dark blue and light blue). Figure (b) plots the modeled efficiency $\gamma(\eta, R)$ for the respective values of R shown in Figure (c). The attained efficiencies are close to the maximum values predicted by the model. The entire sequence is performed deep in the runaway regime bounded by R_{min}.

of evaporation, at the onset of three-body collisions. These two trap configurations are color coded in dark blue and light blue, respectively, in Figure 28.

However, in the presence of other loss mechanisms, e.g. due to the limited trap depth, R can more generally denote the ratio of the lifetime of the ensemble over the elastic collision time. For the data presented, the lifetime in the trap averaged over the entire sequence was measured to be 2.84 s.

For runaway evaporation with constant or increasing elastic collision rate, a lower limit for R can be specified [92]:

$$R_{\text{min}} = \frac{\lambda(\eta)}{\alpha(\eta) - 1}. \tag{3.20}$$

Figure 28c plots the theoretical bounds set by R_{min} using equations (3.16) and (3.20), together with the measured values of R for each step of the evaporation sequence. The runaway regime for a three-dimensional harmonic potential starts at $\eta > 4.59$. Beyond a truncation energy of $\eta = 8$, R_{min} starts to increase rapidly as very few atoms populate the high energy tail of the distribution. Operating in this quasi-static regime offers minimal atom loss but generally requires lifetimes greater than 30 s at the trap frequencies we employ.

While we are operating close to the maximum efficiency as predicted by the model, we are clearly limited by the lifetime of the ensemble. Higher efficiencies and atom numbers may be obtained if the vacuum quality can be improved and the evaporation sequence can be maintained in the quasi static regime.

3.5 Comparison

Since the first demonstration of BEC in 1995 [90], the rate of generating quantum degenerate gases has increased steadily. The fastest BEC machines published to date are compared in Figure 29. These experiments either employ an atom chip (circles) or a dipole trap (squares) for fast and efficient evaporation. Recently, BEC machines are not only getting faster but have also become much more compact [4, 95]. They have since crossed the divide from lab experiments to mobile and transportable devices (semi-filled symbols).

The fastest previously reported apparatus features a repetition rate of 1 Hz with 1.5×10^4 atoms in the condensed phase, using an atom chip [96]. The fastest BEC in a dipole trap was produced in 1.6 s with an atom number of 5×10^4 [102]. To study the overall performance of our setup, we optimized the BEC production for three scenarios: ① fast BEC production, ② BEC at 1 Hz repetition rate and ③ highest atom number in the BEC. The shortest production time can be achieved by reducing the MOT loading time to 350 ms and the duration of the evaporation to 450 ms. Within a total time of 850 ms the apparatus is able to produce BECs of 4×10^4 atoms. For a direct comparison with the previously fastest BEC machine, we optimized the atom number at

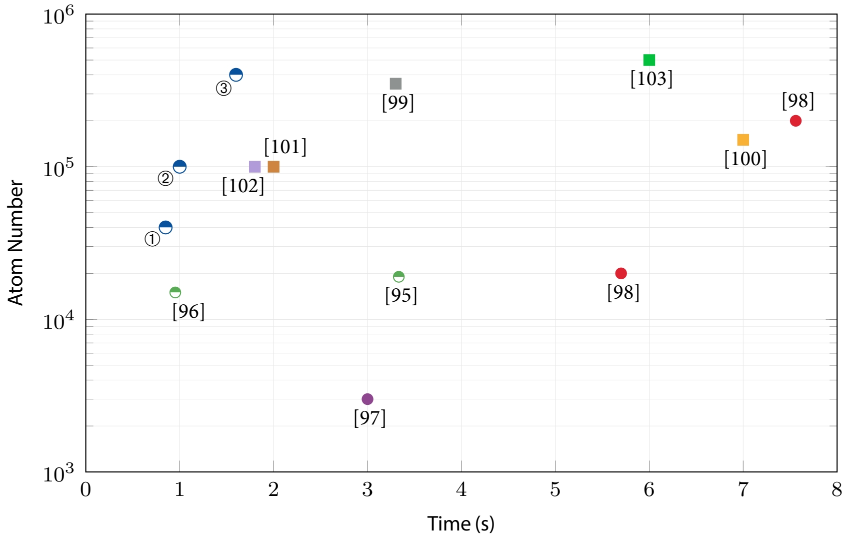

Figure 29: Comparison of the fastest BEC machines. Circles mark atom chip based experiments [95–98], squares indicate experiments using dipole traps [99–103]. Ref. [101] describes a ^{84}Sr experiment. Ref. [102] marks a recent dipole trap setup using ^{174}Yb. Ref. [103] is a hybrid apparatus using a magnetic quadrupole trap and a dipole trap to evaporatively cool metastable ^{4}He. All other experiments use ^{87}Rb. Semi-filled symbols mark compact and transportable setups. The performance of the QUANTUS-2 apparatus is represented by three cases, ① – ③.

a production rate of 1 Hz. With a MOT loading time of 450 ms and a duration of the evaporation of 500 ms, we are able to produce ensembles of 1×10^5 atoms. While our setup produces the highest atom number overall among the fastest BEC machines, its flux of condensed atoms is also on par with the best lab-based devices [104, 105].

These results can be improved further, both in terms of speed and atom number. The biggest handicap for the data presented was the vacuum quality and thereby the lifetime of the atoms. Improving the vacuum quality could reduce the MOT loading time to as little as 150 ms. A similar improvement can also be achieved by increasing the 2D cooling laser power. An increase in lifetime would also lead to higher evaporation efficiencies and thus higher atom numbers. Another approach to increase the atom number in the BEC is to improve the mode matching of the laser cooled atoms with the initial magnetic trap, resulting in a higher initial PSD. This could be achieved by reducing the molasses temperature further or by operating the experiment in microgravity, where the optimal mode matching conditions can be met thanks to the absence of gravitational sag. Consequently, producing BECs of 10^6 atoms at a 1 Hz rate is feasible if these technical issues are addressed.

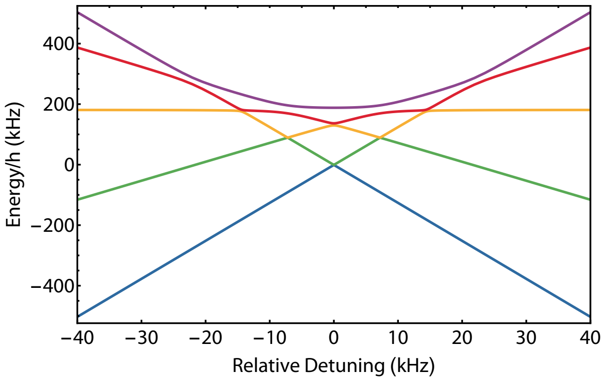

Figure 31: Energy of the adiabatic states over the relative detuning of the RF field. To the left of the resonance, the m_F states are sorted from $m_F = +2$ at the top (purple) to $m_F = -2$ at the bottom (blue). The slopes of the curves over the progression of the plot signify equal m_F states, while the different colors mark the adiabatic states. Thus, a RF ramp over the entire plot range transforms an $m_F = +2$ input state into an $m_F = -2$ output state.

3.6 Adiabatic Rapid Passage

After creation of the BEC, the ^{87}Rb atoms remain in the magnetically sensitive $|F = 2, m_F = 2\rangle$ hyperfine state. A useful tool for reliable population transfer to other substates is an adiabatic rapid passage (ARP) [106]. The transfer is achieved by applying a RF signal to manipulate the eigenstates of the system. With appropriately chosen frequency, magnetic bias field and RF power, the original (diabatic) states can be connected via the dressed states (see Figure 31). Detailed calculations of the eigenstates for the ^{87}Rb $|F = 2\rangle$ manifold under RF dressing can be found in Ref. [107]. An concise account on the experimental optimization in our setup can be found in Ref. [79]. Figure 30 shows the adiabatic population transfer of a BEC initially in $m_F = 2$ to other substates via an RF sweep.

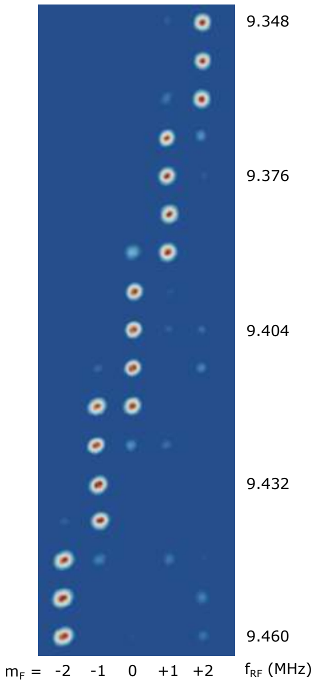

Figure 30: Absorption images of the m_F state population over a RF sweep.

3.7 Summary

The novel source setup and loading scheme is a drastic improvement to the predecessor experiment with a factor of 40 improvement in total atom number and a 12 times shorter preparation time [4]. It generates Bose-Einstein condensates of $4{\times}10^5$ ^{87}Rb atoms every 1.6 seconds, a flux that is on par with the best lab-sized devices. Ensembles of $1{\times}10^5$ atoms can be created at a 1 Hz rate. The speed of the setup allows for a much more efficient use of the μg time available in the drop tower, where the data rate can now be doubled in drop operation and quadrupled in catapult operation.

The significant decrease in BEC production time paired with competitive atom numbers allows for many interesting applications, in both mobile and lab-based experiments. Using ultra-cold atoms as test bodies in atom interferometry is the most obvious implementation. The small momentum width of degenerate atoms is a clear advantage with respect to the efficiency of atom-light-interaction based beam splitters, since the phase sensitivity of an atom interferometer is fundamentally limited by the fidelity of momentum transfer in an atom-based sensor [47]. Additionally, the momentum width is highly relevant for magnetic and optical lensing techniques, where the mode quality of BECs is mandatory to reach extremely low expansion rates.

Publications

The results of this part are published in:

[5] J. Rudolph et al. - ”Degenerate Quantum Gases in Microgravity”,
Microgravity Sci. Technol. **23**, 3, 287-292 (2011), DOI: `10.1007/s12217-010-9247-0`.

[108] J. Rudolph et al. - ”A high-flux BEC source for mobile atom interferometers”,
New J. Phys. **17**, 065001 (2015), DOI: `10.1088/1367-2630/17/6/065001`.

Part II:

Mobile Operation and Microgravity Campaigns

Precise Control of Quantum Gases in Extended Free Fall

> ”It is weight that gives meaning to weightlessness...”
>
> — Isamu Nogushi

CHAPTER 4

Ultra-Cold Atoms in Microgravity

Drop Preparations, Pre-Tests and First Flight

The experiment was transported to the drop tower facility at ZARM, Bremen in December 2013. Here, the final engineering steps and drop system integration took place. Transitioning from lab to drop tower operation comes with a new set of challenges. This chapter summarizes the efforts to prepare the QUANTUS-2 experiment for the continuous use as a freely falling matter-wave sensor. This includes an overview of the necessary modifications, the ground-based pre-tests as well as detailed descriptions of the first drop and catapult launch of the experiment. The drop tower and catapult systems and the operating conditions at the facility are discussed. Additionally, the differences in data acquisition and analysis due to flight systematics and restrictions are discussed. These include post correction of the acquired images due to displacement of the imaging optics, residual drag in the drop tube and rotations of the capsule during free fall.

4.1 Modifications

The most challenging tasks in transitioning from lab to drop tower operation are power management, heat dissipation, communication to the capsule and maintaining mechanical integrity under continuous stress. For successful µg operation the capsule needs to be able to run autonomously for several hours at a time in a hermetically sealed state. To this end, the capsule base structure was added to the system, containing most of the batteries and the communication infrastructure (see Figure 32). A total of eight different voltages are provided by $LiFePO_4$ accumulators, adding up to a capacity of 2464 Wh. Thus, at a power consumption of approximately 365 W the system can run for several hours without recharging. Limited charging capabilities (three of the eight voltages) are present while being docked in the drop tower. A detailed account on the capsule base infrastructure and the battery configuration can be found in Ref. [79].

While providing the electrical power via batteries is straight forward, maintaining system performance while heating the experiment is an uncommon issue for ultracold atom experiments that are typically confined to air-conditioned laboratories. Water-cooling components and supplementary heat sinks had to be added to the capsule to minimize the disturbance. While in the lab, the system is connected to a closed loop cooling water cycle maintained at 20°C via heat sinks on the individual platforms and stringers. When sealed, the capsule temperature increases by approximately 3.2°C per hour without access to water cooling. In the drop tower itself, a water cooling connection is provided both at the top of the tower (drop mode) and at the tower base (catapult mode) that can be used while the tower is evacuated. However, due to limited pump capacity the heat transfer is reduced in comparison to the lab chiller.

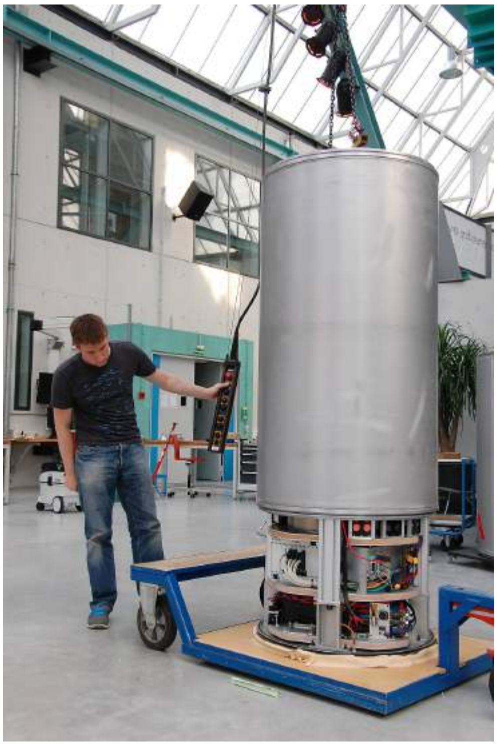

Figure 32: Capsule hull is lowered onto the capsule for the first pre-test. The two visible platforms at the bottom constitute the capsule base structure. The lowest level holds most of the systems batteries. The next platform houses the secondary capsule control computer in charge of communication to the control room.

Communication to the capsule is provided by a WiFi connection with an antenna located in the capsule lid. However, communication issues related to interference in the tower can not easily be simulated in the lab. The total data volume transmitted during operation was reduced to an absolute minimum in anticipation of connectivity issues. Mechanical improvements were added to the system, such a new rubidium reservoir with a robust, valveless design specifically developed for µg-operation [109], to withstand the forces during launch and impact.

4.2 Pre-Tests

After successful integration, several tests were performed to verify standard system performance under drop tower operating conditions. The system was closed with the designated hull and run on batteries for extended periods of time. The three test cases included an extreme test under

Table 6: Summary of the pre-test conditions, the first successful drop and catapult launch. The system performs admirably in autonomous operation. The available run time of the setup exceeds the typical drop duration by over an hour, which grants a substantial safety margin in case of emergency and delayed recovery.

Test conditions	Extreme	Endurance	Typical Drop	Typical Launch
Date	04.07.2014	17.07.2014	18.07.2014	21.10.2014
Location	Lab	Lab	Tower	Tower
Duration	233 min	190 min	165 min	155 min
Battery charging	–	–	interrupted⁺	interrupted⁺
Water cooling	–	interrupted⁺	interrupted⁺	interrupted⁺
Temperature variation#	10°C	6°C	3°C	3°C
Duty cycle laser system	72%	47%	21%	30%
Duty cycle BEC	34%	12%	5%	5%
Max g-level (launch)	–	–	–	27
Max g-level (impact)	–	–	38	36

⁺ during transfer (20 min) + recovery (45 min)
# measured from start to recovery

heavy load without any water-cooling capabilities or recharging of the batteries, an endurance test simulating significant problems during drop operation. The final qualification of the system was accomplished with the first drop and catapult launch of the capsule. The various test conditions are summarized in Table 6.

During the most demanding test run, the system was producing BECs in 8 s intervals over a period of 80 min. Halfway through the test, the fiber coupling of the lasers had decreased by about 15% to 20% without a significant influence on the atom number in the BEC. Only after a rise in laser system temperature of 10°C at the very end of the test, did the fiber coupling and atom number deteriorate substantially. In the endurance test the system was not run continuously and had access to water cooling while in operation. With a moderate temperature increase of 6°C no decrease in performance was observed.

Overall the system performed very well under all test conditions. It can be run on batteries under heavy load for up to three hours without any cooling measures. During a typical drop campaign, the experiment is dropped two to three times a day with only 60 min in between to recharge the batteries. However, due to the charging capabilities in the tower itself (for some of the batteries) and the low duty cycle of the experiment, two drops can be performed back-to-back without recharging.

4.2.1 Payload Rotation

After the second pre-test, the capsule was mounted on a crane and rotated around two horizontal axes to check for loose parts and mechanical instabilities. This procedure was later repeated to measure the performance of the system under various angles (see Figure 33). The systems

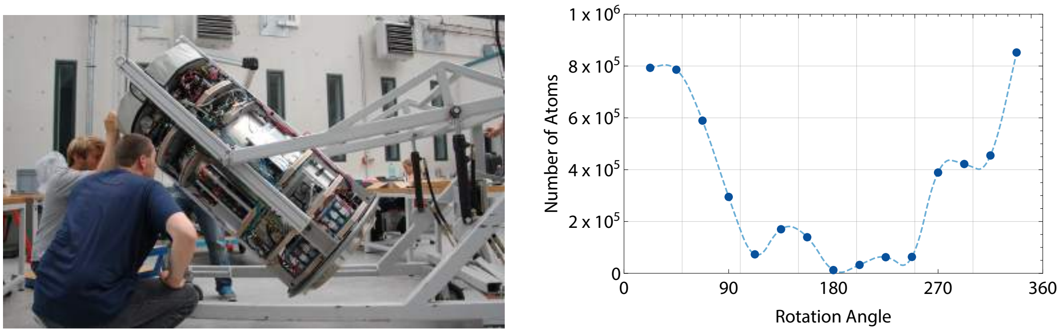

(a) The capsule being rotated around a horizontal axis using a hydraulic crane.

(b) Number of atoms captured in the magnetic trap at various angles.

Figure 33: Rotation of the QUANTUS-2 capsule and system performance at various angles. The rotation procedure is performed to check for loose parts and mechanical problems that are not apparent during lab operation. Using a standard sequence optimized for 1 g operation at zero inclination, the system performs reasonably well up to rotation angle of 90° with respect to the main capsule axis.

performance depends on the orientation of the setup since the atoms are freely falling under the influence of gravity between the optical molasses phase and transfer to the magnetic confinement. The capture of atoms in the magnetic trap is optimized to account for this shift in position, which is why the amount of atoms transferred is diminished when rotating the capsule. Currently, the experimental sequence for molasses cooling and transfer is identical for 1 g and µg operation even though a much more efficient transfer could be achieved using a shallower trap (as discussed in Chapter 3). However, the optimization of a new transfer procedure is very time consuming compared to the limited measurement time available in µg.

In conclusion, the performance of the system is expected to be slightly reduced in µg operation in terms of the starting atom number in the magnetic trap. All other experimental steps up to the generation of the BEC take place in tight confinement, where the presence of gravity is negligible. The frequency of the final RF cut on the onset of condensation needs to be adjusted by about 30 kHz since the gravitational sag reduces the trap bottom energy.

4.3 Drop Tower Qualification

The final qualification steps for the capsule are the first drop and the first catapult launch. Both share the same agenda: ensuring that all lasers remain stabilized, maintaining mechanical integrity and vacuum quality, producing BECs in-flight without loss in performance, and studying the dynamics of the clouds, i.e. its COM motion and expansion.

Secondary to the performance of the system itself, dropping the apparatus also acts as a procedural test of the drop tower infrastructure. There are several differences in respect to the water cooling and battery charging systems in the tower. However, the biggest obstacle are the communication and data transfer between capsule and control computer. Due to interference in the tower, the WiFi connection is very unreliable, slow and brakes off completely at times.

4.3.1 Drop Qualification

Drop Procedure

Prior to beginning the drop procedure, the experiment is switched on to verify that the system works at typical lab performance. Approximately 2.5 h before the actual drop, the setup is set to idle mode with the laser system switched off. The capsule is then detached from the lab equipment an delivered to the drop tower operators in the integration hall. Here, the hull is lowered over the capsule and secured with a buckle at the bottom. It is then transported into the tower, where water cooling, battery charging and WiFi antenna lines are connected to the lid, which is then buckled on to seal the capsule hermetically. The setup is then slowly hoisted upwards and arrives at the top of the tower 2 h before the drop (see Figure 34).

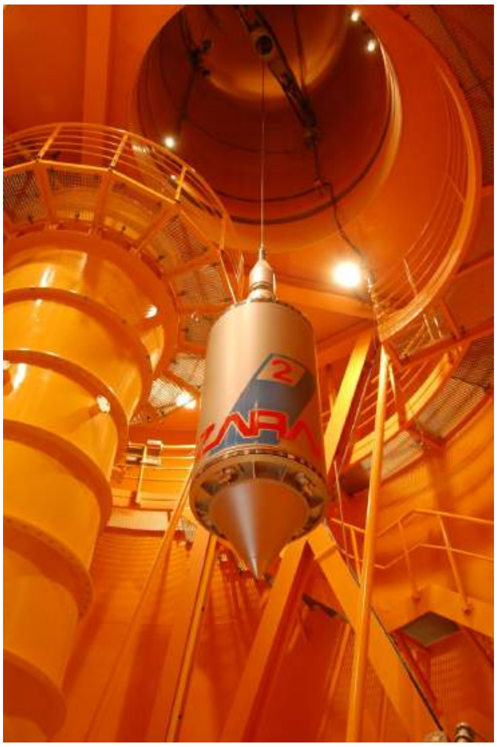

Figure 34: The capsule being hoisted to the top of the drop tube prior to first drop. The deceleration container is visible on the left.

On arrival, the communication with both on-board computers is checked, before the capsule is docked and the charging and water cooling enabled. The tower is then evacuated to a final pressure of about 20 Pa in 1.5 h. The internal capsule pressure is monitored during evacuation as a loss in pressure could lead to overheating of electronic components that rely on some degree of convection cooling.

The laser system is switched on 30 min before the necessary pressure level is achieved. After the tower is evacuated, the system is checked for performance and the drop sequence is set. The charging and water cooling circuits are disabled and the capsule is undocked. After a last check of the BEC performance and the laser lock error signals, the scientists ask for clearance and upload the drop sequence to the capsule. The drop is then initiated by one of the scientists and the capsule is detached after a typical delay of about 4 s. The experimental sequence is triggered by a µg sensor `[ADXL103]` inside the capsule with an additional delay of 6 ms.

After a free fall time of 4.72 s the capsule arrives in the deceleration container and is decelerated over a distance of 4 m with an average peak acceleration of $40g$. The capsule vacuum sensor is closely monitored after impact. Barring an unexpected rise in vacuum pressure, a standard BEC sequence is run immediately after impact, without relocking of the lasers. Upon successful creation of a BEC with typical atom number, the laser system is switched off and the experiment set to idle. The tower is flooded with air until normal pressure is restored, approximately 45 min later. The capsule is then retrieved from the deceleration container and handed back to the scientists.

Several parameters other then the vacuum pressure are also being monitored and recorded during the drop. These include all battery voltages, temperatures at various positions in the capsule, the capsule pressure and the acceleration of the setup as measured by the µg trigger. Later on, monitoring for the atom chip and coil currents as well as continuous monitoring for the laser locks were added.

Once it is established, the WiFi connection is usually maintained over the entirety of the drop. The typical communication with the capsule is sufficiently fast at low data rates, however, transferring images from the capsule can take up to 2 min and halts any other communication attempts. This is not due to bandwidth limitations but rather a problem with package loss and the specific ftp implementation in LabVIEW. This reduces the pre- and post-drop measurement capabilities in the tower somewhat, as lengthy parameter scans are not feasible.

4.3.2 First Drop

The total µg time of 4.72 s available in drop mode is sufficient to produce two BECs consecutively. In Drop #1, two BECs were created using a standard lab sequence and observed after 22 ms and 100 ms TOF, respectively. The first BEC in µg was imaged after the typical TOF for lab experiments. The condensate fraction has changed noticeably due to a shift in trap bottom energy (see Figure 35). The second BEC expanded freely for 100 ms after release, a time unattainable under gravity in our setup, since the atoms fall out of the detection volume after 24 ms. The cloud shows a dominant COM motion towards the chip surface which originates in the specific switch-off sequence in use.

Typically, a BEC is created in the deceleration container immediately after impact. However, after the first drop a standard BEC could not be created for a few minutes. A short spike in vacuum pressure was observed, reaching 5×10^{-7} mbar but normalizing to 2×10^{-10} mbar after 10 min. No other issues, mechanical or otherwise, were apparent after first flight and the system performed as expected. Over the next three drops an equivalent rise in vacuum pressure was

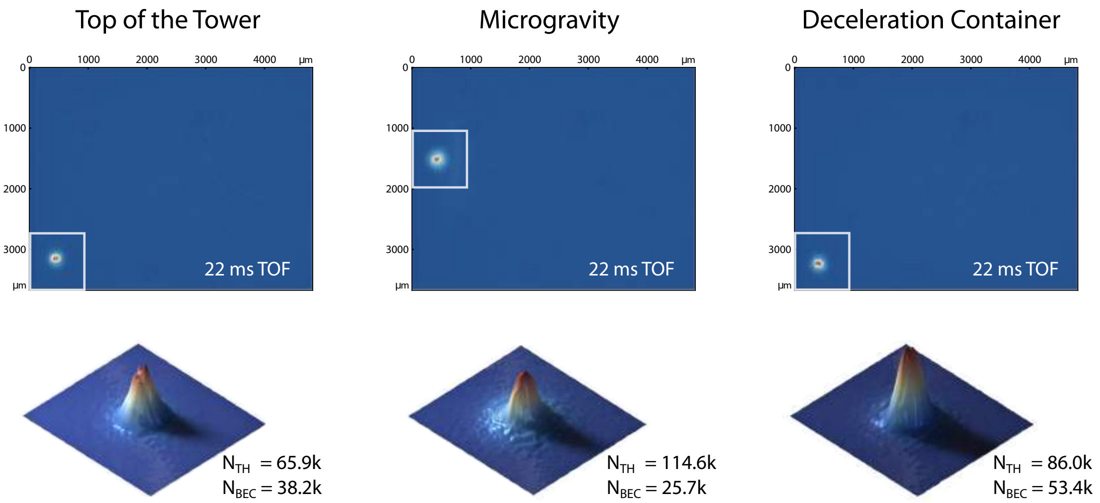

Figure 35: Comparison of the standard BEC sequence before, during and after the first drop. All clouds were imaged after 22 ms TOF. All three sequences show comparable atom numbers within the typical fluctuations. The noticeable differences between $1g$ and $0g$ operation is the cloud location and the condensate fraction. The latter is caused by a shift in trap bottom energy due to the absence of the gravitational sag.

registered with peak values slowly increasing to 6×10^{-6} mbar. Further investigations revealed a small leak on the vacuum seal between the 3D chamber and the aluminum tube housing the differential pumping stage, that would open up under mechanical stress. The leak was closed by re-tightening the seal and no rise in vacuum pressure after impact was observed in the following drops (see Figure 36).

4.3.3 Catapult Qualification

Using the tower's catapult mode, the free fall time can be extended to more then 9 s. However, additional preparations are necessary to operate under even more strenuous conditions. The capsule is accelerated by a pneumatic piston powered by 12 pressure tanks that sit 10 m below the base of the drop tube. The piston applies force to the capsule only via the coin-sized tip of the nose cone. To prevent excess rotation of the capsule which may lead to a collision with the rim of the deceleration container upon impact, the center of mass needs to be within a distance of 1 mm around the vertical geometrical center line [110]. Despite the technical and safety restrictions, substantial rotation around any axis is highly undesirable for the intended measurements of the project.

A commercial six-axes inertial measurement unit (IMU) `[iMAR iIMU-FCAI]` is integrated into the capsule to measure its rotation around three orthogonal axes. Since the atoms move

Figure 36: Vacuum chamber pressure levels immediately after impact during the first drops. Initially, the deceleration caused a steep rise in vacuum pressure. While some pressure signals were expected from the experiences of the first generation, the maximum pressure increased from drop to drop until a potential leak was identified and closed. No substantial rise in vacuum pressure was recorded thereafter.

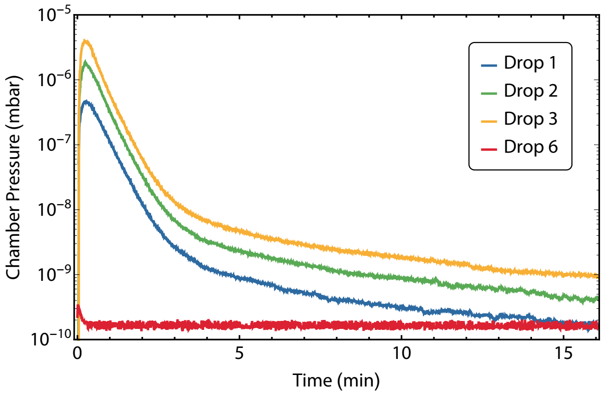

independently of the surrounding apparatus after release from confinement, a rotation of the setup may lead to a shift in position and rotation of the atomic cloud relative to the detection axis. The data recorded by the IMU can then be used to post correct the measurements.

To diminish the rotation of the capsule, it needs to be tared using a multi-axis weighing station where it is rotated around its central axis to determine the center of mass position relative to the axis. Additional taring weights are added to the capsule to correct the center of mass position. A total of 7.5 kg were added to the setup to place the COM within a distance of one tenth of a millimeter to the vertical axis. This increases the gross weight of the capsule to453 kg, limiting the free fall time to 9.0 s for typical catapult pressure levels. No components of the apparatus can be added, moved or removed without re-taring of the capsule, limiting the experimental flexibility during catapult campaigns. Even though the capsule's COM is well aligned to its vertical axis, the inhomogeneous mass distribution may still lead to rotations. Additionally, the frictional forces between the piston tip and the nose cone are unpredictable, leading to variations in the rotation rates between launches.

An additional technical challenge for the apparatus are the substantial forces active during the initial acceleration of the capsule. Instead of the relatively soft transition from $1g$ to $0g$ encountered in drop mode, a spike of up to $30g$ acts on the setup only milliseconds before the start of the experimental sequence. The lasers need to remain locked during launch as relocking is too time-consuming.

Catapult Procedure

The setup is tested and prepared as for drop operation. It is delivered to the drop tower operators 2.5 h before launch. A slightly different lid and nose cone are attached to the capsule. Instead of hoisting the sealed apparatus to the top of the tower, it is placed in a receptacle centered below the drop tube. A retractable motorized supply arm is docked to the capsule lid. It holds the same supply connections as in the drop case. The deceleration container is moved to the side of the drop tower base, ready to swing under the capsule once it is launched.

Upon establishing communication with the on-board computers, the tower is evacuated over the next 1.5 h. When the pressure level dips below 20 Pa, the catapult sequence can be initiated. The supply arm is un-docked and retracted and the hydraulic pressure of the catapult system is ramped up automatically. The piston and capsule are moved downwards to launch position, 9 m below the tower base, in approximately 8 min. Once in position, the scientists have a 5 min window to launch the capsule before the pressure needs to be released to prevent overheating. After launch is initiated, the capsule is accelerated upwards after a typical delay of 4 s. The deceleration container swings into position automatically while the capsule is in flight. All further steps are identical to the drop case.

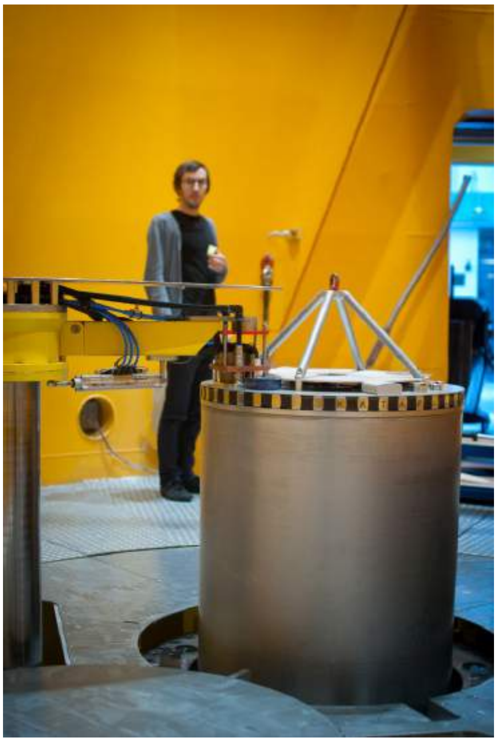

Figure 37: The capsule sits in the catapult receptacle and is docked with the supply arm prior to evacuation of the tower. Once the setup is retracted to launch position 9 m below the drop tube, the scientist have a 5 min launch window before the process is aborted.

The WiFi connection in the tower is very unreliable in catapult operation. While moving down the catapult tube, the connection usually brakes off repeatedly. Due to the long file transfer duration, only very few absorption images can be taken and transferred during the 5 min launch window. Hence, even relocking of the lasers and a subsequent system check is just barely possible within the time limit. This is a stark contrast to drop operation, where the capsule can remain attached at the top of the tower until the system is ready. However, despite the added difficulties and demands connected to catapult operation, the data rate of the experiment in µg can be increased by a factor of two – generating four standard BECs per launch. The maximal TOF for a single BEC can be extended from 2.7 s to approximately 7 s.

4.3.4 First Catapult Launch

The catapult mode of the drop tower offers 9 s of µg time, from the end of the acceleration phase until impact. During the first successful launch (Drop #23), four standard BECs were produced and observed after 25 ms, 50 ms, 75 ms and 100 ms (see Figure 38). The performance did not

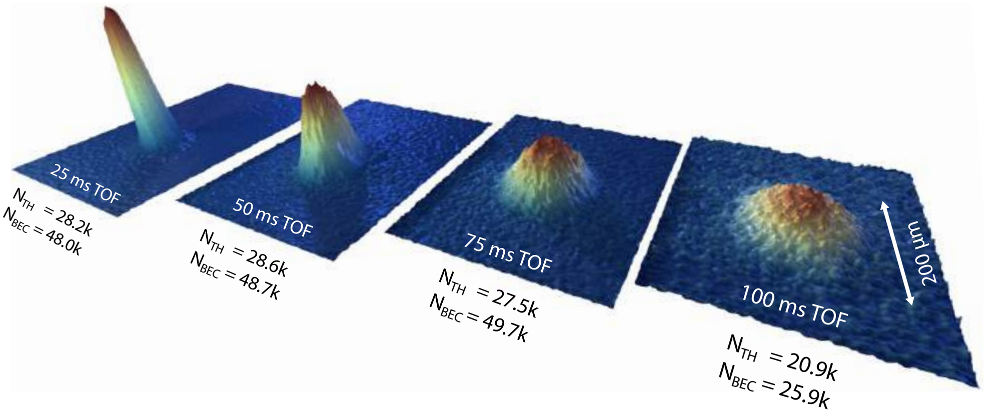

Figure 38: 3D renderings of the absorption images from the first successful catapult launch (Drop #23). Four BECs were prepared consecutively during a single catapult shot and imaged after varying TOFs. The atom numbers during flight appear to be very stable, only declining in the last cloud. Thus, the induced vibrations of the launch mechanism do not negatively impact the performance of the system.

vary over the duration of the flight, indicating that the system works as intended immediately after the acceleration phase. The four clouds observed after different times give insight into the COM motion, its variance, and the expansion of the ensembles. The COM dynamics are discussed in Chapter 5 while the analysis of the expansion of the clouds is presented in Chapter 6.

After the first few catapult launches, some artifacts appeared on some of the absorption images. These observations went hand in hand with an overall decrease in performance. Further investigations showed that particles inside the vacuum chamber would dislodge during the launch acceleration phase and float through the chamber. A video of the detection beam was recorded each over the entire flight in drop and catapult mode. The results confirmed the suspicion that only catapult operation was negatively affected by stray particles.

However, apart from the unwanted objects on the images, the atoms could still be observed cleanly and with sufficient contrast in the majority of cases. Since it is unlikely that the particles hit the cloud directly, the decrease in performance likely stems from beam imbalance during the more crucial steps of the loading sequence such as the compression MOT, moving the compressed cloud towards the chip and the optical molasses phase. A possible source for the particles is the ceramic rim around the chip mount which holds the connection pins the chip structures are bonded to.

4.4 Post-Correction of Data and Flight Systematics

4.4.1 Displacement of Imaging Optics

The sizes and positions of the clouds measured in µg must be precise to within a few micrometers to project the dynamics to longer timescales. Primary goal of the project is to comfortably perform measurements on a BEC for over 7 s, the current limit for free expansion times in the drop tower using the catapult mode. Additionally, the experiment shall extend the control of the atoms to even longer timescales relevant for the upcoming MAIUS missions and other potential space missions (see Chapter 7). Variations of only a few micrometers for short TOFs may constitute unmanageable deviations at longer times. The precise limits will be discussed in the two upcoming chapters.

All measured cloud positions need to be expressed relative to a fixed frame of reference, in our case the capsule coordinate system. However, due to the forces in the tower the detection telescopes move slightly after every impact. Fortunately, the characteristic diffraction patterns in the detection beams can be used to post-correct these positions.

Several small, stationary particles in the detection path form diffraction ring patterns on the primary images. By picking out a few prominent diffraction rings and fitting their respective center positions, all coordinates can be compared to a set reference image. In conjunction with the distinct diffraction stripe pattern of the chip edge, all positions can be referenced to the atom chip and thus the absolute coordinate system. Additionally, the angle of the connecting line between two patterns is compared to the angle of the chip edge to correct for a possible rotation of the camera around its center. The beam images of the secondary detection setup show the science chip wire structures. Thus the cloud position can easily be referenced to the atom chip. Additionally, the distance between the parallel wires can be used to verify the detection angle.

4.4.2 Microgravity Quality and Residual Accelerations

The evacuated drop tower offers artificial weightlessness for several seconds at a time. The quality of the microgravity environment is set by three key contributors to the residual acceleration acting on the capsule:

1. Friction caused by the remaining air in the evacuated drop tube.
2. Centrifugal acceleration due to rotation of the capsule.
3. Vibrations introduced during launch and release.

Figure 39: Drag deceleration over free fall time in drop mode at a tower pressure of $P = 20\,\mathrm{Pa}$. Due to the non-linear velocity dependence, the accumulated position offset Δy during a long TOF (1.5 s) in the middle of the sequence is comparable to offset during a short TOF (0.25 s) at the end of the sequence. Position critical measurements should best be performed during the first half of the sequence.

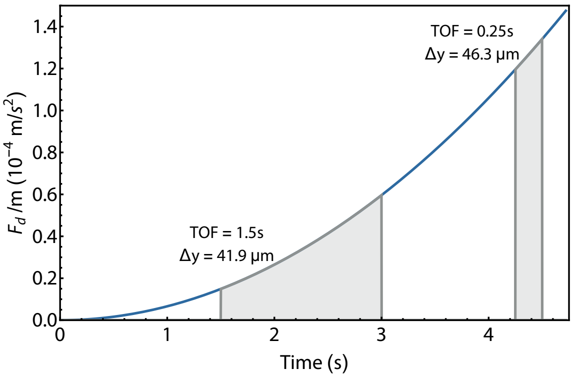

Air Drag

The drop tower volume of $1700\,\mathrm{m}^3$ is evacuated by a three-stage pumping sequence, comprising 18 vacuum pumps with a total nominal pumping capacity of $32000\,\mathrm{m}^3/\mathrm{h}$ [111]. Friction with the residual air in the tower causes an effective drag force acting on the capsule, which can be expressed as

$$F_\mathrm{d}(t) = -\alpha\, v(t) - \beta\, v^2(t), \tag{4.1}$$

with a laminar (v) and turbulent (v^2) contributions. The negative signs indicate that the force is acting against the direction of motion. The low viscosity of the residual air leads to a high Reynolds number and thus negligible linear drag ($\alpha = 0$) [112]. The strength of the remaining contribution is given by

$$\beta = -\frac{\rho\, A\, c_\mathrm{d}}{2}, \tag{4.2}$$

where A is the base area of the capsule, c_d the drag coefficient and ρ the air density, which depends on the residual pressure. For the QUANTUS-2 setup, the following values were used to calculate the air drag: $A = 0.52\,\mathrm{m}^2$, $c_\mathrm{d} = 0.5$ and $m = 453\,\mathrm{kg}$. The drag coefficient depends on the geometrical shape and the value used here is a conservative assessment of the nose cone of the capsule. The velocity v of the capsule is given by

$$v(t) = v_\mathrm{t} \tanh\left[\frac{g\,t}{v_\mathrm{t}}\right], \tag{4.3}$$

where the terminal velocity is

$$v_\mathrm{t} = -\sqrt{\frac{m\,g}{\beta}}. \tag{4.4}$$

Figure 39 shows the calculated drag accumulated over 4.72 s of free fall during a typical drop at a pressure level of 20 Pa. The residual acceleration amounts to $1.5 \times 10^{-5}\,g$. Thus, reaching the advertised μg quality of $10^{-6}\,g$ requires pumping down to a pressure level of 1 Pa. This is usually

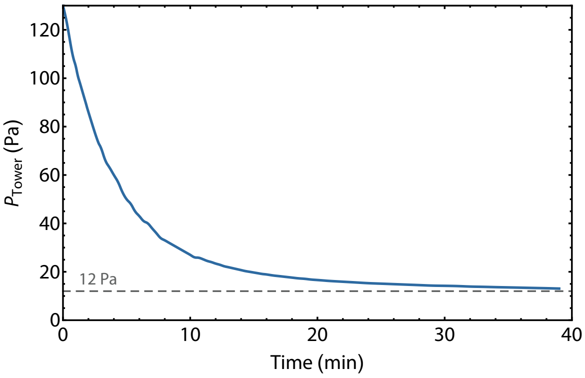

Figure 40: Tower pressure over pumping time during the last pumping stage. These values were recorded at a tower height of 16 m. The exponential decay asymptotically approaches a pressure level of 12 Pa. During typical drop tower operation, the tower is evacuated to levels as low as 14 Pa, which corresponds to a drag deceleration of $1\times10^{-5}g$. However, higher levels are common and the final tower pressure varies from drop to drop.

not feasible due to the outgasing of the Styrofoam grain in the deceleration container. Figure 40 shows the tower pressure over pumping time of the third and last pumping stage, illustrating that a pressure level below 12 Pa can not be obtained in a reasonable time during normal drop tower operation with up to three drops per day.

The residual drag on the capsule is of no immediate concern until the atoms are released from their confinement and fall independently within the confines of their UHV environment. Now, the deceleration of the capsule leads to a position offset along the y-axis, which can amount to a few hundred micrometers for very long TOFs. Due to the velocity dependence, the sequence time of this phase of free evolution is just as important as the total duration, since short TOFs at the very end of the drop can accumulate the same amount of drag as long TOFs at small capsule velocities (see Figure 39). Thus, the sequence timing and tower pressure need to be recorded meticulously to post-correct the µg data. The offset for each individual data point is calculated by integrating F_{d}/m over the respective time interval of the phase of free evolution.

Drag correction becomes more complicated in case of a catapult launch. This stems from the facts that the direction of motion is reversed half way through the flight, the drag coefficients differ between ascent and descent. The most accurate measurements of drag deceleration in the drop tower were performed by tracking the differential acceleration of a free-flyer inside a drop capsule with a laser sensor [112] and with a `[SuperStar EM Sensor]` during a catapult launch (see Figure 41). Since the capsule is equipped with a nose cone at the bottom but no at the top, the drag coefficient is increased during the first half of the flight.

4.4.3 Rotations

The influence of capsule rotations on the µg measurements is twofold. First, a centrifugal force is applied with an effective acceleration of

$$\mathbf{a}_{\mathrm{c}} = \mathbf{r}\,\dot{\boldsymbol{\varphi}}^2, \tag{4.5}$$

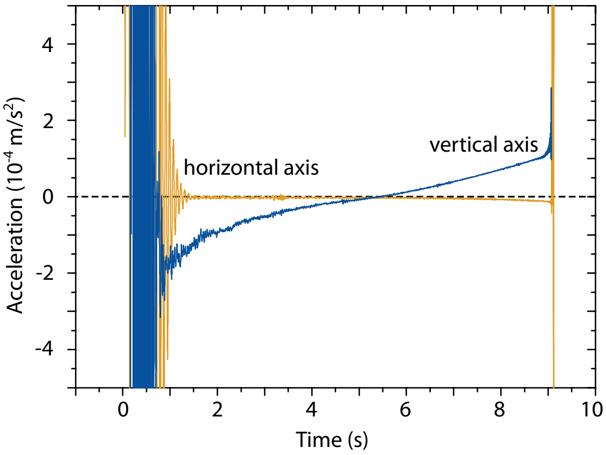

Figure 41: Acceleration measurement during a catapult launch. The capsule is accelerated to launch velocity within the first 400 ms. In contrast to the drop mode, the air drag starts off at the highest value of 2×10^{-4} m/s^2 and then decreases quadratically towards the apogee. On the downward trajectory, the drag deceleration along the vertical axis is slightly reduced due to a different drag coefficient and a rotation of the capsule, as evident from the onset of a drag signal on the horizontal axis. Figure adapted from Ref. [112].

where $\mathbf{r} = (-0.047, +0.123, +0.064)$ m is the distance to the center of rotation and˙ the angular velocity. The distance between the atoms and the COM of the capsule was estimated through taring of the setup. The centrifugal contribution is negligible for most parts of the experimental sequence. Upon release the atoms exit the circular motion on a tangential trajectory with velocity

$$\mathbf{v}_\mathrm{c} = \dot{\boldsymbol{\varphi}} \times \mathbf{r}, \tag{4.6}$$

while the reference frame of the capsule maintains its rotation. A relative distance between the atoms and their expected location is accumulated over time. The position offset after release from the rotating frame is given by

$$\Delta\mathbf{r} = R_x(\dot{\varphi}_x\, t_\mathrm{TOF})\, R_y(\dot{\varphi}_y\, t_\mathrm{TOF})\, R_z(\dot{\varphi}_z\, t_\mathrm{TOF})\, \mathbf{r} - \mathbf{r} - \mathbf{v}_\mathrm{c}\, t_\mathrm{TOF}, \tag{4.7}$$

where $R_i(\varphi_i)$ are the rotation matrices along x, y and z. Second, the rotations alter the spatial orientation of the cloud and thus the projection along the imaging axes and the interferometry beams.

The rotation rates experienced by the QUANTUS-2 setup can be recorded with the IMU. The observed rotations are very different between the two operating modes in the drop tower. During drops, the capsule shows a negligible rotation rate along the the vertical y-axis, but small rotations along the horizontal x- and z-axis of approximately 0.1 °/s. In a catapult launch, the capsule predominantly rotates along the y-axis with an angular speed approaching 1 °/s, while tilting along the horizontal axes at rates of 0.3 – 0.4 °/s (see Figure 42).

Figure 42 (c) and (d) plot the position offsets along the primary axes causes by the rotations over the time of free evolution. In drop operation, a position offset is mainly accrued along the y-axis. The negative sign points towards a slight upwards movement of the cloud in the imaging frame. Overall, the position offsets appears to be negligible for TOFs shorter than two seconds.

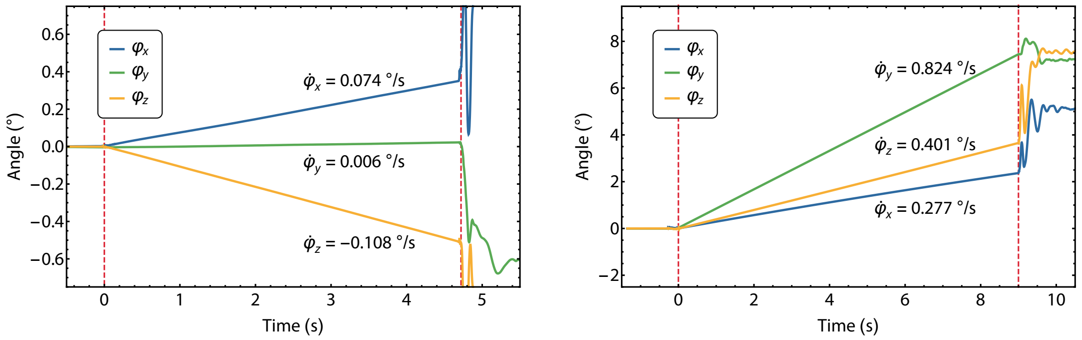

(a) Rotation angles in typical drop operation (Drop #43).

(b) Rotation angles in typical catapult operation (Drop #26).

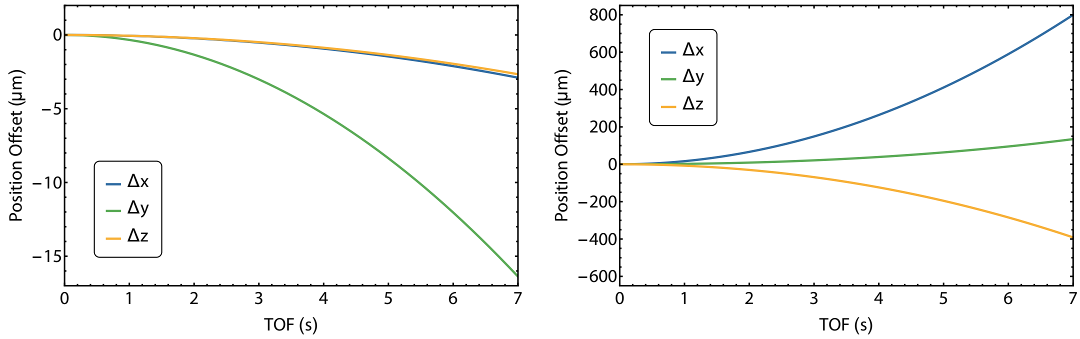

(c) Position offsets over TOF in drop operation.

(d) Position offsets over TOF in catapult operation.

Figure 42: Rotation rates of the capsule during drop and catapult operation. There is a striking difference in rotation rates between the two operating modes, with manageable rotation rates of 0.1 °/s during drops and pronounced rotations after the catapult launch, with angular speeds approaching 1 °/s. Thus, substantial position offsets are accumulated for sequences with extended periods of free evolution.

In catapult operation, the tilt and rotation of the capsule is visible to the naked eye. The setup predominantly rotates along its central axis and large position offsets after TOF are accumulated along x and z. The observed behavior calls for thorough post-correction of the position data via (4.7) as well as angle correction via the acquired rotation rates. The relative movement and rotation between vacuum chamber and atoms is also pivotal for future interferometric measurements (see Chapter 7).

The observed rotation rates in both procedures appear to follow a reproducible trend but show shot-to-shot variations of up to 40% (see Figure 43). Thus, post-correction of the data may require tracing the rotation during every drop instead of using an average value. Despite the noticeable rotation rates in catapult operation, the resulting average acceleration peaks at

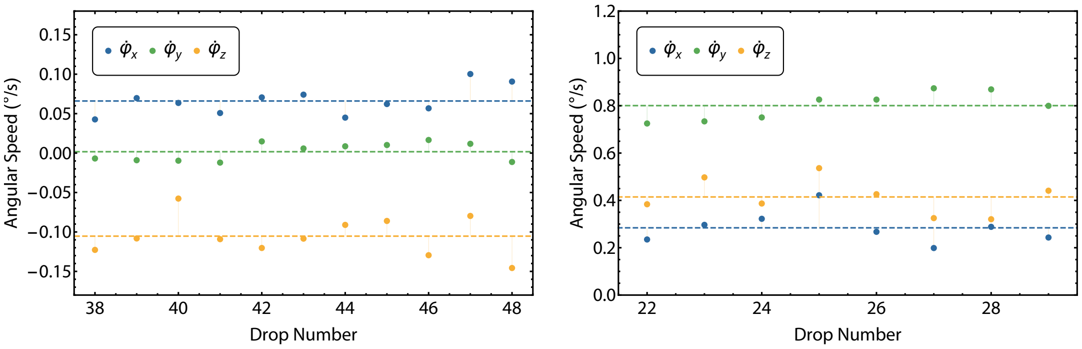

(a) Rotation rates over a drop campaign.

(b) Rotation rates over a catapult campaign.

Figure 43: Angular speeds of the capsule during drops and catapult launches. While the general trend of the rotation rates remains consistent, there is some shot-to-shot variation around the mean angular speeds. In drop operation, these values are: $\overline{\dot{\varphi}}_x = 0.066$ °/s, $\overline{\dot{\varphi}}_y = 0.002$ °/s and $\overline{\dot{\varphi}}_z = -0.105$ °/s. In catapult mode, the mean angular speeds are: $\overline{\dot{\varphi}}_x = 0.284$ °/s, $\overline{\dot{\varphi}}_y = 0.801$ °/s and $\overline{\dot{\varphi}}_z = 0.415$ °/s.

$a_c = 2.5 \times 10^{-6} g$. Thus, the contribution of centrifugal forces to the residual acceleration budget is an order of magnitude smaller than the cumulative drag deceleration. However, even at this level the displacement of the atoms due to rotations can amount to several hundred micrometers.

Vibrations

Release and launch of the capsule induce vibrations that add to the residual accelerations experienced by the setup. The drop causes a sharp transition from $1g$ to $0g$, while the catapult acceleration features a relatively smooth transition from $30g$ to $0g$. Both procedures produce vibrations with amplitudes of up to $10^{-2}g$ that damp out during the first 1.75 to 2 seconds [66]. The residual acceleration over the course of the flight is reduced to approximately $10^{-6}g$. Conceptually, the damping phase coincides with the preparation phase of the BEC and is never used for TOF measurements. Thus, the high initial amplitudes shortly after launch can be neglected.

The residual accelerations caused by vibrations would lead to some velocity scatter after release from the trap. However, the observed velocity scatter in microgravity is lower than typical values encountered in lab operation (see Chapter 5). Therefore, it stands to reason that the residual acceleration budget is dominated by other systematics such as air drag. The relative amplitude of both effects is apparent in Figure 41.

4.5 Summary

The transition from lab-based experiments to drop tower operation was successfully completed with the first successful drop in July 2014 and catapult launch in October 2014. The system performance in the first µg campaigns matches the lab standard and there is no negative impact due to the strenuous conditions in the drop tower. The stability of the laser system and locking procedures during launch and impact is emphatically demonstrated by the creation of a BEC immediately after the acceleration and deceleration phases. The successful thermal and power management combined with the ruggedness of the system shape a compact and mobile apparatus that can be operated autonomously in the drop tower facility or other environments for hours at a time.

The systematic effects encountered during drop tower operation were analyzed and used for reliable post-correction of the µg data. On short time scales, displacement of the imaging optics and air drag constitute the largest deviations that need to be accounted for. For TOFs on the second scale, centrifugal forces from capsule rotations can lead to significant position offsets in catapult operation. Tracking the movement of the imaging frames, the tower pressure and the rotations rates of the capsule is vital to account for all deviations accumulated in drop tower operation. After evaluating the main contributors to the microgravity budget, friction from residual air in the drop tube is the leading systematic, bounding the µg quality at approximately $2 \times 10^{-5} g$ over 4.72 s.

CHAPTER 5

Decompression, Transport and Release

Precise Control of Ultra-Cold Atoms on the Second Scale

Expanding the measurement time on ultra-cold atoms from milliseconds to seconds puts unprecedented demands on their control. During the interferometric measurements envisioned for this project, the atoms will spend the majority of each measurement cycle in free evolution, interrupted only by short laser pulses to span the interferometer. Pristine control over the COM dynamics is vital to enabling detection of the atoms after several seconds and reducing adverse systematic effects in the interferometric measurements. Ideally, the COM position should be reproducible with minimal variance over the course of extended drop tower campaigns. After release, the atoms should be at rest in respect to the apparatus and the ensemble should expand steadily in agreement with its residual energy. Unwanted dynamics of the condensates include COM motion, COM oscillations, breathing modes and higher order excitations [113, 114]. Such phenomena may arise after varying the trap position and parameters non-adiabatically during decompression and transport away from the atom chip.

Moving the condensates away from the chip serves several purposes. The atoms are transported closer to the center of the detection volume, thus increasing the tolerance for COM dynamics and expansion of the cloud. Additionally, unwanted effects due to diffraction of the interferometry beams on the chip edge are reduced, which is a crucial requirement for high-precision measurements. A larger distance from the chip setup also reduces the influence of eddy currents induced in the chip mount while switching coils and chip structures. Distant trap configurations also tend to feature less anharmonicities, which is desirable for the performance of the magnetic lens (see Chapter 6).

Since the magnetic field gradients of chip structures falls off quadratically with the distance, trapping potentials further away from the chip tend to become very shallow as the currents cannot

Figure 44: Absorption image of a BEC after transport and decompression (in situ, Drop #17a). The figure shows the in situ locations of the three relevant trap locations **a**, **b** and **c** in the reference frame of the primary imaging setup. Location **a** is the position of the BEC at the end of the preparation. Location **b** marks the release trap for the first magnetic lensing campaign (BC-SC-lens) and location **c** for the latest lensing campaign (BC-lens), see Chapter 6.

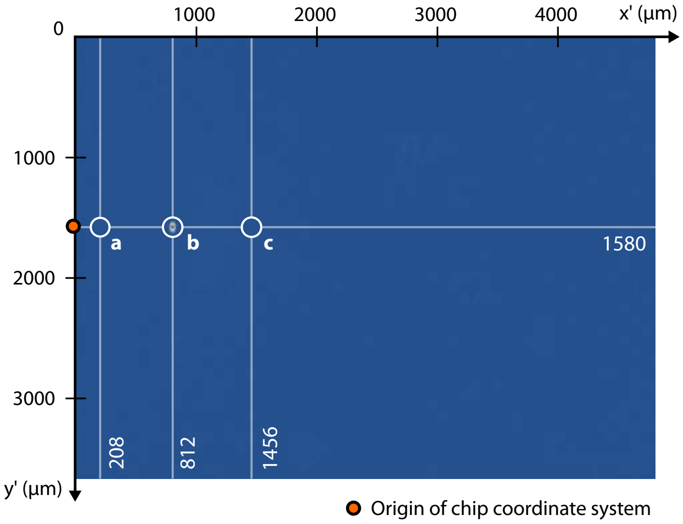

be increased arbitrarily to maintain the curvature and depth of the potential. In these shallow traps, the ensemble becomes more susceptible to excitations because any change in the potential needs to occur much slower than the dynamics of the trap itself. Since the total sequence time for microgravity experiments is limited to a few seconds, these concerns cannot be addressed by arbitrarily long decompression and transport protocols. Furthermore, the condensates start off in close vicinity to the atom chip at very high collision rates as a consequence of the rapid condensation protocol. Here, the lifetime of the BEC is strongly limited by three-body collisions and has to be restored by decompressing the trap fairly quickly. As a result, the microgravity experiments require a scaling procedure for the trapping potential, that aligns with the overall timing demands of drop tower operation without sacrificing control over the dynamics of the BEC.

This chapter will outline the tools and methods to retain the COM of the condensates within the confines of the detection volume and mitigate the influence of COM dynamics to enable detection of the condensates after several seconds of free expansion. Precise control over the cloud dynamics is a crucial requirement for successful collimation of the ensembles through magnetic lensing (see Chapter 6). Excitations can be avoided through slow, adiabatic trap transformations as well as some non-adiabatic methods. Both cases will be presented in this chapter. Afterwards, the complete transfer and release procedures are discussed in chronological order: from holding the atoms in a steep trap in close vicinity to the atom chip, to decompressing the trap and moving the atoms away from the chip surface, to holding the atoms in the new trap, and finally releasing the atoms by switching off the potential.

Table 7: Parameters of the trap configurations used in the microgravity campaigns. While locations **a** and **b** can be used in ground-based experiments, the trap potential at location **c** is too shallow to hold the atoms against gravity.

Location	Trap configuration				Trap frequencies^{+}			Minimum
	BC (A)	SC (A)	x-coil (A)	y-coil (A)	f_x (Hz)	f_y (Hz)	f_z (Hz)	y'_0 (μm)
a	6	2	0.5	−1.5	24.5	442.2	448.0	208
			0.1		24.5	531.5	536.3	
b	6	2	0.5	−0.6	17.5	54.9	62.2	812
c	6	2	0.1	−0.374	9.1	28.1	24.8	1456

$^{+}$ trap frequencies along the eigenaxis of the trap, which may be rotated in respect to the chip coordinate system

5.1 Detection Volume Constraints and Trap Configurations

The detection volume of the primary imaging setup is defined by the effective size of the camera's CCD chip. The setup images a 4816 μm × 3669 μm rectangular cutout of the detection beam (see Chapter 2). The atoms need to be retained within that volume for a successful measurement. Optimally, the condensate should remain in the center of the image as the center of the interferometry beams is located approximately 1920 μm from the atom chip. Figure 44 shows an in situ absorption image of a BEC in μg, decompressed and transported about 834 μm away from the atom chip. The origin location of the absolute coordinate system referenced to the atom chip is located approximately 22 μm to the left of the image. As explained in the previous chapter, inertial forces during launch and impact of the capsule shift the detection window relative to the absolute coordinate system due to displacement of the detection optics. In the following, coordinate positions x' and y' refer to locations on the raw images of the primary imaging setup, while $x_c{}'$ and $y_c{}'$ positions refer to post-corrected data that has been projected on the absolute reference frame with coordinates x, y and z (see Chapter 4).

The position of the atoms after creation of the BEC is marked as location **a**. Most parts of this chapter revolve around transporting the atoms from here to location **b** and **c**, two decompressed traps further away from the chip surface. While location **b** can be reached by lowering the potential pseudo-adiabatically, non-adiabatic methods needed to be implemented for excitation-free transfer to location **c**. The latter can not be used in ground-based operations since the gravitational sag overcomes the trapping potential. All decompression and transport attempts need to be performed in microgravity. The parameters for the three trap configurations are summarized in Table 7.

Table 8: Calculated time constraint for pseudo-adiabatic decompression between trap configurations. The three decompression trajectories for ω considered here are a linear ramp, a sigmoid ramp (5.5) and a square root-type ramp (5.3). The different ramp types are illustrated in Figure 45.

Transfer route	$\omega(0)$ (rad/s)	$\omega(t_\mathrm{f})$ (rad/s)	Ramp type	t_f constraint (ms)
a → **b**	$2\pi \times 448.0$	$2\pi \times 62.2$	Linear	$t_\mathrm{f} \gg 12.3$
(x-coil = 0.5 A)			Sigmoid	$t_\mathrm{f} \gg 0.2$
			Sqrt	$t_\mathrm{f} \gg 0.4$
a → **c**	$2\pi \times 536.3$	$2\pi \times 24.8$	Linear	$t_\mathrm{f} \gg 197$
(x-coil = 0.1 A)			Sigmoid	$t_\mathrm{f} \gg 1.1$
			Sqrt	$t_\mathrm{f} \gg 1.1$

5.2 Adiabaticity

The most intuitive way of accomplishing excitation-free transport and decompression is to vary the trap parameters adiabatically. Adiabaticity in quantum mechanics generally refers to a slow process, where the system follows at all times the instantaneous eigenvalues and eigenstates of the time-dependent Hamiltonian. However, a truly adiabatic process would require an infinitely slow transition. In practical applications it is more useful to define criteria for approximate adiabaticity, involving a process that is slow compared to the typical time scales involved [115]. A common criterion for nearly adiabatic transformations for a two-level system initially in state $|n\rangle$ is

$$\sum_{m \neq n} \left| \frac{\hbar \langle m \,|\, \partial_t \,|\, n \rangle}{E_n - E_m} \right| \ll 1. \tag{5.1}$$

In case of a stationary one-dimensional harmonic oscillator with angular frequency ω, the condition for the speed of frequency variations (compression and decompression) becomes

$$\left| \frac{\sqrt{2}}{8} \frac{\dot{\omega}(t)}{\omega^2(t)} \right| \ll 1. \tag{5.2}$$

The left side of the equation is equivalent to the occupation of the first excited state [115]. The fastest approach satisfying this condition is to distribute $\dot{\omega}/\omega^2$ uniformly along the trajectory y keeping $\dot{\omega}/\omega^2$ constant [116]. With duration t_f, this gives the following trajectory for ω:

$$\omega(t) = \frac{\omega(0)}{1 + t/t_\mathrm{f}\left(\omega(0)/\omega(t_\mathrm{f}) - 1\right)}, \tag{5.3}$$

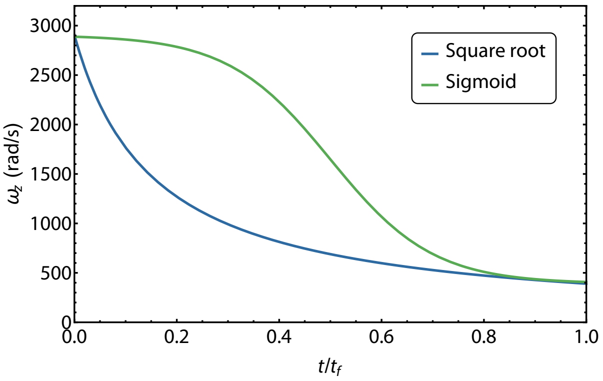

Figure 45: Comparison of a sigmoid (5.5) and a square root-type (5.3) frequency ramp for decompression from location **a** to **b**. While the ramps are largely different over the majority of the trajectory, they share the same smooth approach to the target value, leading to the close proximity in time constraints (see Table 8).

implying that

$$t_{\mathrm{f}} \gg \frac{\sqrt{2}}{8}\left|\frac{1}{\omega(t_{\mathrm{f}})} - \frac{1}{\omega(0)}\right| = \frac{\sqrt{2}}{8}\left|\frac{1}{2\pi \times 62.2\,\mathrm{Hz}} - \frac{1}{2\pi \times 448.0\,\mathrm{Hz}}\right| \approx 0.4\,\mathrm{ms} \tag{5.4}$$

for an optimal adiabatic decompression of ω_z from location **a** to **b**. In comparison, a linear frequency ramp would require $t_f \gg 12.3$ ms, whereas as sigmoid frequency ramp demands $t_{\mathrm{f}} \gg 1.9$ ms. One can calculate the error level of the ground state energy to find a proper ramp duration for approximate adiabatic decompression, a practical and conservative approach is to operate the ramp ten times slower than the t_{f} constraint calculated from (5.2).

While the most efficient frequency ramp (5.3) yields the smallest error and time constraint, it is hard to realize experimentally as all the current carrying structure have a non-vanishing current response. Hence, they cannot be switched arbitrarily fast and the initial and final slopes of the ramp are limited by the characteristic switching time. Luckily, the adiabaticity criterion is most crucial towards the end of the ramp and most ramps with a smooth approach similar to (5.3) will work reasonably well (see Figure 45). A sigmoid-type ramp such as

$$\omega_{\mathrm{sig}}(t) = \frac{-\omega(0) + \omega(t_{\mathrm{f}})}{1 + e^{-10(t/t_{\mathrm{f}}-0.5)}} + \omega(0), \tag{5.5}$$

is most practical as the smooth shape sidesteps switching time constrains without significantly increasing the demands on t_{f}. The calculations summarized in Table 8 show that breathing mode excitations should be avoidable with reasonably smooth ramp shapes and timing margins.

5.3 Shortcuts to Adiabaticity (STA)

The estimated switching time constrains for various ramp types illustrate that breathing mode excitations are of lesser concern when using appropriately smooth ramp shapes with durations in excess of 25 ms. We avoid such short ramps in any case, as COM oscillations become apparent immediately. To analyze why the timing demands to prevent COM oscillation are different from breathing mode excitations, the discussion needs to be extended to a generalized scaling theory for ultra-cold atoms in harmonic confinement.

Some quantum systems described by a time-dependent Hamiltonian $H(t)$ support a dynamical invariant $I(t)$ that satisfies

$$i\hbar\frac{\partial I(t)}{\partial t} - \left[H(t), I(t)\right] = 0 \tag{5.6}$$

and is called Lewis-Riesenfeld invariant [117]. It is defined as

$$I(t) = \sum_n \left|\phi_n(t)\right\rangle \lambda_n \left\langle\phi_n(t)\right| \tag{5.7}$$

with orthonormal eigenvectors $|\phi_n(t)\rangle$ and real constants λ_n [118]. The time-independent expectation values for an arbitrary solution $|\Psi(t)\rangle$ of the Schrödinger equation

$$i\hbar\partial_t \left|\Psi(t)\right\rangle = H(t)\left|\Psi(t)\right\rangle \tag{5.8}$$

can then be expanded in dynamical modes $|\Psi_n(t)\rangle$ with time-independent amplitudes c_n:

$$\left|\Psi(t)\right\rangle = \sum_n c_n \left|\Psi_n(t)\right\rangle, \quad \left|\Psi_n(t)\right\rangle = e^{i\alpha_n(t)}\left|\phi_n(t)\right\rangle. \tag{5.9}$$

The exponents $\alpha_n(t)$ are called Lewis-Riesenfeld phases, defined as

$$\alpha_n(t) = \frac{1}{\hbar}\int_0^t dt' \left\langle\phi_n(t')\right| i\hbar\partial_{t'} - H(t') \left|\phi_n(t')\right\rangle. \tag{5.10}$$

The evolution of the system can then be described by a time-dependent unitary evolution operator

$$U(t) = \sum_n e^{i\alpha_n(t)} \left|\phi_n(t)\right\rangle \left\langle\phi_n(0)\right|, \tag{5.11}$$

obeying

$$i\hbar\frac{\partial U}{\partial t} = H(t)\,U. \tag{5.12}$$

Ultimately, the Hamiltonian of the system can be expressed as

$$H = -\hbar\sum_n \left|\phi_n(t)\right\rangle \partial_t\alpha_n(t) \left\langle\phi_n(t)\right| + i\hbar\sum_n \left|\partial_t\,\phi_n(t)\right\rangle \left\langle\phi_n(t)\right|, \tag{5.13}$$

which depends on an arbitrary choice of phase functions $\alpha_n(t)$. Imposing boundary conditions such that H and $I(t)$ commute at initial and final times allows for excitation free trap transformations, while the evolution of the system can be customized according to the technical demands of the experiment. This procedure is often termed the inverse engineering method [118, 119].

5.3.1 Non-Interacting Gas in One Dimension

The dynamics of a non-interacting gas in one dimensional harmonic confinement is described by the Hamiltonian

$$H(x, p, t) = \frac{p^2}{2m} + \frac{m}{2}\omega^2(t) \left[x - x_0(t)\right]^2 . \tag{5.14}$$

A variation of the the trap frequency $\omega(t)$ and the trap minimum position $x_0(t)$ leads to a displacement of the COM position $x_{\mathrm{cm}}(t)$ and a variation of the size of the ensemble by an amount given by a scaling factor $b(t)$. This change may be expressed via a time-dependent unitary time evolution operator U, yielding a new Hamiltonian [120]

$$H' = \frac{p^2}{2m} + \frac{m}{2}\omega^2(t) \left[x - x_0(t)\right]^2 + \frac{1}{b^2(t)}\, U \left[\frac{x - x_{\mathrm{cm}}(t)}{b(t)}\right] . \tag{5.15}$$

An invariant $I(t)$ for this system exists if $\omega(t)$, $x_0(t)$ and $b(t)$ satisfy the auxiliary equations [121]

$$\ddot{b}(t) + \omega^2(t)\, b(t) = \frac{\omega^2(0)}{b^3(t)}, \tag{5.16}$$

$$\ddot{x}_{\mathrm{cm}}(t) + \omega^2(t) \left[x_{\mathrm{cm}}(t) - x_0(t)\right] = 0. \tag{5.17}$$

Therefore, trajectories for $x_{\mathrm{cm}}(t)$ and $b(t)$ can be constructed such that H' and I commute at initial and final times. Thus, the system arrives at the same instantaneous eigenvalues after the time evolution.

5.3.2 Bose-Einstein Condensates

Dynamical invariants have been studied predominantly for systems quadratic in position and momentum such as the time-dependent harmonic oscillator [117]. The Hamiltonian of a many-body system of N interacting particles in three-dimensional harmonic confinement is given by

$$H(\mathbf{r}, \mathbf{p}, t) = \sum_{i=1}^{N} \left[\frac{\mathbf{p}_i^2}{2m} + V(\mathbf{r}_i, t)\right] + \sum_{i,j,i\neq j} U(\mathbf{r}_j - \mathbf{r}_i), \tag{5.18}$$

where U is the interatomic potential and V the external potential given by

$$V(\mathbf{r}, t) = \sum_{i\in x,y,z} \frac{m}{2}\omega_i^2(t) \left(r_i - r_i^0(t)\right)^2 . \tag{5.19}$$

Finding an invariant for such a system is not straight-forward. However, solutions analogous to (5.16) and (5.17) can be found using the single particle wave function instead [122]. A BEC can be described in mean-field theory by the time-dependent Gross-Pitaevskii equation (GPE)

$$i\hbar\partial_t\psi(\mathbf{r},t) = \left[-\frac{\hbar^2}{2m}\Delta + V(\mathbf{r},t) + g\left|\psi(\mathbf{r},t)\right|^2\right]\psi(\mathbf{r},t), \tag{5.20}$$

where the interactions between the atoms are parametrized by

$$g = \frac{4\pi\hbar^2 a}{m} \quad \text{with } a \approx 100a_0 \text{ for } {}^{87}\text{Rb}. \tag{5.21}$$

Here, a_0 is the Bohr radius and a the approximate s-wave scattering length. Using the single particle wavefunction $\psi(\mathbf{r},t)$, one finds the familiar auxiliary equations: [119]

$$\ddot{b}_i + \omega_i^2(t)\, b_i = \frac{\omega_i^2(0)}{b_i b_x b_y b_z} \qquad \forall i \in \{x,y,z\} \tag{5.22}$$

$$\ddot{r}_i^{\text{cm}} + \omega_i^2(t)\left[r_i^{\text{cm}} - r_i^0(t)\right] = 0. \tag{5.23}$$

The GPE is invariant under these transformations either in the non-interacting limit [123, 124] or in the Thomas-Fermi approximation, where the kinetic energy term can be neglected [119, 125]. Since COM oscillations are of greater concern for our transfer protocols, this chapter will focus on (5.23), while (5.22) and the Thomas-Fermi approximation will be revisited in the next chapter.

5.3.3 STA for Atom Chips

For magnetic traps created by atom chips the steepness and the minimum position of the potential are both correlated to the strength of the bias field. Therefore, it is convenient to merge both decompression and transport into one process using a single current ramp for the bias coil (y-coil). Decompressing the trap in situ and shifting the trap minimum with constant trap frequencies afterwards would require two sets of at least three simultaneous current ramps for structures with widely different inductances and switching characteristics (see Chapter 2).

Since excitations due to decompression such as breathing modes can be neglected for conservative ramp times with appropriately designed ramp shapes, the transfer protocol can be reduced to one-dimensional transport along the z-axis. The relevant auxiliary equation (5.23) simplifies to

$$\ddot{z}_{\text{cm}} + \omega_z^2(t)\left[z_{\text{cm}} - z_0(t)\right] = 0. \tag{5.24}$$

Since both trap position and trap frequency depend on the bias field strength, $\omega_z(t)$ can be expressed in terms of $z_0(t)$. Their relationship can be obtained from the Biot-Savart simulations of the chip potential (see Figure 46). The data can be fitted with either a very precise or a simpler

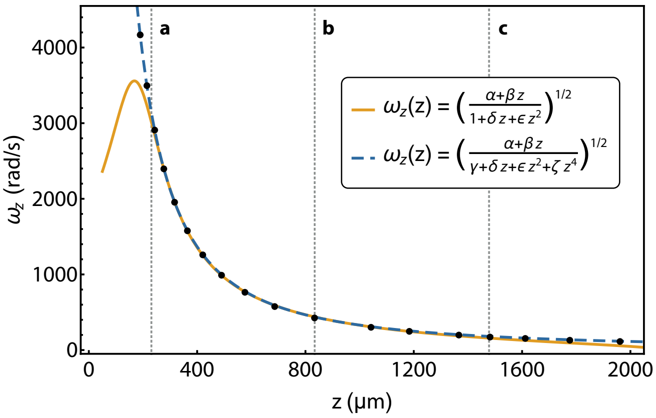

Figure 46: Relationship between trap frequency and trap position along the z-axis. The data points were obtained from Biot-Savart simulations of the chip potential. The dashed blue curve represents a precise fit function for ω_z, while the orange curve follows a simpler model. The latter is sufficiently accurate in the region of interest between location **a** and **c**, with an error below 0.1 %.

model, with the advantage of the latter being a simple analytical expression. In this case, the trap frequency is approximated by

$$\omega_z^2(z_0) = \frac{\alpha + \beta\, z_0}{1 + \delta\, z_0 + \epsilon\, z_0^2} \tag{5.25}$$

$$\text{with}\quad \alpha = 3.61{\times}10^6,\quad \beta = 1.71{\times}10^9,\quad \delta = 8.64{\times}10^3,\quad \epsilon = 2.53{\times}10^7. \tag{5.26}$$

Substituting (5.25) in (5.24) and solving for $z_0(t)$ yields

$$z_0(t) = \frac{1}{2\,(\beta + \epsilon\, \ddot{z}_{\text{cm}})} \left(\alpha + \beta\, z_{\text{cm}} + \delta\, \ddot{z}_{\text{cm}} \mp \sqrt{\Omega(t)}\right), \tag{5.27}$$

$$\Omega(t) = \left(-\alpha - \beta\, z_{\text{cm}} - \delta\, \ddot{z}_{\text{cm}}\right)^2 - 4\left(\alpha\, z_{\text{cm}} + \ddot{z}_{\text{cm}}\right)\left(\beta + \epsilon\, \ddot{z}_{\text{cm}}\right). \tag{5.28}$$

Equations (5.27) and (5.28) establish an analytical relation between any shortcut trajectory for the BEC satisfying (5.24) and the required trap evolution. The shape of the chosen COM trajectory will be identical for any ramp duration, while $z_0(t)$ varies significantly with t_{f}. For sufficiently long times $z_0(t)$ and $z_{\text{cm}}(t)$ will converge, restoring the adiabatic case.

Using the auxiliary equation (5.24), a multitude of valid trajectories can now be designed. Note that contrary to adiabatic transformations, the eigenstates of the system are only fixed at the end points and the evolution of the eigenstates of the system during trap transformations is willfully ignored. In practice, this may lead to erratic behavior and unfeasible demands on certain experimental parameters. This can be circumvented by introducing additional boundary conditions and choosing proper function archetypes such as a sinusoidal [126] or a polynomial [121]

$$z_{\text{cm}}(t) = \sum_n \xi_n s^n \tag{5.29}$$

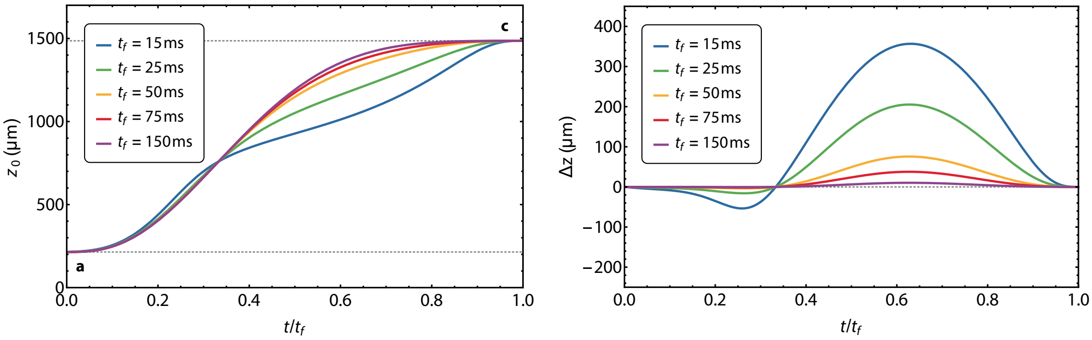

(a) Trap trajectories for various transfer durations.

(b) Offset to adiabaticity for various durations.

Figure 47: Comparison of trap trajectories for various transfer times for a polynomial (5.31) ramp from location **a** to **c**. At long transfer durations approaching t_f = 200 ms the trap trajectory converges with the COM trajectory.

with $s = t/t_\mathrm{f}$. The amount and values of free parameters ξ_n of these function are then determined via the boundary conditions. Due to experimental switching time constraints, desirable shortcut trajectories should be similar in shape to the sigmoid ramp (5.5) with a smooth start and smooth approach to the final value. This can be expressed with the following constraints:

$$\begin{aligned} &z_\mathrm{cm}(0) = o, && \dot{z}_\mathrm{cm}(0) = 0, && \ddot{z}_\mathrm{cm}(0) = 0, && z_\mathrm{cm}(t_\mathrm{f}) = d, \\ &\dot{z}_\mathrm{cm}(t_\mathrm{f}) = 0, && \ddot{z}_\mathrm{cm}(t_\mathrm{f}) = 0, && \dddot{z}_\mathrm{cm}(t_\mathrm{f}) = 0, && \ddddot{z}_\mathrm{cm}(t_\mathrm{f}) = 0, \end{aligned} \tag{5.30}$$

where o is the origin, d the final location and t_f the transfer duration. The boundary conditions are more lenient towards the start and more stringent towards the end of the transfer. The resulting ramp takes the functional form

$$z_\mathrm{cm}(t) = (d - o)\left(35\,s^3 - 105\,s^4 + 126\,s^5 - 70\,s^6 + 15\,s^7\right) + o. \tag{5.31}$$

Figure 47 depicts the trap trajectories $z_0(t)$ resulting from (5.31) for various transfer times from location **a** to **c**. For short durations, $z_0(t)$ and $z_\mathrm{cm}(t)$ diverge considerably. This can be an issue due to anharmonicities in the trapping potential, which are a known property of chip traps, specifically along the axis pointing away from the chip surface. The implications of higher-order contributions to the potential are detailed in Chapter 6. Here, unwanted effects can be managed by limiting the deviation $\Delta z = z_\mathrm{cm} - z_0$. This can be achieved by using conservative ramp durations and by designing a more sophisticated ramp that distributes Δz more evenly over the trajectory. The sinusoidal ramp [127]

$$z_{\mathrm{cm}}(t) = \frac{(d-o)}{48\pi} \left\{ 48\pi\ s\ f(t) - 27 \sin\left[2\pi\ s\ f(t)\right] + \sin\left[6\pi\ s\ f(t)\right] \right\} + o \tag{5.32}$$

with auxiliary function

$$f(t) = \frac{1 + a\,s + b\,s^2}{1 + a + b} \quad \text{with } \ a = -1.319 \ \text{ and } \ b = 0.704 \tag{5.33}$$

contains two free parameters a and b, which can be used to adjust the trajectory and limit the maximal deviation Δz_{max}. With (5.32), the latter can be reduced by a factor of two in comparison to the polynomial ramp (see Figure 48b).

The adiabaticity criterion for the decompression (5.2) during the example trajectories in Figure 48 may still be satisfied along the steep trap axes ω_z and ω_y for ramp durations of 25 ms. However, the shallow trap axes with frequency ω_x varies only slightly in this process. Due to the coupling of the trap frequency scalings in (5.22) the rapid decompression along the two other axes may lead to substantial excitations along the x-direction, which in turn can excite oscillations in the other two dimensions. Figure 48 (c) and (d) show the progression of ω_x^2 in comparison to the frequency variation along z. While all trap directions may individually fulfill their adiabaticity criterion, the coupling leads to a significant violation along the weak axis. Utilizing such short ramp times without inducing excitations is possible only by including (5.22) into the requirements of the shortcut trajectory. Then, additional boundary conditions for the trap frequencies and aspect ratios can be set to ensure excitation-free transfer.

In the presence of anharmonicities, such short ramp times are undesirable in any case because of the pronounced increase in Δz. There are some advanced strategies for shortcuts to adiabatic transport with anharmonic traps [126]. In general, more complex potentials

$$V(z,t) = \frac{m}{2}\omega_z^2(t)\left[z - z_0(t)\right]^2 + \frac{m}{3}\frac{\omega_z^2(t)}{L_3(t)}\left[z - z_0(t)\right]^3 + \ \dots \tag{5.34}$$

yield extended auxiliary equations

$$\ddot{z}_{\mathrm{cm}} + \omega_z^2(t)\left[z_{\mathrm{cm}} - z_0(t)\right] + \frac{\omega_z^2(t)}{L_3(t)}\left[z_{\mathrm{cm}} - z_0(t)\right]^2 + \ \dots \ = 0. \tag{5.35}$$

Much like $\omega_z(t)$, the high-order scaling factors such as $L_3(t)$ depend on the scaling and position of the trap and are therefore implicitly time-dependent through $z_0(t)$. The scaling factors can be extracted from the Biot-Savart simulations and introduced as a fit function analogous to (5.25).

Ultimately, the two competing strategies are either to use the harmonic approximation and ramp times in the vicinity of 150 ms to keep Δz within a few micrometers, or to include the

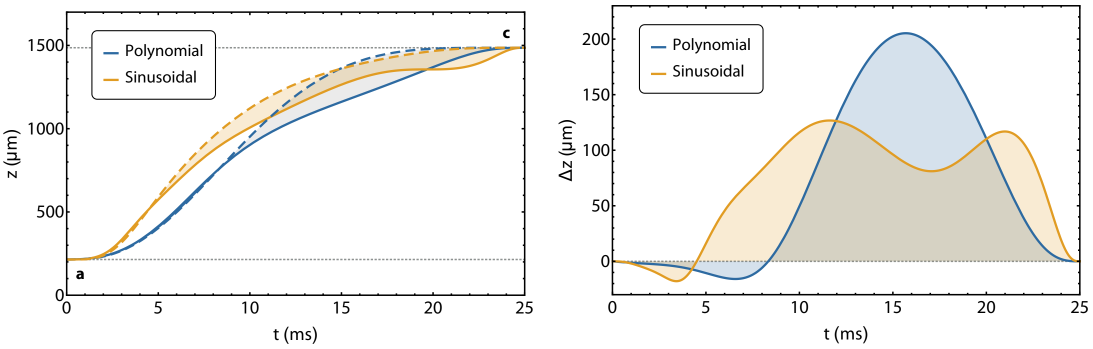

(a) Comparison of the polynomial and sinusoidal trap trajectories.

(b) Offset to adiabaticity for the polynomial and sinusoidal trap trajectories.

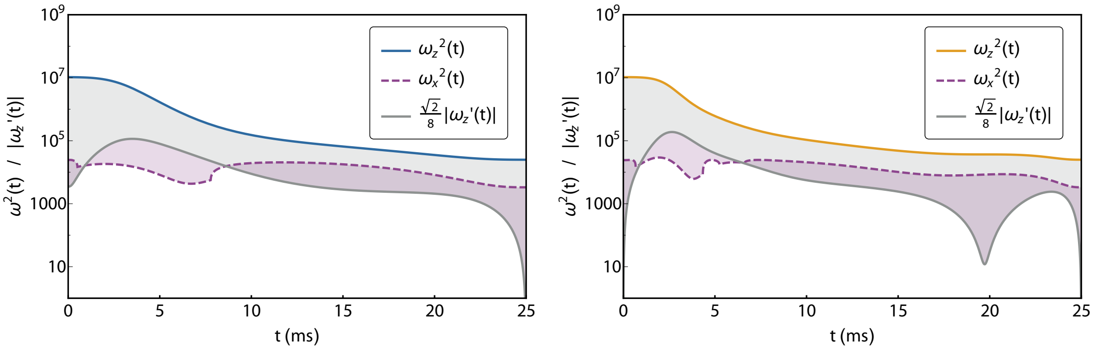

(c) Illustration of the adiabaticity criterion for the decompression during the polynomial ramp.

(d) Illustration of the adiabaticity criterion for the decompression during the sinusoidal ramp.

Figure 48: Comparison of a polynomial and sinusoidal trajectory for a $t_f = 25$ ms transfer from location **a** to **c**. Figure (a) contrasts the COM trajectories of both approaches (dashed lines) and the corresponding trap positions (solid lines). The offsets to adiabaticity are compared in (b), showing a factor of two reduction in the maximal deviation with the sinusoidal approach. Figures (c) and (d) illustrate the adiabaticity criterion (5.2) for ω_z and include the dynamics along the weak axis with ω_x. Such rapid transformations of the asymmetric trap will likely cause substantial excitations along the x-direction.

anharmonic contributions and rely on the validity of the simulations concerning the trap deformations. If successful, the latter would allow for ramp durations as low as 25 ms for excitation-free transport from location **a** to **c**. Faster times would compromise the adiabaticity of the decompression and may be limited by the switching times and response of the bias coil.

Transfer to closer positions such as from location **a** to **b** are less critical and can be reached via a slow, adiabatic trajectory. Figure 49 compares three different approaches for a $t_f = 250$ ms transfer. The maximum deviation Δz_{max} between the desired trap trajectory to satisfy (5.24) and the actual ramp is well below 1 µm for every function.

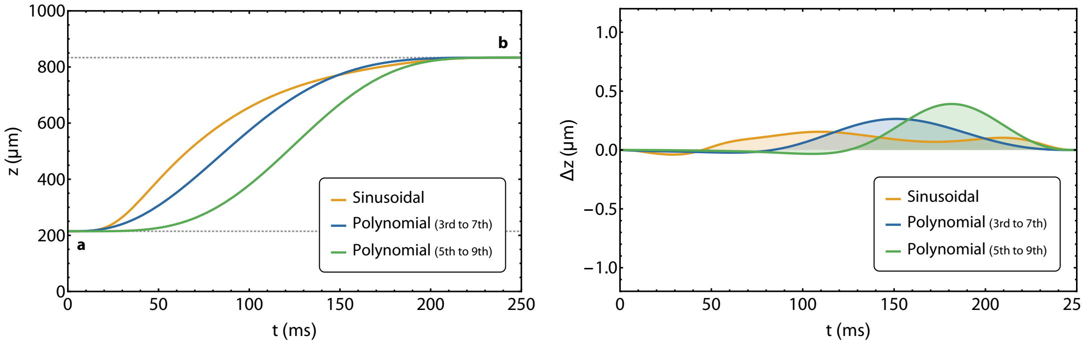

(a) Comparison of several trap trajectories.

(b) Offset to adiabaticity for several trap trajectories.

Figure 49: Comparison of a sinusoidal and two polynomial trajectories for a $t_f = 250\,\mathrm{ms}$ transfer from location **a** to **b**. All COM trajectories are in good agreement with the required trap positions, with a maximum deviation of less than 1 µm.

5.4 Implementation

Successful implementation of the decompression, transport and release protocols hinges on translating the desired time-dependence of the potential into a real magnetic field dynamic as experienced by the atoms. Several degrees of abstraction need to be bridged to obtain the proper field response to a calculated ramp shape. Scaling trajectories and switching commands are issued via control voltages to a set of current drivers. All current-carrying structures have a characteristic current response, that depends on the properties of the structure, the current driver and its voltage supply. The current through the structures then generates a magnetic field topology, whose time-dependence may be altered by eddy current induced in the surrounding assembly.

The manipulation and characterization of the step response functions for the current carrying structures is documented in Chapter 2. Generally, the switching times vary from a few hundred microseconds for chip structures to several milliseconds for coils. This disparity becomes relevant when many structures are ramped simultaneously, e.g. during switch-off procedures or magnetic lensing pulses (see Chapter 6). Such sequences can either be dragged out to suit the slowest structure (usually the bias coil) or the current requests can be altered to obtain the same response for every structure. This can be achieved via a convolution of the Fourier transforms of the request and step response functions (for details see Ref. [79]). Using such modified request functions allows to produce the exact current signals required.

Due to the non-linear scaling of trap properties such as frequency and position with the applied current, ramps and waveforms applied via the current will not produce the desired

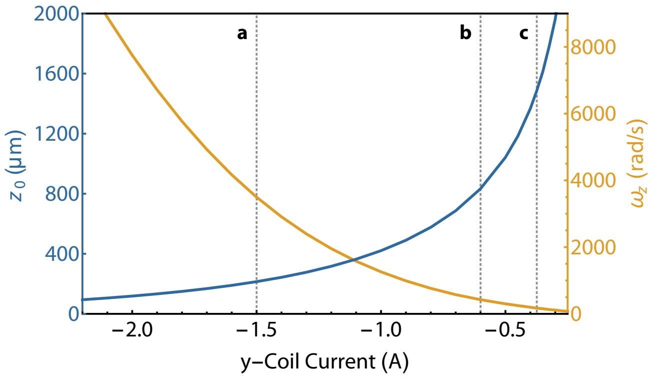

Figure 50: Scaling of the trap position and trap frequency along the z-axes over the bias coil current. The data was extracted from the Biot-Savart chip simulations for microgravity conditions. The non-linear current scaling of both trap properties implies that ramps and waveforms applied to the current will be deformed by the current response of the system.

results (see Figure 50). Consequently, the parameter trajectories need to be converted with conversion functions.

5.5 Decompression and Transport

After cooling the atoms to degeneracy, they remain in a moderately steep trap at location **a**. The ensemble is already decompressed once during the evaporation sequence at the onset of three-body collisions. After the final RF ramp, the rates for such events are again approaching the Hertz regime. Holding the atoms in this trap for too long leads to atom loss and heating of the cloud. Hence, a rapid decompression is desirable to prevent atom loss and retain the chosen condensate fraction. The need for rapid decompression clashes with the desire to transfer the atoms without disturbance. Due to the absence of dissipation at this stage, any fast variation of the trap properties can lead to undamped excitations that are difficult or impossible to mitigate.

5.5.1 Transfer to Location **b**

In the first microgravity campaigns, the atoms were transported to a distance of approximately 800 µm from the chip surface at location **b**. The moderate decrease in trap frequencies has several advantages. First, the trapping potential can be tested in lab operation under gravity. Second, the transfer procedure can be performed with minimal excitations without resorting to more elaborate STA protocols which were implemented at a later time.

While the exact trap properties are somewhat modified in lab operation due to the gravitational sag, both traps feature a similar geometric mean of the trapping frequencies. To gauge the appropriate ramp time and compare different transfer ramps, the scaling procedure was performed using linear and sigmoid ramp shapes (see Figure 51). After transfer to the final destination, the atoms were released after varying hold times and imaged after 22 ms TOF.

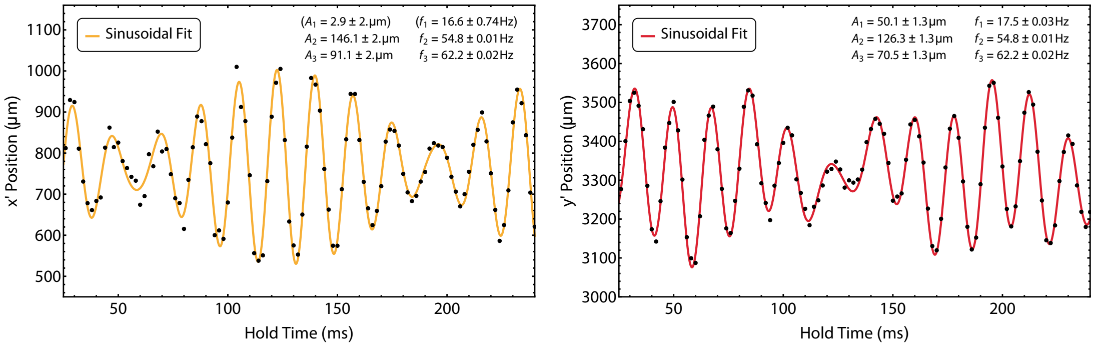

(a) x'-position over hold time in the trap after linear transfer with $t_\mathrm{f} = 150\,\mathrm{ms}$.

(b) y'-position over hold time in the trap after linear transfer with $t_\mathrm{f} = 150\,\mathrm{ms}$.

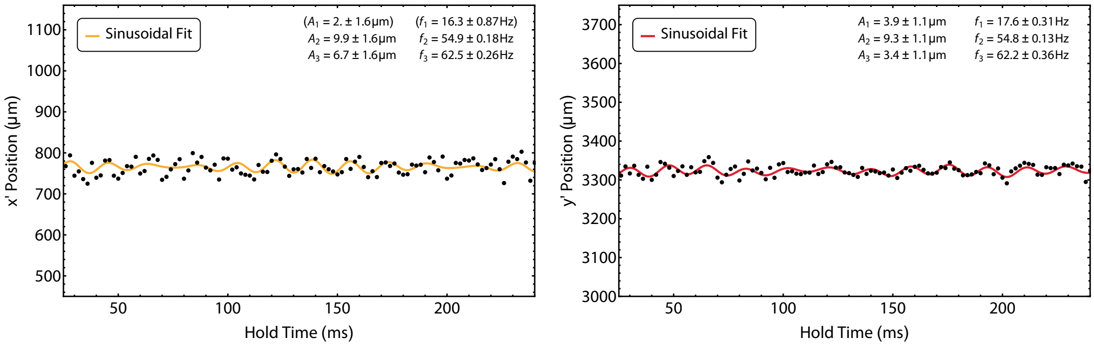

(c) x'-position over hold time in the trap after sigmoid transfer with $t_\mathrm{f} = 150\,\mathrm{ms}$.

(d) y'-position after sigmoid transfer over hold time in the trap with $t_\mathrm{f} = 150\,\mathrm{ms}$.

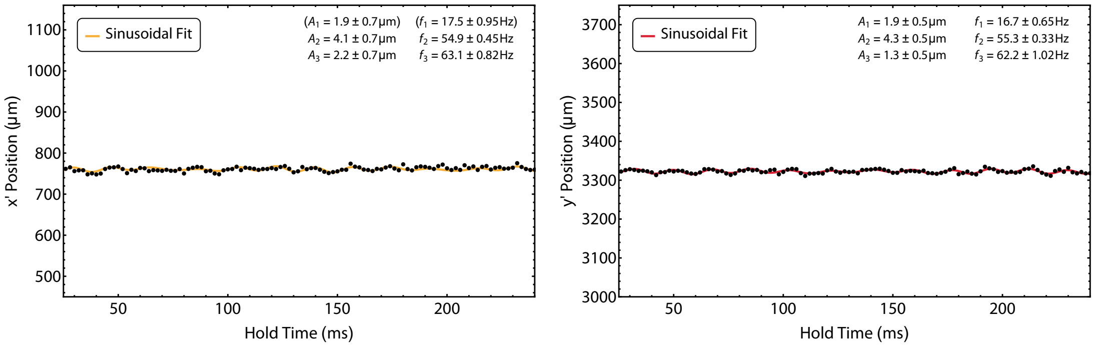

(e) x'-position after sigmoid transfer over hold time in the trap with $t_\mathrm{f} = 250\,\mathrm{ms}$.

(f) y'-position after sigmoid transfer over hold time in the trap with $t_\mathrm{f} = 250\,\mathrm{ms}$.

Figure 51: COM position over hold time at location **b** in lab operation after various transfer ramps. The atoms were imaged after 22 ms TOF. The linear transfer over 150 ms leads to large COM oscillations and three trap frequencies can reliably be extracted from the fits. A sigmoid ramp of the same duration reduce the oscillation amplitudes significantly without fully suppressing them. Extending the ramp time to 250 ms diminishes the amplitudes to a level that is comparable to the overall position uncertainty. The fits in the x'-direction can only extract two of the frequencies with confidence, f_2 and f_3.

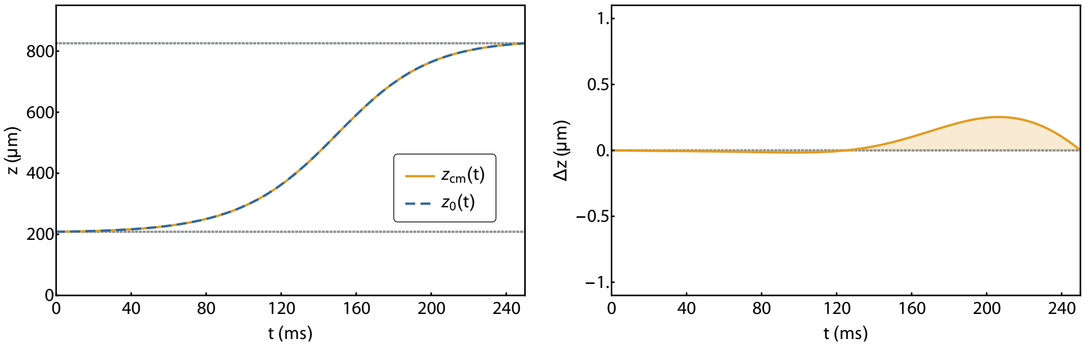

(a) Comparison of the COM and trap trajectories.

(b) Deviation between COM and trap trajectories.

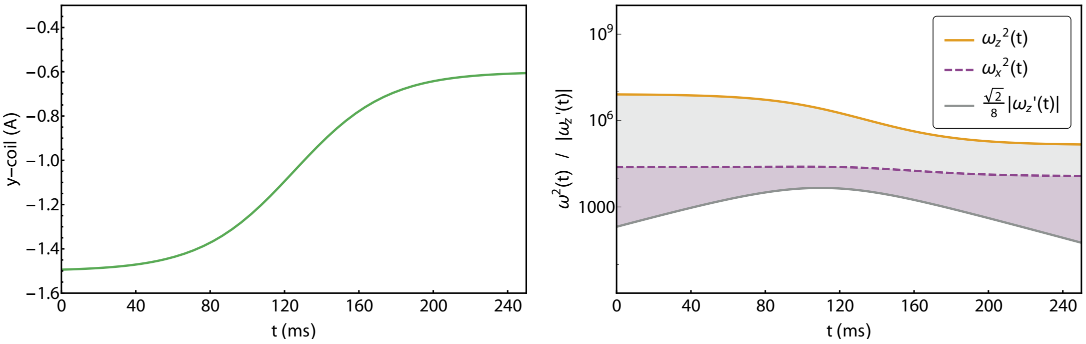

(c) Sigmoid current ramp (5.5) for the y-coil.

(d) Adiabaticity criterion for the the decompression.

Figure 52: Analysis of the sigmoid current ramp used to transfer the atoms to location **b**. The maximal deviation between the trap center position and the COM of the atoms is less than 0.5 μm over the duration of the ramp (b). The prolonged decompression satisfies the adiabaticity criterion along the z-axes by several orders of magnitude (d). Erratic behavior of ω_x is not expected when comparing the progression of ω_x to the trap variation along the steep axes.

As expected, the linear current ramp leads to prominent COM oscillations with fitted trap frequencies $(f_x, f_y, f_z) = (17.5 \pm 0.03,\ 54.8 \pm 0.01,\ 62.2 \pm 0.02)\,\mathrm{Hz}$. Note that these values differ slightly from the simulated trap frequencies in microgravity from Table 7. A sigmoid current ramp can reduce the amplitude of the oscillations substantially. After extending the ramp duration to $t_f = 250\,\mathrm{ms}$, the sinusoidal fits can barely extract the trap frequencies as the standard deviation of the observables approaches $\sigma_{x'} = 5.98\,\mu\mathrm{m}$ and $\sigma_{y'} = 4.89\,\mu\mathrm{m}$ with a standard error of 0.57 μm and 0.46 μm, respectively. Increasing the ramp duration further does not appear to reduce the position variance further. Thus, the latter current ramp was selected for transfer of the BEC to location **b** in the microgravity campaigns.

When analyzing the chosen ramp with the STA formalism (which happened long after the fact), it is evident that the COM position of the atoms is virtually identical with the trap position with a maximal deviation of less than 0.5 µm (see Figure 52). As a consequence, the sigmoid current ramp should be reasonably well suited to mitigate any trap oscillations, even when simply using a current ramp instead of the inverse engineering method. At the time, ramps and waveforms were generally applied via current ramps that could instantly be implemented for any parameter change via the control system. Due to the non-linear relationship between the bias coil current and both the trap position and frequency (seeFigure 50), the resulting ramp is elongated in the beginning and contracted at the end. Thus, the trap frequency remains close to its initial value for the first 80 ms which leads to some unwanted heating that reduces the condensate fraction. This effect was compensated experimentally by choosing a more aggressive final RF cut. This results in a lower atom number in the BEC for the following experiments. One other concern is the lack of proper boundary conditions which may result in a non-zero final acceleration which may lead to excitations.

COM Dynamics

To evaluate the transfer to the intermediate chip distance and study the stability of the system, the QUANTUS-2 capsule was dropped and catapulted 25 times in a span of three weeks for its first targeted microgravity campaign. Each data point represents an identically prepared BEC that was transferred from location **a** to location **b** and released after a variable hold time in the final trap. The condensates were imaged after 100 ms TOF. Each catapult shot produced four data points (enumerated as a, b, c, d), while each drops produced two (enumerated as a, b). Figure 53 shows the $x_c{}'(z)$ center position over the hold time with the data points labeled with their respective drop number and sequence letter. The histogram of the data indicates a non-Gaussian distribution but does not clearly show the typical shape for an oscillation, two symmetric peaks on the edges of the distribution and diminishing population in the center. The variance reduced by a factor of two compared to the expected value inferred from ground-based experiments (see Figure 51).

The cloud position after TOF depends on the amplitude of the in situ oscillation $A_{\text{in situ}}$, the time of the switch-off t_{hold} and the time of free evolution t_{TOF}. $A_{\text{in situ}}$ can be inferred from the observed position offset to the in situ position via

$$x(t_{\text{TOF}}) = A_{\text{in situ}} \left[\sin(\omega\, t_{\text{hold}} + \varphi) + \omega \cos(\omega\, t_{\text{hold}} + \varphi)\, t_{\text{TOF}}\right], \tag{5.36}$$

where φ is a phase offset. For high trap frequencies ω and long expansion times the equation simplifies to

$$x(t_{\text{TOF}}) = A_{\text{in situ}}\, \omega \cos(\omega\, t_{\text{hold}} + \varphi)\, t_{\text{TOF}}, \tag{5.37}$$

Figure 53: COM position of the BEC in x_c'-direction over hold time at location **b**. The data was acquired over 25 drops and catapult launches and is labeled with the respective drop number and sequence letter. The positions are post-corrected to the absolute coordinate system.

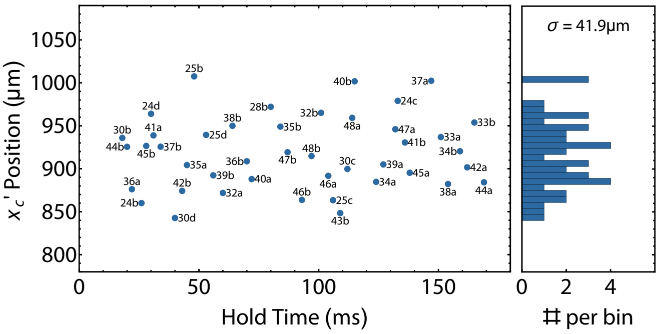

Figure 54: Fitted COM dynamics at location **b**. The plot shows the data set from Figure 53 fitted to a sinusoid. The amplitude of the oscillation A_{TOF} = 52.12 ± 5.2 μm corresponds to an in situ amplitude of $A_{\mathrm{in\ situ}}$ = 0.69 ± 0.07 μm. The fitted frequency f = 60.42 ± 0.31 Hz deviates from the simulated value by 2.9% (see Table 7)

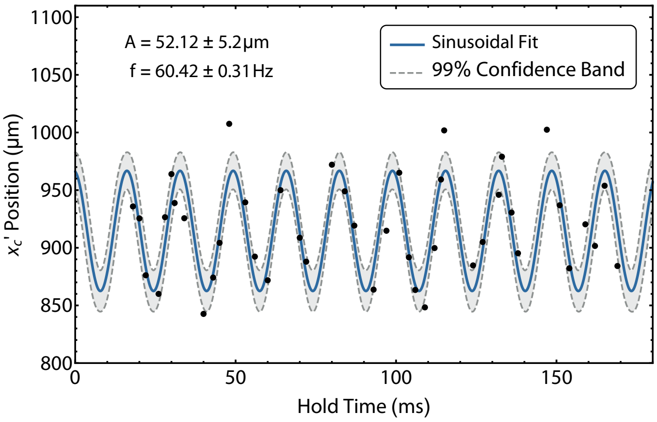

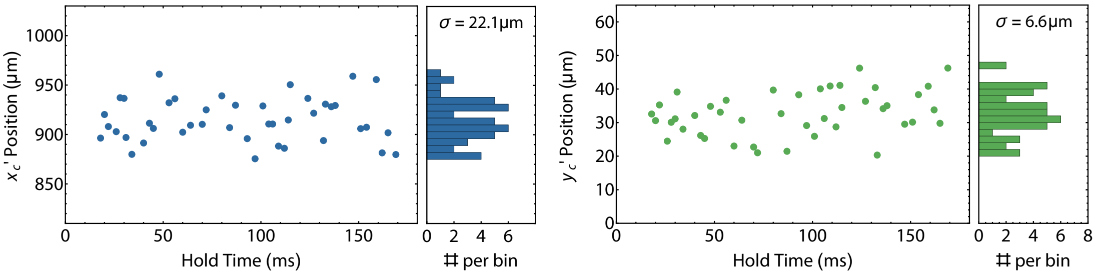

(a) Corrected COM position in x_c'-direction over hold time in the trap.

(b) COM position in y_c'-direction over hold time in the trap.

Figure 55: COM position uncertainty after transfer to location **b**. The position data along the x_c'-direction has been corrected by subtracting the expected position from the fit in Figure 54. In the process, the standard deviation in x_c' is reduced by a factor of two. The final position uncertainties after 100 ms TOF are given by the standard deviations $\sigma_{x_c'}$ = 22.1 μm and $\sigma_{y_c'}$ = 6.6 μm with a standard error of 3.4 μm and 1.0 μm, respectively.

and the observed amplitude A_{TOF} can be converted via

$$A_{\mathrm{TOF}} = A_{\text{in situ}}\, \omega\, t_{\mathrm{TOF}}. \tag{5.38}$$

This simplification is generally applicable after 100 ms TOF for the steep trap directions. In the following, (5.38) is used to infer the in situ amplitudes unless otherwise stated.

Fitting the $x_c^{'}(z)$ position data to a single-frequency sinusoid recovers the trap frequency along the transfer direction $f_z = 60.42 \pm 0.31$ Hz with an amplitude $A_{\mathrm{TOF}} = 52.12 \pm 5.2$ µm (see Figure 54). The amplitude of the inferred in situ oscillations along the $x_c^{'}$ imaging axis is thus $A_{\text{in situ}} = 1.37 \pm 0.14$ µm Subtracting the estimated position difference from the mean position after TOF reduces the standard deviation of the $x_c^{'}$ positions by a factor of two. Extending the fit to two and three frequencies yields an additional reduction of only2 µm each, signifying a lack of statistical significance. Hence, COM oscillations after transfer can only be observed in one dimension along the transfer trajectory. This is underscored by the low position variance along the other imaging axis.

The post-corrected COM position distribution in $x_c{'}$ and the position distribution in $y_c{'}$ after 100 ms TOF feature a standard deviation of $\sigma_{x_c{'}} = 22.1$ µm and $\sigma_{y_c{'}} = 6.6$ µm with a standard error of 3.4 µm and 1.0 µm, respectively (see Figure 55). If these uncertainties scale with TOF akin to velocity scatter, then the inferred velocity uncertainties after release from this particular trap are $\Delta v_{x'} = 221$ µm/s and $\Delta v_{y'} = 66$ µm/s.

Source Performance and Reproducibility

The atom numbers and condensate fractions vary largely over the course of the campaign (see Figure 56). This is owed in part to the prolonged decompression that compromises the atom number performance. Large shot-to-shot variation were also often the results of smaller technical issues with the experiment and the time demand of running a system at optimal performance during an ongoing drop campaign. Over the course of the campaign, the mean atom number observed after 100 ms TOF is 0.67×10^5 with a standard deviation of 0.47×10^5. The mean condensate fraction is 0.46 with a standard deviation of 0.17. In comparison, with optimal lab performance the system produces 3×10^5 atoms with a condensate fraction of 0.8 with an identical sequence.

Size Dynamics

The atom number fluctuations may complicate identifying possible high-order excitations in the condensate. Rescaling the TF radii of the clouds to a reference atom number of 50000 allows for a comparison of the sizes and identify possible size oscillations (seeFigure 57). The TF radii do not appear to vary harmonically and the uncertainties can be attributed to both the atom number

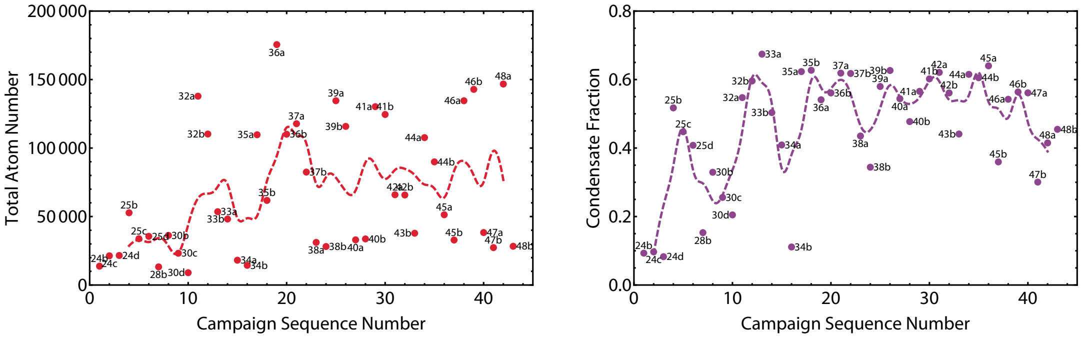

(a) Total atom number in chronological order.

(b) Condensate fraction in chronological order.

Figure 56: System performance in terms of total atom number and condensate fraction over the µg campaign. The data is labeled with the respective drop number and sequence letter. The dashed lines represent moving averages over every five data points for the total atom number and over every three data points for the condensate fraction. The atom number fluctuations exceed the standard lab fluctuations (see Chapter 3).

fluctuations and the rescaling of the clouds. The aspect ratio of the clouds is independent of the atom number. The data shows a small variance with a standard deviation of$\sigma = 0.08$ and a standard error of 0.012. However, attempts to extract size oscillations via a sinusoidal fit remain inconclusive.

In summary, transport and decompression to location**b** in µg leads to residual COM oscillations along the transfer trajectory but not the other axes. The oscillation along $x'(z)$ features an in situ amplitude of less than one micrometer and appears to be phase coherent over many weeks and drops. Despite the substantial thermal and mechanical strain on the capsule, the setup produces consistent results and allows for extended measurement campaigns yielding cohesive data sets. Knowing the phase and frequency of the residual oscillation, the final trap can now be switched-off at a turning point to mitigate the dynamics completely. No higher-order excitations were observed in the microgravity campaign.

5.5.2 Transfer to Location c

Transfer and decompression to large chip distances such as location **c** can not be tested in lab-operation as the trapping potential becomes to weak to hold the atoms against gravity. Successful transfer relies on the Biot-Savart simulations of the chip potential and the STA protocols outlined in this chapter. The chosen trajectory is calculated from the sinusoidal approach (5.32) with a ramp duration of $t_f = 150$ ms. In contrast to the previous transfer protocol, the trap bottom field applied via the x-coil is reduced by setting the current to 0.1 A to limit the rotation of the trap axes at small scalings (see Chapter 6).

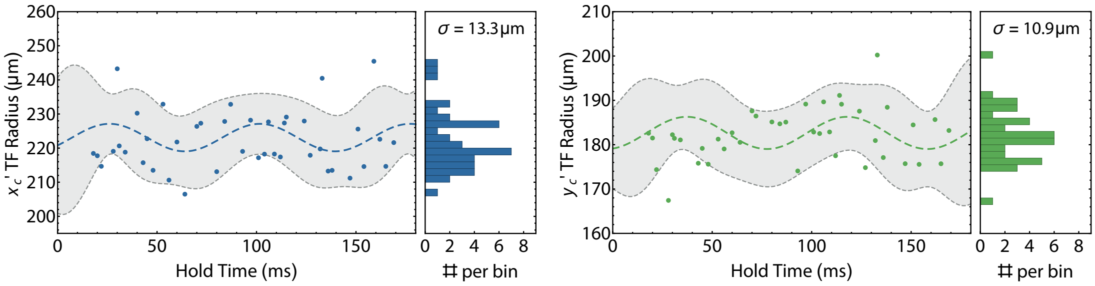

(a) Rescaled TF radius in $x_c{}'$-direction over hold time in the trap.

(b) Rescaled TF radius in $y_c{}'$-direction over hold time in the trap.

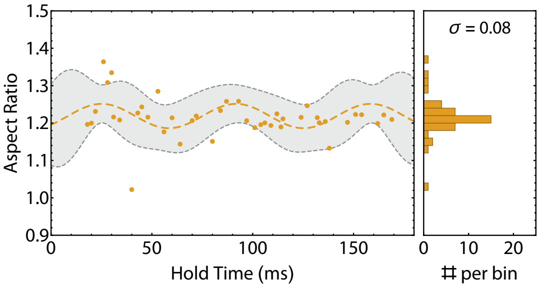

(c) Aspect ratio of the BEC over hold time in the trap.

Figure 57: Rescaled TF radii and aspect ratios over hold time in the trap after 100 ms TOF. Rescaling of the atom number adds some additional uncertainty to the data. No statistically significant fit for size oscillations can be obtained along any imaging axes. The aspect ratio of the cloud shows very little variance which is echoed by the large error in the fit attempt. The shaded regions signify 90% confidence intervals for sinusoidal fit attempts of the data.

The transfer trajectory and its characteristics are displayed in Figure 58. The deviation Δz between trap minimum and cloud COM is limited to approximately 5 µm to diminish the influence of anharmonicities in the trapping potential. The associated y-coil current ramp features a quick decline before slowly reaching its target value. This leads to a much quicker decompression than in the previous case and the system performance after decompression is improved as both atom number and condensate fraction can be maintained. However, the steeper initial decompression together with the reduction in ramp duration by 100 ms is likely to cause some size oscillations in the ensemble (see Figure 58d)

COM Dynamics

In comparison to the previous transfer protocol, only limited data is available to estimate the residual dynamics in the final trap. As in the previous location, the atoms were imaged 100 ms after release while varying the hold time in the trap. The COM dynamics mirror the findings from the last campaign, with residual oscillations along the $x_c{}'$ direction and inclusive data along $y_c{}'$ due to the small variance in the sample (see Figure 59).

Despite very few data points, the COM oscillations in $x_c{}'$ can be extracted via a sinusoidal fit, yielding a trap frequency of $f = 25.73 \pm 0.2$ Hz. The acquired frequency deviates from the

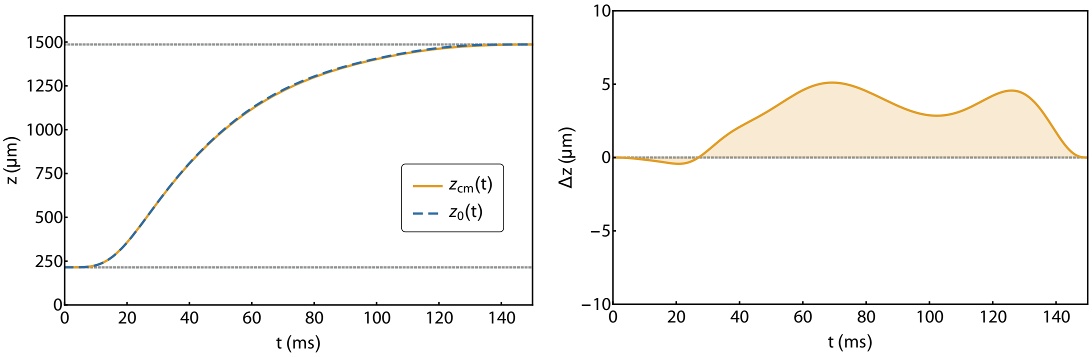

(a) Comparison of the COM and trap trajectories.

(b) Deviation between COM and trap trajectories.

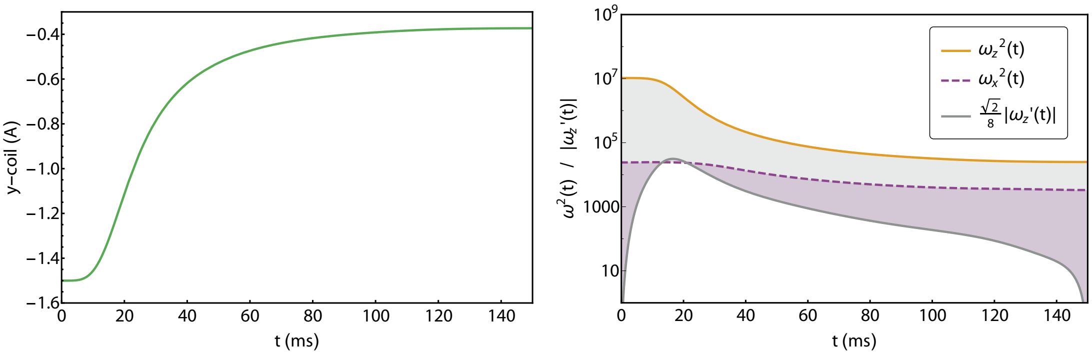

(c) Final current ramp applied to the y-coil.

(d) Adiabaticity criterion for the the decompression.

Figure 58: Analysis of the sinusoid ramp used to transfer the atoms to location **c**. The maximal deviation between the trap center position and the COM of the atoms is less than 6 μm over the duration of the ramp (see figure (b)). The faster decompression in comparison to the previous transfer protocol causes a substantial decline in the geometric trap frequency after only20 ms. While the adiabaticity criterion is satisfied along the z-axis, the protocol is likely to cause size oscillations along the x-axis (see figure (d)).

simulated value by 3.9% (see Table 7). The measured amplitude $A_{\mathrm{TOF}} = 73.84 \pm 7.41$ μm translates to an in situ amplitude of $A_{\text{in situ}} = 4.57 \pm 0.46$ μm. Subtracting the expected position difference in respect to the mean from the data reduces the standard deviation from $\sigma_{x_c'} = 43.36$ μm to $\sigma_{x_c'} = 9.26$ μm. In comparison to the residual position uncertainty of 22.1 μm at location **b**, the position uncertainty appears to be reduced substantially.

The COM position data along y_c' was corrected for residual drag in accordance with the respective tower pressure and sequence timing (see Chapter 4). The pre- and post-correction position uncertainties are $\sigma_{y_c'} = 7.13$ μm with a standard error of 2.38 μm and $\sigma_{y_c'} = 5.66$ μm with a standard error of 1.89 μm, signifying a reduction in the standard deviation of 25% due to drag correction. The estimated remaining uncertainty in the COM position implies a residual

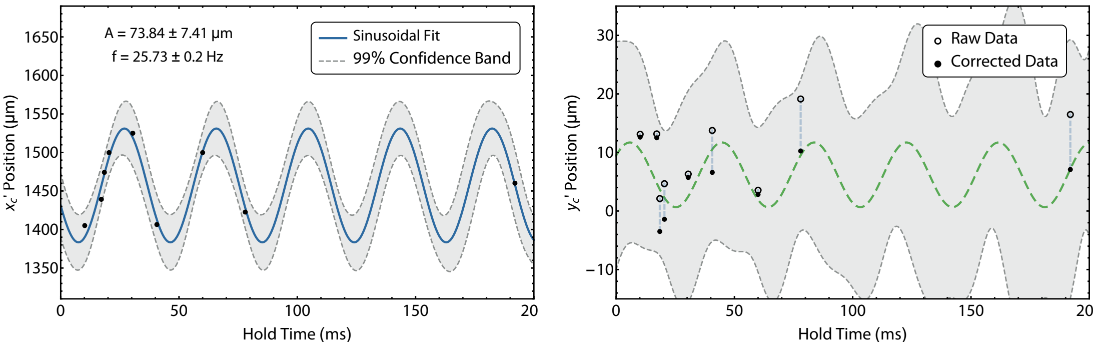

(a) COM position in $x_c{}'$-direction over hold time in the trap.

(b) COM position in $y_c{}'$-direction over hold time in the trap.

Figure 59: COM position over hold time at location **c**. Clear COM oscillations can be seen in the $x_c{}'$-direction. The position data in the $y_c{}'$-direction is post-corrected for drag displacement. Here, no clear COM oscillations can be extracted from the limited data set.

velocity scatter of $\Delta v_{x_c{}'} = 99.8\,\mu\text{m/s}$ and $\Delta v_{y_c{}'} = 56.6\,\mu\text{m/s}$. However, these values may be inflated by residual magnetic field gradients and unresolvable oscillations.

Size Dynamics

The observed TF radii show signs of size oscillations after transfer (see Figure 60). A distinct sinusoidal oscillation is visible in the rescaled radii along the $x_c{}'$ direction. Curiously, the fitted frequency $f = 21.43 \pm 0.46\,\text{Hz}$ does not coincide with any of the simulated or measured trap frequencies. The conversion of the amplitude $A_{\text{TOF}} = 23.49 \pm 4.09\,\mu\text{m}$ after TOF to the in situ oscillation results in $A_{\text{in situ}} = 0.87 \pm 0.16\,\mu\text{m}$ for a cloud of 50000 atoms. To put this in perspective, the in situ TF radii of such a cloud calculated with (6.6) and the simulated trap frequencies from Table 7 are $R_x = 22.24\,\mu\text{m}$, $R_y = 7.20\,\mu\text{m}$ and $R_z = 8.16\,\mu\text{m}$. Thus, the oscillation would correspond to a variation of the radius in $x_c{}'(z)$ direction of approximately 10%.

The variation in TF radii along $y_c{}'$ over the hold time is reduced by 2/3 in respect to $x_c{}'$. The sinusoidal fit to the data is much less conclusive and suffers from the small amount of data points and any interpretation is highly speculative. Interestingly, the fit recovers a frequency very similar to the one in $x_c{}'$ direction and phases of both oscillation appear to match. Note that the $y_c{}'$ direction is a 45° projection of the x- and y-axis and the observed radius is likely a projection of two oscillations.

The clearest signal can be obtained from the aspect ratio of both observed radii, which is not subject to fluctuations in the atom number or condensate fraction. Figure 60c shows clear size oscillations which appear to be following a single sinusoid with frequency $f = 19.54 \pm 0.3\,\text{Hz}$

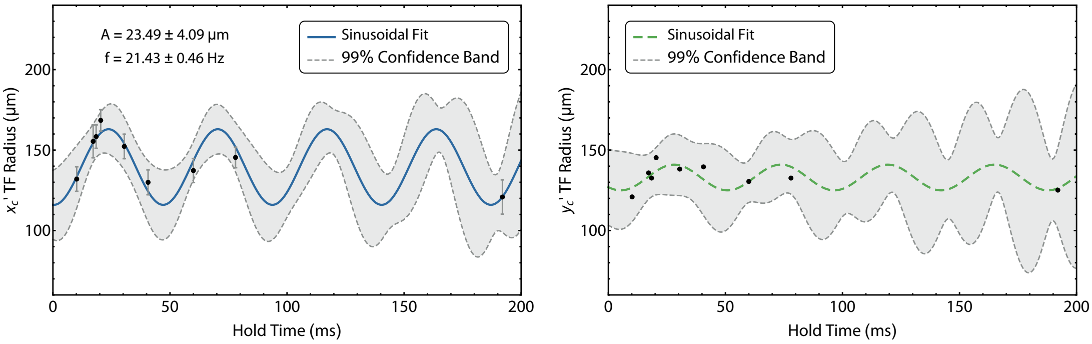

(a) Rescaled TF radius in $x_c{}'$-direction over hold time in the trap, observed after TOF.

(b) Rescaled TF radius in $y_c{}'$-direction over hold time in the trap, observed after TOF.

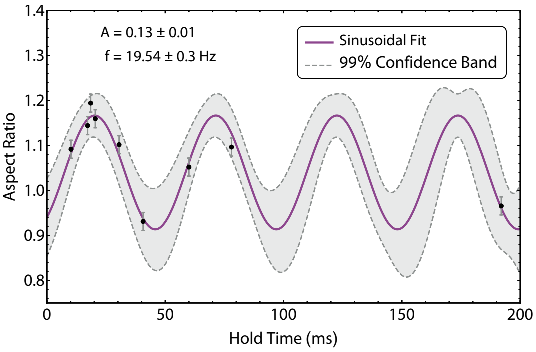

(c) Aspect ratio of the BEC over hold time in the trap, observed after TOF.

Figure 60: Rescaled TF radii and aspect ratio over hold time in the trap after 100 ms TOF. Rescaling of the atom number adds some uncertainty to the data as indicated by the error bars. A clear size oscillation can be extracted in the $x_c{}'$ direction. The fit attempt in the $y_c{}'$ direction remains inconclusive. The aspect ratio is immune to atom number fluctuations and confirms distinct size oscillations with a frequency in the proximity of 20 Hz.

and amplitude $A_{\text{TOF}} = 0.13 \pm 0.01$. Again, the limited data points indicate size oscillations with a single frequency that sits in between the geometrical trap frequencies.

Preliminary data from the second detection angle predicts substantial size variations along the shallow x-axis, which is consistent with the most likely origin of the size oscillations: an excessively quick decompression in the presence of a very shallow trap frequency along the x direction (see Figure 58d). These leads can be interpreted as one of two likely scenarios:

1. The induced size oscillations along x cause excitations in the other two directions via (5.22), resulting in three size oscillation frequencies that interfere with each other through interactions. In this case the single recovered frequency would have to be explained by insufficient data and sampling parts of more complex size variations.

2. The fast decompression causes a collective excitation driven by the excursion along the x-axis. The apparent oscillation of the aspect ratio would exclude the monopole mode and hint at a quadrupole excitation were the radii along the two steep trap axes oscillate in phase with each other and out of phase with the x-radius.

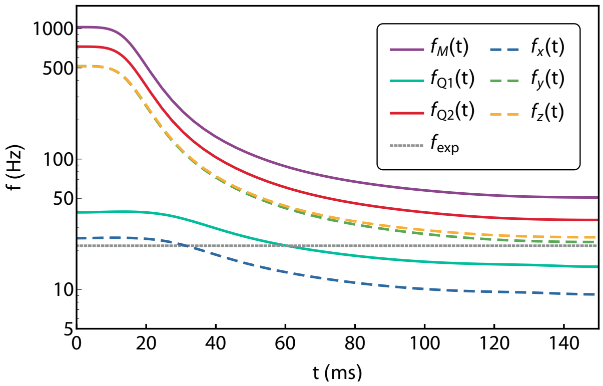

Figure 61: Frequencies of low-lying modes of the BEC during transfer according to (5.39) and (5.40). Collective monopole (M) and radial quadrupole excitations (Q2) are associated with frequencies in excess of the radial trap frequencies. Three-dimensional quadrupole excitations (Q1) with frequencies below 40 Hz are likely excited during transfer and are consistent with the experimental value $f_{\mathrm{exp}} = 19.56\,\mathrm{Hz}$ of the aspect ratio oscillation frequency.

The latter assumes that the radial trap frequencies are similar enough to satisfy cylindrical symmetry, i.e. $\omega_y \simeq \omega_z = \omega_r$. The frequencies of collective modes in such a system obey

$$\omega^2_{\mathrm{Q1,M}} = \omega_r^2 \left(2 + \frac{3}{2}\gamma^2 \mp \frac{1}{2}\sqrt{16 - 16\gamma^2 + 9\gamma^4}\right), \tag{5.39}$$

$$\omega^2_{\mathrm{Q2}} = 2\omega_r^2. \tag{5.40}$$

where γ is the ratio between ω_z and ω_r. The " + " solution of (5.39) pertains to monopole excitations while the " − " solution corresponds to three-dimensional quadrupole excitations, where the radial size oscillates out of phase with the axial size [128]. Equation (5.39) describes two-dimensional quadrupole oscillations in the radial plane. Since ω_z, ω_r and γ change throughout the transfer to location **c**, it is difficult to pin-point when exactly the excitations are induced and what happens to their frequency as the trap is decompressed further. Figure 61 illustrates the different excitation frequencies in comparison to the trap frequencies and their time evolution during transfer. All but one of the low-lying modes of the BEC feature multiples of the radial trap frequencies, far exceeding the value observed in the experiments. Q1-excitations are a likely candidate to explain the observed oscillations at a frequency of approximately 20 Hz.

To investigate the likelihood of a quadrupole excitation, the x' and y' data is pooled with preliminary data from the second detection angle. These come with a large uncertainty in the absolute atom number which is detrimental to clearly identifying size dynamics. The second imaging angle offers an unobstructed view of the cloud size along the y-axis and a projection of the x and z radii. The quadrupole mode in question features two synchronous oscillations of similar amplitude along the radial directions y and z, that evolve out of phase with a third oscillation a along x. Fitting such a mode to the complete data set yields good agreement considering the low number of data points and the uncertainty in the radii as a result of the varying atom number (see Figure 62). The fit extracts a common frequency $f_{\mathrm{exp}} = 21.56 \pm 0.43\,\mathrm{Hz}$ with mean radii $\overline{R}_x = 104.3 \pm 4.9\,\mu\mathrm{m}$, $\overline{R}_y = 142.8 \pm 2.9\,\mu\mathrm{m}$, $\overline{R}_z = 139.2 \pm 2.5\,\mu\mathrm{m}$

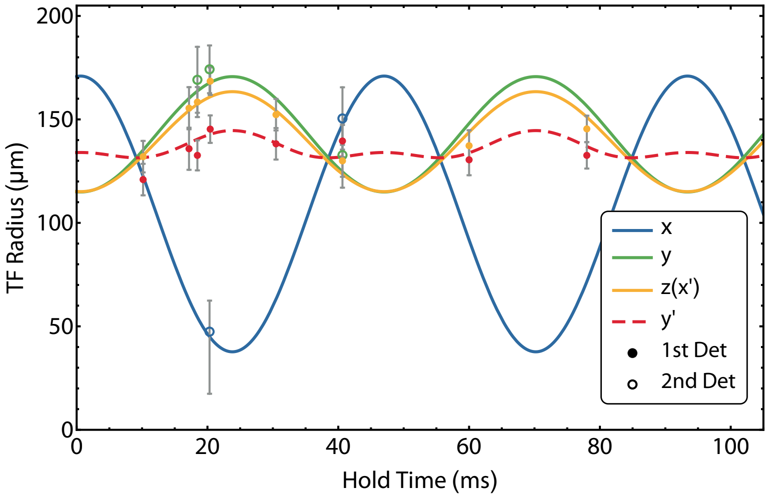

Figure 62: Quadrupole mode fit to the TF radii over the hold time in the trap. All TF radii are rescaled to an atom number of 50000. The error bars reflect the uncertainty of the rescaling process. The four data sets for the x, y, z and y' direction are extracted from images of the primary and secondary imaging angle. The data is then fitted to a Q1 quadrupole mode, i.e. three oscillations with the same frequency, two of which oscillate in phase with each other and out of phase with the third. The single model fits the complete data set simultaneously to the three oscillations (x, y, z) and the projection of two of those oscillations (y'). The recovered frequency is $f_{\text{exp}} = 21.56 \pm 0.43$ Hz.

and amplitudes $A_x = 66.6 \pm 8.6\,\mu\text{m}$, $A_y = 27.9 \pm 4.8\,\mu\text{m}$, $A_z = 24.2 \pm 4.5\,\mu\text{m}$ after 100 ms TOF. These values corresponds to in situ oscillation amplitudes of $A_{x,\text{in situ}} = 5.5 \pm 0.7\,\mu\text{m}$, $A_{y,\text{in situ}} = 0.9 \pm 0.2\,\mu\text{m}$ and $A_{z,\text{in situ}} = 0.8 \pm 0.2\,\mu\text{m}$. To fit the projected radii along y' the projection angle is adjusted by 12° to include a slight rotation of the x and y trap axis in respect to the absolute coordinate system. The available data appears to be consistent with a Q1-type mode oscillation. However, the measured frequency does not coincide with the expected frequency of that mode the final trap $f_{\text{Q1}}(t = 0.15\,\text{s}) = 14.96$ Hz. This could potentially be linked to a break in the cylindrical symmetry as the trap is decompressed. The two radial trap axes feature a small deviation in frequency. Initially, this deviation amounts to less than 1% of the absolute trap frequencies but grows to over 16% in the final trap (for the simulated values in Table 7). Clearly, more measurement campaigns are necessary to expand the data sets and confirm or refute the presented arguments.

Knowledge of the exact size dynamics of the BEC during decompression is crucial for understanding and designing future shortcut trajectories and magnetic lensing sequences. The current attempts of neglecting the coupling of the three trap axes during decompression and focusing only on mitigating dipole oscillations will need to be extended to a more complete model. Not only does the current decompression induce size oscillations in the condensates,

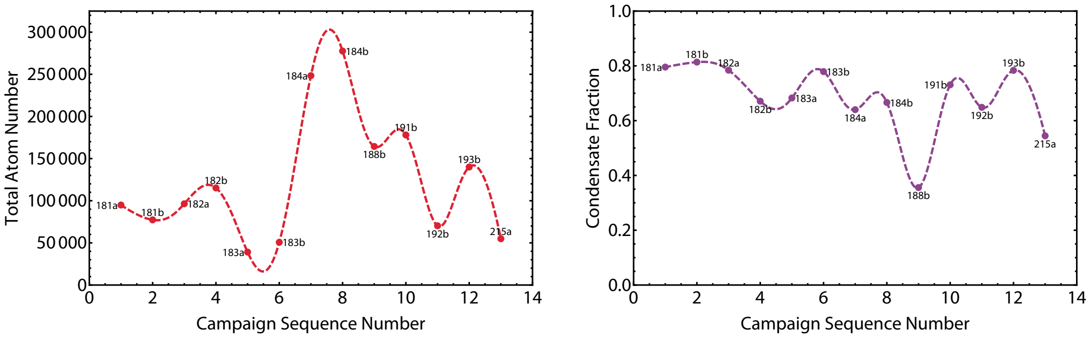

(a) Total atom number in chronological order.

(b) Condensate fraction in chronological order.

Figure 63: System performance in terms of total atom number and condensate fraction over the µg campaign. The data is labeled with the respective drop number and sequence letter. With the improved transfer procedure, the source performance is increased substantially in comparison to the previous campaigns.

these dynamics may constitute higher-order collective excitations that are not necessarily included in the common STA framework. The role of collisions in BECs and their inclusion in shortcut approaches may need to be extended beyond the usual mean field approximation.

Understanding and controlling the size dynamics of the BEC is of utmost importance as they define the input state and the success of the subsequent magnetic lens. Gaining access to such coherent and predictable oscillation modes of the BEC could considerably advance the magnetic lensing tools and methods. The rapid decompression into a shallow potential is in itself a type of lensing process, where the velocity spread of the ensemble can be reduced by switching off the trap at the appropriate time [49]. The implications of such control mechanisms for the magnetic lens are discussed in Chapter 6.

Source Performance and Reproducibility

While the amount of drops and acquired data points is much smaller than in the previous campaign, both the atom number and the condensate fraction are much improved in absolute value and consistence. The mean atom number observed after 100 ms TOF is 1.24×10^5 with a standard deviation of 0.75×10^5. The mean condensate fraction of 0.68 with a standard deviation of 0.13 (see Figure 63). The performance is also much more consistent between data points recorded during the same drop. The higher atom numbers and condensate fractions are a result of many small technical improvements, making the experiment more stable overall, and the new transfer trajectory which includes a significantly faster decompression.

Figure 64: Measured current response to the switch-off protocol. The y-coil is shut-off via step response while the two chip structures receive the appropriate request signal to match the current progression. The result is a switch-off time of 0.98 ms which is significantly faster than the settle time of the coil (see Table 5). This procedure is especially warranted when switching off the trap at high trap frequencies.

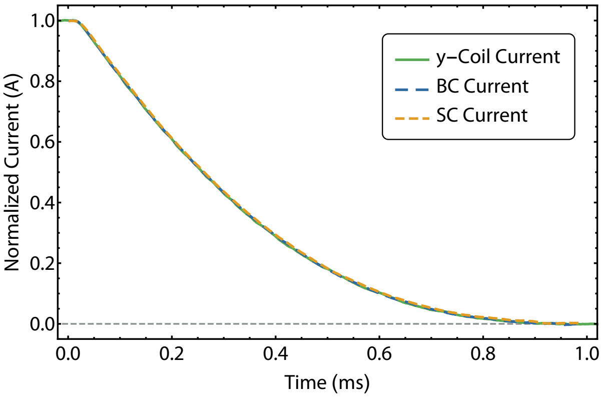

5.6 Switch-Off

Switching off the current-carrying structures instantaneously leads to a significant COM motion towards the atom chip in ground operation. Due to the disparity in switching times between chip structures and coils, the switch-off dynamics are given by the step response of the y-coil. Releasing the atoms from the trapping configuration without disturbance calls for a protocol to simultaneously shut-off all relevant structures in a coherent way as any mismatch might cause a sudden shift of the trap center. This is especially relevant in lab operation where the trapping potential is deformed under gravity and the atoms are typically released from relatively steep traps. For such applications it is useful to ramp the chip structures in a way to match the current progression of the bias coil.

The step response of the y-coil traces the typical curve for a critically damped system (see Chapter 2). Thus, the fastest transition to zero field is given by the fall time, the first intersection with the target value. The trapping potential can be switched-off by forcing the same intersection with all structures. However, the steep slope of the function may be vulnerable to a mismatch and introduce additional scatter in the procedure. Instead, one can make use of the overshoot of the system by requesting a step response to the absolute value of the maximum overshoot, thus generating a smooth approach to zero field. In this case, the switching time is given by the peak time which for the y-coil sits at approximately 0.98 ms. The matching current ramps for the chip structures will than mimic the y-coil for the 0 to 0.98 ms interval (see Figure 64). If necessary, the mean COM motion can than be minimized experimentally by fine tuning the ramp duration for the chip structures and adjusting the constant bias and quantization field.

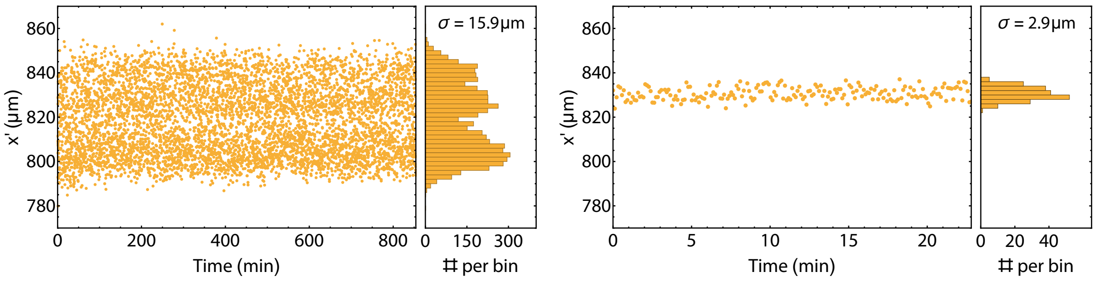

(a) COM position in x'-direction in lab operation. The position uncertainty has a standard deviation of $\sigma = 15.92\,\mu\mathrm{m}$.

(b) COM position in x'-direction in battery operation. The position uncertainty has a standard deviation of $\sigma = 2.92\,\mu\mathrm{m}$.

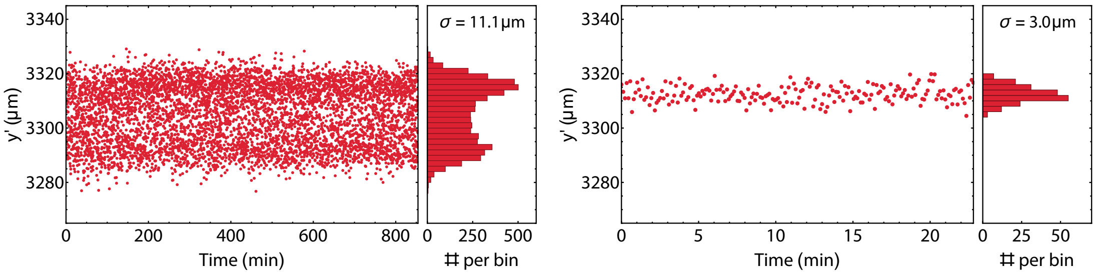

(c) COM position in y'-direction in lab operation. The position uncertainty has a standard deviation of $\sigma = 11.13\,\mu\mathrm{m}$.

(d) COM position in y'-direction in battery operation. The position uncertainty has a standard deviation of $\sigma = 3.04\,\mu\mathrm{m}$.

Figure 65: COM position uncertainty after transfer to location **b** during normal lab operation and battery operation. Note that the trap parameters are slightly different from the values in Table 7 due to the influence of gravity. All measurement were taken after 22 ms TOF and a hold time of 100 ms. When the capsule is connected to the power supplies, the histogram shows a clear sign of oscillations that can be traced back to the 50 Hz signal of the main power line. Once the system is disconnected, the position uncertainty is reduced to a narrow Gaussian distributions indicative of residual technical noise. Once the system is at operating temperature, there is no measurable drift of the mean COM position.

5.7 COM Motion and Position Uncertainty

A stable and predictable COM motion after switch-off and a reproducible cloud position is imperative for all subsequent steps in the experiment. Pristine control of the COM dynamics keeps the atoms in the detection volume for many seconds and enables the systematic analysis of position sensitive tools such as the magnetic lens. The mean COM motion usually depend on the specific field decay which is determined by the release trap and the switch-off procedure. Generally, the final velocity after release can be tuned via several parameters. The biggest challenge in suppressing the residual motion of the condensates is the reliable determination of its magnitude. Uncertainty in the COM position after TOF can be a result of a position offset caused by small fluctuations and drifts of the resistance and temperature of the current-carrying structures. The aforementioned effects would result in a small position scatter that remains constant over time. More troublesome is an uncertainty in the final velocity with an associated velocity scatter which scales with the TOF.

To estimate the position uncertainty and gauge the quality of the scarce microgravity data, statistical analysis was performed on large data sets of equally prepared BECs. In typical lab-based operation, the capsule batteries are all connected to their respective power supply and the capsule ground is referenced to the power outlet. In an overnight measurement, the center position of the clouds was recorded over 15 hours and 6000 data points (see Figure 65a and Figure 65c). The large variance of the center position is caused by the 50 Hz oscillation of the power mains, which couples into the system via some of the current drivers. Repeating the same measurement in battery operation, where the capsule is completely disconnected from all other lap equipment, yields a much smaller standard deviation of $\sigma_{x'} = 2.92\,\mu\mathrm{m}$ and $\sigma_{y'} = 3.04\,\mu\mathrm{m}$ and a standard error of 0.21 µm each. The latter data set comprises 200 identically prepared BECs. In all of the above measurements, the atoms were released from a trap at location **b** with a mean radial trap frequency of approximately 60 Hz and imaged after 22 ms TOF.

The observed uncertainty in the cloud position scales both with the TOF and the frequency of the release trap. To quantify the dependence on the trapping potential, the measurement was repeated at various chip distances and trap frequencies (seeFigure 66). The velocity scatter in x' scales linearly with the the trap frequency at a rate of approximately 3.2 µm/s/Hz. The uncertainty in y' appears to be constant for most trap frequencies and increases only towards the steepest traps. The different scaling for the two may be caused by the fact that the y' direction is a projection of the x and the y trap axes and the frequency along x varies only slightly over the trap variations. Additionally, the increased uncertainty along the x' axis could be explained by the susceptibility of the trap position on that axis to small current fluctuations. Unfortunately, the gravitational sag sets a lower limit for the trap frequencies attainable in lab operation. Together with the relatively short observation times this limits the minimal observable scatter to just under 3 µm/22 ms = 136 µm/s. In comparison, the observed residual velocity scatter in the first µg campaign were as low as 66 µm/s at a mean radial trap frequency of approximately 60 Hz.

Experimental data of the trap position after TOF in µg, where the the atom were released after constant hold time in the final trap, is very limited. In these data sets, the atoms remained in the magnetically sensitive $m_F = 2$ hyperfine state during free expansion. Thus the position information may be skewed by residual magnetic field gradients. Figure 67 shows the mean COM velocity and its uncertainty for release from the trap configurations at location **b** and **c**. The y' positions in the data sets were post corrected for residual drag in the drop tower. The COM uncertainties are inferred from weighted fits of the data with fixed in situ positions. The error bars are given by the standard deviation of the position data at each measured time.

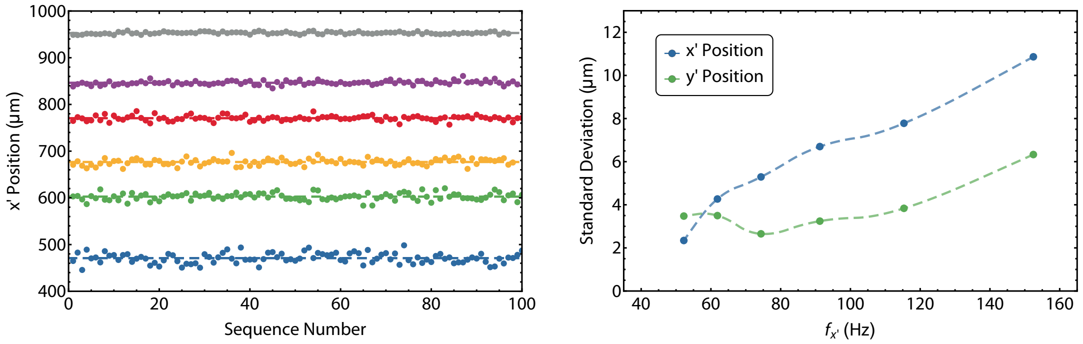

(a) x'-position uncertainty at varying trap frequencies and chip distances.

(b) Standard deviation of the COM positions at varying trap frequencies.

Figure 66: COM position uncertainty over the trap frequency. Figure (a) shows the position of 100 equally prepared BECs after decompression to various trap frequencies and chip distances. The atoms are imaged after 22 ms TOF. Figure (b) plots the standard deviation of the x' and y' position at these trap frequencies and locations. While the uncertainty in the y' position uncertainty remains relatively constant for all but the steepest trap, the standard deviation in x' decreases approximately linearly with the trap frequency.

The acquired velocity scatter at location **b** in x' and y' direction are 267.0 μm/s and 88.5 μm/s, respectively. These values agree with the residual scatter after post correction from the first μg campaigns (see Figure 55). The mean COM motion in x' and y' are 122.4 μm/s and 433.3 μm/s, respectively. The atoms were released after a hold time of 28.5 ms and imaged after varying TOF.

At location **c**, the velocity scatter appears to be reduced substantially to 15.1 μm/s and 13.5 μm/s, which is well below the expected scaling of the uncertainty with the trap frequency. These values can likely be attributed to the low data rate. The mean COM velocity along the x' and y' axes are 107.6 μm/s and 79.5 μm/s, respectively. The reduced velocities are advantageous to minimize displacement between the atoms and the magnetic lens. Here, the atoms were released after a hold time of 18.46 ms and imaged after varying TOF.

Post Lens COM Dynamics

The best data sets for determining the COM dynamics on the time scale of several seconds is the position data of the lensed BECs. A magnetic lensing sequence was performed at both location **b** and **c**, after which the atoms were transferred to the $m_F = 0$ hyperfine state and imaged after up to 2 s of free evolution (see Chapter 6). The collimated clouds can be observed much longer than the initial ensembles and evolve mostly unaffected by residual magnetic fields. Figure 68 depicts the COM dynamics of the collimated ensembles. The magnetic lens has a strong influence on both the mean velocity and its uncertainty for both imaging directions and chip distances.

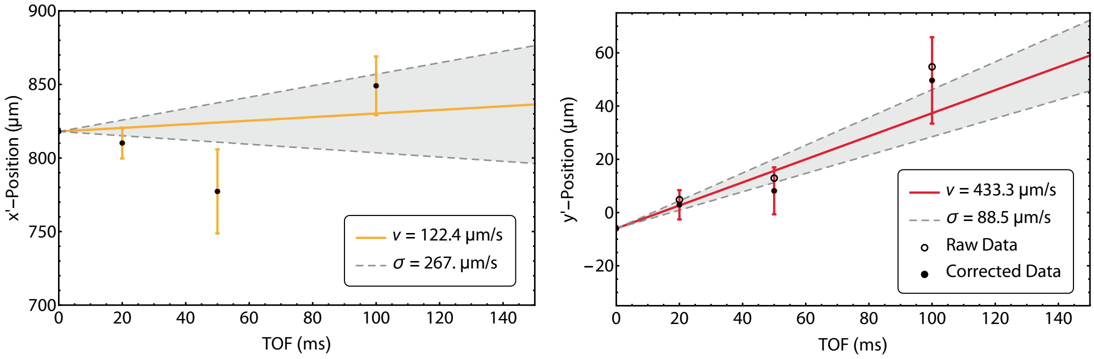

(a) COM position in x'-direction over TOF in µg. (b) COM position in y'-direction over TOF in µg.

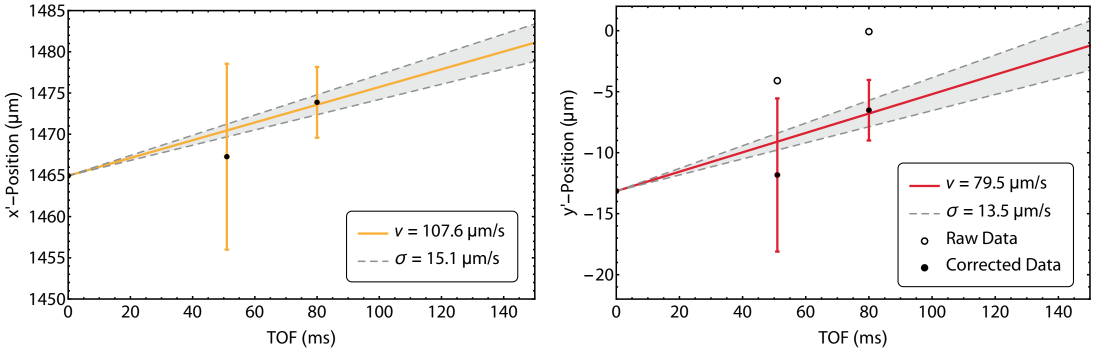

(c) COM position in x'-direction over TOF in µg. (d) COM position in y'-direction over TOF in µg.

Figure 67: COM velocity and velocity scatter in microgravity after release at locations **a** and **b**. Figures (a) and (b) show the data set acquired after release at a chip distance of 816 µm. Despite the low data rate, the position uncertainty after TOF appears consistent with previous µg campaigns. Figures (c) and (d) plot the velocity scatter after release at a chip distance of 1465 µm. The data suggest a sizable reduction in position uncertainty after TOF. The y' positions in both data sets were post corrected for residual drag.

After the BC-SC-lens at location **b**, the mean COM velocity is $v_{x'} = 541.2\,\mu\text{m/s}$ and $v_{y'} = -237.7\,\mu\text{m/s}$, moving away from the chip surface and upwards in the imaging frame. The motion away from the atom chip has accelerated, while the motion in the perpendicular axis has reversed, indicating a mismatch of the cloud and lens positions. The mean COM velocity after the BC-lens at location **c** shows the opposite behavior. The condensate is moving towards the chip surface and downwards in the imaging frame with velocities $v_{x'} = -414.5\,\mu\text{m/s}$ and $v_{y'} = 332.2\,\mu\text{m/s}$, again symptomatic of a position mismatch. However, since the pre-lens position data is somewhat unreliable, exact prediction of the offsets is currently difficult. Especially in the y'-direction, the estimated cloud position varies largely with the drag correction. However, the µg data for the pre-lens position before the BC-lens has been acquired late in the µg sequence time and at high

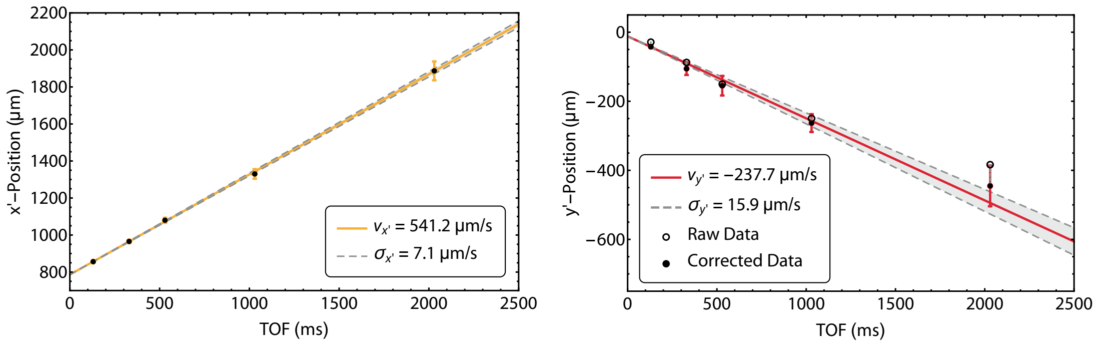

(a) COM position in x'-direction after magnetic lens (BC-SC).

(b) COM position in y'-direction after magnetic lens (BC-SC).

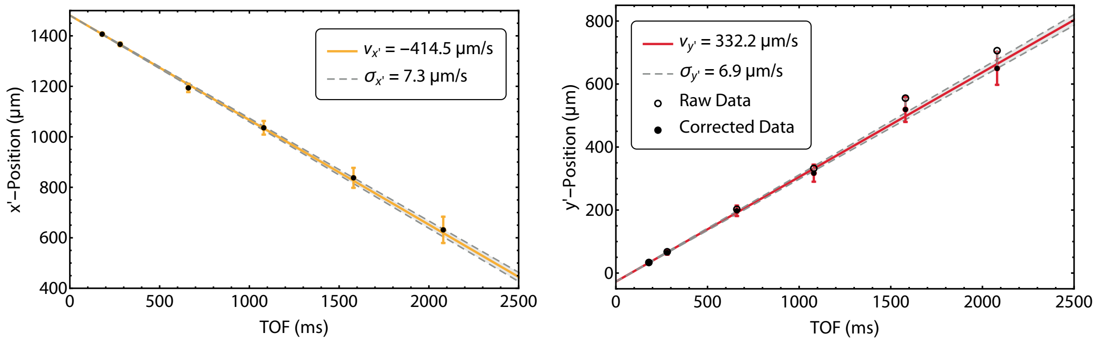

(c) COM position in x'-direction after magnetic lens (BC).

(d) COM position in y'-direction after magnetic lens (BC).

Figure 68: COM velocity and velocity scatter in microgravity after magnetic lens at locations **b** and **c**. After the lensing pulse, the atoms are transferred to the $m_F = 0$ hyperfine state. The y' positions in both data sets were post corrected for residual drag. The atoms were imaged after varying TOF, which includes the period of free expansion before the lens. The collimation of the condensates appears to reduce the velocity uncertainty in both data sets.

capsule velocities. Overall, the final mean COM velocities span a wide range along both imaging axes, indicating that the values can be tuned arbitrarily by proper positioning of the lens.

The velocity scatter after the magnetic lens appears drastically reduced for both data sets. The improvement is most striking for the BC-SC-lens, where the position uncertainty is reduced to 3% in x' and 18% in y' of the pre-lens values. The final velocity scatter determined from the error of a weighted linear fit is $\sigma_{x'} = 7.1$ µm/s and $\sigma_{y'} = 15.9$ µm/s. While the improvement due to the BC-lens is less pronounced because of the reduced initial uncertainty, the final COM stability is just as pristine. With a residual uncertainty of $\sigma_{x'} = 7.3$ µm/s and $\sigma_{y'} = 6.9$ µm/s, the COM position of the collimated clouds can be controlled with utmost precision. Note that the uncertainty in $v_{y'}$ is reduced further with increased drag coefficient for both data sets. Consequently, the conservative assessment of the drag correction from Chapter 4 might be an

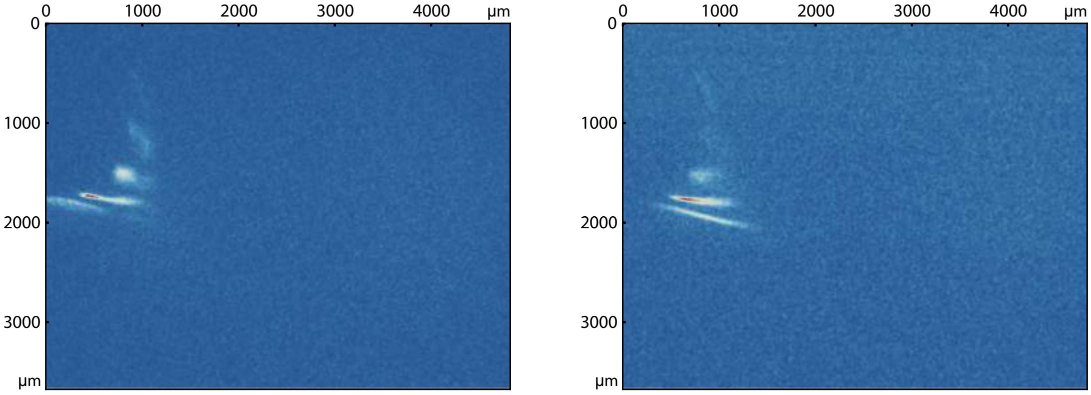

(a) All current-carrying structures connected. (Drop #91a)

(b) Mesoscopic chip structures disconnected. (Drop #91b)

Figure 69: A lensed BEC in m_F state mixture imaged after 491 ms TOF. A Gaussian lens pulse (BC-SC) is applied to the condensate before distributing the atoms over several m_F hyperfine states via an ARP. Subsequently, the clouds evolve freely with all current-carrying structures connected (a) and with all mesoscopic structures disconnected (b). From bottom to top, the $m_F = 2$, $m_F = 1$ and $m_F = 0$ states are clearly visible on both images. The majority of the atoms reside in $m_F = +1$. Disconnecting the mesoscopic structures reduces the displacement along the x'-axis – the gradient along y' remains the same.

underestimation. The origin of the substantial reduction in velocity scatter can be explained by the lensing action, whose very principle is the deceleration of atoms proportional to their velocity (see Chapter 6). Thus, applying the lensing field has a homogenizing effect on the various input velocities.

5.8 Gradients

When mixing the m_F hyperfine states with an ARP after the lens, the different clouds separate over time, indicating a differential acceleration from a residual magnetic field gradient. The magnitude of the magnetic field gradient is given by

$$\nabla B = -\frac{m\,a}{m_f\, g_F\, \mu_B}, \tag{5.41}$$

where a is the observed acceleration, g_F the dimensionless magnetic moment and μ_B the Bohr magneton. It was suspected early on that residual currents through the structures may cause small gradient that become evident at longer TOFs. This theory was put to the test by imaging identically prepared BECs distributed over several m_F states and disconnecting structures for one of the images (see Figure 69). The separation of the states is clearly altered by disabling

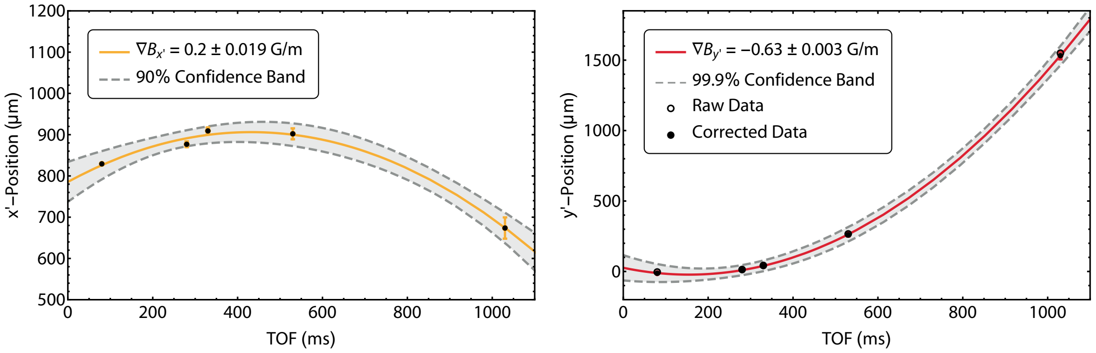

(a) x'-position over TOF (BC-SC-lens).

(b) y'-position over TOF (BC-SC-lens).

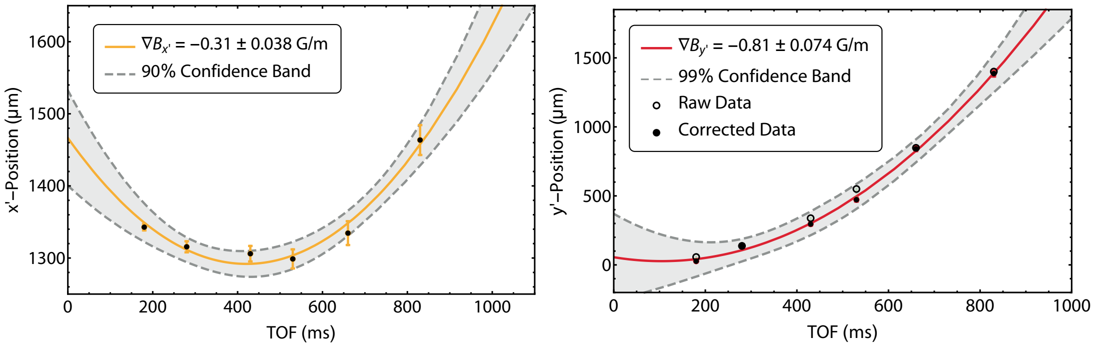

(c) x'-position over TOF (BC-lens).

(d) y'-position over TOF (BC-lens).

Figure 70: COM position after magnetic lensing and subsequent free evolution in the $m_F = 2$ state. The curvature of the trajectory is indicative of a residual acceleration from magnetic field gradients. While the measurements for the axis pointing away from the atom chip give inconclusive results, there is a reproducible gradient parallel to the chip surface.

the mesoscopic structures. The system was upgraded so that all unused structures can be disconnected on demand. Now, only the x-coil remains active during TOF to provide the quantization axis.

Even with all unused structures disconnected during free evolution, clear evidence of residual magnetic field gradients remain. The most concise data on this subject are the two lensing campaigns were the condensates evolved in the $m_F = 2$ state on time scales of up to one second (see Figure 70). During the BC-SC-lens campaign at location **b**, the measured residual gradients are $\nabla B_{x'} = 0.20 \pm 0.019$ G/m and $\nabla B_{y'} = -0.63 \pm 0.003$ G/m. These values are surprisingly high considering the two-layer mu-metal shield, the effort that was put into setting up a titanium vacuum chamber and limiting the components within the magnetically shielded area to non-magnetic components. For the next lensing campaign at location **c**, the measured gradients are $\nabla B_{x'} = -0.31 \pm 0.038$ G/m and $\nabla B_{y'} = -0.81 \pm 0.074$ G/m. The gradient along x' is reversed compared to the previous data set and the assessment is inconclusive. The remaining quantization field was reduced for the second campaign which could indicate that the gradient in the direction pointing away from the atom chip is self inflicted. The largest displacement and field gradient is oriented parallel to the chip and its magnitude is consistent over both campaigns.

To identify the sources of the field gradients, sensitive measurements protocols for ground-based magnetometry need to be developed. While the amplitude of the residual fields is surprising, these gradients remain constant over many weeks in lab operation, while traversing the 110 m steel tube of the drop tower and during extended drop campaigns. Thus, the field source is definitively located inside the capsule, and most likely inside the magnetically shielded region. While gradients of such magnitude may be detrimental to high-precision atom interferometry in the future, there is currently no evidence of adverse effects for the magnetic lens.

5.9 Summary

This chapter presented the tools and methods to bridge a wide range of trap frequencies and locations via adiabatic and non-adiabatic transfer methods. Successful transfer to large chip distances was demonstrated without the introduction of excessive excitations. Due to the stability of the system and the phase coherence of the residual dynamics, they were easily mitigated through the switch-off procedure. The distant trap location shows signs of size oscillations which could be a collective excitation of the condensate. Future shortcuts to adiabaticity will need to be extended to either disable these excitations or generate them deliberately for the purpose of designing the input state for the magnetic lens. STA procedures of the future will also need to include the dynamic anharmonicities in the potential.

Excellent control over the COM dynamics of the condensates is crucial to enabling high-precision measurements in microgravity on the second scale. This chapter shows that the kinematics of the clouds can be controlled sufficiently to enable detection of the atoms after several seconds of free propagation. The mean COM velocity can be tuned arbitrarily via positioning of the magnetic lens. The residual velocity scatter was reduced to 7 μm/s allowing for precise predictions of the cloud location. In summary, the observation time of the condensates is not limited by the COM dynamics and the control mechanisms are sufficient to probe the atoms over the entire microgravity time span offered by the drop tower.

CHAPTER 6

Matter-Wave Lensing with Atom Chips

Collimating Ultra-Cold Atoms with Anharmonic Potentials

One of the most crucial properties of atomic ensembles as sources for atom interferometry is their rate of expansion, i.e. their velocity spread. The velocity spread is a useful quantity in determining the potential measurement time of the ensemble, as detection of the atoms after TOF relies on sufficient density of the cloud. Together with the initial size, the velocity spread defines the size and density at any given time after release, quantities that are relevant for many systematic effects in interferometric measurements (see Chapter 7).

Furthermore, the fidelity of a beam splitting pulse in an atom interferometer depends on the velocity spread of the atomic cloud since different velocity classes within the ensemble will experience different Rabi frequencies [32, 47]. The Gaussian intensity distribution of the interferometer beams leads to an additional variation of the Rabi frequency as the cloud expands in size. Hence, the requirements on the divergence of the atomic clouds are especially stringent when the interferometer is extended to macroscopic time scales, where the individual pulses are separated by several seconds of free evolution. Thus, the high precision measurements envisioned in this project require pristine control of the residual expansion of the condensates and manipulation of the velocity spread through experimental techniques beyond evaporative cooling.

Size and density restrictions are highly relevant in the context of observability. The cloud density needs to be maintained above the threshold for spatially resolved imaging techniques, while the maximal cloud size is set by the position in the detection volume. In the microgravity campaigns of the predecessor experiment QUANTUS-1, condensates could be observed for up to one second of free evolution [4]. The contrast in a Bragg atom interferometer diminished much sooner, after about 500 ms [56]. Thus, the dwindling density of dilute clouds is a severe limitation on macroscopic timescales.

Tools to collimate the ensembles are essential for extending both the expansion time and the interferometry time into the ten second range. So called delta-kick cooling (DKC) or magnetic lensing techniques [125, 129] were successfully employed in QUANTUS-1 to improve the measurement time of a BEC interferometer in microgravity to 700 ms [56]. A magnetically lensed cloud was barely observable after two seconds of free evolution. However, the limited starting atom number prohibited more decisive results. The microgravity campaigns presented here illustrate the progress in extending the measurement time with BECs in microgravity to new limits.

To this end, the chapter will outline the theoretical background of collimating BECs with conservative potentials. The requirements for optimal lens performance and the most crucial parameters are presented. The peculiarities of magnetic lensing with atom chip traps, most notably higher order corrections to harmonic potentials, are discussed. The theoretical models are then contrasted with experimental data obtained in the microgravity campaigns.

6.1 BEC Dynamics in Time Dependent Potentials

The evolution of a pure BEC at zero temperature is governed by the time dependent Gross-Pitaevskii equation (GPE)

$$i\hbar\partial_t\psi(\mathbf{r},t) = \left[-\frac{\hbar^2}{2m}\Delta + V(\mathbf{r},t) + g\left|\psi(\mathbf{r},t)\right|^2\right]\psi(\mathbf{r},t), \tag{6.1}$$

where the interactions between the atoms are given by

$$g = \frac{4\pi\hbar^2 a}{m} \quad \text{with } a \approx 100a_0. \tag{6.2}$$

Here, a_0 is the Bohr radius and a the approximate s-wave scattering length for ^{87}Rb atoms. In three-dimensional harmonic confinement the potential has the form

$$V(\mathbf{r},t) = \frac{m}{2}\left(\omega_x^2(t)\,x^2 + \omega_y^2(t)\,y^2 + \omega_z^2(t)\,z^2\right). \tag{6.3}$$

To calculate the complete dynamics of the BEC in the process of magnetic lensing, (6.1) has to be solved numerically. However, some approximations can be used to study individual aspects of the collimation process. The sequence can be separated into the initial expansion of the ensemble, where the interactions between the atoms dominate the dynamics, and the lensing process where the interactions are negligible but the kinetic energy of the ensemble is relevant.

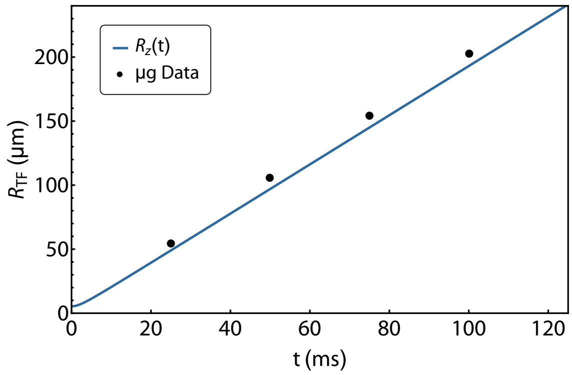

Figure 71: Free expansion of the condensate observed at different times of flight. The blue curve represents the evolution of the cloud radius in the x'-direction according to (6.12) and (6.7), while the data points are the TF radii extracted from fitting the absorption images displayed in Figure 72. The experimental data was rescaled to $N = 50000$. The expansion of the condensate appears to be underestimated since the influence of the thermal component of the ensemble is not taken into account.

When considering the initial size and expansion of the BEC, the kinetic energy term in the GPE can be disregarded and the wave function in this so called Thomas-Fermi (TF) approximation is

$$\psi(\mathbf{r},0) = \left(\frac{\mu - V(\mathbf{r},0)}{g}\right)^{1/2}, \tag{6.4}$$

where μ is the chemical potential given by

$$\mu = \frac{\hbar\overline{\omega}}{2}\left(\frac{15\,N\,a}{a_{\text{ho}}}\right)^{2/5} \quad \text{with } \overline{\omega} = \Big(\omega_x(0)\,\omega_y(0)\,\omega_z(0)\Big)^{1/3}. \tag{6.5}$$

Here, $a_{\text{ho}} = \sqrt{\hbar/m\overline{\omega}}$ is given by the harmonic oscillator ground state and the individual radii are

$$R_i = a_{\text{ho}}\left(\frac{15\,N\,a}{a_{\text{ho}}}\right)^{1/5}\frac{\overline{\omega}}{\omega_i(0)}, \quad \text{with } i \in \{x,y,z\}. \tag{6.6}$$

Thus, the initial size of the condensate is defined by the number of atoms N and the trap frequencies $\omega_i(0)$.

Once the BEC is released from its confining potential, the TF approximation is not applicable since a variation to the trapping potential converts potential to kinetic energy, which can no longer be neglected [125]. However, the TF radii $R_i(t)$ follow the classical trajectories

$$R_i(t) = R_{\text{i}}\,b_i(t) \qquad \text{with } i \in \{x,y,z\}, \tag{6.7}$$

given by the scaling parameters $b_i(t)$, as long as they satisfy the differential equations

$$b_i'' + \omega_i^2(t)\,b_i - \frac{\omega_i^2(0)}{b_i b_x b_y b_z} = 0. \tag{6.8}$$

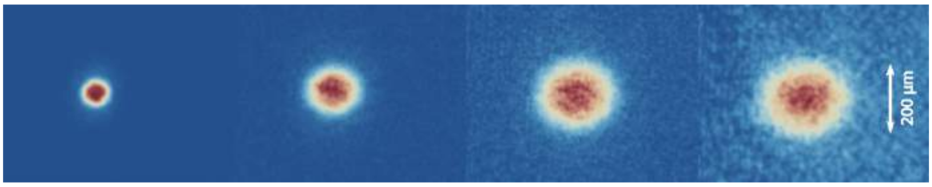

Figure 72: Four BECs observed 25, 50, 75 and 100 ms after instantaneous switch-off of the confining potential with trap frequencies (f_x,f_y,f_z)=(17.5, 54.9, 62.2) Hz. The spatial distribution of the condensates is in good agreement with the inverted parabola profile described in Equation 6.12.

Thus, the evolution of the radii is only implicitly density dependent through broadening of the initial size. Upon release through an instantaneous switch-off of the trap, the differential equations simplify to

$$b_i'' - \frac{\omega_i^2(0)}{b_i b_x b_y b_z} = 0, \tag{6.9}$$

with the common solutions

$$b_i(t) = \left(1 + \omega_i^2(0)\, t^2\right)^{1/2} \tag{6.10}$$

exploited in time-of-flight measurements [48]. They describe the free evolution of the ensemble in the time independent case (see Figure 71).

By rescaling the wave function $\psi(r_i, t) \rightarrow \tilde{\psi}(r_i/b_i(t), t)$, the variation of the potential is absorbed in the rescaling transformation, yielding a generalized version of the GPE [125]

$$\left[i\hbar\partial_t + \frac{\hbar^2}{2m}\sum_i \frac{1}{b_i^2(t)}\partial_{r_i}^2\right]\tilde{\psi}(\mathbf{r},t) = \frac{\left[-\mu + V(\mathbf{r},0) + g\left|\psi(\mathbf{r},t)\right|^2\right]}{b_x(t)\, b_y(t)\, b_z(t)}\tilde{\psi}(\mathbf{r},t), \tag{6.11}$$

to which the TF approximation can be applied. The time dependent density is then given by

$$\left|\tilde{\psi}(\mathbf{r},t)\right|^2 = \frac{\mu - \sum_i \frac{m}{2}\omega_i^2(0)\, r_i^2/b_i^2(t)}{g\, b_x(t)\, b_y(t)\, b_z(t)}, \tag{6.12}$$

which gives an approximate, analytical expression for the dynamics of a BEC in time dependent harmonic potentials that is in good agreement with cloud radii observed in absorption images (see Figure 72). Unfortunately, the scaling approach can not easily be extended to include higher order terms in the confining potential, which are highly relevant in the lensing process presented in the following section.

6.2 Magnetic Lensing

The collimation process of the ensemble can more easily be explored when the interactions are neglected and the BEC is described as a wave packet evolving from an harmonic oscillator ground state. Neglecting the interactions for this analysis is appropriate, as the density is generally reduced by orders of magnitude in the initial expansion prior to the lens. For the purpose of this discussion, the effects of the interactions are only relevant in influencing the initial size of the ensemble.

In the absence of interactions, the initial size of the BEC is defined by the width of the harmonic oscillator ground state

$$a_i = \sqrt{\frac{\hbar}{m\omega_i}}, \qquad \text{with } i \in \{x, y, z\}. \tag{6.13}$$

The corresponding wave function of the system is thus given by

$$\psi_0(\mathbf{r}) = \frac{1}{\pi^{3/4}(a_x a_y a_z)^{1/2}}\, e^{-x^2/2a_x^2}\, e^{-y^2/2a_y^2}\, e^{-z^2/2a_z^2}. \tag{6.14}$$

Once the BEC is released from its confining potential through an instantaneous switch-off, it will expand according to [130]

$$\psi_0(\mathbf{r}, t) = \frac{1}{\pi^{3/4}} \prod_i a_i^{-1/2} \left(1 + i\omega_i t\right)^{-1/2}\, e^{-r_i^2/\left[2a_i^2(1+i\omega_i t)\right]}. \tag{6.15}$$

As in the TF description, reducing the expansion rate of the ensemble is achieved by reducing the trap frequencies ω_i as much as possible before release. Decompression of the final trap appears to be a straightforward approach to cooling the ensemble. However, there are certain limitations in reducing the kinetic energy through adiabatic decompression.

In lab-based experiments, the decompression to very shallow traps is hindered by deformations of the potential due to gravity. This gravitational sag sets a lower limit for feasible trap frequencies in the direction of gravity, that has to be circumvented by compensating measures. A three-dimensional temperature of 450 ± 80 pK was reached using a gravito-magnetic trap with a mean frequency of one hertz [131]. The potential was adiabatically decompressed over ten seconds and at the expense of reducing the atom number by several orders of magnitude. An additional intermediate delay of five seconds between decompression steps was necessary to phase out excitations.

In μg, atomic clouds can in principle be decompressed to arbitrarily shallow traps. However, the required time of several tens of seconds for adiabatic decompression along with the large increase in cloud size renders this approach impractical. Together with the atom loss due to evaporation and background collisions on such timescales, a slow adiabatic decompression leads

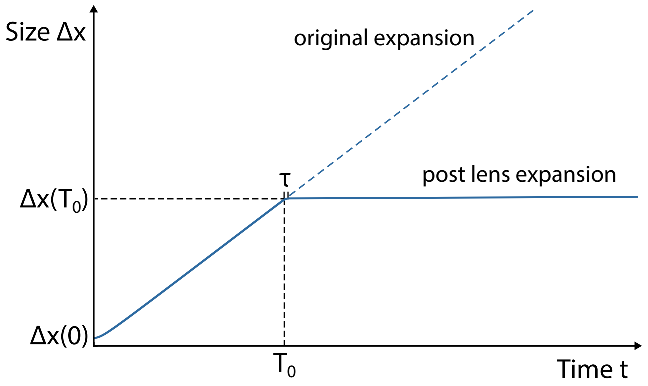

Figure 73: Time evolution of the size of the cloud during a magnetic lensing sequence. From the initial size $\Delta x(0)$, the cloud expands more rapidly in the beginning until th ballistic regime is reached. At time $t = T_0$ a lensing pulse with duration τ collimates the ensemble and almost completely diminishes the expansion.

to large, dilute clouds that are highly susceptible to excitations, magnetic field imperfection, stray fields, wave front distortions and gravity gradients. These circumstances make adiabatic expansion to picokelvin and sub-picokelvin temperatures unfeasible for our experiments and the envisioned interferometric measurements.

Instead, shortcuts to adiabaticity analogous to the methods presented in Chapter 5 can be used to reduce the expansion rates. One such method is magnetic lensing. For this technique, the atoms are released from the trap and expand according to (6.10) until a linear correlation between position and momentum is established and each atom expands ballistically according to

$$x(t) = v\,t + x_0. \tag{6.16}$$

Neglecting the initial size of the ensemble and assuming $x_0 = 0$ for all atoms yields

$$p = \frac{m\,x(t)}{t}. \tag{6.17}$$

After time T_0, the potential is switched on again for a brief time τ, changing the momentum of each atom by

$$\Delta p = -\frac{dV}{dx}\,\tau = -m\omega^2 x(T_0)\,\tau. \tag{6.18}$$

The momentum kick is proportional to the current position $x(T_0)$ of each atom and with appropriate pulse timing such that

$$\tau\,T_0 = \omega^{-2}, \tag{6.19}$$

all atoms should receive a kick equal but opposite to their current momentum and ideally be at rest after the procedure (see Figure 73). The degree to which (6.19) can be fulfilled for an ensemble of atoms hinges on several key conditions:

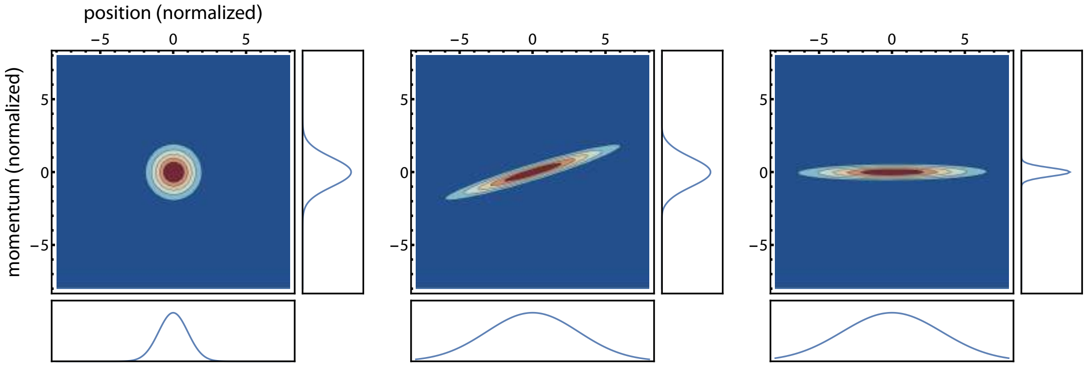

(a) Initial distribution ($t = 0$) (b) After free expansion ($t = T_0$) (c) After the lens ($t = T_0 + \tau$)

Figure 74: Phase space evolution during a magnetic lensing sequence with harmonic potential. The initial expansion of the ensemble causes a phase space shear, broadening the spatial distribution while leaving the momentum distribution unchanged. Then, applying the lensing potential causes a clockwise rotation of the phase space distribution until the momentum width is minimized.

I. The influence of interactions can be neglected and a linear correlation between position and momentum is reached.

II. The initial size of the ensemble is small enough to be neglected.

III. The lensing potential is harmonic at all times over the spatial extend of the cloud.

IV. The cloud and the lensing potential are concentric.

To explore these restrictions and the influence of their violation, the lensing process can be visualized in phase space.[1] Without interactions, the dynamics of the system in phase space are identical to the dispersion of a wave packet and its shape and spread can be described classically according to the Ehrenfest theorem.[2] We can thus illustrate the phase space distribution by the Liouville density function where the width of the distribution are given by $|\psi(x,t)|^2$ and $|\phi(p,t)|^2$ [133].

In the following examples, the size of the wave packet evolves according to

$$\Delta x(t) = a\sqrt{1 + \frac{c^2 t^2}{m^2 a^2}} \quad \text{and} \quad \Delta p(t) = c, \tag{6.20}$$

---

[1] Alternatively to the classical phase space picture, a quantum description of the phase space dynamics with Wigner functions can be used [132].

[2] The Ehrenfest theorem states that the expectation values for position and momentum obey Newton's classical equations of motion.

and the initial width a and c are given by (6.13) and $c = \hbar/a$. During free expansion, the dispersion of the momentum distribution Δp stays constant while the spatial dispersion $\Delta x(t)$ increases with time due to classical phase space shear (see Figure 74b). The shearing invokes a linear correlation between position and momentum, which is a fair assumption as long as no external forces act on the wave packet. Thus, in this example condition **I** is fulfilled by definition. In a practical scenario this can be achieved by sufficient free expansion from a point source, which in turn relays the restriction onto the initial size of the ensemble, i.e. condition **II**.

After some time of free evolution, the magnetic lens is applied and the momentum distribution is altered according to (6.18). The momentum shift results in a rotation of the phase space distribution around the origin until the width of $|\phi(p,t)|^2$ is minimized (see Figure 74c). Hence, the final width and effective temperature depend on the amount of cloud shearing before the lens. Since the phase space density is conserved during rotation, the lensing sequence trades off spatial dispersion for momentum dispersion and the final effective temperature is given by

$$T_f = \left(\frac{\Delta x(0)}{\Delta x(T_0)} \right)^2 T_i, \tag{6.21}$$

where T_i is the initial effective temperature [134]. This expression quantifies the influence of a finite initial width on the temperature reduction (condition **II**).

6.3 Velocity Spread and Effective Temperatures

The velocity spread of an atomic ensemble is often expressed as the temperature of the cloud. A classical gas in thermal equilibrium follows the Maxwell-Boltzmann velocity distribution

$$f(v_x, v_y, v_z) = \left(\frac{m}{2\pi k_\mathrm{B} T} \right)^{3/2} \exp\left[-\frac{m(v_x^2 + v_y^2 + v_z^2)}{2 k_\mathrm{B} T} \right], \tag{6.22}$$

with the individual variances

$$\sigma_{v_x}^2 = \sigma_{v_y}^2 = \sigma_{v_z}^2 = \frac{k_\mathrm{B} T}{m} \tag{6.23}$$

and total variance

$$\sigma_v^2 = \sigma_{v_x}^2 + \sigma_{v_y}^2 + \sigma_{v_z}^2 = \frac{3 k_\mathrm{B} T}{m}. \tag{6.24}$$

Thus, if the the velocity spread given by σ_v is known, it can directly be converted to the thermodynamic temperature T. After release from the trap, the atomic cloud features a Gaussian spatial distribution, whose variance $\sigma_{r_i}^2$ along each axis is related to the in situ temperature via

$$k_{\mathrm{B}}T = \frac{m\omega_i^2}{1+\omega_{r_i}^2 t_{\mathrm{TOF}}^2}\,\sigma_{r_i}^2 \quad \text{with } i \in \{x, y, z\}, \tag{6.25}$$

where ω_i^2 are the release trap frequencies [48]. Once the ensemble has reached the ballistic regime, the temperature can be interfered from the slope of the expansion via

$$k_{\mathrm{B}}T = \frac{m\,\Delta\sigma_{r_i}^2}{\Delta t^2}. \tag{6.26}$$

After free expansion, interactions within the ensemble diminish and the equilibrium state is suspended. Thus, the atomic cloud does not feature a thermodynamic temperature. This is especially relevant after the manipulation of the momentum distribution through magnetic lensing, where the inferred temperatures after the process do not relate to the in situ temperature prior to release. In these cases, the expansion rate of the ensemble is often expressed as an equivalent effective temperature or kinetic temperature that is not to be confused with the thermodynamic property.

The velocity distribution of a BEC does not follow the Maxwell-Boltzmann statistic and the BEC features a parabolic shape instead of the Gaussian profile of the thermal cloud. Thus, the size of the ensemble is given by the TF radii R_i instead of the σ_{r_i}. While the TF radii define the outer edges of the cloud, the spatial width used for temperature conversion via (6.25) and (6.26) is defined by the spatial variance of the sample. Thus, to compare the velocity spread of a BEC to that of a thermal ensemble, one has to compare the variances σ^2 of the respective distributions $P(x)$, which are given by

$$\sigma^2 = \int dx\; P(x)(x-\mu)^2, \tag{6.27}$$

where μ is the mean of the distribution and can be neglected in this case. Thus, the variance of the spatial TF distribution for each direction is given by

$$\sigma_{R_i} = \frac{R_i}{\sqrt{7}} \approx 0.378 R_i, \tag{6.28}$$

and a thermal velocity spread derived from σ_{r_i} should be compared to σ_{R_i}. Using (6.28), an effective temperature can also be ascribed to the BEC via (6.25) and (6.26) with the same caveats expressed above.

In contrast to the thermal ensemble, a BEC released from an anisotropic trap features different expansion rates along the different spatial axes, which depend on the number of atoms and the respective trap frequency. Therefore, the three spatial directions feature independent effective temperatures. The three-dimensional velocity spread and effective temperature of the BEC is given by the sum of the individual variances, just like in the thermal case. Furthermore, the expansion of the BEC explicitly depends on the atom number. Thus, smaller ensembles will feature a smaller velocity spread and effective temperature and the atom number should always be stated as reference.

6.3.1 Anharmonicities

The lens dynamics change drastically upon the introduction of higher order terms to the potential, i.e. violations of condition **III**:

$$V(x) = \frac{m}{2}\omega^2 x^2 + \frac{m}{3}\frac{1}{L3}\omega^2 x^3 + \frac{m}{4}\frac{1}{L4}\omega^2 x^4, \tag{6.29}$$

where $L3$ and $L4$ are scaling factors for the relative strength of the anharmonic corrections.

Previous evaluations of the effects of anharmonicities and their impact on high-precision measurements have been focused on keeping the influence of aberrations smaller than the final momentum spread, i.e. retaining the parabolic shape of the condensate [8, 135]. This discussion deals with realistic chip potentials that are inherently anharmonic and cause distinct cloud deformations. The phenomenology of anharmonic lenses, their repercussions for the phase space distribution of BECs and tools to limit the influence of aberrations on the overall velocity spread of the ensembles are reviewed.

While the anharmonicities observed in chip traps can usually be tolerated in the initial trapping potential due to the small size of the cloud in the trap, they are of great concern in the lensing potential because of the large spatial extend that is desirable according to (6.21). Figure 75 illustrates the lens dynamics with cubic and quartic corrections, bending the edges of the ellipse away from the $p = 0$ axis. Initially, the influence of such deformations are only visible in the momentum distribution. Only after time of flight do they appear as deformations in the spatial shape of the cloud.

In the cubic case, the asymmetry in the potential leads to both edges of the ellipse being bend in the same direction in momentum space (see Figure 75a). Hence, the resulting tails in the spatial distribution move in the same direction with one passing through the center of the cloud. During this time, the cloud initially appears to shrink in width and subsequently expand again, thus feigning a focus of the cloud (see Figure 77). If the lensing sequence is experimentally optimized to collimate the cloud, one would indeed be compensating a false focusing effect at first. Therefore, it is advisable to optimize the collimation in the far field. Generally, the collimation time given by (6.19) is still the optimal lens duration and leads to the smallest final velocity spread. However, even in the far field picture the central feature of the cloud is smaller in width than in the harmonic case (see Figure 79a and Figure 79b). This stems from the fact that

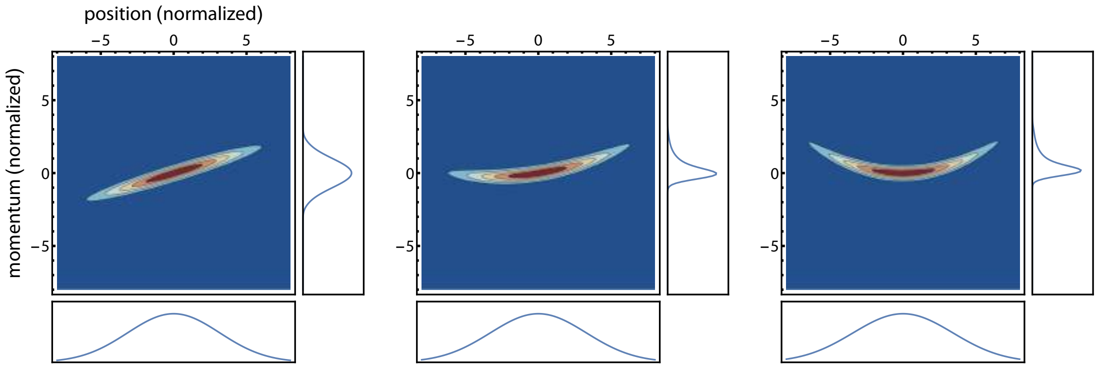

(a) Time series of a magnetic lens with **cubic anharmonicity**. From left to right: Distribution after initial expansion ($t = T_0$), halfway through the lens ($t = T_0 + \tau/2$) and after the lens ($t = T_0 + \tau$).

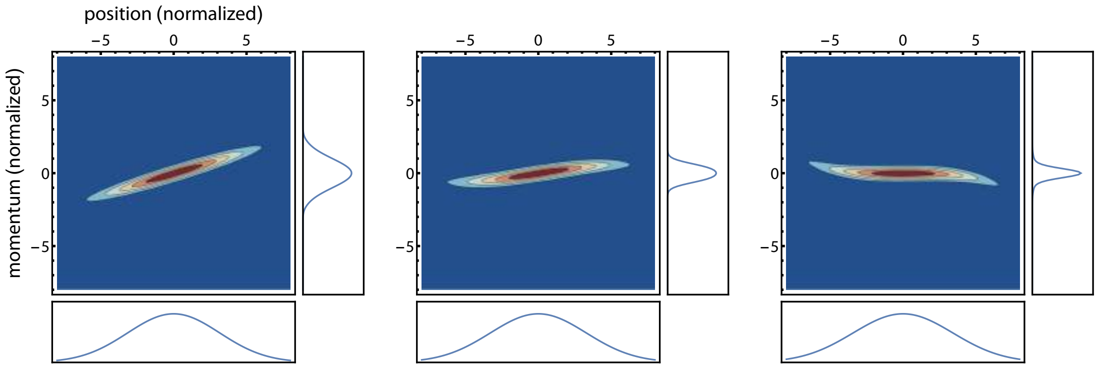

(b) Time series of a magnetic lens with **quartic anharmonicity**. From left to right: Distribution after initial expansion ($t = T_0$), halfway through the lens ($t = T_0 + \tau/2$) and after the lens ($t = T_0 + \tau$).

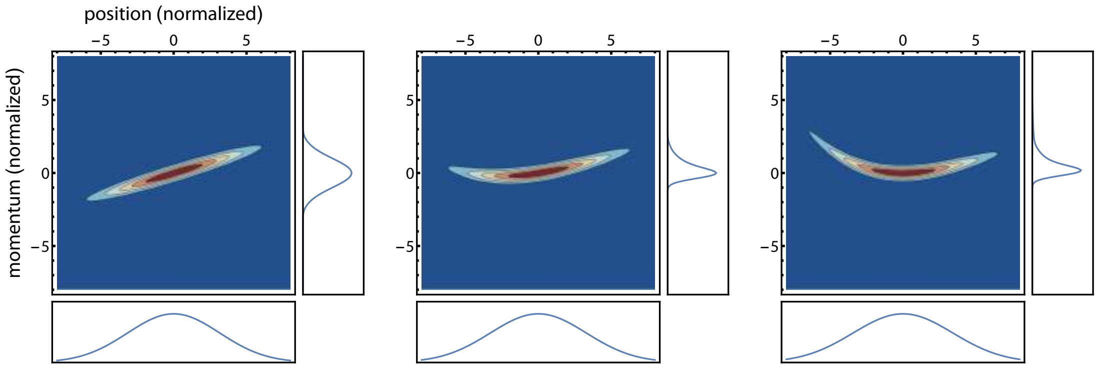

(c) Time series of a magnetic lens with **cubic and quartic anharmonicity**. From left to right: Distribution after initial expansion ($t = T_0$), halfway through the lens ($t = T_0 + \tau/2$) and after the lens ($t = T_0 + \tau$).

Figure 75: Evolution of the phase space distribution during anharmonic lensing pulses. The deformations of the potential bend the edges of the distribution due to non-uniform rotation. Cubic aberrations bend both edges in the same direction in momentum space while quartic aberrations accelerate these atoms in opposite directions. When combined, the contributions amplify each other on the left edge and counteract each other on the right.

Figure 76: Comparison of the lensing potential with and without anharmonicities. The scaling factors $L3$ and $L4$ for the anharmonicities used in the phase space simulations were rescaled to reflect the distortion in the lensing potential used in the BC-SC-lens. The anharmonicities lead to steeper potential towards the atom chip. On the other side of the trap minimum, cubic and quartic contributions counteract each other and cause a relatively flat progression.

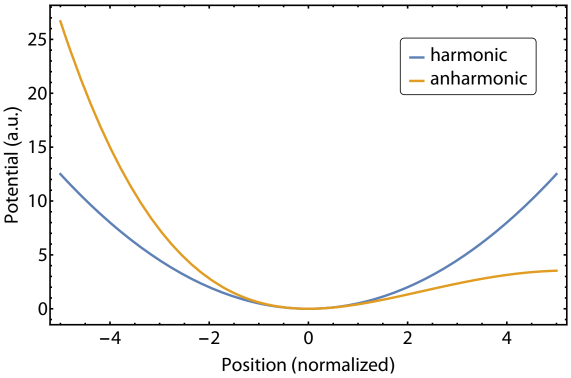

Figure 77: Time evolution of the radii obtained from fitting the central feature of the spatial distribution. The anharmonic lens initially causes a steep decrease in spatial width. This false focus is a result of one of the edges of the cloud passing the central feature in the phase space distribution (see Figure 79). Afterwards, the central peak features a steeper slope than in the harmonic case and thus the effective temperature is negatively impacted by the anharmonicities.

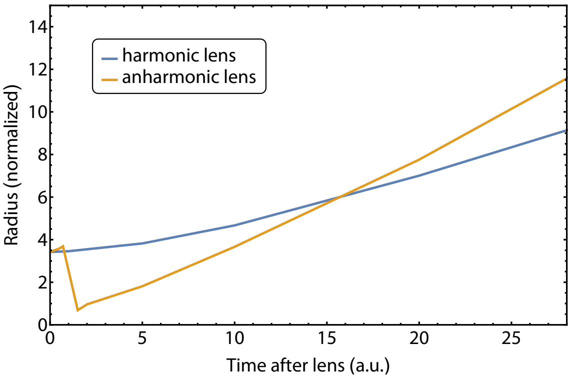

atoms on the edges of the distribution are accelerated relative to the cloud center, which can be considered a velocity selection effect. Thus, in the far field picture the cubic corrections lead to a pronounced peak of very cold atoms with a dilute tail that is constantly expanding away from the cloud.

The quartic anharmonicity in the lens potential bends the edges in opposite directions, resulting in two symmetric tails in the spatial distribution (see Figure 75b), evolving in opposite directions. The evolution of the spatial profile displays a much simpler dynamic, with a central peak whose width is steadily broadened by residual shearing and two symmetric wings moving towards and through the center of the cloud. The focal broadening observed in the wings is analogous to spherical aberrations in conventional optics, where the focal point of light rays depends on the distance from the lens center. In conventional optics, such aberration effects are commonly suppressed by manipulation of the lens curvature, for example through the use of aspheric lenses. Unfortunately, the curvature of the lensing potentials used in our experiments can not be manipulated arbitrarily.

The realistic potentials encountered in experimental lensing attempts prominently feature both cubic and quartic anharmonicities (see Figure 76). The cubic corrections are the dominant effect in any available trap configuration generated by the atom chip setup. However, the exact

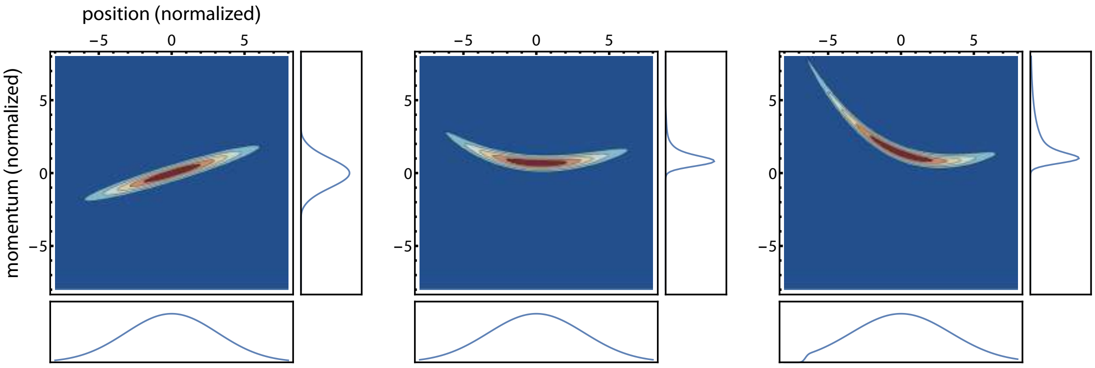

Figure 78: Phase space density distribution during an anharmonic lensing pulse with position offset relative to the condensate. From left to right: Distribution after initial expansion ($t = T_0$), halfway through the lens ($t = T_0 + \tau/2$) and after the lens ($t = T_0 + \tau$). The offset in combination with the anharmonicities significantly alters the final distribution and the state defined by the harmonic collimation condition (6.19) no longer features the narrowest momentum distribution.

ratio of the scaling factors $L3$ and $L4$ depends on the wire configuration, field strength and distance from the chip surface. Together, the cubic and quartic terms provoke a phase space distribution with asymmetric tails, since their effects are equal on one edge of the cloud and opposite on the other (see Figure 75c).

The distortions of the spatial distribution from anharmonic lensing potentials also depend on the position offset between the potential minimum and the cloud center (condition **IV**). In the harmonic case, such an offset merely translates to a COM motion of the ensemble without altering the shape of the cloud. However, in the anharmonic case the lensing action is changed since the potential is significantly steeper in one direction and shallower in the other (see Figure 78). Thus, if the anharmonicities given by $L3$ and $L4$ are constant over the region of interest, their influence is decreased or increased depending on the sign of the offset and of the anharmonicities. The spatial distribution after time of flight changes significantly in the presence of field distortions, even for small offsets. Figure 79c shows the initial time evolution of the phase space distribution after an anharmonic lens with a position offset equal to two times the insitu cloud radius. While the spatial profiles initially appear similar in comparison to a concentric lens (see Figure 79b), the long term evolution of the distribution looks very different. The considerably larger tail in the momentum profile causes the distribution to roll over and spread out substantially after some time. Figure 78 suggests that in the presence of a position offset, the collimation could be improved by varying the lens strength or duration. However, the exact position of the cloud is subject to position scatter explored in Chapter 5.

The added complexity stemming from the anharmonicities is not only detrimental to the final shape of the ensemble but also to the experimental optimization of the lens. The absorption images of the BECs contain information about the spatial profile but not the full phase space distribution. In the case of a harmonic lens, collimation is verified by maintaining a certain width and quantifying the residual spreading of the ensemble. In the presence of aberrations, the desired evolution of the cloud radius can be indistinguishable from a simple focus of the lens. Furthermore, the collimation condition is only a rough estimate for proper collimation as the effective lens strength depends on the particular position offset. While the tail of the spatial distribution could potentially aid in analyzing the dynamics, its extend is unreliable since the population of the tail also depends on the position offset. Additionally, the density of the cloud varies with the atom number in the experiment and parts of the tail may be masked by the density limit of the absorption imaging process.

6.3.2 Mitigation Strategies

Depending on the shape and origin of the distortion to the potential, the anharmonicities permit different mitigation strategies. However, simply suppressing deformations through limiting the cloud size during expansion and lensing is not feasible. The distortions of the potential tend to decrease with distance from the chip structures. Hence, one strategy that is being explored is to move the atoms to a distant trap configuration in the hopes on limiting the anharmonicities (see Chapter 5). However, the Biot-Savart simulations of the chip potentials only predict a moderate decrease in lens aberrations with distance and complementary strategies may be necessary.

One general mitigation strategy is to manipulate the overall field curvature with additional current carrying structures. The atom chip offers an abundance of wire structures that are part of the magnetic field simulation and their usefulness can thus be investigated theoretically. However, there is no straight forward way to resolve the cubic distortion to the potential since it stems from the field decay over distance, which is common to all chip structures. In the future, additional structures may be added to the experiment for just that purpose. The current atom chip setup was not designed specifically do deal with lens aberrations but future designs could be.

Analogue to conventional optics, symmetric distortions proportional to$L4$ can be alleviated by a series of lenses [132]. To this end, a defocussing lens can be realized through m_F state manipulation (see Chapter 3), effectively inverting the lensing potential. In such a sequence, a longer initial expansion is followed by the first lensing pulse that is focusing instead of collimating the cloud. Hence, the phase space shear is reverted in the following free evolution and the spatial width decreases while approaching the focal point. After some time, a second lens with inverted field properties causes a counter-clockwise rotation in phase space to collimate the cloud. The sequence can be designed such that the final state matches the simple collimation case depicted in

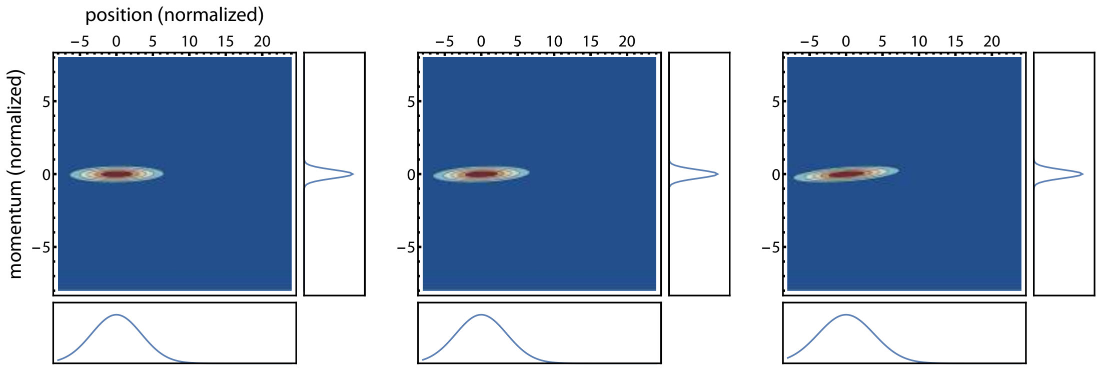

(a) Time series of the **free expansion after a harmonic lens**, starting from $t = T_0 + \tau$.

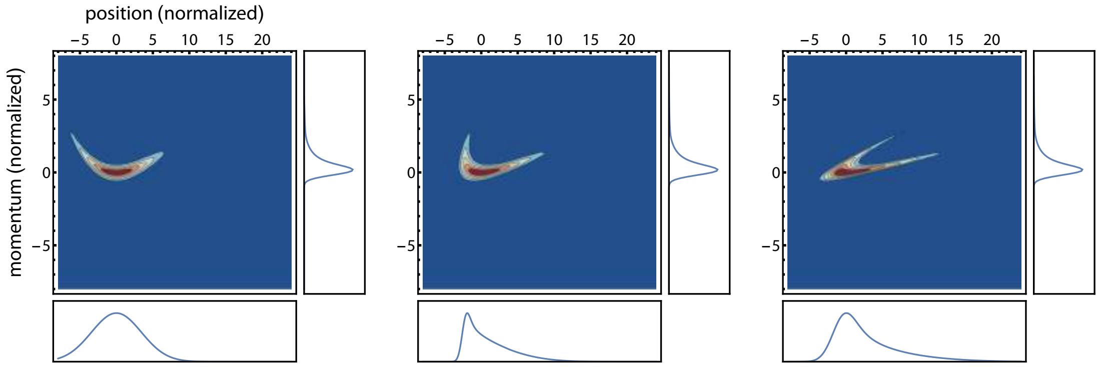

(b) Time series of the **free expansion after an anharmonic lens**, starting from $t = T_0 + \tau$.

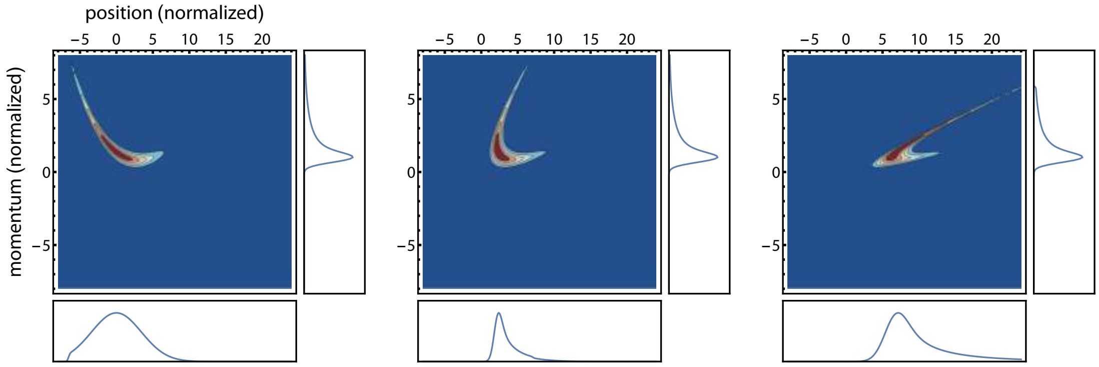

(c) Time series of the **free expansion after an anharmonic lens with position offset**, starting from $t = T_0 + \tau$.

Figure 79: Time evolution of the phase space density distribution after magnetic lensing pulses. Figure (a) shows the time evolution after a harmonic lens. Figure (b) depicts the same time series after magnetic lensing with cubic and quartic anharmonicities. Figure (c) illustrates the evolution after the same anharmonic lens with position offset. The spatial distributions of the clouds after the anharmonic lenses show a drastic reduction in width of the central feature. Thus, despite satisfying the collimation condition the clouds appear to feature a focus. The position offset of the lens significantly changes the time evolution of the ensemble.

Figure 74c. The lensing sequence is equivalent to an Galilean telescope in conventional optics with one convergent and one divergent lens. Due to the symmetry of the aberrations, the telescope scheme can reduce the distortions stemming from the tails of the phase space distribution.

In summary, anharmonicities in conjunction with a position offset can lead to erratic behavior of the phase space distribution. This causes significant problems in the analysis and optimization of the collimation process. Detailed simulations of the phase space dynamics are necessary to model the cloud deformations. Useful mitigation strategies such as a matter-wave telescope are being explored theoretically for future implementation in the microgravity campaigns. Quantitative three-dimensional simulations of the time evolution before, during and after the anharmonic lenses are necessary to further the understanding of the effects of distortions in high-precision interferometric measurements.

6.3.3 Experimental Implementation

As in the theoretical examples in Section 6.2, the lensing potential is often identical to the trapping potential. Depending on the trap configuration, the potential is generated by up to six current carrying structures: the meso-H, the base chip, the science chip and the three bias coils (see Chapter 3). In contrast to the theoretical derivations, the lens does not necessarily require the full trapping potential. Instead, it is usually scaled down via the applied currents and the action of the lens can be adjusted using three parameters: the time of initial expansion T_0, the lens scaling factor and the lens duration τ. The latter two comprise the pulse shape of the lens.

The Ioffe-Pritchard type trapping and lensing potentials generated by the atom chip share some common characteristics such as the cigar-shaped field geometry. Two spatial directions have very similar trap frequencies while the third direction features relatively shallow confinement. Hence, there is no straightforward approach to collimate the atomic cloud in all three dimensions using the same field geometry. Not only do the collimation conditions differ for the three directions, the required initial expansion time to achieve the same final expansion rate also varies.

With careful selection of the lensing potential, the collimation problem can be reduced from three to two dimensions (see Table 9). Hence, the cloud can in principle be collimated in both those direction with a single cylinder-type lens.

Due to the large asymmetry, the third axis will barely be influenced by collimating any or both of the others. A one-dimensional cylinder-type lens using wire structures perpendicular to the middle wire of the previous lens could be used to collimate the third axis independently. Due to the shallowness of the potentials at greater chip distances, the expansion into a shallow trap configuration would lead to a temperature reduction below one nanokelvin even without lensing. However, temperatures in the low picokelvin range are difficult to achieve in this manner.

Table 9: Comparison of the lens attributes and parameters used in the microgravity campaigns. The BC-lens is distinguished by the lower trap frequencies, the cylindrical symmetry and reduced anharmonicities given by the distortions coefficients $1/L3$ and $1/L4$.

Lens	Full Potential (Hz)	Scaling	$L3$ (μm)	$L4$ (μm^2)	Pulse shape	T_0	τ
BC-SC	17.5, 54.9, 62.2	0.244	368	582 576	Gaussian	30 ms	6 ms[+]
BC	5.5, 22.5, 22.5	0.3	868	3 672 900	Box	80 ms	2.64 ms

[+] The exact pulse shape is given by (6.30).

6.4 Magnetic Lensing in Microgravity

The drop tower campaigns concerned with the implementation of magnetic lensing in μg are split in two parts. In the first part, a BC-SC-lens is used at an intermediate chip distance of approximately 0.8 mm. The trap properties as well as the transport towards this location have been investigated extensively in dedicated μg campaigns described in the previous chapter. Since the residual dynamics of the ensemble after transfer are well controlled and understood, lensing with the BC-SC potential enables the study of magnetic lensing without interference from unwanted phenomena originating in the transport. The goal of these first lensing attempts is to test the experimental implementation of the lens and replicate the results of the collimation process with simulations. Consequently, the actual performance of the lens in terms of the final effective temperature of the ensemble is a secondary concern.

The second part of the magnetic lensing campaigns is the realization of a BC-lens at greater chip distance of approximately 1.5 mm. The properties of the lensing potential that can be generated at this location are generally more conducive to realize useful lens topologies. The similarity in two of the three trap frequencies in principle enables the collimation along two dimensions. Additionally, the more remote BC-lens features distortions coefficients $1/L3$ and $1/L4$ which are reduced by a factor of 2.4 and 6.8, respectively. The downside of the lens location is the more sophisticated transport protocol and the susceptibility of the trapping potential to excitations. The goals of the BC-lens are the realization of two-dimensional collimation, demonstration of the reduced influence of anharmonicities, achieving simpler experimental implementation of the lensing pulse and mitigation of many of the observed issues in the BC-SC-lens such as rotation and translation of the lensing potential. The parameters for both lens configurations are summarized in Table 9.

The analysis of the lens dynamics through absorption images is a complicated task for several reasons. First, the images display the spatial distribution at the time of the measurement but do not grant direct insight into the momentum distribution. The shape of the momentum distribution and hence the effective temperature of the ensemble can only be deduced from the evolution of the spatial profile. Second, the primary detection setup (see Chapter 2) images the projection of the atomic cloud on a two-dimensional plane. One axis of the projected image corresponds to the z-axis pointing away from the atom chip. This is the direction that features significant distortions from amharmonicities. The other axis of the images is a projection of the two other geometric axes (x and y) at a 45 degree angle. If the ensemble is rotated relative to the coordinate system due to a rotation of the trapping or lensing potential the effective angle changes accordingly. Consequently, with the primary imaging setup only the z direction, which features significant distortions, can be observed unobstructed and without ambiguity.

To resolve some of these issues, a secondary imaging system was added to the apparatus during the later stages of the campaigns. While the quantitative characterization is still pending, it serves to show the approximate size and aspect ratio of the ensemble from an alternative perspective. Due to the interference of both imaging setups, the following absorption images were acquired with only one camera in operation at a time.

6.4.1 First Results

The first lensing attempts were used to test pulsing the lens potential, investigating the influence of the lens on the COM dynamics and estimating the severity of the field distortions. For the first few drops, a sigmoid-type ramp was used to switch on and off the lensing potential over 6 ms after a short initial expansion of 20 ms. The absorption images show a significant reduction in size compared to free evolution (see Figure 80). The profile in the z-direction in Figure 80b seems barely distorted 50 ms after the lensing pulse. However, 300 ms after the lens the spatial distribution features a prominent tail in the z-direction (see Figure 80c). The observations mirror the dynamics encountered in the phase-space simulations. Initially, only the momentum distribution is distorted by the anharmonicities. Then over time, the distortions transfer to the spatial distribution (Figure 79b). These findings substantiate the assertion that the anharmonicities can not be alleviated by limiting the cloud size and sampling a smaller volume of the potential as even shorter initial expansion times are not feasible.

6.4.2 BC-SC-Lens

The BC-SC-lens is generated by a scaled down version of the release potential, using the Base-Z, the Science-Z, the x-coil and the y-coil. While the x-coil current stays constant during the lens, the other components are all expected to drive the same Gaussian waveform

$$f_{\text{Gauss}}(t) \propto \exp\left[-\frac{(t - T_0 - \tau/2)^2}{2(0.11774\,\tau)^2}\right] \tag{6.30}$$

to maintain the aspect ratio over the duration of the pulse. Since the structures vary in there inductivity and current response, the slower structures such as the$y$-coil are each driven by an

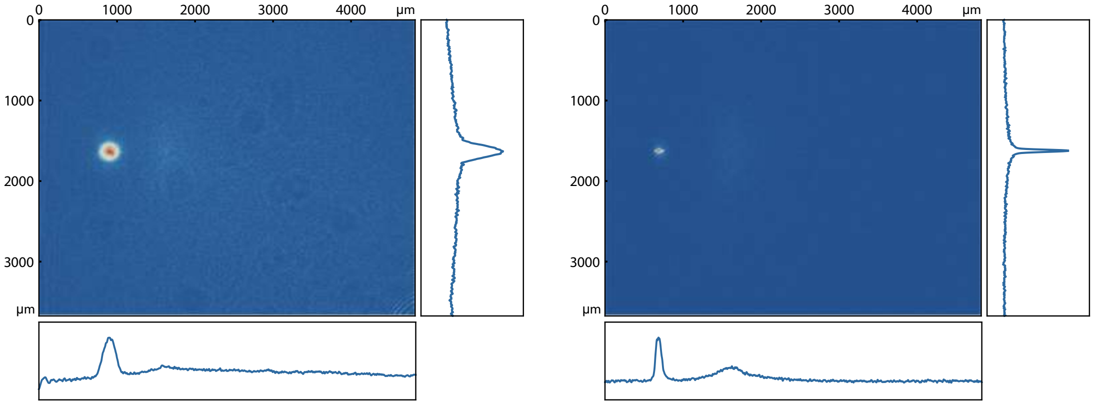

(a) A freely expanding BEC after 75 ms TOF (Drop #23c).

(b) A BEC after lensing ($T_0 = 20\,\text{ms}, \tau = 6\,\text{ms}$, Sigmoid) and 50 ms TOF (Drop #61a).

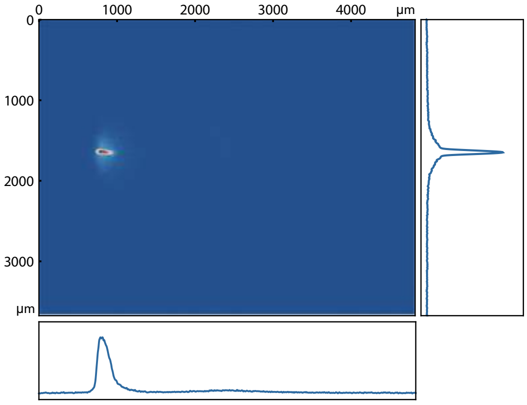

(c) A BEC imaged 300 ms after lensing (Drop #65a).

Figure 80: Size and shape comparison between lensed clouds and a freely expanding BEC. Figure (a) and (b) show absorption images after similar TOFs. Guided by the scaling approach simulations, a pronounced reduction of the expansion rate was achieved straightaway. The cloud shape after lensing in figure (c) develops a distinct tail in the $x'(z)$-direction, as expected from the phase space simulations.

adjusted pulse that was calculated by using the characteristic step response of the structure to obtain the same Gaussian current response for all structures.

The field response to the currents is given by the scaling functions obtained from the Biot-Savart simulations of the chip potential (see Figure 81). These functions give the harmonic trap frequencies along the eigenaxes of the trap for a current scaling from zero to one, where the latter corresponds to the release trap (see Figure 81a). Unfortunately, the trap axes feature some rotation in respect to the geometrical axes at low current scalings. This causes a rotating lens in the reference frame of the atoms and alters the scaling functions accordingly (see Figure 81b). Hence, which one of the directions experiences a stronger lensing effect depends on the maximal lens scaling, pulse shape and duration.

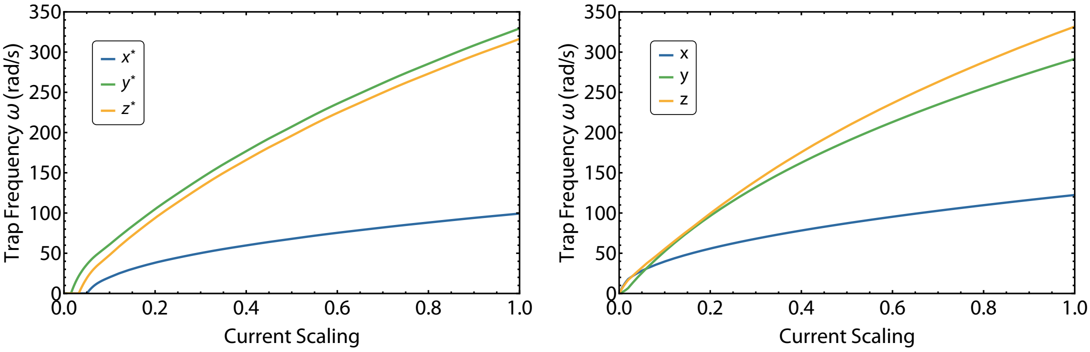

(a) Trap frequencies ω over current scaling in the eigensystem of the trap.

(b) Trap frequencies ω over current scaling along the geometrical axes.

Figure 81: Scaling functions for the trap frequencies over the scaled currents extracted from Biot-Savart simulations of the chip potential. The frequency scalings in figure (a) were derived from a harmonic fit of the potential in the eigensystem of the trap. Figure (b) shows the same scalings in the geometric reference frame.

The effective lens pulse along the geometric axes for a maximal current scaling of 0.244 is illustrated in Figure 82. Generally, the action of the lens is a cumulative effect and thus independent of the pulse shape. However, since the deviations from the input waveform, the rotation of the lens and the hierarchy of the trap frequencies are not independent of the current scaling, the exact pulse shape can have a significant influence on the lens dynamics. An additional concern is that the actual field response as experienced by the atoms may be distorted due to eddy currents induced by the lens pulse. Thus, the manipulation of the ensemble could potentially also depend on the pulse duration.

Using the scaling approach (6.7) and (6.8) with the realistic scaling functions from Figure 81b, two BC-SC-lens sequences are contrasted in Figure 83. The lens on the left is designed to collimate the z-axis, while the one on the right attempts to collimate the y-axis. Both lenses use a Gaussian pulse shape with 6 ms duration and an initial expansion time of $T_0 = 30$ ms. All examples are rescaled to an atom number of $N = 50000$. Even though the trap frequency of the two directions are very similar, the proper lens scaling differs significantly. Additionally, it is evident from Figure 83b, that the dynamics of the radii are interdependent and a focus in any direction distorts the evolution of the others. The expected time evolution of the radius in such a case is not at all intuitive and the optimization process needs to be guided by reliable simulations. Despite the fact that the findings of the scaling approach simulations can not directly be applied to all directions due to the anharmonicities, they are still a fast and convenient tool to identify the proper collimation conditions and theoretical temperature limits.

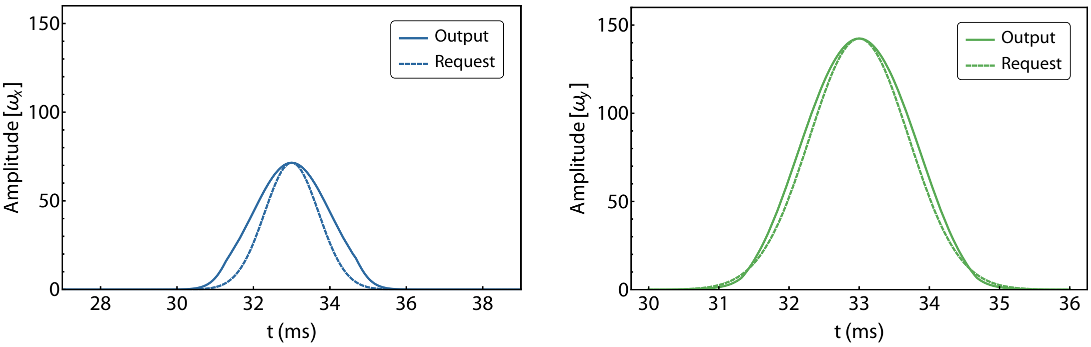

(a) Field response in x-direction.

(b) Field response in y-direction.

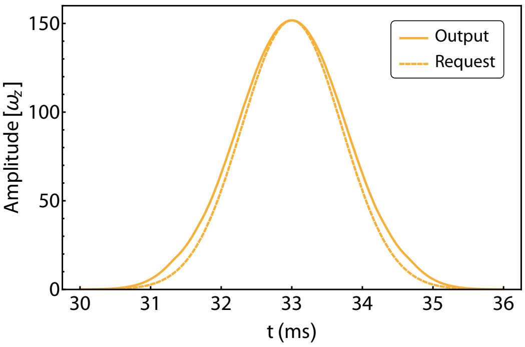

(c) Field response in z-direction.

Figure 82: Calculated field response of the BC-SC-lens in comparison to the Gaussian request function in x-, y- and z-direction. Due to the rotation of the lens at low current scalings the effective lens pulse (solid lines) shows significant deviations from the input waveform (6.30) (dashed lines). Consequently, the pulse shape of the lens can noticeably alter the lens dynamics. The lens parameters are given in Table 9.

From the evolution of the TF-radii in dependence of the lens duration, the lens scaling and the time of initial expansion T_0, limits for the velocity spread and effective temperature can be estimated. In comparison to Figure 83a, Figure 84 shows different lenses scaled to optimally collimate the cloud in the z-direction after varying times T_0. The effective temperature is calculated from the linear slope after five seconds of free evolution. For a relatively short initial expansion of 15 ms, the lens pulse acts on the cloud before it has reached the ballistic regime and the time evolution of the cloud radius features significant curvature. The lower limit for the effective temperatures is 4.83 pK, one hundred times higher then after a 30 ms initial expansion. Figure 84b shows negligible residual curvature and the lens allows for a lower temperatures limit of a few femtokelvin (if anharmonicities can be neglected). Extending the free expansion phase to 50 ms simultaneously increases the radius of the ensemble to over100 µm. Hence, the appropriate value of T_0 depends on the maximal tolerable size of the cloud and the influence of anharmonicities in the lens potential that are being sampled.

Since only one main axes can be observed directly and this axis features the highest trap frequency, the first lensing attempts aimed at collimating the$z$-direction and consolidating the chip and lens simulations with the experimental results. Matching the collimation condition

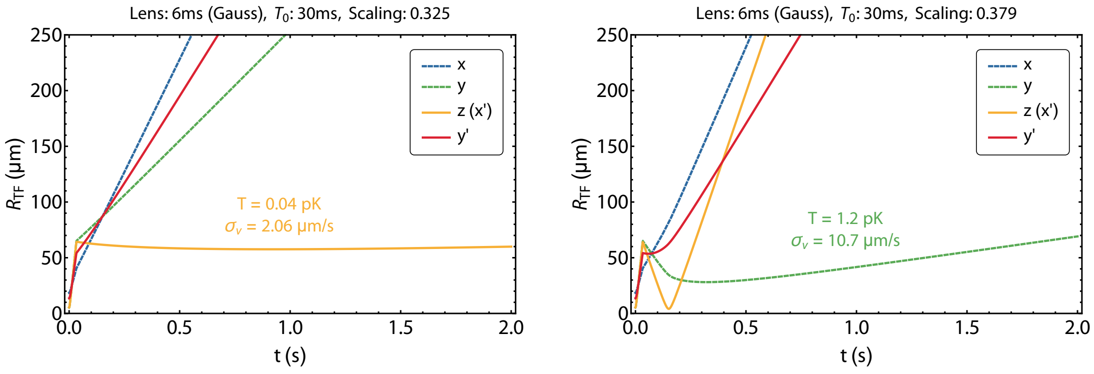

(a) Lens parameters for z-collimation.

(b) Lens parameters for y-collimation.

Figure 83: Lens pulses optimized to collimate the two steep trap axes with a BC-SC-lens. These lens schemes represent the lowest possible one-dimensional temperatures achievable with the first experimental lensing sequence. Figure (b) exemplifies the strong interdependence of the individual axes as the evolution of the y-radius is warped significantly by the focus in the z-direction.

in the z-direction is difficult due to the cloud tail. Hence, the following analysis is based on the size of the prominent central feature. While this procedure excludes the tail, the expansion rate of the central peak is a true effective temperature with the only caveat that the temperature reduction can not solely be attributed to the lens but also to velocity selection.

Unfortunately, analyzing and optimizing lens dynamics is difficult in both imaging directions. As discussed above, the cloud shape in the z-direction noticeably distorted by the anharmonicities. The y'-direction is initially difficult to interpret because, for example, a focus of the cloud along the y-axis would be masked by the larger width along the x-direction. Additionally, the lens rotates in the $x - y$ plane at low lens scalings, thus rotating the cloud. This effectively alters the projection angle, which can not be determined from the images of the primary detection setup. However, after the addition of the second imaging apparatus, the measurement campaigns were augmented with absorption images from other perspectives that grant insight into the angle of the cloud after the lens.

The rotation rate of the $x-y$ axes depends on the strength of the additional bias field provided by the x-coil that defines the trap bottom offset field. Reducing the x-coil current during the lens theoretically reduces the rotation but experimentally it significantly changes the observed lens dynamics (see Figure 85a). While the comparison yields different cloud angles at lower bias fields, an unwanted rotation of the cloud was still present. Thus, in the following results the current was maintained at 0.5 A until the effects of the rotating lens can be simulated and are well understood theoretically.

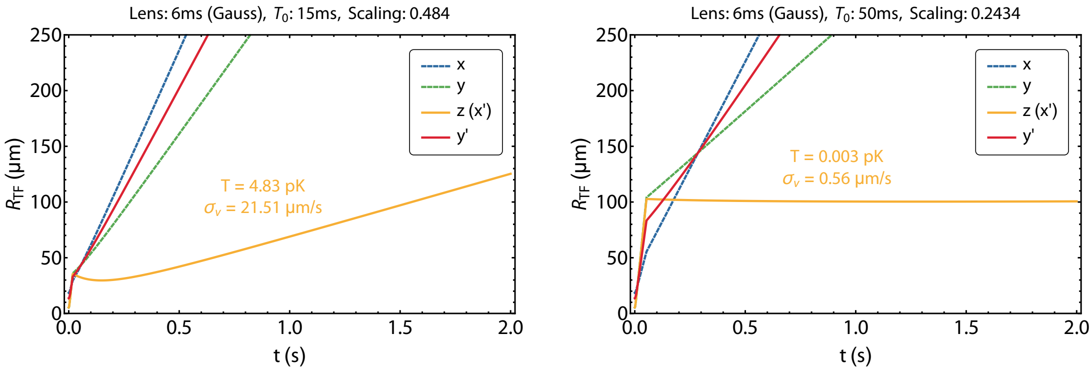

(a) Optimal z-collimation with $T_0 = 15$ ms.

(b) Optimal z-collimation with $T_0 = 50$ ms.

Figure 84: Comparison of optimal z-collimation conditions for different values of T_0. After release from the BC-SC trap configuration, an initial expansion of15 ms leads to a theoretical effective temperature limit of 4.83 pK. For significantly colder temperatures in the low fK regime T_0 needs to be increased to 50 ms, which involves extending the initial cloud radius to more than 100 µm.

Lens Characterization in $m_F = 2$

The first acquired time series of the evolution after magnetic lensing was performed with the Gaussian BC-SC-lens detailed in Table 9. The initial lens parameters for $z(x')$-collimation were extracted from the scaling approach simulations (see Figure 83a). The predicted current scaling of 0.325 led to substantial focusing of the cloud in both observable directions and was thus reduced to 0.244. In fact, the lens strength appears to be systematically underestimated by the scaling approach simulations. Other experimental optimizations include small variations of the y-coil current, which allows to compensate the COM motion via a displacement of the lens. In a harmonic lensing potential, only the curvature of the field is responsible for the lensing action and a displacement does not change the strength of the lens. However, in the presence of anharmonicities a compensation of residual COM motion is associated with varying the lens action along the respective axis.

During the first lens campaigns, small gauging currents were applied to any unused structures to compensate zero currents from the current drivers and prevent unwanted offset fields. Later on, unused structures were completely disconnected (see Chapter 2). The ability to disconnect current carrying structures turned out to be a necessary requirement to study ensembles during long periods of free evolution in magnetically sensitive hyperfine states.

The time series of the free evolution of the lensed ensemble is illustrated in Figure 86. The first five absorption images were acquired with the primary imaging setup and show a BEC that appears very well collimated in both observable directions, despite the pronounced tail

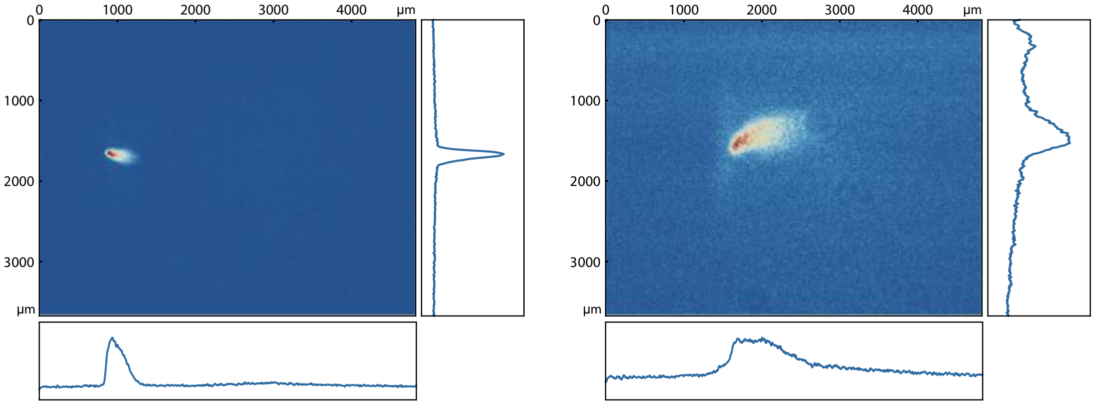

(a) Lens with x-coil current 0.5 A.

(b) Lens with x-coil current 0.1 A.

Figure 85: Absorption images of lensed clouds after 300 ms TOF (Drop #111). The only difference between these two sequences is the x-coil current during the lens, which sets the trap bottom energy and has a strong influence on the rotation of the lens.

in the $z(x')$-direction. These findings are surprising since the projection of the x-axis on the y'-direction should dominate the imaging axes and thus the cloud elongation along x should lead to a larger and steadily increasing radius along y'. The only reasonable explanation for such an occurrence is that the cigar shaped ensemble is rotated relative to the imaging plane. In fact, an absorption image from the secondary imaging setup (Figure 86f) reveals the obvious rotation of the cloud. The effective projection angle of the primary imaging setup is thus shifted from 45° to 10° for the analysis of these measurements. The cloud features an additional tilt of approximately 13° in respect to the x'-axis that appears to be constant over the range of measurement times.

Due to the COM motion of the ensembles the observation time in this campaign was limited to about 1 s after the lens. Even after disconnecting every current carrying structure but the ones responsible to provide a small quantization field, sizable magnetic field gradients remain in the vacuum chamber (see Chapter 5). These gradients accelerate the atoms over time and shift the cloud center to the edge of the imaging window.

Lens Characterization in $m_F = 0$

To extend the observation time further, the atoms are transferred to the $m_F = 0$ state via an ARP after the lensing pulse (see Chapter 3). Additionally, a magnetic field gradient is applied for a short time to separate the residual atoms in the neighboring m_F states. The acquired data set spans free expansion times from 100 ms to 2000 ms after the lens. The cloud is still barely detectable after up to 2700 ms but the signal-to-noise ratio is too low for quantitative analysis.

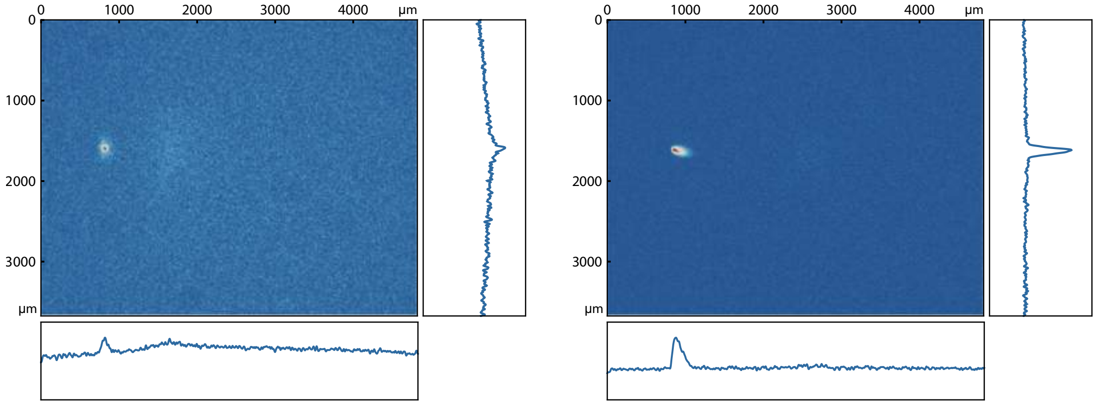

(a) TOF = 50 ms (Drop #117b)

(b) TOF = 250 ms (Drop #117a)

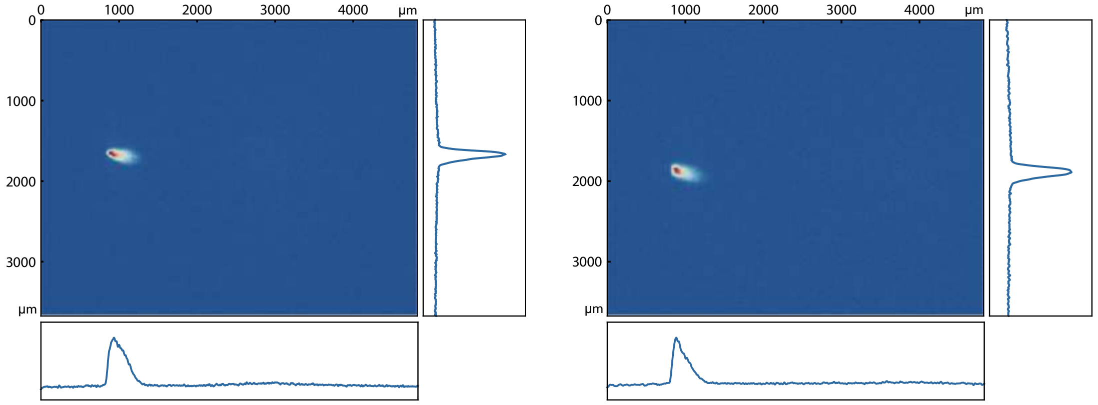

(c) TOF = 300 ms (Drop #111a)

(d) TOF = 500 ms (Drop #116a)

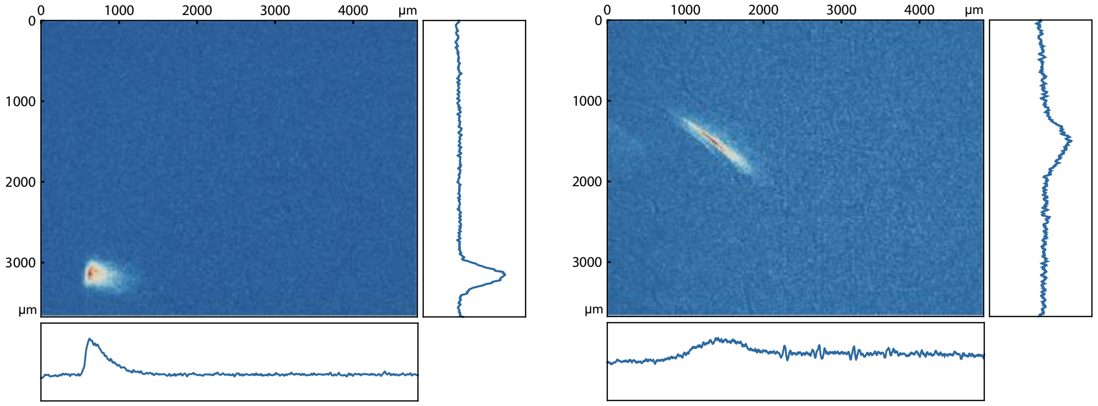

(e) TOF = 1000 ms (Drop #118)

(f) TOF = 1000 ms, 2$^{\text{nd}}$ detection (Drop #124a)

Figure 86: Time series of BECs after a BC-SC-lens and subsequent free evolution in the $m_F = 2$ hyperfine state. The lens parameters are: $T_0 = 30\,\text{ms}, \tau = 6\,\text{ms}$, Gaussian. Due to residual magnetic gradients in the apparatus, the COM motion along the y'-axis limits the measurements time to 1 s.

Thus, in the $m_F = 0$ state the observation of the ensemble is not limited by the residual COM motion but by the collimation of the cloud.

There is no evidence that the residual gradients in the vacuum chambers have a measurable influence on the lensing pulse itself. On the contrary, the two data sets in the different hyperfine states appear to be consistent and can be merged for quantitative analysis. The size of the ensemble was determined by fitting the TF-radii in the absorption images (see Figure 87). All images were rotates by 13° to compensate the x'-tilt. In the $z(x')$-direction, the measured radius refers to the central peak of the spatial distribution and thus underestimates the size due to the anharmonicities (as expected from the phase-space simulations in Figure 79). Since the size of the ensemble depends on the number of atoms in the condensate, all data points as well as the theoretical model are rescaled to the average atom number of the data set $N = 30820$. The data points are contrasted with the expansions dynamics expected from scaling approach simulations in Figure 88.

The evolution of the cloud radii in both x'- and y'-direction shows only moderate expansion for the first 500 ms and a steeper slope on longer time scales. While the radii along the two imaging directions are fairly similar initially, a clear disparity is established 1000 ms after the lens. No clear focus can be observed in any direction. The virtually constant cloud size at early times in the x'-direction could be explained by the expected evolution of the central peak (see Figure 77). A false focusing of the cloud is not observed in this case since the lens is not collimated. Hence, the phase-space distribution of the cloud after the lens would appear similar to the center image in Figure 75c. Here, the left wing of the distribution is much less pronounced and no prominent peak in the spatial distribution is expected as the wing passes the central peak.

Several inconsistencies remain when comparing the experimental results to the scaling approach model:

- The strength of the lens appears to be underestimated in general as scaling factors > 0.32 should be necessary to approach collimation for any of the axes.
- The expansion along the two steep directions are very similar, suggesting that the difference in effective trap frequency for the lens is much smaller than expected.
- The ensemble appears well collimated in both imaging directions for the first 500 ms and then experiences a steep increase in expansion rate despite the absence of foci.

A possible explanation for the different lens scaling could be a discrepancies between the currents applied to the structures and the actual magnetic field that is induced. Eddy currents during the lens pulse could potentially alter the lens duration and lead to the apparent increase in lensing action. The similarity in the expansion dynamics is generally a positive occurrence but significantly harder to study as the analysis of the x' data is hampered by the anharmonicities. The

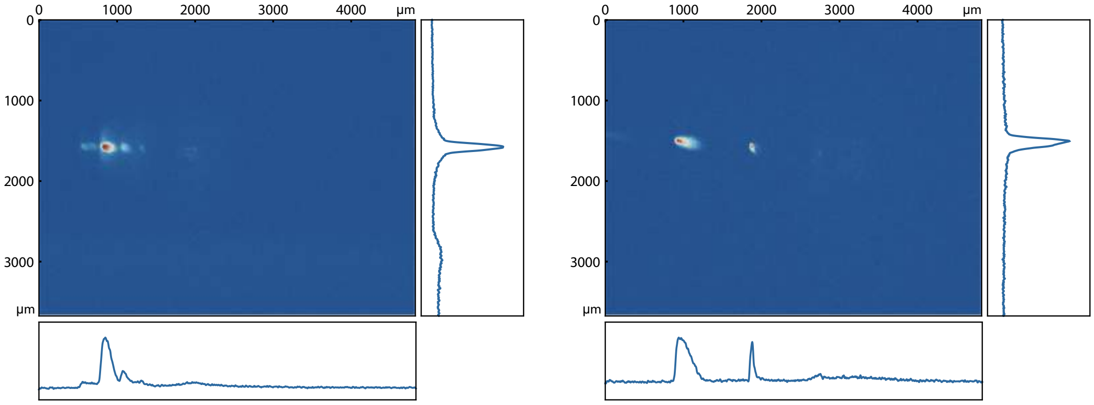

(a) TOF = 100 ms (Drop #129b)

(b) TOF = 300 ms (Drop #128a)

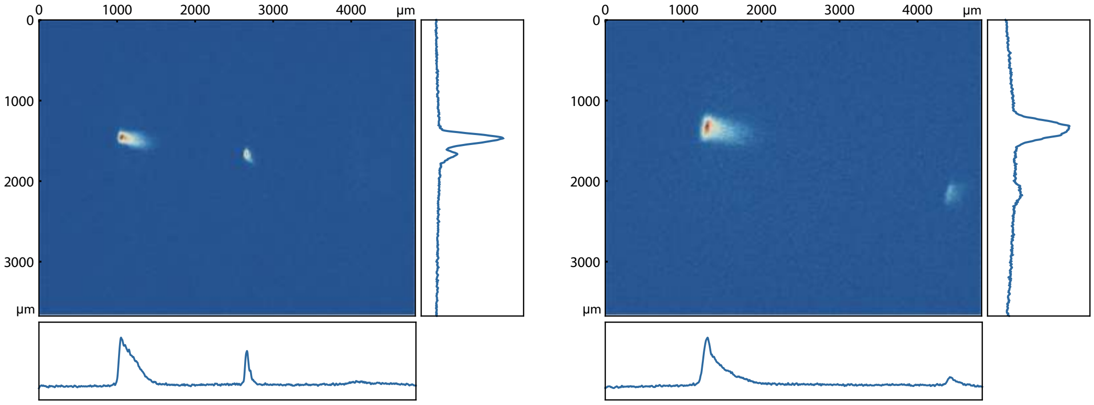

(c) TOF = 500 ms (Drop #129a)

(d) TOF = 1000 ms (Drop #132a)

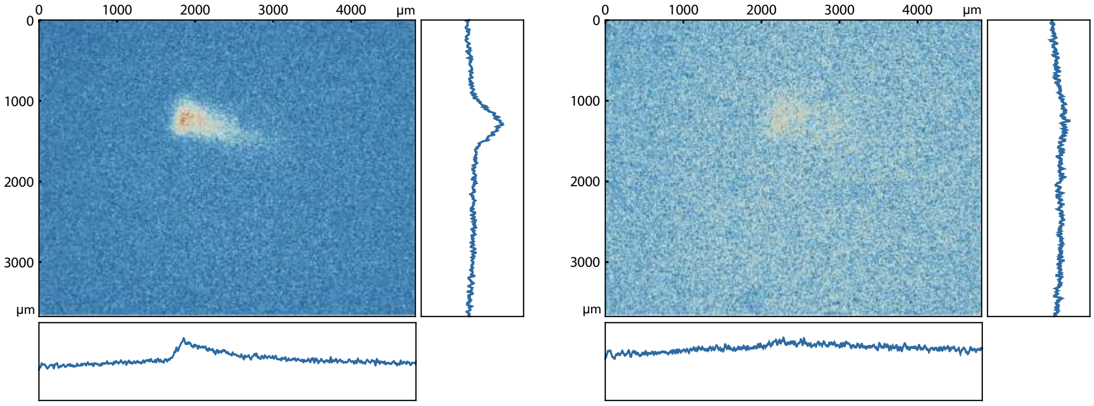

(e) TOF = 2000 ms (Drop #130)

(f) TOF = 2700 ms (Drop #127)

Figure 87: Time series of BECs after a BC-SC-lens and subsequent free evolution in the $m_F = 0$ hyperfine state. The lens parameters are: $T_0 = 30\,\text{ms}, \tau = 6\,\text{ms}$, Gaussian. The ARP to the $m_F = 0$ state also slightly populates neighboring hyperfine states. A Stern-Gerlach kick is applied after the ARP to spatially separate the states and observe the cloud unobstructed at all times.

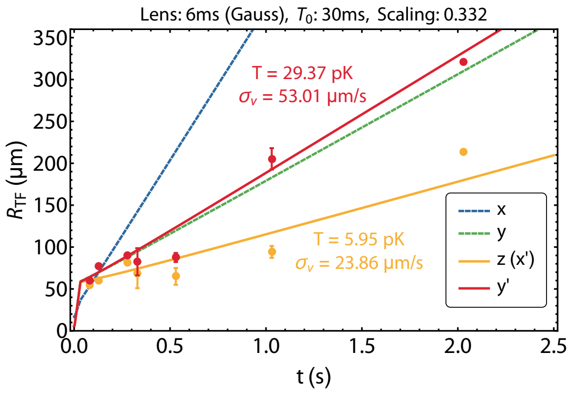

Figure 88: Comparison of the BC-SC-lens data to the scaling approach simulations. The following assumptions were used: the projection angle of the primary imaging setup is corrected to 10°, the $z(x')$ scaling is reduced by 3.7% relative to the y'-direction. The scaling functions from (6.7) and (6.8) are then fitted to the experimental data using the current scaling as the only fit parameter. The error bars correspond to the standard deviation of the radii in cases where more than one data point was available, but are not included in the fit.

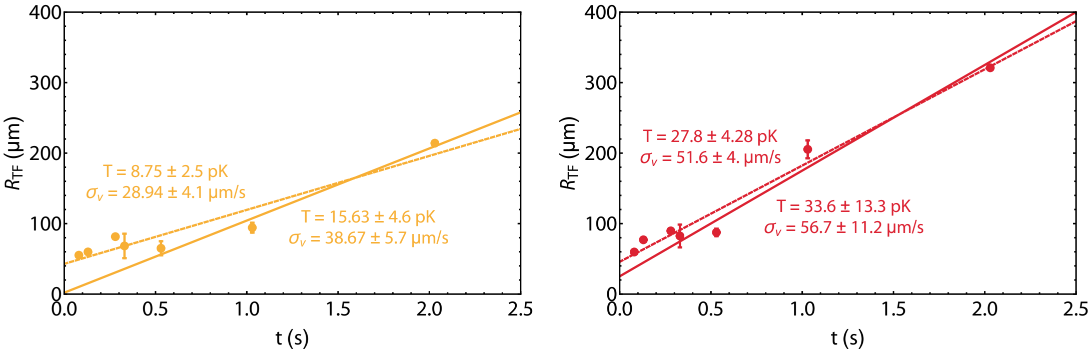

(a) Linear fits to x' lens data.

(b) Linear fits to y' lens data.

Figure 89: Linear fits to the accumulated BC-SC-lens data. The dashed lines represent linear fits to the full data sets while the solid lines correspond to fits for data points upwards of 500 ms. The effective temperatures are derived from the slope of the lines via (6.23) and the uncertainty is given by the standard error of the fits.

apparent collimation on shorter timescales with subsequent expansion can easily be explained in the x'-direction. However, the radius along the y'-axis should not feature a drastic change in expansion rate in the absence of a focus. The radii after long TOFs could potentially be inflated due to the limited lifetime and diminishing density of the cloud. To reduce such effects, the atom number of all data points was post-corrected with an estimate lifetime of 15 s prior to rescaling. Shortcomings of the theoretical approach are the fact that neither the rotation during the lens nor the anharmonicities are accurately reflected in the theoretical model. A quantitative three-dimensional model of the lens dynamics in anharmonic potentials is currently in preparation and promises to clear up the remaining discrepancy.

Extracting the residual expansion rates from the absorption images in Figure 87 is achieved via linear fits of the data sets (see Figure 89), yielding the following one-dimensional velocity spreads and temperatures:

$$\begin{aligned} \sigma_{v_{x'}} &= 28.94 \pm 4.1\,\mu\text{m/s} \quad \rightarrow \quad T_{x'} = 8.75 \pm 2.5\,\text{pK}, \\ \sigma_{v_{y'}} &= 51.6 \pm 4.0\,\mu\text{m/s} \quad \rightarrow \quad T_{y'} = 27.8 \pm 4.28\,\text{pK}. \end{aligned}$$

Conservatively, one could limit the evaluation to the data points starting at 500 ms after the lens and representing the long term ballistic expansion of the ensemble. These fits yield:

$$\begin{aligned} \sigma_{v_{x'}} &= 38.67 \pm 5.7\,\mu\text{m/s} \quad \rightarrow \quad T_{x'} = 15.63 \pm 4.6\,\text{pK}, \\ \sigma_{v_{y'}} &= 56.7 \pm 11.2\,\mu\text{m/s} \quad \rightarrow \quad T_{y'} = 33.6 \pm 16.3\,\text{pK}. \end{aligned}$$

The uncertainty in these values is given by the standard error of the fits.

Despite the difficulties in modeling the lens dynamics, the adjusted scaling approach simulations offers reasonable estimates for the velocity spread of $\sigma_{v_{x'}} = 23.86\,\mu\text{m/s}$ and $\sigma_{v_{y'}} = 53.01\,\mu\text{m/s}$ (see Figure 88). These values correspond to effective temperatures of 5.95 pK and 29.37 pK, respectively. Translated to the chip coordinate system, the residual velocity spreads along the geometric axes are (136.7, 48.2, 23.9) µm/s, equivalent to one-dimensional effective temperatures of (195.2, 24.2, 5.95) pK. Thus, the comparison of the adjusted scaling model to the experimental data implies a residual three-dimensional velocity spread σ_v and a three-dimensional effective temperature T of:

$$\sigma_v = 146.8\,\mu\text{m/s} \quad \rightarrow \quad T = 73.2\,\text{pK}.$$

Unfortunately, the reliability of the analysis is limited by the small number and quality of data points towards long expansion times. The diminishing signal to noise ratio calls into question the validity of the size rescaling for dilute clouds. Since atoms are lost to background collisions or fail to be detected due to the low densities of the clouds, data points after long times of flight are likely inflated. To alleviate these issues as much as possible, the rescaled radii are post-corrected for background losses associated with a lifetime of 15 s.

The lens sequence presented here was characterized with a lens scaling that was adjusted experimentally on relatively short times scales and does not reflect the collimation condition in any of the axes. Therefore, the expansion rates can be reduced further simply by increasing the current scaling and optimizing the lens collimation on longer timescales. One disadvantage of pursuing the BC-SC-lensing scheme further are the observed rotations of the cloud. They may impede proper analysis of the lens dynamics as well as hinder a sequential collimation of the shallow axes. The latter would be necessary given the cigar-like aspect ratio of the ensemble, which results in an effective temperature along the x-axis in the nanokelvin range. An additional

Figure 90: Scaling functions for the trap frequencies of the BC-lens over the current scaling extracted from Biot-Savart simulations of the chip potential. Due to the reduction of the rotation rate, there is no intersection between the two steep trap axes. The cylindrical symmetry is slightly broken by the anharmonicities. Note that their influence on ω_z depends on the exact position offset between lens and atomic cloud.

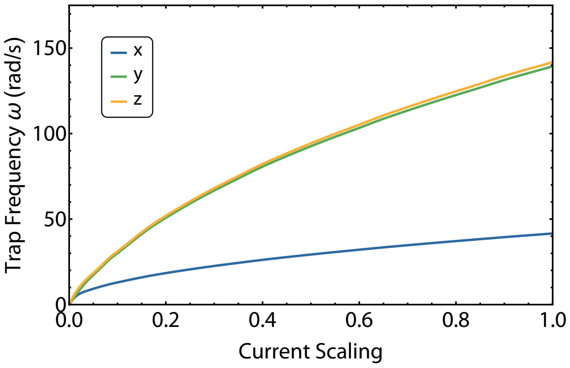

concern is the distorted shape of the cloud in the $z(x')$-direction and its implications as a source for atom interferometry.

6.4.3 BC-Lens

Building on the experience from the first lens campaign, a new trapping and lensing potential was identified whose properties are generally more conducive to achieving effective temperatures in the low picokelvin and sub-picokelvin regimes. The main advantages of the new lensing sequence are its simplicity and the increased distance from the atom chip (see Chapter 5). Every individual chip structure can generate a trapping potential with two equal trap frequencies at one specific distance. For the BC, this position is located approximately 1470 µm away from the chip surface. Deriving efficient protocols for excitations-free transfer becomes more troublesome at such distances, but the benefits such as the ability to simultaneously collimate two axes and the reduced anharmonicities far outweigh the efforts.

In contrast to the previous lens, the lensing pulse is not generated by a downscaled version of the trapping potential. This is a consequence of the demanding transfer protocol which is simplified substantially by only varying the bias coil (y-coil) current to move the atoms away from the chip. Changing to a different trapping potential before transfer would require its own elaborate shortcut trajectory for every current carrying structure involved to avoid excitations. Hence, the atoms remain in a hybrid BC-SC trap prior to release and are subsequently lensed using only the Base-Z structure. Co-location of atoms and lens is ensured by consulting the Biot-Savart simulations for both potentials.

To overcome some of the issues of the BC-SC-lens, the new lensing pulse is implemented differently. The trap bottom energy is reduced by limiting the x-coil current to 0.1 A to reduce the rotation of the lens. As a result, the scaling functions of the BC-lens along the geometrical axes do not feature intersections at low current scalings (see Figure 90). While the two steep axes should feature identical current scalings by design, the two are slightly offset due to the anharmonicities along z. The actual offset largely depends on the exact position offset between atoms and lens and thus the COM motion during initial expansion. The BC-lens features significantly lower trap frequencies than its predecessor and thus requires a longer initial expansion of $T_0 = 80\,\mathrm{ms}$. While the prolonged time may lead to larger position offsets, is allows for lowest theoretical temperatures along the two steep axes that are well within the femtokelvin range.

During the lens, all coil current are held constant and the pulsing is achieved using only the single Base-Z structure. Instead of applying a Gaussian waveform, the chip structure is switched on and off instantaneously. Due to the short switching time of the chip structures of about 0.175 ms, the current response should display a box-shaped pulse in reasonable approximation. Hence, the majority of the lensing action is applied at the same current scaling and circumvents the erratic behavior at low lens scalings. Now, the lens does not integrate over variations in trap frequency ratios, $L3/L4$ ratios, translations or rotations of the lens. This drastic simplification will also ease the theoretical description of the lens dynamics.

Lens Characterization in $m_F = 2$

The $m_F = 2$ series covers post lens expansion times of up to 750 ms (see Figure 91). The clouds in the $m_F = 2$ state were observable up to 1000 ms after the BC-SC-lens. However, the COM motion induced by the BC-lens is not increased but rather reduced in comparison. The previous lens happened to start with a COM in opposition of the acceleration by the residual gradients.

The central feature of the cloud appears to be shrinking in both observable direction, which indicates focussing of the ensemble. The absorption images show the typical tail in the x'-direction which appears more cohesive in comparison to the BC-SC-lens. There is no noticeable rotation of the cloud evident in the the images recorded by the primary imaging setup.

Lens Characterization in $m_F = 0$

As after the BC-SC-lens, the atoms are transferred to the $m_F = 0$ state via an ARP to extend the observation time further. The neighboring m_F states are separated by a short magnetic field gradient pulse. The $m_F = 0$ data set again spans free expansion times from 100 ms to 2000 ms after the lens (see Figure 92). As in the previous case, the lensing action is not measurably influenced by the residual gradients and the expansion dynamics are consistent over the different m_F states. The data set displays the same focusing effect along both imaging axes. On time scales of 1000 ms and up, some images show a bow shaped structure along y'. This may originate in a position offset between atoms and the anharmonic lens or in a relative angle between release trap and lens.

Additionally, the analysis of the cloud shape is complicated by the fact that the ensemble is released from an exceedingly shallow potential. As a result, the size of the thermal component of the cloud is on the same order as the condensate and experiences similar lensing action. Thus,

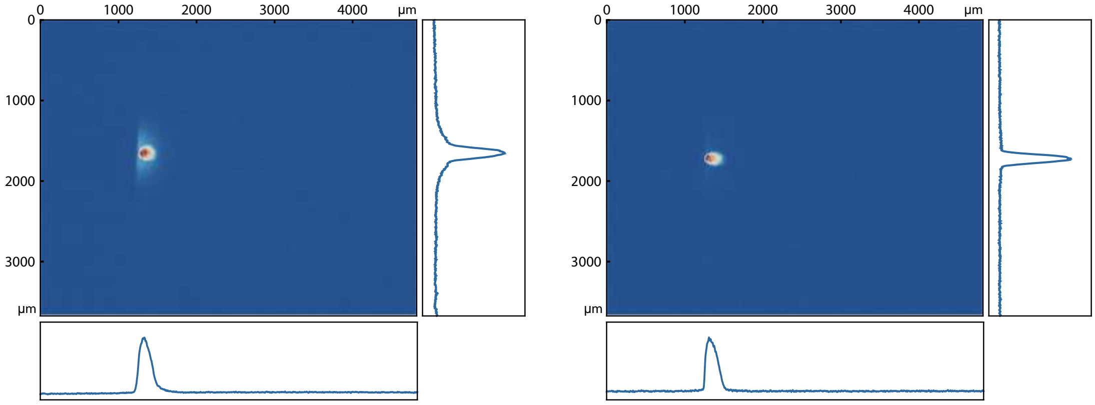

(a) TOF = 100 ms (Drop #189b) (b) TOF = 200 ms (Drop #190a)

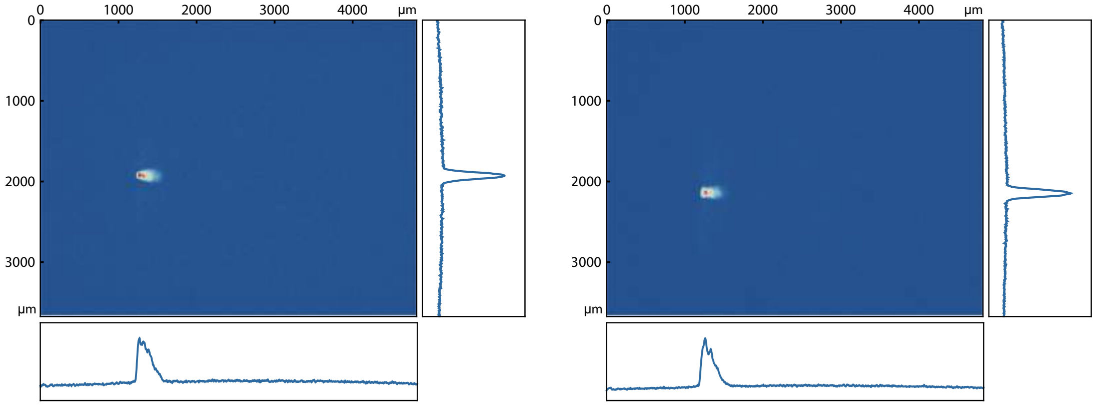

(c) TOF = 350 ms (Drop #190b) (d) TOF = 450 ms (Drop #187b)

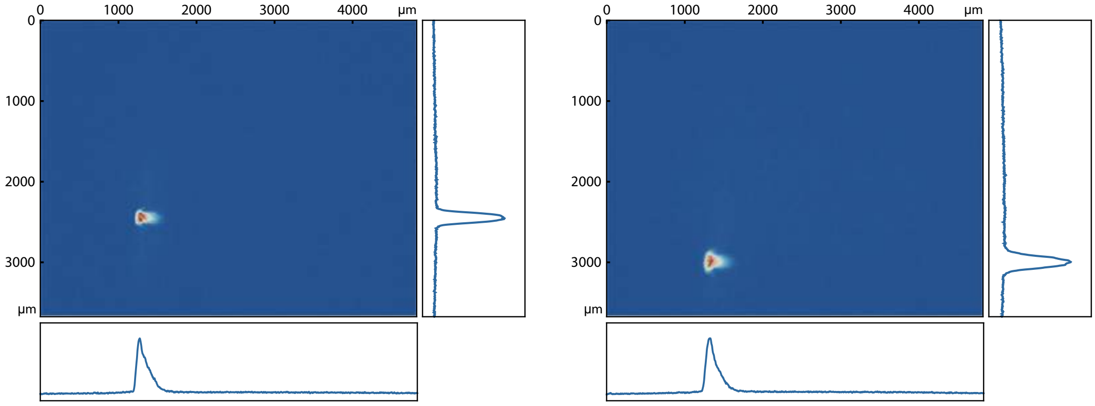

(e) TOF = 580 ms (Drop #191a) (f) TOF = 750 ms (Drop #189a)

Figure 91: Time series of BECs after a BC-lens in the $m_F = 2$ hyperfine state. The lens parameters are: $T_0 = 80$ ms, $\tau = 2.64$ ms, Box pulse. Due to residual magnetic gradients in the apparatus, the COM motion along the y'-axis limits the measurements time to 750 ms.

the images show two overlapping clouds and the characteristic tail in the x' profile can not easily be distinguished from the thermal fraction. At times, both components appear displaced in the absorption images further underlining the fact that the anharmonic tail may generally be overestimated in the BC-lens data (see Figure 92d).

In Figure 92g, the cloud shows only minimal signs of the anharmonic tail after 2000 ms of free evolution. This could be due to a favorable condensate fraction of that particular shot or due to the fact that the cloud is not collimated so neither is the tail. Because of its much lower density it fades out first as the signal-to-noise ratio diminishes. Overall, the size of the central feature on the primary detection images compares to the 2000 ms shot of the BC-SC-lens (Figure 87e). However, the cloud appears much more shapely with reduces deformations and the rotations of the ensemble are reduced significantly.

Figure 92h, obtained with the secondary imaging setup, shows the cloud from two different angles 1000 ms after the lens. It is evident that the rotation along the z-axis is reduced substantially, from approximately 35° after the BC-SC-lens (see Figure 86f) to about 12°. However, the analysis of the exact angle is obstructed by the overlap with the thermal cloud.

Generally, the cloud seems implausibly well collimated in all three dimensions despite the fact that the lens should only significantly alter the collimation along the y- and z-axis. To reproduce these results theoretically, either the release trap frequency or the lens along the shallow x-axis would have to be overestimated or underestimated by significant margin of up to 50%. Such large deviations can be caused by higher-order excitations, altering the size and velocity distribution at the time of the lens. The existence of such excitations after the shortcut ramp to the target location was already verified experimentally (see Chapter 5). Due to these variations in the starting conditions, the lens is currently difficult to model until the in situ size dynamics are fully characterized. Figure 62 indicates that the TF radii are far from their equilibrium sizes at the relevant hold time of $t_{\text{hold}} = 18.46\,\text{ms}$. Thus, the unlikely collimation along the shallow axis stems from switching of the release potential at a convenient time. On the other hand, the y and z radii appear enlarged at the time of the switch-off, which could explain why the lens strength is underestimated by the scaling approach simulations. Figure 93 depicts all BC-lens data from both imaging angles. While the progression of the harmonic axes can be matched qualitatively, the z-direction is not well represented by the model due to the anharmonicities.

The data set from the primary imaging setup is displayed in Figure 94. Both imaging directions appear to show a focus of the ensemble. However, the radius along the x'-direction diminishes very fast initially, then recovers slowly and steadily. Such an asymmetric narrowing contradicts the expected behavior of a focused cloud, especially since the long term expansion should be much steeper as a result of the focal point. The x'-radius seem to be more in line with the predicted false-focusing of the cloud encountered in Figure 77. Hence, the ensemble could likely

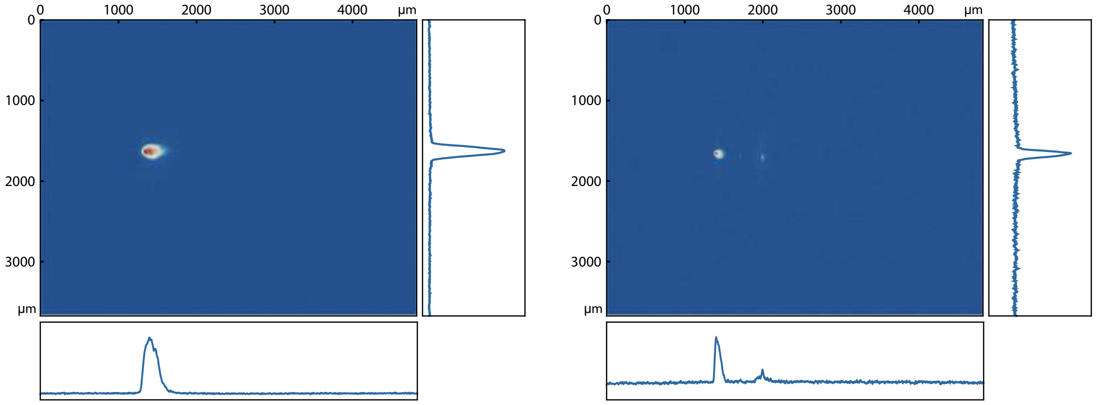

(a) TOF = 100 ms (Drop #195a)

(b) TOF = 200 ms (Drop #203a)

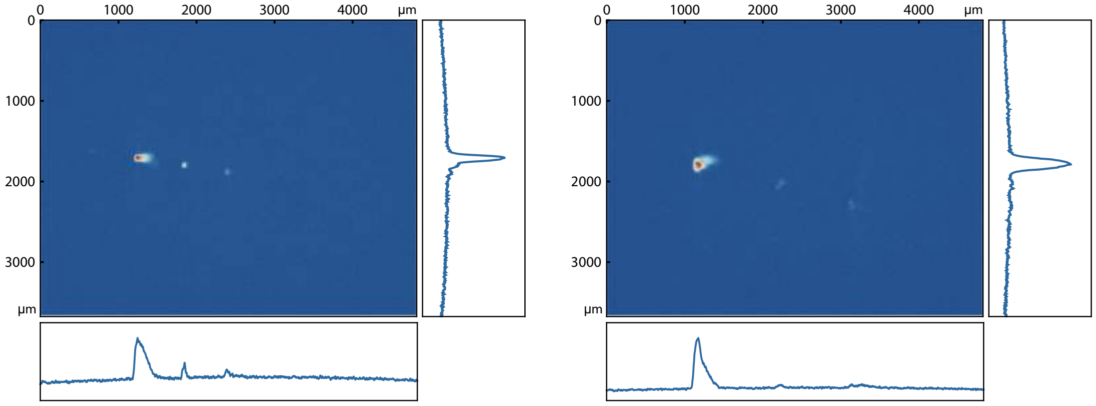

(c) TOF = 350 ms (Drop #194b)

(d) TOF = 580 ms (Drop #193a)

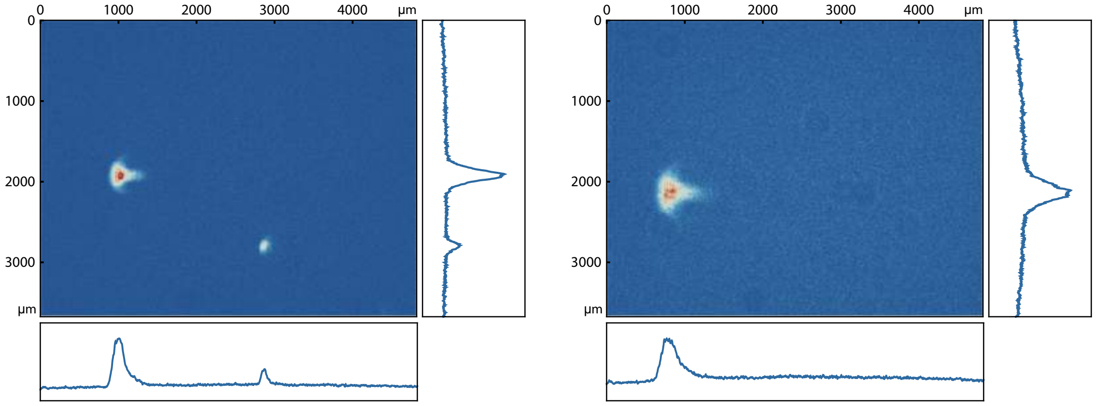

(e) TOF = 1000 ms (Drop #196a)

(f) TOF = 1500 ms (Drop #197a)

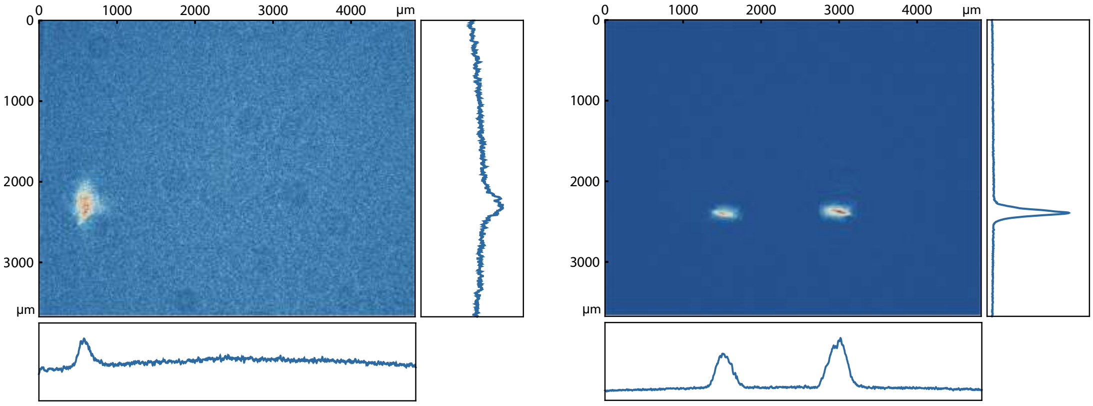

(g) TOF = 2000 ms (Drop #198a)

(h) TOF = 1000 ms, 2^{nd} detection (Drop #199a)

Figure 92: Time series of BECs after a BC-lens and subsequent free evolution in the $m_F = 0$ hyperfine state. The lens parameters are: $T_0 = 80$ ms, $\tau = 2.64$ ms, Box pulse. The ARP to the $m_F = 0$ state also slightly populates neighboring hyperfine states. A Stern-Gerlach kick is applied after the ARP to spatially separate the states and observe the cloud unobstructed at all times. The thermal fraction of the ensemble is similar in size to the condensate and can appears displaced in some pictures.

be very close to the collimation condition along x'. On the other hand, the false-focusing effect could be masking a slight focus of the cloud. A linear fits to the data sets upwards of 500 ms gives an expansion rate of $\sigma_{v_{x'}} = 41.71 \pm 4.1$ µm/s which corresponds to an effective temperature of $T_{x'} = 18.2 \pm 3.6$ pK.

In the y'-direction, the narrowing of the cloud is consistent with a focus in the y-direction, somewhere between 500 ms and 1000 ms after the lens. This indicates that either the lens potential along y is in fact slightly steeper than along the z-axis, or the discrepancy is causes by the size dynamics in the release trap. A linear fits to the data set upwards of 500 ms gives a residual expansion rate of $\sigma_{v_{y'}} = 92.83 \pm 6.1$ µm/s which corresponds to an effective temperature of 90.1 ± 12.0 pK. If the data point two seconds after the lens is excluded from the fit, the values are 80.75 ± 7.0 µm/s and 68.2 ± 12.0 pK. Disregarding the data point is justified since the OD of the cloud has already dropped of substantially and not all the atoms initially in the cloud can be detected. This situation is compounded with the fact that losses from background collisions are starting to have a measurable effect after such long expansion times. Since all of the radii are rescaled to a common atom number, clouds with undervalued atom number will be inflated in size. To counteract this effect, the rescaled radii are post-corrected for background losses associated with a lifetime of 15 s.

The atom numbers from the secondary imaging setup are not well calibrated yet, leading to some uncertainty in the rescaling process. However, the preliminary data is consistent with

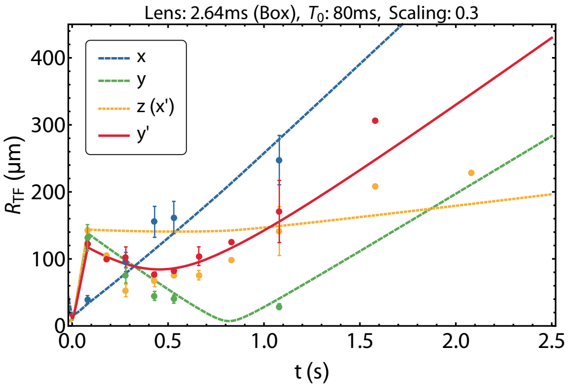

Figure 93: Comparison of the BC-lens data to the scaling approach simulations. All radii are rescaled to the average condensate atom number of $N = 93000$. The figure shows an attempt of retracing the cloud radii by adjusting the starting condition to reflect the in situ size oscillations of the cloud. The lens scaling in the y-direction was increased by 8.9%. The error bars in the x'- and y'-direction correspond to the standard deviation of the radii. In the x- and y-direction, they reflect the uncertainty in the atom number.

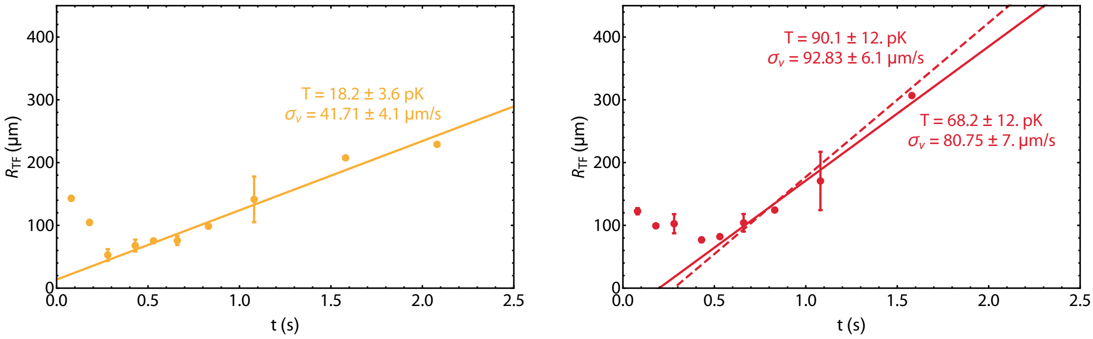

(a) Linear fits to x' lens data.

(b) Linear fits to y' lens data.

Figure 94: Linear fits to the accumulated BC-lens data. The error bars correspond to the standard deviation of the radii in cases where more than one data point was available but are not included in the fit. The lines represent linear fits to the data points upwards of 1000 ms. The effective temperature are derived from the slope of the lines and the uncertainty in given by the standard error of the fits.

both the primary imaging data and the findings of the scaling approach simulations. Figure 95 shows the composite data for the three geometric axes x, y and z. The data for the x-direction is fitted with linear model weighted by the atom number uncertainty. The extracted expansion rate is 93.2 ± 10.7 μm/s which corresponds to an effective temperature of 90.7 ± 20.7 pK. It is noteworthy that this temperature is not the result of the magnetic lens but of the shallow release potential in conjunction with size oscillations in the trap and a convenient switch-off time. For the y-direction, the linear fit is applied to the data on the left of the focal point and the progression after the focus is estimated by the reverse slope. The extracted expansion rate is 57.0 ± 7.9 μm/s which corresponds to an effective temperature of 34.0 ± 9.4 pK. In summary,

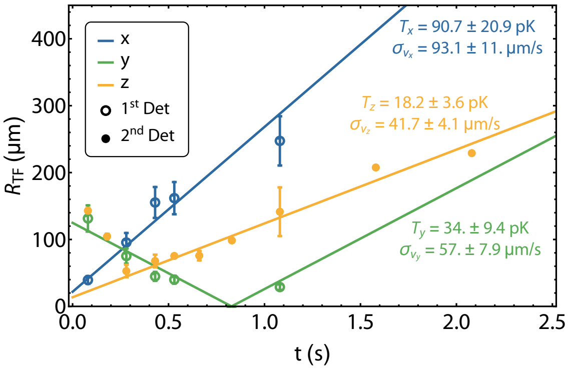

Figure 95: Composite BC-lens data for the three geometric axes x, y and z. All radii are rescaled to the average condensate atom number of $N = 93000$. The residual expansion rates are extracted from linear fits that are weighted by the atom number uncertainty for the x- and y-directions. The expansion along the z-axes is likely underestimated as the analysis is limited to the central feature of the cloud and neglects the residual atoms in the tail.

the individual expansion rates along the three geometric axes are:

$$\sigma_{v_x} = 93.2 \pm 10.7\,\mu\text{m/s} \quad \rightarrow \quad T_x = 90.7 \pm 20.7\,\text{pK},$$
$$\sigma_{v_y} = 57.0 \pm 7.9\,\mu\text{m/s} \quad \rightarrow \quad T_y = 34.0 \pm 9.4\,\text{pK},$$
$$\sigma_{v_z} = 41.7 \pm 4.1\,\mu\text{m/s} \quad \rightarrow \quad T_z = 18.2 \pm 3.6\,\text{pK}.$$

These findings are consistent with the scaling approach simulations (see Figure 93). For an average atom number of $N = 93000$, the composite data set implies a residual three-dimensional velocity spread σ_v and a three-dimensional effective temperature T of:

$$\sigma_v = 116.9 \pm 13.9\,\mu\text{m/s} \quad \rightarrow \quad T = 47.6 \pm 11.3\,\text{pK}.$$

The analysis of the absorption images neglects the tail in the z-direction, which is constantly thinning out and expanding away from the peak of the ensemble. Thus, the temperature is likely underestimated. In the absence of anharmonicities, the z-direction would show a similar progression and temperature as the y-direction. This assumption relies on the fact that the initial conditions from the size oscillations in the release trap appear to be reasonably well matched at the time of release (see Chapter 5) and the BC-lens features two symmetric axes by design. However, due to the presence of anharmonicities the matching of the two directions is hard to evaluate.

The obtained effective temperatures are the result of characterizing the very first BC-lensing sequence and no attempts to minimize the expansion rates have been performed. Thus, the presented values are nowhere close to the minimal temperatures that can be achieved. The observed size oscillations in the release trap have tremendous influence on the lens dynamics and optimizing the collimation process of the lens goes hand in hand with controlling the higher order excitations of the ensemble. This is exemplified by the significantly reduced expansion rate along the shallow trap axes. Thus, tailoring the input state of the lens could reduce the expansion rate along the x-axis to the point where the ensemble can be collimated to an effective three-dimensional temperature in the femtokelvin range with a single lensing pulse.

6.5 Summary

This chapter discussed the dynamics of BECs in time dependent potentials, the collimation of ultra-cold atoms with magnetic fields and the effects of anharmonicities in the lensing process. The experimental implementation, pulse shaping and campaign planning was guided by the Biot-Savart simulations of the chip potential and scaling approach simulations of the expansion of the atomic clouds.

The expansion dynamics of magnetically lensed BECs can be understood reasonably well qualitatively but exact predictions require better modeling efforts. Several new approaches are being pursued within the QUANTUS collaboration. Numerically solving the three-dimensional GPE with the full three-dimensional chip potential may grant insight into the influence of rotations and anharmonicities. Complementary to this computationally intensive approach, a three-dimensional model of the classical kinematics during the lens is being explored. These calculation are a quantitative extension to the phase-space simulation presented in this chapter and can be performed either numerically or analytically. Properly gauging the secondary imaging setup and reconstructing the three-dimensional shape of the cloud will be very helpful in understanding the lens dynamics.

In the first dedicated microgravity campaign, a BC-SC-lens was used to reduce the velocity spread of the ensemble to approximately $\sigma_v = 146.8\,\mu\text{m/s}$, which corresponds to a three-dimensional effective temperature of $T = 73.2\,\text{pK}$ at an average atom number in the condensed phase of $N = 30820$. Obtaining such a low temperature in the very first lensing attempts showcases the maturity of the technologies and outstanding reliability of the Biot-Savart simulations. These effective temperatures are already sufficient to enable free expansion times of up to 2.7 s, equaling the longest observation times that have ever been realized [49]. However, the shape of the cloud after the lens was significantly distorted by the lens aberrations (see Figure 96).

During the second microgravity campaign, the influence of the anharmonicities was reduced by using a lensing potential at greater chip distance. Here, the collimation of the ensemble was improved further despite the fact that the chosen lens sequences is focusing the cloud in at least one direction. The cloud shape is significantly improved compared to the previous lens (see Figure 96). The estimated velocity spread of the ensemble is $\sigma_v = 116.9 \pm 13.9\,\mu\text{m/s}$ with a three-dimensional effective temperature of $T = 47.6 \pm 11.3\,\text{pK}$ at an average atom number in the condensed phase of $N = 93000$. Despite the fact that the lens has not been optimized, these values represent the lowest three-dimensional effective temperature that has ever been realized (see Chapter 7). With this reduction in expansion rates, we are fast approaching the

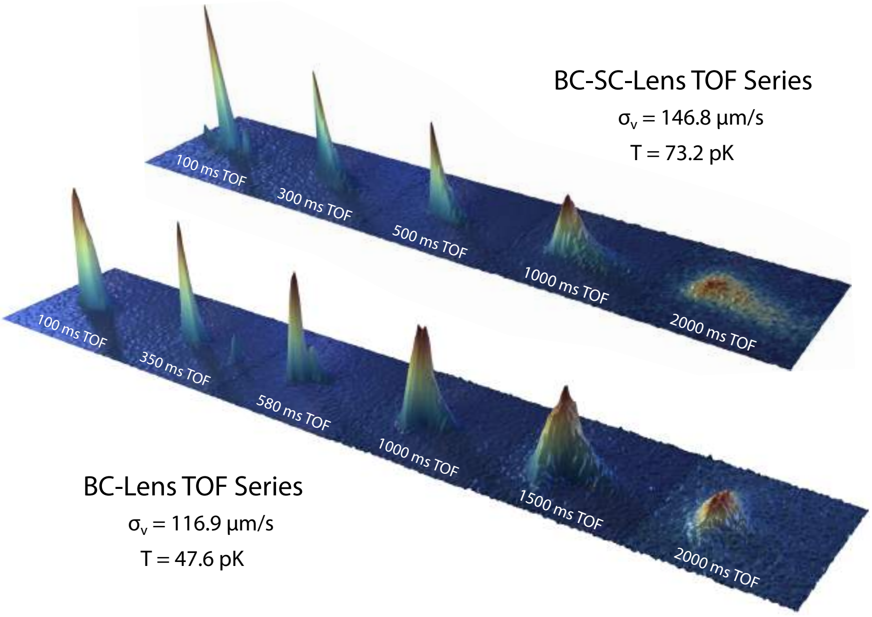

Figure 96: Three-dimensional illustration of the TOF series for both lens sequences. Despite the low expansion rates neither one of the lenses is collimating the ensemble, leading to a diminishing signal after 2000 ms TOF. The shape of the cloud is significantly improved after the BC-lens compared to the BC-SC-lens. The cloud profiles in the pictures are scaled individually.

maximal consecutive measurement time in drop operation and future optimization on longer times scales will require catapult campaigns.

The observed expansion rates can be decreased further in future campaigns by optimizing the lens collimation and exploiting the size dynamics of the BEC in the release trap to tailor the input state of the magnetic lens. Inducing higher-order collective excitations with a single oscillation frequency promises great synergy with the cylinder-type lenses created with atom chips (see Chapter 5).

Many of the encountered issues of magnetic lensing with atom chips were alleviated with technical solutions, leaving the remaining anharmonicities in the BC-lensing potential as the last significant issue moving forward towards high-precision interferometric measurements. Additional mitigation strategies such as multi-lens sequences are currently being explored.

Publications

Some of the results of this part are published in:

[136] J. Rudolph et al. - ”Cover Picture: Fortschritte der Physik”, Fortschritte der Physik – Progress of Physics **63**, 1-12 (2015), DOI: `10.1002/prop.201570001`.

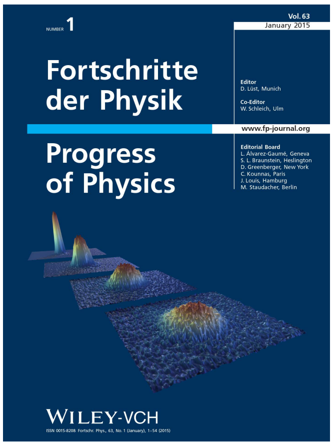

NUMBER 1

Vol. 63
January 2015

Fortschritte
der Physik

Editor
D. Lüst, Munich

Co-Editor
W. Schleich, Ulm

www.fp-journal.org

Progress
of Physics

Editorial Board
L. Álvarez-Gaumé, Geneva
S. L. Braunstein, Heslington
D. Greenberger, New York
C. Kounnas, Paris
J. Louis, Hamburg
M. Staudacher, Berlin

WILEY-VCH

ISSN 0015-8208 Fortschr. Phys., 63, No. 1 (January), 1–54 (2015)

CHAPTER 7

Conclusion and Outlook

The central result of this thesis is the development of a transportable ultra-cold atom machine for high precision measurements in microgravity. It enables the use of mobile and robust quantum sensors in a variety of demanding environments. Many proposals for space missions on ballistic rockets [109], satellites [15] and the ISS [8] rely on the rapid advancement of ultracold atom technology towards miniaturized and integrated devices with manageable volume, weight and power consumption. The apparatus presented in this thesis fulfills these criteria while maintaining a competitive source performance. This was achieved through integrated laser sources [137], extensive development of non-commercial, highly integrated electronics [77] and elaborate optimization efforts on atom chip-based source technology [108]. The attained source flux of 4×10^5 condensed atoms in 1.6 seconds compares to state-of-the-art lab-based experiments and is a crucial step towards the source specifications requested for rocket tests and spaceborne metrology. In continuous µg operation, the present source performance can be optimized even further without physical changes to the design. The source atom number can be increased to 10^6 atoms simply by improving the transfer efficiency to the initial magnetic trap, which is limited by gravitational sag in ground operation. The apparatus showcases the versatility of atom chips, previously considered for fast evaporative cooling but not necessarily for high atom numbers. This is possible through tailoring the velocity profile of a high-flux vapor cell source to the demands of a compact chip design with characteristically low capture volume and velocity. The QUANTUS-2 setup exemplifies the maturity of chip-based BEC machines as competitive sources for matter-wave interferometry.

Meeting the requirements for catapult operation in the Bremen Drop Tower substantiates that the mechanical demands for space missions can be met with the current state of the technologies. The robustness and speed of the setup were demonstrated with the creation of four consecutive BECs within the 9 seconds of a single catapult launch, starting less than 100 milliseconds after an acceleration phase with 35 g magnitude. Due to the low power consumption of 365 W, the device can operate on batteries for up to four hours without any charging or cooling measures. This time can easily be extended by changing the battery configuration. The volume and weight of the design already allow for mobile operation, but can be reduced further by replacing the drop tower specific support structure. In 208 drops and 9 catapult launches, the apparatus displayed seamless transition from lab-based to µg operation, delivering consistent and reproducible results despite the continuous stress, large temperature variations and numerous impacts of the capsule. The system can be operated remotely without the need for manual intervention. The experiment underwent several weeks of drop campaigns without the need for re-adjustments or optimization.

In comparison to other compact devices, QUANTUS-2 is equipped with extensive magnetic shielding to enable high-precision measurements. This permits advancing the control over atomic clouds on the micrometer level without the influences of external fields, even when traversing the 110 meter steel tube of the drop tower. Through the manipulation of the magnetic hyperfine states with RF radiation, residual magnetic field gradients within the magnetically shielded region have been quantified using a Stern-Gerlach type measurements after several seconds of free evolution. Being able to employ the atoms as probes for residual fields allows to identify possible field sources and guide design decisions for future sensors as magnetic offset fields and gradients are among the toughest constraints for high-precision AI sensitivity.

The control over the COM motion of the atoms in the $|F = 2, m_F = 0\rangle$ hyperfine state shows extraordinary precision with a standard error of approximately 7 µm/s. Overall, the COM motion is sufficiently low for detection of the BEC after up to seven seconds of free evolution – if proper collimation of the condensate can be achieved through magnetic lensing. The COM motion is mostly unaffected by the initial velocity of the cloud and is set by the position offset between the ensemble and the lens. Thus, it can be tuned arbitrarily over a wide range of COM velocities.

Several key characteristics of magnetic lensing with atom chips were identified and explored. With careful parameter selection, the geometry of typical chip traps can be reduced to a two-dimensional cylindrical symmetry. Finding such a configuration requires a detailed model of the atom chip potential. Simulating the lens dynamics is also indispensable to comprehend and address rotations of the trap axes during the lens, that may introduce additional effects such as shearing of the cloud. One of the most idiosyncratic properties of chip traps are the anharmonicities introduced to the potential, specifically the cubic term stemming from the decay of the magnetic field strength with increased distance from the atom chip. Sampling these anharmonicities results in deformation of the TF profile and simple lens simulations based on the evolution of the TF radii fail to properly reflect the expansion dynamics along the affected direction.

During the first lensing attempt in microgravity, the expansion of the condensate was reduced to $\sigma_v = 146.8$ µm/s, which implies a three-dimensional effective temperature of $T = 73.2$ pK for an average atom number of $N = 30820$. Absorption images of the lensed cloud show a pronounced tail as a result of the anharmonicities in the potential. The shallow axes of the cloud was barely affected by the lens and remained at a relatively high effective temperature of $T_x = 195.2$ pK. In the next campaign, a lensing potential at greater chip-distance with two-dimensional symmetry was used to collimate the atoms. Using, in situ size oscillations in the release trap to modify the input state of the lens, the expansion rate of the ensemble in three dimensions was reduced to $\sigma_v = 116.9 \pm 13.9$ µm/s, equivalent to a three-dimensional effective temperature of $T = 47.6 \pm 11.3$ pK at an average atom number of $N = 93000$. The time evolution of the BEC after lensing shows a clear focus in at least one of the directions, indicating that the collimation of the cloud can be improved substantially by adjusting the strength of the lens. The noticeable reduction in expansion rate along the shallow axis to an effective temperature of $T_x = 90.7 \pm 20.9$ pK has to be attributed to the in situ size variations and an beneficial switch-off time. This signifies great synergy between high-order collective excitations and magnetic lensing, specifically in cylindrical symmetry. Therefore, both radial and longitudinal expansion rates can be optimized to effective temperatures in the femtokelvin regime by varying input state and lens. The tail in the spatial distribution appears significantly reduced in comparison to the first lensing campaign as a result of the larger chip distance. Additional strategies to mitigate the effects of anharmonicities further, such as employing additional chip structures or a matter-wave telescope, are being explored.

Once the collimation of the BEC is optimized and the cloud deformation are sufficiently suppressed, the experiment will embark on matter-wave interferometry in extended free fall. The setup is equipped with light sources for both Bragg and Raman interferometry. Starting with Bragg interferometry techniques already tested with the first generation apparatus [46], QUANTUS-2 will aim to extend the interferometer time to the limits of the drop tower.

The effective temperatures achieved in the microgravity campaigns are the lowest values that have been reported to date. In three dimensions, the effective temperature was smaller by at least a factor of seven compared to the best previous experiment [138] and an order of magnitude smaller than the next best source for atom interferometry [49]. The effective temperatures of individual degrees of freedom are equally competitive with values as low as 6 pK, overcoming previous limits by almost an order of magnitude [49, 138–141]. These results were achieved while maintaining a competitive atom number, which highlights the superiority of lensed BECs as a source for interferometry over velocity selection from thermal gases.

Table 10: Selected systematic phase contributions of a Mach-Zehnder type atom interferometer under gravity. These systematics can be addressed directly by controlling the size σ_r, velocity spread σ_v and density n_0 of the atoms. The parameters for the phase estimations are: $T = 3\,\mathrm{s}$, $\sigma_r = 1\,\mathrm{mm}$, $\sigma_v = 70\,\mu\mathrm{m/s}$, $R_{\mathrm{eff}} = 10^5$, $N = 10^6$, $k_{\mathrm{eff}} = 4\pi/780\,\mathrm{nm}$, $a = 100a_0$ with Bohr radius a_0, $T_{zz} = -2g/R_{\mathrm{e}}$ with $R_{\mathrm{e}} = 6365\,\mathrm{km}$. For a complete list of parameters and phase terms see Refs [8, 144, 145].

Phase term	Phase shift	Rel. magnitude	Description
$k_{\mathrm{eff}}\, g\, T^2$	1.42×10^9	1	Newtonian gravity
$k_{\mathrm{eff}}\, T_{zz}\, \sigma_r T^2$	-0.4464	3.14×10^{-10}	Gravity gradient (position)
$k_{\mathrm{eff}}\, T_{zz}\, \sigma_v T^3$	-0.0937	6.59×10^{-11}	Gravity gradient (velocity)
$-k_{\mathrm{eff}}/(2R_{\mathrm{eff}})\,(\sigma_r + \sigma_v T)^2$	-0.0001	8.29×10^{-14}	Wave fronts
$4\pi\hbar a/m\, n_0 T$	$+0.0129$	9.06×10^{-12}	Mean field

7.1 Sensitivity Limits for High-Precision Measurements

The largest systematic phase contributions in a high-precision matter-wave interferometer are gravity gradients, residual magnetic fields, wave front distortions, beam splitter efficiency and mean field interactions [15, 43]. The QUANTUS-2 setup is uniquely qualified to explore and mitigate these limitation as the magnetic lensing techniques can be used to tailor the size, density and velocity spread of the clouds.

For a high-precision measurement akin to a UFF test with $\eta = 10^{-13}$, the magnetic field gradient over the interrogation zone needs to be controlled to 50 µG/m [43]. In QUANTUS-2, these demands only apply to a distance of a few centimeters instead of several meters in the case of large atomic fountains. In a compact apparatus, the relevant volume can be probed in its entirety using ultra-cold atoms as magnetometers [142]. Both wave front distortions and beam splitter efficiency scale with the spatial extend of the BEC and its dynamics during the interferometer sequence. Therefore, a well controlled, collimated cloud is the best candidate to evade those limitations. Several systematic phase contributions related to size, density and temperature of the atoms are listed in Table 10. Some of these effects are intertwined and there is generally a trade-off between having small cloud sizes to reduce gravity gradient effects and having sufficiently low densities to suppress mean field interactions. Since the collimation of the lens depends on sufficient initial expansion, mean field effects can be reduced by expanding the ensemble prior to interferometry. One would then have to employ other strategies to mitigate gravity gradient effects such as alterations to the interferometer sequence [143].

The relevance of size, density and temperature dependent effects emphasizes the indispensability of pristine lensing techniques for high-precision matter-wave interferometers. Therefore, the anharmonicities in the lensing potential may present a crucial limitation. While the abberation effects might be manageable on the sensitivity level aimed at with QUANTUS-2, new strategies and designs need to be developed to reduce the intrinsic anharmonicities in chip traps for future sensors. QUANTUS-2 constitutes a pathfinder mission by exploring some of the most relevant systematics of matter-wave interferometry on macroscopic time scales as well as the characteristics and limitations of chip-based sources.

The sensitivity of interferometric measurements is ultimately bounded by the quantum projection noise (QPN) limit [146]. For a single measurement of the acceleration on an ensemble of N atoms using a double diffraction matter-wave interferometer is given by

$$\delta a = \frac{1}{2\,C\,\sqrt{N}\,k_{\mathrm{eff}}\,T^2}, \tag{7.1}$$

where C is the contrast of the interferometer. Assuming perfect contrast and a two-photon momentum transfer, a conservative estimate for the sensitivity limit of an interferometer using the QUANTUS-2 source is

$$\delta a_{\mathrm{cons.}} = 9.82 \times 10^{-11}\,\mathrm{m/s^2}, \tag{7.2}$$

for $N = 10^5$ detected Rb atoms and a total interferometer time of $2T = 2\,\mathrm{s}$. Under optimal conditions this limit may by extended to

$$\delta a_{\mathrm{opt.}} = 5.45 \times 10^{-12}\,\mathrm{m/s^2}, \tag{7.3}$$

using $N = 4{\times}10^5$ atoms and a total time of $2T = 6\,\mathrm{s}$. The sensitivity of a dual species measurement such as a UFF test is ultimately defined by the least sensitive individual interferometer. Therefore, the sensitivity largely depends on the choice for the seconds atomic species and its limitations.

7.2 Potassium Upgrade for Dual Species Interferometry

In the future, the setup will be expanded to dual species operation with the addition of a potassium laser system. It will feature the same functionality as the rubidium system – trapping and cooling atoms from background vapor, absorption imaging, as well as Bragg and Raman interferometry. In principle, all three available potassium isotopes ^{39}K, ^{40}K and ^{41}K can be used. The most likely candidate for a second bosonic species in ^{41}K since it can be cooled to quantum degeneracy directly through RF evaporation, the same technique used for ^{87}Rb [147]. ^{41}K also has the highest chances to compete with the source performance of ^{87}Rb atoms. The bosonic ^{39}K has the disadvantage of attractive interactions that would need to be manipulated using a Feshbach resonance and a strong magnetic field [148], making it the most undesirable of the three. The fermionic ^{40}K can be cooled to a degenerate Fermi gas using ^{87}Rb as a sympathetic coolant, which has already been demonstrated in an atom chip based setup [149]. The most likely candidates for the use in a dual species UFF test are ^{41}K, for usability and miscibility reasons, and ^{40}K, opening up the opportunity to compare the free fall of bosons to fermions.

7.3 Future Microgravity Missions

The ability to demonstrate high-flux sources for mobile devices is at the heart of current sensor proposals [8, 13, 15]. All experiments rely on a competitive source atom number of at least10^6 atoms and interferometer times of several seconds. Thus, the compact and robust source design presented in this thesis is a likely candidate for future experiments.

The QUANTUS-2 design was already adapted for a third generation apparatus within the QUANTUS collaboration that is designed for operation on a ballistic rocket [109] and aims to implement the tools developed by QUANTUS-2 on timescales larger than nine seconds in up to six minutes of µg. The launch of the MAIUS-1 mission from the Esrange Space Center in Kiruna, Sweden is anticipated for 2016. The MAIUS-1 payload (see Figure 97) was put in operation using the first generation laser system of QUANTUS-2. The source optimization process was successfully implemented in the rocket payload. In the upcoming month, QUANTUS-2 will perform the necessary pre-studies in µg to develop the methods and automated sequences for a successful mission. Two additional rocket missions with identical source design are currently in development. The MAIUS-2 and -3 missions will pioneer dual-species matter-wave interferometry in space. MAIUS-2 will aim for sequential operation while MAIUS-3 will perform simultaneous measurements. QUANTUS-2 will again serve as a pathfinder mission for potassium and dual-species operation in µg.

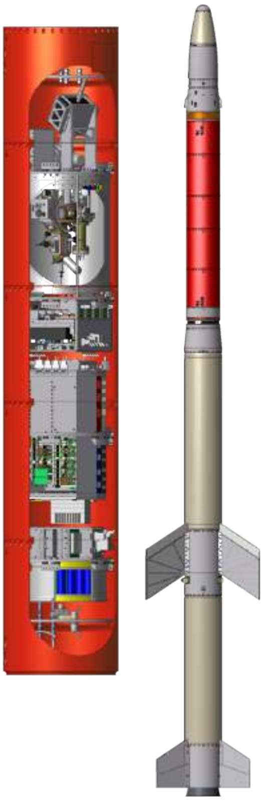

Figure 97: CAD drawing of the MAIUS-1 mission payload and its sounding rocket platform [109].

Next to the three sounding rocket missions, QUANTUS-2 serves as a design baseline for the satellite mission proposal STE-QUEST [150]. Here, a dual-species atom interferometer using the two rubidium isotopes ^{85}Rb and ^{87}Rb shall perform a UFF test with a sensitivity of one part in 10^{15}. A hybrid trap setup consisting of the QUANTUS-2 chip design and a crossed optical dipole trap is proposed to generate and collimate BECs of both isotopes. Using double diffraction techniques, the mixture is probed for a total interferometer time of $2T = 10\,\mathrm{s}$. The satellite is to be operated on a highly elliptical orbit for a mission time of up to five years.

7.4 Other Applications

The compact BEC source system presented in this thesis is not only of interest for mobile applications but any experiment that benefits from high repetition rates. The reduction of the BEC production time by one order of magnitude immediately leads to a significant improvement on the sensitivity of atom interferometers, a field where great efforts are made to design machines with high data rate [151]. It is also of great interest for studying non-classical correlations in BECs and hence for quantum optics experiments with atoms in general.

State-of-the-art quantum enhanced magnetometers [152–154] would be three times to one order of magnitude more sensitive, reaching the sub-$\mathrm{pT}/\sqrt{\mathrm{Hz}}$ regime. Any experiment requiring large statistics, for example to monitor correlations in quantum many-body systems [155, 156], would dramatically benefit from such a source by dividing the total time to take the data by a factor of 3 to 10. However, the use of the source is not restricted to fundamental physics, but provides a new tool for earth observation with improved accuracy in geodesy and geophysics.

A transportable quantum gravimeter (QG-1) is currently in development within the collaborative research center geoQ. The design of the apparatus is heavily based on the QUANTUS-2 source setup. The experiment is poised to perform absolute gravimetry with quasi-continuous measurements to enable monitoring oceanic, atmospheric and hydrological mass variations as well as solid Earth processes [157].

7.5 Summary

Compact chip-based BEC machines are promising sources for high-precision quantum sensors. The robustness and maturity of the technologies pave the way for quantum gas experiments in field operation and in space. The QUANTUS-2 setup is in a unique position to routinely access excellent microgravity conditions and explore the potential of quantum sensors in new parameter ranges that are inaccessible in ground-based devices. It will continue to act as a pathfinder mission for future space experiments and develop the tools and strategies for tests of fundamental physics beyond the lab environment.

Bibliography

[1] M. de Angelis, A. Bertoldi, L. Cacciapuoti, A. Giorgini, G. Lamporesi, M. Prevedelli, G. Saccorotti, F. Sorrentino, and G. M. Tino. “Precision gravimetry with atomic sensors”. *Measurement Science and Technology* 20.2 (2009), p. 022001. DOI: `10.1088/0957-0233/20/2/022001`.

[2] R. Bouchendira, P. Cladé, S. Guellati-Khélifa, F. Nez, and F. Biraben. “New Determination of the Fine Structure Constant and Test of the Quantum Electrodynamics”. *Phys. Rev. Lett.* 106 (8 2011), p. 080801. DOI: `10.1103/PhysRevLett.106.080801`.

[3] A. D. Ludlow, M. M. Boyd, J. Ye, E. Peik, and P. O. Schmidt. “Optical atomic clocks”. *Rev. Mod. Phys.* 87 (2 2015), pp. 637–701. DOI: `10.1103/RevModPhys.87.637`.

[4] T. van Zoest, N. Gaaloul, Y. Singh, H. Ahlers, W. Herr, S. T. Seidel, W. Ertmer, E. Rasel, M. Eckart, E. Kajari, S. Arnold, G. Nandi, W. P. Schleich, R. Walser, A. Vogel, K. Sengstock, K. Bongs, W. Lewoczko-Adamczyk, M. Schiemangk, T. Schuldt, A. Peters, T. Könemann, H. Müntinga, C. Lämmerzahl, H. Dittus, T. Steinmetz, T. W. Hänsch, and J. Reichel. “Bose-Einstein Condensation in Microgravity”. *Science* 328.5985 (2010), pp. 1540–1543. DOI: `10.1126/science.1189164`.

[5] J. Rudolph, N. Gaaloul, Y. Singh, H. Ahlers, W. Herr, T. A. Schulze, S. T. Seidel, C. Rode, V. Schkolnik, W. Ertmer, E. M. Rasel, H. Müntinga, T. Könemann, A. Resch, S. Herrmann, C. Lämmerzahl, T. van Zoest, H. Dittus, A. Vogel, A. Wenzlawski, K. Sengstock, N. Meyer, K. Bongs, M. Krutzik, W. Lewoczko-Adamczyk, M. Schiemangk, A. Peters, M. Eckart, E. Kajari, S. Arnold, G. Nandi, W. P. Schleich, R. Walser, T. Steinmetz, T. W. Hänsch, and J. Reichel. “Degenerate quantum gases in microgravity”. *Microgravity Science and Technology* 23.3 (2011), pp. 287–292. DOI: `10.1007/s12217-010-9247-0`.

[6] R. Geiger, V. Ménoret, G. Stern, N. Zahzam, P. Cheinet, B. Battelier, A. Villing, F. Moron, M. Lours, Y. Bidel, A. Bresson, A. Landragin, and P. Bouyer. “Detecting inertial effects with airborne matter-wave interferometry”. *Nat. Comm.* 2 (2011), p. 474. DOI: `10.1038/ncomms1479`.

[7] C. Schubert, J. Hartwig, H. Ahlers, K. Posso-Trujillo, N. Gaaloul, U. Velte, A. Landragin, A. Bertoldi, B. Battelier, P. Bouyer, F. Sorrentino, G. M. Tino, M. Krutzik, A. Peters, S. Herrmann, C. Lämmerzahl, L. Cacciapouti, E. Rocco, K. Bongs, W. Ertmer, and E. M. Rasel. "Differential atom interferometry with ^{8}7Rb and ^{8}5Rb for testing the UFF in STE-QUEST" (2013). arXiv: `1312.5963 [physics.atom-ph]`.

[8] J. Williams, S.-w. Chiow, N. Yu, and H. Müller. "Quantum test of the equivalence principle and space-time aboard the International Space Station". *New Journal of Physics* 18.2 (2016), p. 025018. DOI: `10.1088/1367-2630/18/2/025018`.

[9] N. Yu, J. Kohel, J. Kellogg, and L. Maleki. "Development of an atom-interferometer gravity gradiometer for gravity measurement from space". English. *Applied Physics B* 84.4 (2006), pp. 647–652. ISSN: 0946-2171. DOI: `10.1007/s00340-006-2376-x`.

[10] S. Dimopoulos, P. W. Graham, J. M. Hogan, and M. A. Kasevich. "Testing General Relativity with Atom Interferometry". *Phys. Rev. Lett.* 98 (11 2007), p. 111102. DOI: `10.1103/PhysRevLett.98.111102`.

[11] H. Müller, S.-w. Chiow, S. Herrmann, S. Chu, and K.-Y. Chung. "Atom-Interferometry Tests of the Isotropy of Post-Newtonian Gravity". *Phys. Rev. Lett.* 100 (3 2008), p. 031101. DOI: `10.1103/PhysRevLett.100.031101`.

[12] K.-Y. Chung, S.-w. Chiow, S. Herrmann, S. Chu, and H. Müller. "Atom interferometry tests of local Lorentz invariance in gravity and electrodynamics". *Phys. Rev. D* 80 (1 2009), p. 016002. DOI: `10.1103/PhysRevD.80.016002`.

[13] J. M. Hogan, D. M. Johnson, S. Dickerson, T. Kovachy, A. Sugarbaker, S.-w. Chiow, P. W. Graham, M. A. Kasevich, B. Saif, S. Rajendran, P. Bouyer, B. D. Seery, L. Feinberg, and R. Keski-Kuha. "An atomic gravitational wave interferometric sensor in low earth orbit (AGIS-LEO)". *General Relativity and Gravitation* 43.7 (2011), pp. 1953–2009. DOI: `10.1007/s10714-011-1182-x`.

[14] G. Tino, F. Sorrentino, D. Aguilera, B. Battelier, A. Bertoldi, Q. Bodart, K. Bongs, P. Bouyer, C. Braxmaier, L. Cacciapuoti, N. Gaaloul, N. Gürlebeck, M. Hauth, S. Herrmann, M. Krutzik, A. Kubelka, A. Landragin, A. Milke, A. Peters, E. Rasel, E. Rocco, C. Schubert, T. Schuldt, K. Sengstock, and A. Wicht. "Precision Gravity Tests with Atom Interferometry in Space". *Nuclear Physics B - Proceedings Supplements* 243–244 (2013). Proceedings of the IV International Conference on Particle and Fundamental Physics in SpaceProceedings of the IV International Conference on Particle and Fundamental Physics in Space, pp. 203–217. ISSN: 0920-5632. DOI: `10.1016/j.nuclphysbps.2013.09.023`.

[15] D. N. Aguilera, H. Ahlers, B. Battelier, A. Bawamia, A. Bertoldi, R. Bondarescu, K. Bongs, P. Bouyer, C. Braxmaier, L. Cacciapuoti, C. Chaloner, M. Chwalla, W. Ertmer, M. Franz, N. Gaaloul, M. Gehler, D. Gerardi, L. Gesa, N. Gürlebeck, J. Hartwig, M. Hauth, O. Hellmig, W. Herr, S. Herrmann, A. Heske, A. Hinton, P. Ireland, P. Jetzer, U. Johann, M. Krutzik, A. Kubelka, C. Lämmerzahl, A. Landragin, I. Lloro, D. Massonnet, I. Mateos, A. Milke, M. Nofrarias, M. Oswald, A. Peters, K. Posso-Trujillo, E. Rasel, E. Rocco, A. Roura, J. Rudolph, W. Schleich, C. Schubert, T. Schuldt, S. Seidel, K. Sengstock, C. F. Sopuerta, F. Sorrentino, D. Summers, G. M. Tino, C. Trenkel, N. Uzunoglu, W. von Klitzing, R. Walser, T. Wendrich, A. Wenzlawski, P. Weßels, A. Wicht, E. Wille, M. Williams, P. Windpassinger, and N. Zahzam. "STE-QUEST - A test of the universality of free fall using cold atom interferometry". *Classical and Quantum Gravity* 31.11 (2014), p. 115010. DOI: `10.1088/0264-9381/31/11/115010`.

[16] P. Hamilton, M. Jaffe, P. Haslinger, Q. Simmons, H. Müller, and J. Khoury. "Atom-interferometry constraints on dark energy". *Science* 349.6250 (2015), pp. 849–851. DOI: `10.1126/science.aaa8883`.

[17] C. M. Will. "The Confrontation between General Relativity and Experiment". *Living Reviews in Relativity* 9.3 (2006). DOI: `10.12942/lrr-2006-3`.

[18] F. W. Hehl, P. von der Heyde, G. D. Kerlick, and J. M. Nester. "General relativity with spin and torsion: Foundations and prospects". *Rev. Mod. Phys.* 48 (3 1976), pp. 393–416. DOI: `10.1103/RevModPhys.48.393`.

[19] M. A. Hohensee, H. Müller, and R. B. Wiringa. "Equivalence Principle and Bound Kinetic Energy". *Phys. Rev. Lett.* 111 (15 2013), p. 151102. DOI: `10.1103/PhysRevLett.111.151102`.

[20] L. de Broglie. "The reinterpretation of wave mechanics". English. *Foundations of Physics* 1.1 (1970), pp. 5–15. ISSN: 0015-9018. DOI: `10.1007/BF00708650`.

[21] A. D. Cronin, J. Schmiedmayer, and D. E. Pritchard. "Optics and interferometry with atoms and molecules". *Rev. Mod. Phys.* 81 (3 2009), pp. 1051–1129. DOI: `10.1103/RevModPhys.81.1051`.

[22] J. B. Fixler, G. T. Foster, J. M. McGuirk, and M. A. Kasevich. "Atom Interferometer Measurement of the Newtonian Constant of Gravity". *Science* 315.74 (2007), pp. 74–77. DOI: `10.1126/science.1135459`.

[23] G. Lamporesi, A. Bertoldi, L. Cacciapuoti, M. Prevedelli, and G. M. Tino. "Determination of the Newtonian Gravitational Constant Using Atom Interferometry". *Phys. Rev. Lett.* 100 (5 2008), p. 050801. DOI: `10.1103/PhysRevLett.100.050801`.

[24] A. Peters, K. Y. Chung, and S. Chu. “Measurement of gravitational acceleration by dropping atoms”. *Nature* 400 (1999), pp. 849–852. DOI: `10.1038/23655`.

[25] J. E. Debs, P. A. Altin, T. H. Barter, D. Döring, G. R. Dennis, G. McDonald, R. P. Anderson, J. D. Close, and N. P. Robins. “Cold-atom gravimetry with a Bose-Einstein condensate”. *Phys. Rev. A* 84 (3 2011), p. 033610. DOI: `10.1103/PhysRevA.84.033610`.

[26] A. Louchet-Chauvet, T. Farah, Q. Bodart, A. Clairon, A. Landragin, S. Merlet, and F. Pereira Dos Santos. “The influence of transverse motion within an atomic gravimeter”. *New Journal of Physics* 13.6 (2011), p. 065025. DOI: `10.1088/1367-2630/13/6/065025`.

[27] D. S. Durfee, Y. K. Shaham, and M. A. Kasevich. “Long-Term Stability of an Area-Reversible Atom-Interferometer Sagnac Gyroscope”. *Phys. Rev. Lett.* 97 (24 2006), p. 240801. DOI: `10.1103/PhysRevLett.97.240801`.

[28] J. K. Stockton, X. Wu, and M. A. Kasevich. “Bayesian estimation of differential interferometer phase”. *Phys. Rev. A* 76 (3 2007), p. 033613. DOI: `10.1103/PhysRevA.76.033613`.

[29] A. Gauguet, B. Canuel, T. Lévèque, W. Chaibi, and A. Landragin. “Characterization and limits of a cold-atom Sagnac interferometer”. *Phys. Rev. A* 80 (6 2009), p. 063604. DOI: `10.1103/PhysRevA.80.063604`.

[30] K. Takase. “Presicion rotation rate measurements with a mobile atom interferometer”. PhD thesis. Stanford University, Stanford, CA, 2008.

[31] G. Tackmann, P. Berg, C. Schubert, S. Abend, M. Gilowski, W. Ertmer, and E. M. Rasel. “Self-alignment of a compact large-area atomic Sagnac interferometer”. *New Journal of Physics* 14.1 (2012), p. 015002. DOI: `10.1088/1367-2630/14/1/015002`.

[32] P. R. Berman. *Atom Interferometry*. Academic Press, San Diego, CA, 1997.

[33] M. Kasevich and S. Chu. “Atomic interferometry using stimulated Raman transitions”. *Phys. Rev. Lett.* 67 (2 1991), pp. 181–184. DOI: `10.1103/PhysRevLett.67.181`.

[34] P. J. Martin, B. G. Oldaker, A. H. Miklich, and D. E. Pritchard. “Bragg scattering of atoms from a standing light wave”. *Phys. Rev. Lett.* 60 (6 1988), pp. 515–518. DOI: `10.1103/PhysRevLett.60.515`.

[35] H. Müller, S.-w. Chiow, S. Herrmann, and S. Chu. “Atom Interferometers with Scalable Enclosed Area”. *Phys. Rev. Lett.* 102 (24 2009), p. 240403. DOI: `10.1103/PhysRevLett.102.240403`.

[36] P. Cladé, S. Guellati-Khélifa, F. ç. Nez, and F. ç. Biraben. “Large Momentum Beam Splitter Using Bloch Oscillations”. *Phys. Rev. Lett.* 102 (24 2009), p. 240402. DOI: `10.1103/PhysRevLett.102.240402`.

[37] R. Charrière, M. Cadoret, N. Zahzam, Y. Bidel, and A. Bresson. "Local gravity measurement with the combination of atom interferometry and Bloch oscillations". *Phys. Rev. A* 85 (1 2012), p. 013639. DOI: `10.1103/PhysRevA.85.013639`.

[38] G. D. McDonald, C. C. N. Kuhn, S. Bennetts, J. E. Debs, K. S. Hardman, M. Johnsson, J. D. Close, and N. P. Robins. "$80\hbar k$ momentum separation with Bloch oscillations in an optically guided atom interferometer". *Phys. Rev. A* 88 (5 2013), p. 053620. DOI: `10.1103/PhysRevA.88.053620`.

[39] H. Müller, S.-w. Chiow, Q. Long, S. Herrmann, and S. Chu. "Atom Interferometry with up to 24-Photon-Momentum-Transfer Beam Splitters". *Phys. Rev. Lett.* 100 (18 2008), p. 180405. DOI: `10.1103/PhysRevLett.100.180405`.

[40] S.-w. Chiow, T. Kovachy, H.-C. Chien, and M. A. Kasevich. "$102\hbar k$ Large Area Atom Interferometers". *Phys. Rev. Lett.* 107 (13 2011), p. 130403. DOI: `10.1103/PhysRevLett.107.130403`.

[41] S. M. Dickerson, J. M. Hogan, A. Sugarbaker, D. M. S. Johnson, and M. A. Kasevich. "Multiaxis Inertial Sensing with Long-Time Point Source Atom Interferometry". *Phys. Rev. Lett.* 111 (8 2013), p. 083001. DOI: `10.1103/PhysRevLett.111.083001`.

[42] L. Zhou, Z. Xiong, W. Yang, B. Tang, W. Peng, K. Hao, R. Li, M. Liu, J. Wang, and M. Zhan. "Development of an atom gravimeter and status of the 10-meter atom interferometer for precision gravity measurement". English. *General Relativity and Gravitation* 43.7 (2011), pp. 1931–1942. ISSN: 0001-7701. DOI: `10.1007/s10714-011-1167-9`.

[43] J. Hartwig, S. Abend, C. Schubert, D. Schlippert, H. Ahlers, K. Posso-Trujillo, N. Gaaloul, W. Ertmer, and E. M. Rasel. "Testing the universality of free fall with rubidium and ytterbium in a very large baseline atom interferometer". *New Journal of Physics* 17.3 (2015), p. 035011. DOI: `10.1088/1367-2630/17/3/035011`.

[44] T. Lévèque, A. Gauguet, F. Michaud, F. Pereira Dos Santos, and A. Landragin. "Enhancing the Area of a Raman Atom Interferometer Using a Versatile Double-Diffraction Technique". *Phys. Rev. Lett.* 103 (8 2009), p. 080405. DOI: `10.1103/PhysRevLett.103.080405`.

[45] N. Malossi, Q. Bodart, S. Merlet, T. Lévèque, A. Landragin, and F. P. D. Santos. "Double diffraction in an atomic gravimeter". *Phys. Rev. A* 81 (1 2010), p. 013617. DOI: `10.1103/PhysRevA.81.013617`.

[46] H. Ahlers, H. Müntinga, A. Wenzlawski, M. Krutzik, G. Tackmann, S. Abend, N. Gaaloul, E. Giese, A. Roura, R. Kuhl, C. Lämmerzahl, A. Peters, P. Windpassinger, K. Sengstock, W. P. Schleich, W. Ertmer, and E. M. Rasel. "Double Bragg Interferometry". *Phys. Rev. Lett.* 116 (17 2016), p. 173601. DOI: `10.1103/PhysRevLett.116.173601`.

[47] S. S. Szigeti, J. E. Debs, J. J. Hope, N. P. Robins, and J. D. Close. "Why momentum width matters for atom interferometry with Bragg pulses". *New Journal of Physics* 14.2 (2012), p. 023009. DOI: `10.1088/1367-2630/14/2/023009`.

[48] W. Ketterle, D. S. Durfee, and D. M. Stamper-Kurn. "Making, probing and understanding Bose-Einstein condensates". *Proceedings of the International School of Physics "Enrico Fermi", Course CXL, edited by M. Inguscio, S. Stringari and C.E. Wieman* (1999), pp. 67–176. DOI: `10.3254/978-1-61499-225-7-67`.

[49] T. Kovachy, J. M. Hogan, A. Sugarbaker, S. M. Dickerson, C. A. Donnelly, C. Overstreet, and M. A. Kasevich. "Matter Wave Lensing to Picokelvin Temperatures". *Phys. Rev. Lett.* 114 (14 2015), p. 143004. DOI: `10.1103/PhysRevLett.114.143004`.

[50] J. G. Williams, S. G. Turyshev, and D. H. Boggs. "Progress in Lunar Laser Ranging Tests of Relativistic Gravity". *Phys. Rev. Lett.* 93 (26 2004), p. 261101. DOI: `10.1103/PhysRevLett.93.261101`.

[51] S. Schlamminger, K.-Y. Choi, T. A. Wagner, J. H. Gundlach, and E. G. Adelberger. "Test of the Equivalence Principle Using a Rotating Torsion Balance". *Phys. Rev. Lett.* 100 (4 2008), p. 041101. DOI: `10.1103/PhysRevLett.100.041101`.

[52] S. Merlet, Q. Bodart, N. Malossi, A. Landragin, F. P. D. Santos, O. Gitlein, and L. Timmen. "Comparison between two mobile absolute gravimeters: optical versus atomic interferometers". *Metrologia* 47.4 (2010), p. L9. DOI: `10.1088/0026-1394/47/4/L01`.

[53] L. Zhou, S. Long, B. Tang, X. Chen, F. Gao, W. Peng, W. Duan, J. Zhong, Z. Xiong, J. Wang, Y. Zhang, and M. Zhan. "Test of Equivalence Principle at 10^{-8} Level by a Dual-Species Double-Diffraction Raman Atom Interferometer". *Phys. Rev. Lett.* 115 (1 2015), p. 013004. DOI: `10.1103/PhysRevLett.115.013004`.

[54] M. G. Tarallo, T. Mazzoni, N. Poli, D. V. Sutyrin, X. Zhang, and G. M. Tino. "Test of Einstein Equivalence Principle for 0-Spin and Half-Integer-Spin Atoms: Search for Spin-Gravity Coupling Effects". *Phys. Rev. Lett.* 113 (2 2014), p. 023005. DOI: `10.1103/PhysRevLett.113.023005`.

[55] D. Schlippert, J. Hartwig, H. Albers, L. L. Richardson, C. Schubert, A. Roura, W. P. Schleich, W. Ertmer, and E. M. Rasel. "Quantum Test of the Universality of Free Fall". *Phys. Rev. Lett.* 112 (20 2014), p. 203002. DOI: `10.1103/PhysRevLett.112.203002`.

[56] H. Müntinga, H. Ahlers, M. Krutzik, A. Wenzlawski, S. Arnold, D. Becker, K. Bongs, H. Dittus, H. Duncker, N. Gaaloul, C. Gherasim, E. Giese, C. Grzeschik, T. W. Hänsch, O. Hellmig, W. Herr, S. Herrmann, E. Kajari, S. Kleinert, C. Lämmerzahl, W. Lewoczko-Adamczyk, J. Malcolm, N. Meyer, R. Nolte, A. Peters, M. Popp, J. Reichel, A. Roura, J. Rudolph, M. Schiemangk, M. Schneider, S. T. Seidel, K. Sengstock, V. Tamma, T.

Valenzuela, A. Vogel, R. Walser, T. Wendrich, P. Windpassinger, W. Zeller, T. van Zoest, W. Ertmer, W. P. Schleich, and E. M. Rasel. “Interferometry with Bose-Einstein Condensates in Microgravity”. *Phys. Rev. Lett.* 110 (9 2013), p. 093602. DOI: `10.1103/PhysRevLett.110.093602`.

[57] ZARM. *Center of Applied Space Technology and Microgravity.* `https://www.zarm.uni-bremen.de/`.

[58] T. van Zoest. “Realisierung erster quantenentarteter Gase unter Schwerelosigkeit”. PhD thesis. Leibniz Universität Hannover, 2008.

[59] D. Becker. “Realisierung eines kompakten und frequenzstabilen Diodenlasersystems für die Lasermanipulation von Kalium”. Bachelor Thesis. Leibniz Universität Hannover, 2009.

[60] V. Schkolnik. “Realisierung eines kompakten und schmalbandigen Diodenlasersystems zur Kühlung und Manipulation von Rubidium”. Diploma Thesis. Leibniz Universität Hannover, 2010.

[61] J. Rudolph. “Towards atom interferometry in microgravity”. Diploma Thesis. Leibniz Universität Hannover, 2010.

[62] M. Rabinovic. “Vorbereitung der Inbetriebnahme der 2D+ MOT des Experiments QUANTUS-II”. Bachelor Thesis. Leibniz Universität Hannover, 2010.

[63] D. Becker. “Demonstration einer neuartigen kompakten chip-basierten Quelle kalter Atome”. Master Thesis. Leibniz Universität Hannover, 2011.

[64] P. Jahn. “Aufbau eines Lasersystems zur Manipulation und Detektion von Kaliumatomen”. Bachelor Thesis. Leibniz Universität Hannover, 2011.

[65] W. Herr. “Eine kompakte Quelle quantenentarteter Gase hohen Flusses für die Atominterferometrie unter Schwerelosigkeit”. PhD thesis. Leibniz Universität Hannover, 2013.

[66] *ZARM Drop Tower Bremen User Manual.* Available at `https://www.zarm.uni-bremen.de/`. Drop Tower Operation and Service Company ZARM FABmbH. 2012.

[67] X. Baillard, A. Gauguet, S. Bize, P. Lemonde, P. Laurent, A. Clairon, and P. Rosenbusch. “Interference-filter-stabilized external-cavity diode lasers”. *Optics Communications* 266.2 (2006), pp. 609–613. DOI: `10.1016/j.optcom.2006.05.011`.

[68] M. Gilowski, C. Schubert, M. Zaiser, W. Herr, T. Wübbena, T. Wendrich, T. Müller, E. M. Rasel, and W. Ertmer. “Narrow bandwidth interference filter-stabilized diode laser systems for the manipulation of neutral atoms”. *Opt. Commun.* 280 (2007), pp. 443–447. DOI: `10.1016/j.optcom.2007.08.043`.

[69] D. W. Preston, C. E. Wieman, and K. M. Siegbahn. “Doppler free-saturated absorption spectroscopy: Laser spectroscopy”. *Am. J. Phys* 64.11 (1996), pp. 1432–1436. DOI: `10.1119/1.18457`.

[70] C. Grzeschik. PhD thesis. Humboldt-Universität zu Berlin, 2016.

[71] D. A. Steck. *Rubidium 87 D Line Data*. `http://steck.us/alkalidata/`.

[72] J. Reichel, W. Hänsel, and T. W. Hänsch. “Atomic Micromanipulation with Magnetic Surface Traps”. *Phys. Rev. Lett.* 83 (17 1999), p. 3398. DOI: `10.1103/PhysRevLett.83.3398`.

[73] S. Wildermuth, P. Krüger, C. Becker, M. Brajdic, S. Haupt, A. Kasper, R. Folman, and J. Schmiedmayer. “Optimized magneto-optical trap for experiments with ultracold atoms near surfaces”. *Phys. Rev. A* 69 (3 2004), p. 030901. DOI: `10.1103/PhysRevA.69.030901`.

[74] F. Reinhard. “Design and Construction of an Atomic Clock on an Atom Chip”. PhD thesis. Laboratoire Kastler Brossel, SYRTE (Observatoire de Paris), 2009.

[75] A. Grote. “Ultracold ^{87}Rb: From quantum metrology to two photon ionisation”. PhD thesis. Universität Hamburg, 2016.

[76] T. Könemann. “Konzeption, Entwicklung und Umsetzung von atomoptischen Fallturmexperimenten fur den Einsatz unter Schwerelosigkeit am Fallturm Bremen”. PhD thesis. Universität Bremen, 2009.

[77] T. Wendrich. *LASUS – Laser Systeme unter Schwerelosigkeit*. `http://www.iqo.uni-hannover.de/552.html`.

[78] M. A. Popp. PhD thesis. Leibniz Universität Hannover, 2016.

[79] T. Sternke. PhD thesis. Universität Bremen, 2016.

[80] R. Storn and K. Price. “Differential evolution - a simple and efficient heuristic for global optimization over continuous spaces”. *J. Glo. Opt.* 11 (1997), pp. 341–359. DOI: `10.1023/A:1008202821328`.

[81] K. Price, R. Storn, and J. Lampinen. *Differential Evolution - A Practical Approach to Global Optimization*. Springer-Verlag, 2005. ISBN: 3-540-20950-6. DOI: `10.1007/3-540-31306-0`.

[82] I. Geisel, K. Cordes, J. Mahnke, S. Jöllenbeck, J. Ostermann, J. Arlt, W. Ertmer, and C. Klempt. “Evolutionary optimization of an experimental apparatus”. *Applied Physics Letters* 102.21, 214105 (2013). DOI: `10.1063/1.4808213`.

[83] E. L. Raab, M. Prentiss, A. Cable, S. Chu, and D. E. Pritchard. “Trapping of Neutral Sodium Atoms with Radiation Pressure”. *Phys. Rev. Lett.* 59 (23 1987), pp. 2631–2634. DOI: `10.1103/PhysRevLett.59.2631`.

[84] K. Dieckmann, R. J. C. Spreeuw, M. Weidemüller, and J. T. M. Walraven. “Two-dimensional magneto-optical trap as a source of slow atoms”. *Phys. Rev. A* 58 (5 1998), pp. 3891–3895. DOI: `10.1103/PhysRevA.58.3891`.

[85] S. Chaudhuri, S. Roy, and C. S. Unnikrishnan. “Realization of an intense cold Rb atomic beam based on a two-dimensional magneto-optical trap: Experiments and comparison with simulations”. *Phys. Rev. A* 74 (2 2006), p. 023406. DOI: `10.1103/PhysRevA.74.023406`.

[86] S. Chu, L. Hollberg, J. E. Bjorkholm, A. Cable, and A. Ashkin. “Three-dimensional viscous confinement and cooling of atoms by resonance radiation pressure”. *Phys. Rev. Lett.* 55 (1 1985), pp. 48–51. DOI: `10.1103/PhysRevLett.55.48`.

[87] P. W. H. Pinkse, A. Mosk, M. Weidemüller, M. W. Reynolds, T. W. Hijmans, and J. T. M. Walraven. “Adiabatically Changing the Phase-Space Density of a Trapped Bose Gas”. *Phys. Rev. Lett.* 78 (6 1997), pp. 990–993. DOI: `10.1103/PhysRevLett.78.990`.

[88] S. Haroche, J. C. Gay, and G. Grynberg, eds. *D. E. Pritchard and K. Helmerson and A. G. Martin ”Atom Traps”, in: Proceedings of the 11th International Conference on Atomic Physics*. 179. World Scientific, Singapore. 1989.

[89] K. B. Davis, M.-O. Mewes, M. A. Joffe, M. R. Andrews, and W. Ketterle. “Evaporative Cooling of Sodium Atoms”. *Phys. Rev. Lett.* 74 (26 1995), pp. 5202–5205. DOI: `10.1103/PhysRevLett.74.5202`.

[90] M. H. Anderson, J. R. Ensher, M. R. Matthews, C. E. Wieman, and E. A. Cornell. “Observation of Bose-Einstein Condensation in a Dilute Atomic Vapor”. *Science* 269 (1995), pp. 198–201. DOI: `10.1126/science.269.5221.198`.

[91] J. Simonet. “Optical traps for ultracold metastable Helium atoms”. PhD thesis. Laboratoire Kastler Brossel, Université Pierre et Marie Curie, (Paris VI), 2011.

[92] W. Ketterle and N. J. Van Druten. “Evaporative cooling of trapped atoms”. *Advances in Atomic, Molecular, and Optical Physics* 37 (1996), pp. 181–236. DOI: `10.1016/S1049-250X(08)60101-9`.

[93] G. L. Oppo, S. M. Barnett, E. Riis, and M. Wilkinson, eds. *J. T. M. Walraven “Atomic hydrogen in magnetostatic traps”, in: Quantum Dynamics of Simple Systems*. IOP, Bristol. 1996.

[94] O. J. Luiten, M. W. Reynolds, and J. T. M. Walraven. “Kinetic theory of the evaporative cooling of a trapped gas”. *Phys. Rev. A* 53(1) (1996), pp. 381–389. doi: `10.1103/PhysRevA.53.381`.

[95] D. M. Farkas, K. M. Hudek, E. A. Salim, S. R. Segal, M. B. Squires, and D. Z. Anderson. “A compact, transportable, microchip-based system for high repetition rate production of Bose-Einstein condensates”. *Applied Physics Letters* 96.9, 093102 (2010). doi: `10.1063/1.3327812`.

[96] D. M. Farkas, E. A. Salim, and J. Ramirez-Serrano. “Production of Rubidium Bose-Einstein Condensates at a 1 Hz Rate” (2014). arXiv: `1403.4641v2 [physics.atom-ph]`.

[97] M. Horikoshi and K. Nakagawa. “Atom chip based fast production of Bose-Einstein condensate”. *Applied Physics B* 82.3 (2006), pp. 363–366. issn: 0946-2171. doi: `10.1007/s00340-005-2083-z`.

[98] M. H. T. Extavour, L. J. LeBlanc, T. Schumm, B. Cieslak, S. Myrskog, A. Stummer, S. Aubin, and J. H. Thywissen. “Dual Species Quantum Degeneracy of ^{4}0K and ^{8}7Rb on an Atom Chip”. *AIP Conference Proceedings* 869.1 (2006), pp. 241–249. doi: `10.1063/1.2400654`.

[99] T. Kinoshita, T. Wenger, and D. S. Weiss. “All-optical Bose-Einstein condensation using a compressible crossed dipole trap”. *Phys. Rev. A* 71 (1 2005), p. 011602. doi: `10.1103/PhysRevA.71.011602`.

[100] J.-F. Clément, J.-P. Brantut, M. Robert-de-Saint-Vincent, R. Nyman, A. Aspect, T. Bourdel, and P. Bouyer. “All-optical runaway evaporation to Bose-Einstein condensation”. *Phys. Rev. A* 79 (6 2009), p. 061406. doi: `10.1103/PhysRevA.79.061406`.

[101] S. Stellmer, R. Grimm, and F. Schreck. “Production of quantum-degenerate strontium gases”. *Phys. Rev. A* 87 (1 2013), p. 013611. doi: `10.1103/PhysRevA.87.013611`.

[102] R. Roy, A. Green, R. Bowler, and S. Gupta. “Rapid cooling to quantum degeneracy in dynamically shaped atom traps”. *Phys. Rev. A* 93 (4 2016), p. 043403. doi: `10.1103/PhysRevA.93.043403`.

[103] Q. Bouton, R. Chang, A. L. Hoendervanger, F. Nogrette, A. Aspect, C. I. Westbrook, and D. Clément. “Fast production of Bose-Einstein condensates of metastable helium”. *Phys. Rev. A* 91 (6 2015), p. 061402. doi: `10.1103/PhysRevA.91.061402`.

[104] E. W. Streed, A. P. Chikkatur, T. L. Gustavson, M. Boyd, Y. Torii, D. Schneble, G. K. Campbell, D. E. Pritchard, and W. Ketterle. “Large atom number Bose-Einstein condensate machines”. *Review of Scientific Instruments* 77.2, 023106 (2006). doi: `10.1063/1.2163977`.

[105] Y.-J. Lin, A. Perry, R. Compton, I. Spielman, and J. Porto. “Rapid production of ^{87}Rb Bose-Einstein condensates in a combined magnetic and optical potential”. *Phys. Rev. A* 79 (6 2009), p. 063631. DOI: `10.1103/PhysRevA.79.063631`.

[106] M. M. T. Loy. “Observation of Population Inversion by Optical Adiabatic Rapid Passage”. *Phys. Rev. Lett.* 32 (15 1974), pp. 814–817. DOI: `10.1103/PhysRevLett.32.814`.

[107] S. T. Seidel. “Manipulation von Bose-Einstein-Kondensaten unter Schwerelosigkeit”. Diploma Thesis. Leibniz Universität Hannover, 2009.

[108] J. Rudolph, W. Herr, C. Grzeschik, T. Sternke, A. Grote, M. Popp, D. Becker, H. Müntinga, H. Ahlers, A. Peters, C. Lämmerzahl, K. Sengstock, N. Gaaloul, W. Ertmer, and E. M. Rasel. “A high-flux BEC source for mobile atom interferometers”. *New Journal of Physics* 17.6 (2015), p. 065001. DOI: `10.1088/1367-2630/17/6/065001`.

[109] S. Seidel. “Eine Quelle für die Interferometrie mit Bose-Einstein-Kondensaten auf Höhenforschungsraketen”. PhD thesis. Leibniz Universität Hannover, 2014.

[110] P. von Kampen, U. Kaczmarczik, and H. J. Rath. “The new Drop Tower catapult system”. *Acta Astronautica* 59.1–5 (2006). Space for Inspiration of Humankind, Selected Proceedings of the 56th International Astronautical Federation Congress, Fukuoka, Japan, 17-21 October 2005Space for Inspiration of Humankind, Selected Proceedings of the 56th International Astronautical Federation Congress, Fukuoka, Japan, 17-21 October 2005, pp. 278–283. ISSN: 0094-5765. DOI: `10.1016/j.actaastro.2006.02.041`.

[111] H. Dittus. “Drop tower Bremen: A weightlessness laboratory on Earth”. *Endeavour* 15.2 (1991), pp. 72–78. ISSN: 0160-9327. DOI: `10.1016/S0160-9327(05)80008-0`.

[112] H. Selig, H. Dittus, and C. Lämmerzahl. “Drop Tower Microgravity Improvement Towards the Nano-g Level for the MICROSCOPE Payload Tests”. *Microgravity Science and Technology* 22.4 (2010), pp. 539–549. ISSN: 1875-0494. DOI: `10.1007/s12217-010-9210-0`.

[113] D. S. Jin, J. R. Ensher, M. R. Matthews, C. E. Wieman, and E. A. Cornell. “Collective Excitations of a Bose-Einstein Condensate in a Dilute Gas”. *Phys. Rev. Lett.* 77 (3 1996), pp. 420–423. DOI: `10.1103/PhysRevLett.77.420`.

[114] M.-O. Mewes, M. R. Andrews, N. J. van Druten, D. M. Kurn, D. S. Durfee, C. G. Townsend, and W. Ketterle. “Collective Excitations of a Bose-Einstein Condensate in a Magnetic Trap”. *Phys. Rev. Lett.* 77 (6 1996), pp. 988–991. DOI: `10.1103/PhysRevLett.77.988`.

[115] J.-F. Schaff. “Shortcuts to adiabaticity for ultracold gases”. PhD thesis. Université de Nice-Sophia Antipolis, 2012.

[116] X. Chen, A. Ruschhaupt, S. Schmidt, A. del Campo, D. Guéry-Odelin, and J. G. Muga. "Fast Optimal Frictionless Atom Cooling in Harmonic Traps: Shortcut to Adiabaticity". *Phys. Rev. Lett.* 104 (6 2010), p. 063002. DOI: `10.1103/PhysRevLett.104.063002`.

[117] H. R. Lewis and W. B. Riesenfeld. "An Exact Quantum Theory of the Time-Dependent Harmonic Oscillator and of a Charged Particle in a Time-Dependent Electromagnetic Field". *Journal of Mathematical Physics* 10.8 (1969), pp. 1458–1473. DOI: `10.1063/1.1664991`.

[118] E. Torrontegui, S. Ibáñez, S. Martínez-Garaot, M. Modugno, A. del Campo, D. Guéry-Odelin, A. Ruschhaupt, X. Chen, and J. G. Muga. "Chapter 2 - Shortcuts to Adiabaticity". In: *Advances in Atomic, Molecular, and Optical Physics*. Ed. by P. R. B. Ennio Arimondo and C. C. Lin. Vol. 62. Advances In Atomic, Molecular, and Optical Physics. Academic Press, 2013, pp. 117–169. DOI: `10.1016/B978-0-12-408090-4.00002-5`.

[119] J.-F. Schaff, P. Capuzzi, G. Labeyrie, and P. Vignolo. "Shortcuts to adiabaticity for trapped ultracold gases". *New Journal of Physics* 13.11 (2011), p. 113017. DOI: `10.1088/1367-2630/13/11/113017`.

[120] H. R. Lewis and P. G. L. Leach. "A direct approach to finding exact invariants for one-dimensional time-dependent classical Hamiltonians". *Journal of Mathematical Physics* 23.12 (1982), pp. 2371–2374. DOI: `10.1063/1.525329`.

[121] E. Torrontegui, S. Ibáñez, X. Chen, A. Ruschhaupt, D. Guéry-Odelin, and J. G. Muga. "Fast atomic transport without vibrational heating".*Phys. Rev. A* 83 (1 2011), p. 013415. DOI: `10.1103/PhysRevA.83.013415`.

[122] A. K. Dhara and S. V. Lawande. "Feynman propagator for time-dependent Lagrangians possessing an invariant quadratic in momentum". *Journal of Physics A: Mathematical and General* 17.12 (1984), p. 2423. DOI: `10.1088/0305-4470/17/12/014`.

[123] Y. Kagan, E. L. Surkov, and G. V. Shlyapnikov. "Evolution of a Bose-condensed gas under variations of the confining potential". *Phys. Rev. A* 54 (3 1996), R1753–R1756. DOI: `10.1103/PhysRevA.54.R1753`.

[124] J. G. Muga, X. Chen, A. Ruschhaupt, and D. Guéry-Odelin. "Frictionless dynamics of Bose–Einstein condensates under fast trap variations". *Journal of Physics B: Atomic, Molecular and Optical Physics* 42.24 (2009), p. 241001. DOI: `10.1088/0953-4075/42/24/241001`.

[125] Y. Castin and R. Dum. "Bose-Einstein Condensates in Time Dependent Traps". *Phys. Rev. Lett.* 77 (27 1996), pp. 5315–5319. DOI: `10.1103/PhysRevLett.77.5315`.

[126] E. Torrontegui, X. Chen, M. Modugno, S. Schmidt, A. Ruschhaupt, and J. G. Muga. "Fast transport of Bose–Einstein condensates". *New Journal of Physics* 14.1 (2012), p. 013031. DOI: `10.1088/1367-2630/14/1/013031`.

[127] This ramp was designed and calculated by Robin Corgier (corgier@iqo.uni-hannover.de).

[128] R. M. W. van Bijnen, N. G. Parker, S. J. J. M. F. Kokkelmans, A. M. Martin, and D. H. J. O'Dell. "Collective excitation frequencies and stationary states of trapped dipolar Bose-Einstein condensates in the Thomas-Fermi regime".*Phys. Rev. A* 82 (3 2010), p. 033612. DOI: `10.1103/PhysRevA.82.033612`.

[129] H. Ammann and N. Christensen. "Delta Kick Cooling: A New Method for Cooling Atoms". *Phys. Rev. Lett.* 78 (11 1997), pp. 2088–2091. DOI: `10.1103/PhysRevLett.78.2088`.

[130] C. J. Pethick and H. Smith. *Bose-Einstein condensation in dilute gases*. Cambridge university press, 2002. DOI: `10.1017/CBO9780511802850`.

[131] A. E. Leanhardt, T. A. Pasquini, M. Saba, A. Schirotzek, Y. Shin, D. Kielpinski, D. E. Pritchard, and W. Ketterle. "Cooling Bose-Einstein Condensates Below 500 Picokelvin". *Science* 301.5639 (2003), pp. 1513–1515. DOI: `10.1126/science.1088827`.

[132] G. Condon, A. Fortun, J. Billy, and D. Guéry-Odelin. "Phase-space manipulations of many-body wave functions". *Phys. Rev. A* 90 (6 2014), p. 063616. DOI: `10.1103/PhysRevA.90.063616`.

[133] R. G. Littlejohn. "The semiclassical evolution of wave packets". *Physics Reports* 138 (1986), pp. 193–291. DOI: `10.1016/0370-1573(86)90103-1`.

[134] T. Aoki, T. Kato, Y. Tanami, and H. Nakamatsu. "δ-kick cooling using the Ioffe-Pritchard potential". *Phys. Rev. A* 73 (6 2006), p. 063603. DOI: `10.1103/PhysRevA.73.063603`.

[135] M. Krutzik. "Matter wave interferometry in microgravity". PhD thesis. Humboldt-Universität zu Berlin, 2014.

[136] J. Rudolph, H. Ahlers, and E. M. Rasel. "Cover Picture: Fortschritte der Physik". *Fortschritte der Physik – Progress of Physics* 63.1 – 12 (2015). ISSN: 1521-3978. DOI: `10.1002/prop.201570001`.

[137] M. Schiemangk, K. Lampmann, A. Dinkelaker, A. Kohfeldt, M. Krutzik, C. Kürbis, A. Sahm, S. Spießberger, A. Wicht, G. Erbert, G. Tränkle, and A. Peters. "High-power, micro-integrated diode laser modules at 767 and 780nm for portable quantum gas experiments". *Appl. Opt.* 54.17 (2015), pp. 5332–5338. DOI: `10.1364/AO.54.005332`.

[138] P. Medley, D. M. Weld, H. Miyake, D. E. Pritchard, and W. Ketterle. "Spin Gradient Demagnetization Cooling of Ultracold Atoms". *Phys. Rev. Lett.* 106 (19 2011), p. 195301. DOI: `10.1103/PhysRevLett.106.195301`.

[139] A. S. Oja and O. V. Lounasmaa. "Nuclear magnetic ordering in simple metals at positive and negative nanokelvin temperatures". *Rev. Mod. Phys.* 69 (1 1997), pp. 1–136. DOI: `10.1103/RevModPhys.69.1`.

[140] J. Tuoriniemi and T. Knuuttila. "Nuclear cooling and spin properties of rhodium down to picokelvin temperatures". *Physica B: Condensed Matter* 280.1–4 (2000), pp. 474–478. ISSN: 0921-4526. DOI: `10.1016/S0921-4526(99)01839-6`.

[141] T. Knuuttila. "Nuclear Magnetism and Superconductivity in Rhodium". PhD thesis. Helsinki University of Technology, 2000.

[142] S. Wildermuth, S. Hofferberth, I. Lesanovsky, S. Groth, P. Krüger, J. Schmiedmayer, and I. Bar-Joseph. "Sensing electric and magnetic fields with Bose-Einstein condensates". *Applied Physics Letters* 88.26 (2006), p. 264103. DOI: `10.1063/1.2216932`.

[143] A. Roura, W. Zeller, and W. P. Schleich. "Overcoming loss of contrast in atom interferometry due to gravity gradients". *New Journal of Physics* 16.12 (2014), p. 123012. DOI: `10.1088/1367-2630/16/12/123012`.

[144] S. Dimopoulos, P. W. Graham, J. M. Hogan, and M. A. Kasevich. "General relativistic effects in atom interferometry". *Phys. Rev. D* 78 (4 2008), p. 042003. DOI: `10.1103/PhysRevD.78.042003`.

[145] J. M. Hogan, D. M. S. Johnson, and M. A. Kasevich. "Light-pulse atom interferometry". In: *Atom Optics and Space Physics*. Ed. by E. Arimondo, W. Ertmer, W. P. Schleich, and E. M. Rasel. 2009, p. 411. arXiv: `0806.3261 [physics.atom-ph]`.

[146] W. M. Itano, J. C. Bergquist, J. J. Bollinger, J. M. Gilligan, D. J. Heinzen, F. L. Moore, M. G. Raizen, and D. J. Wineland. "Quantum projection noise: Population fluctuations in two-level systems". *Phys. Rev. A* 47 (5 1993), pp. 3554–3570. DOI: `10.1103/PhysRevA.47.3554`.

[147] T. Kishimoto, J. Kobayashi, K. Noda, K. Aikawa, M. Ueda, and S. Inouye. "Direct evaporative cooling of ^{41}K into a Bose-Einstein condensate". *Phys. Rev. A* 79 (3 2009), p. 031602. DOI: `10.1103/PhysRevA.79.031602`.

[148] C. D'Errico, M. Zaccanti, M. Fattori, G. Roati, M. Inguscio, G. Modugno, and A. Simoni. "Feshbach resonances in ultracold 39 K". *New Journal of Physics* 9.7 (2007), p. 223. DOI: `10.1088/1367-2630/9/7/223`.

[149] S. Aubin, S. Myrskog, M. H. T. Extavour, L. J. LeBlanc, D. McKay, A. Stummer, and J. H. Thywissen. “Rapid sympathetic cooling to Fermi degeneracy on a chip”. *Nature Physics* 2 (2006), pp. 384–387. DOI: `10.1038/nphys309`.

[150] T. Schuldt, C. Schubert, M. Krutzik, L. Bote, N. Gaaloul, J. Hartwig, H. Ahlers, W. Herr, K. Posso-Trujillo, J. Rudolph, S. Seidel, T. Wendrich, W. Ertmer, S. Herrmann, A. Kubelka-Lange, A. Milke, B. Rievers, E. Rocco, A. Hinton, K. Bongs, M. Oswald, M. Franz, M. Hauth, A. Peters, A. Bawamia, A. Wicht, B. Battelier, A. Bertoldi, P. Bouyer, A. Landragin, D. Massonnet, T. Lévèque, A. Wenzlawski, O. Hellmig, P. Windpassinger, K. Sengstock, W. von Klitzing, C. Chaloner, D. Summers, P. Ireland, I. Mateos, C. F. Sopuerta, F. Sorrentino, G. M. Tino, M. Williams, C. Trenkel, D. Gerardi, M. Chwalla, J. Burkhardt, U. Johann, A. Heske, E. Wille, M. Gehler, L. Cacciapuoti, N. Gürlebeck, C. Braxmaier, and E. Rasel. “Design of a dual species atom interferometer for space”. *Experimental Astronomy* (2015), pp. 1–40. DOI: `10.1007/s10686-014-9433-y`.

[151] A. V. Rakholia, H. J. McGuinness, and G. W. Biedermann. “Dual-Axis High-Data-Rate Atom Interferometer via Cold Ensemble Exchange”. *Phys. Rev. Applied* 2 (5 2014), p. 054012. DOI: `10.1103/PhysRevApplied.2.054012`.

[152] M. Vengalattore, J. M. Higbie, S. R. Leslie, J. Guzman, L. E. Sadler, and D. M. Stamper-Kurn. “High-Resolution Magnetometry with a Spinor Bose-Einstein Condensate”. *Phys. Rev. Lett.* 98 (20 2007), p. 200801. DOI: `10.1103/PhysRevLett.98.200801`.

[153] W. Muessel, H. Strobel, D. Linnemann, D. B. Hume, and M. K. Oberthaler. “Scalable Spin Squeezing for Quantum-Enhanced Magnetometry with Bose-Einstein Condensates”. *Phys. Rev. Lett.* 113 (10 2014), p. 103004. DOI: `10.1103/PhysRevLett.113.103004`.

[154] C. F. Ockeloen, R. Schmied, M. F. Riedel, and P. Treutlein. “Quantum Metrology with a Scanning Probe Atom Interferometer”. *Phys. Rev. Lett.* 111 (14 2013), p. 143001. DOI: `10.1103/PhysRevLett.111.143001`.

[155] T. Schumm, S. Hofferberth, L. M. Andersson, S. Wildermuth, S. Groth, I. Bar-Joseph, J. Schmiedmayer, and P. Kruger. “Matter-wave interferometry in a double well on an atom chip”. *Nature Physics* 1 (2005), pp. 57–62. DOI: `10.1038/nphys125`.

[156] T. Langen, R. Geiger, M. Kuhnert, B. Rauer, and J. Schmiedmayer. “Local emergence of thermal correlations in an isolated quantum many-body system”. *Nature Physics* 9 (2013), pp. 640–643. DOI: `10.1038/nphys2739`.

[157] geoQ. *Relativistic Geodesy and Gravimetry with Quantum Sensors*. `http://www.geoq.uni-hannover.de/`.

List of Publications

J. Rudolph, W. Herr, C. Grzeschik, T. Sternke, A. Grote et al. - ”A high-flux BEC source for mobile atom interferometers”, New J. Phys. **17**, 065001 (2015),
DOI: `10.1088/1367-2630/17/6/065001`.

T. Schuldt, C. Schubert, M. Krutzik, L.G. Bote et al. - ”Design of a dual species atom interferometer for space”, Exp. Astron. **38**, 1-40 (2015),
DOI: `10.1007/s10686-014-9433-y`.

J. Rudolph, H. Ahlers and E. M. Rasel - ”Cover Picture: Forschritte der Physik”, Forschritte der Physik – Progress of Physics **63**, 1-12 (2015),
DOI: `10.1002/prop.201570001`.

D. N. Aguilera, H. Ahlers, B. Battelier et al. - ”STE-QUEST - Test of the Universality of Free Fall Using Cold Atom Interferometry”, Classical and Quantum Gravity **31**(11), 115010 (2014),
DOI: `10.1088/0264-9381/31/11/115010`.

H. Müntinga, H. Ahlers, M. Krutzik, A. Wenzlawski et al. - ”Interferometry with Bose-Einstein Condensates in Microgravity”, Phys. Rev. Lett. **110**, 093602 (2013),
DOI: `10.1103/PhysRevLett.110.093602`.

M. de Angelis, M. C. Angonin, Q. Beaufils, C. Becker et al. - ”iSense: A Portable Ultracold-Atom-Based Gravimeter”, Procedia Computer Science **7**, 334 - 336 (2011),
DOI: `10.1016/j.procs.2011.09.067`.

J. Rudolph, N. Gaaloul, Y. Singh, H. Ahlers et al. - ”Degenerate Quantum Gases in Microgravity”, Microgravity Sci. Technol. **23**, 3, 287-292 (2011),
DOI: `10.1007/s12217-010-9247-0`.

Acknowledgements

I wish to thank all the people who were involved in making this ambitious project a success. Setting up and operating this experiment has been a team effort every step of the way. Waldemar Herr started designing and planning the device in 2008 and thanks to his foresight, tenacity and attention to detail it grew into one of the best machines of its kind. When I joined the project in July 2009 he had a very clear vision of what were were going to build over the next few years. I am very thankful for his enduring support, from my first day in the lab to helping my edit my thesis seven years later. Many other people were involved in the early stages of the experiment and helped setting up the capsule in Hannover: Vladimir Schkolnik, Dennis Becker, Christina Rode, Mihail Rabinovic, Maike Lachmann, Philipp Jahn and Manuel Popp. The time in Hannover is marked by exciting results like the first MOT in 2011 and the first BEC in 2012. Thank you for your help in bringing the QUANTUS-2 machine to life.

In 2013, the system was prepared for a complete overhaul with new electronics and a new laser system to get ready for the drop tower. A new team started to form with Christoph Grzeschik, Tammo Sternke, Alexander Grote from Berlin, Bremen and Hamburg, respectively. Together we completed the move to Bremen in December 2013, got the system ready for the first drop in July 2014 and the first catapult launch in October 2014. Sitting in the control room and waiting for the first µg images to transfer from the capsule were some of the most suspenseful moments in my life. The time in Bremen leading up to and including the first drop campaigns was without a doubt the most strenuous period. Joined by Christian Deppner in 2014, we successfully completed over 200 drops and managed to get some very promising results that suggest a bright future for the experiment. None of the progress would have been possible without the commitment and dedication of my teammates. Thank you for putting up with me, the long hours, the Monday morning deliveries, the triple drop days, the numerous train rides and the many overnight stays in hotels.

I am indebted to Holger Ahlers, Hauke Müntinga and Naceur Gaaloul for many enlightening discussions, guidance and support over the years. Many of the theoretical models and calculations in this thesis are the product of open and thorough debates with some or all of you. Your

help was invaluable in the publications we have composed over the years. Collaborating with you has been an absolute pleasure. Thank you Ernst Rasel for giving me the opportunity to work on such an exceptional project. Your optimism and trust despite all the setbacks and delays has helped me to stay focused and determined. Thank you for working so hard to enable projects like this, that let us do things no one else in the world is doing. Thank you to Wolfgang Ertmer for mentoring and supporting me over the years.

Thank you to all the members of the QUANTUS team, especially to Thijs Wendrich whose expertise in electronics is indispensable and without whose designs the miniaturization of the system would not have been possible. Thank you to all members of the IQO in Hannover, including the secretarial staff and the workshop crew whose constant support is much appreciated. Thank you to the member of the ZARM in Bremen. A special thank you to Ludger Burlage and Matthias Meyer of the ZARM Droptower Operation and Service Company for managing the tower operations and safely recovering our capsule after every drop.

I am thankful for a wonderful stay in the Kasevich group in Stanford. Working with Mark Kasevich, Jason Hogan, Susannah Dickerson and Alex Sugarbaker has been a fantastic experience and I was able to learn a lot in a very brief time. Thank you to Jakob Reichel and his group in Paris for helping us build our atom chip in their facilities.

Thank you to the DLR for generously funding the QUANTUS projects for over a decade. I would also like to acknowledge financial support in form of a scholarship by the Hannover School for Laser, Optics and Space-Time Research (HALOSTAR) from October 2009 until September 2012.

Vielen Dank an meine Freunde und meine Familie, die mich während meines Studiums und meiner Promotion unterstützt haben. Besonders im schweren letzten Jahr habt ihr mir sehr geholfen und mich nicht aufgeben lassen. Ohne euch hätte ich es nicht geschafft.